Imperial College of Science, Technology and Medicine
Department of Mechanical Engineering

Expander design and optimisation for Electric Turbocompounding and Organic Rankine Cycle systems in waste heat recovery applications

María Eva Álvarez Regueiro

Submitted in part fulfilment of the requirements for the degree of
Doctor of Philosophy in Mechanical Engineering of the University of London and
the Diploma of Imperial College, August, 2023

Declaration of Originality

I declare this thesis to be my own work, and the appropriate citations are included to acknowledge the work of others. Parts of the work have been previously published as conference proceedings; where this is the case this has also been made clear.

María Eva Álvarez Regueiro

Copyright Declaration

Abstract

This thesis investigates the effect 3D blade features and non-radial blading on the performance of radial turbines for waste heat recovery applications. To address the problem, two design methodologies were developed and used for the analysis: a low-order meanline model accounting for non-ideal gas effects and a 3D parametric model coupled with CFD.

The design of expanders for waste heat recovery systems considered in this thesis are electric turbocompounding (ETC) and Organic Ranking cycle (ORC). These are challenging compared to traditional radial turbomachinery as ETC operates at a low-pressure ratio with direct waste heat and ORC operates at a high-pressure ratio with refrigerants.

Meanline modelling was able to predict the efficiency and mass flow of radial turbines both with air and refrigerants as working fluids with a relative root mean square error (RRMSE) of less than 1% between meanline and CFD results. This accuracy was achieved after calibration of the loss coefficients with CFD. Moreover, optimum radial turbine designs were obtained for the ORC and ETC applications achieving total-to-static efficiency of 79.98% and 82.86%, respectively. However, meanline modelling has limitations in predicting losses accurately and capturing the effect of 3D geometry modifications on performance. To overcome the loss prediction limitation, a second calibration of the loss coefficients is suggested by minimising the error between the loss breakdown in meanline and the loss breakdown in CFD. Although the error in loss distribution prediction meanline and CFD decreased after this second calibration, the RRMSE in efficiency increased up to 4.4% and 3.6% in ORC and ETC applications, respectively.

The 3D parametric model coupled with CFD was used to address the meanline model limitation to predict the effect of 3D geometry modifications. For ORC application, the effect of cone angle of the rotor meridional profile was evaluated, while the effect non-radial fibre blading was assessed for the ETC application. The geometry modifications were introduced after finding optimum baseline geometries with the 3D parametric model for the turbines. The efficiency of the optimum designs obtained by 3D parametric model and the meanline approach was similar, showing a 1.3pp increase only for the ORC turbine.

The modification of the cone angle of the ORC rotor for the same meridional profile (same radii, blade angles and blade heights) led to a maximum efficiency difference of 2pp, while the meanline model predicted no difference. The non-radial fibre assessment concluded that lower incidence angles can improve efficiency. The optimum non-radial fibre blade design ($\beta_{blade,4} = 20^{\circ}$) showed an increase of 0.3% in efficiency in single passage simulations compared to the baseline ETC design, which was radial fibred. The improved performance was also demonstrated experimentally at Imperial College's test rig, showing a maximum efficiency increase of 2pp at design point.

Acknowledgements

I would like to express my sincere gratitude to my main supervisor, Prof. Ricardo Martinez-Botas, for his invaluable guidance, support and mentorship throughout my PhD journey. Your expertise, insightful contributions and constructive feedback have been instrumental in shaping my research. I am immensely grateful for the trust you placed in me and the opportunities you provided for me to grow as a researcher.

I would also like to extend my appreciation to my second supervisor, Dr. Maria Esperanza Barrera Medrano, for her crucial role in my research. I am deeply thankful for the time and energy you dedicated to my growth and success. Thanks to UTM team, especially Prof. Srithar Rajoo for being my third supervisor in Malaysia and letting me be part of an international project.

I am grateful to my colleagues from the Turbo Group. Bijie, for all the aerodynamics and CFD knowledge you shared with me. Aakeen, Andrew, Caro, and Pablo, for their support and friendship during the last 4 years. Your camaraderie has made my journey more enjoyable, and I am thankful for the memories we have shared. I would also like to acknowledge Harminder, Chris and Peter for their exceptional help in the lab with experiments. I could not forget the former members of the group, Karim, Karl, Miles, and Xiaofeng for their contributions to my research and for making me feel welcome to the group during the first half of my PhD.

I would like to express my immense gratitude to my friends in London, Clara, Nicolas, and Luca. Your friendship has been a source of comfort and joy, and I am thankful for the memories we have shared. I would also like to thank my friends from Spain for their encouragement and interest in my work throughout my PhD journey. Their support and kindness have been greatly appreciated.

Lastly, I want to thank my parents and family, especially my brother, Carlos, for their love and unwavering support throughout my life and my partner, Manuel. Your support has been a source of strength and happiness, and I am thankful for the unconditional love and understanding you have given me despite the distance.

I am deeply thankful to all these amazing people for their impact on my life and for making this journey possible.

Contents

List of Tables

List of Figures

Nomenclature

Latin Symbols

Δs	Entropy Change
$\dot{S}_{gen}$	Entropy Generation Rate
A	Area
a	Sonic velocity
A_{eff}	Effective area
b	Blade height
c	Velocity in the absolute frame or reference
D, d	Diameter
E	Voltage
h	Enthalpy
$\dot{m}$	Mass flow rate
M	Mach number
N_n	Number of Nozzle Vanes
N_r	Number of Rotor Blades
$Nrpm$	Rotational Speed
p	Pressure

$\dot{W}$	Power output
r	Radius
s_{gen}	Specific Entropy Generation
T	Temperature
τ	Torque
U	Blade tip speed
V	Velocity
w	Velocity in the relative frame or reference
Z_r	Rotor Length
CAE	Computer-aided engineering
CFD	Computational fluid dynamics
ETC	Electric turbocompounding
i	Incidence Angle
K	Loss Coefficient
MTJA	Malaysia and Thailand joint authority
n	Heat Capacity Ratio [-]
ORC	Organic Rankine cycle
pp	Efficiency Percentage Points
TEF	Thermoelectric generation
WHR	Waste heat recovery
z	Axial Position

Greek Symbols

α	Absolute Flow Angle

α_{nozzle}	Nozzle Vane Angle
β	Relative Flow Angle
β_{blade}	Rotor Blade Angle
δ_b	Deviation angle
Δh	Enthalpy drop
ϵ_r	Radial tip clearance
ϵ_z	Axial tip clearance
η	Isentropic efficiency
θ	Circumferential angle
γ	Hub and shroud angles for non-radial blading definition
ω	Angular velocity
PR	Pressure ratio
ψ	Cone angle
ρ	Density
ϕ	Flow coefficient
σ	Standard deviation
ψ	Loading coefficient
ϵ	Turbulence dissipation rate

Subscripts

0	Stagnation conditions
$2, 4, 6$	Turbine stages
act	Actual
cl	Tip Clearance losses

d	Turbulence dissipation
e	Exit Losses
in	In
inc	Incidence losses
iso	Isentropic
$loss$	Internal losses
n	Nozzle losses
opt	Optimum
out	Outlet
p	Passage losses
te	Trailing edge losses
ts	Total-to-static
tt	Total-to-total

Chapter 1

Introduction

This chapter puts in context the research topic of this thesis. First, the overall energy context is presented, showing the large contribution fossil fuels still have in the global energy mix. Some of the areas most difficult to decarbonise are discussed, highlighting the environmental footprint of the Oil & Gas industry in particular.

The industrial project in which this research is framed is explained and the role of waste heat recovery technologies for decarbonisation and energy transition is introduced. Finally, the thesis outline and the scholarly output are summarised in this chapter.

1.1 Background and Context

Since 2012, the primary energy demand has grown 1.3% per annum [3]. Renewables have played an important role in this increase; between 2019 and 2021 the increase in primary energy was entirely driven by renewable energy sources. The energy consumption from fossil fuels remained constant in this period. Oil saw a decrease in demand (-8 EJ) compared to pre-pandemic levels, but this was offset by higher natural gas (5 EJ) and coal (3 EJ) consumption. Figure 1.1 shows the primary energy annual growth in the period 2012-2021 with the shares by fuel in the last 4 years [3–6].

Global primary energy demand has experienced its fastest annual growth in 2021, reaching its highest levels at 595 EJ[1], 5.8% (31 EJ) more than in 2020 and 1.3% (8 EJ) more than pre-pandemic levels [3, 19]. The pandemic hit hard the economy and production worldwide leading to the largest decline in primary energy demand since World War II of 4% (-23 EJ) between 2019 and 2020 [19]. However, the recovery in the global economy after the pandemic has been the main responsible for the rise in energy consumption, particularly in emerging economies, with China accounting for over a third of the primary energy demand growth in 2021. China was also the only country in which energy demand increased between 2019 and 2020, leading to an accumulated rise in primary energy demand of 15 EJ in the 2019-2021 period. On the other hand, for Organisation for Economic Co-operation and Development (OECD) countries the energy demand in 2021 decreased by 8 EJ compared to 2019 levels, despite the annual growth of 10 EJ in 2021.

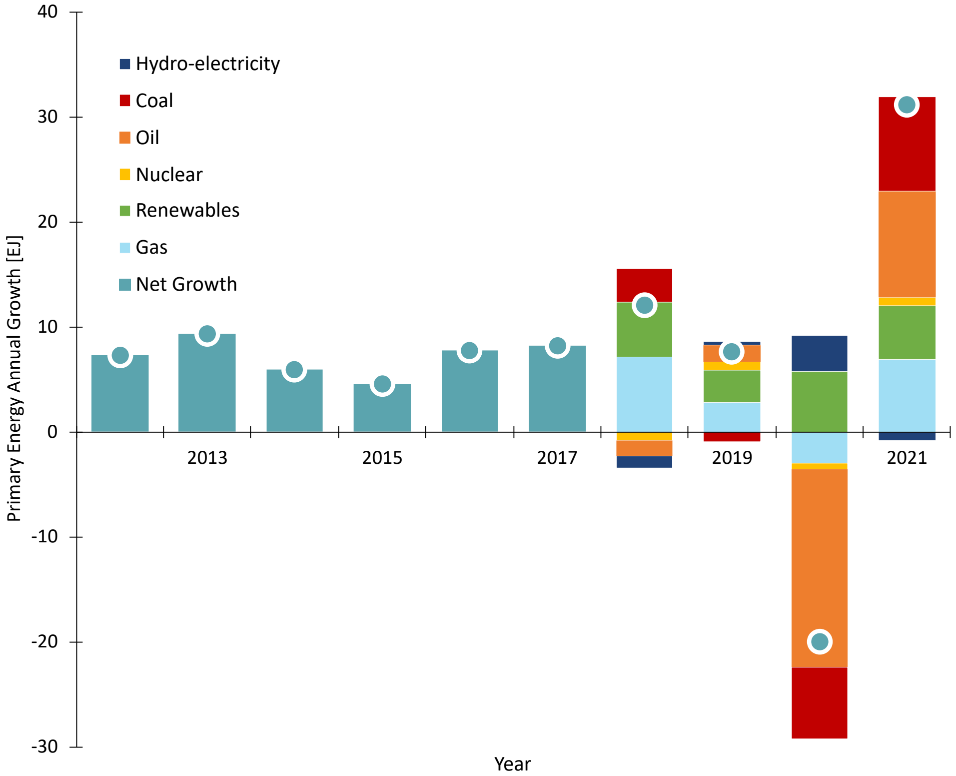

Figure 1.1: Average annual global primary energy demand growth by fuel from 2012 to 2021 [3–6]

Although the use of renewable energy has spread worldwide and fossil fuel demand did not increase, fossil fuels still accounted for over 80% of the primary energy mix in 2019 and 2021 [3, 7], according to the International Energy Agency and BP. Figure 1.2 shows the worldwide primary energy mix by sector and fuel.

---

[1] EJ stands for exajoules and has the following equivalence: $1EJ = 10^9 MJ = 23.9 Mtoe$

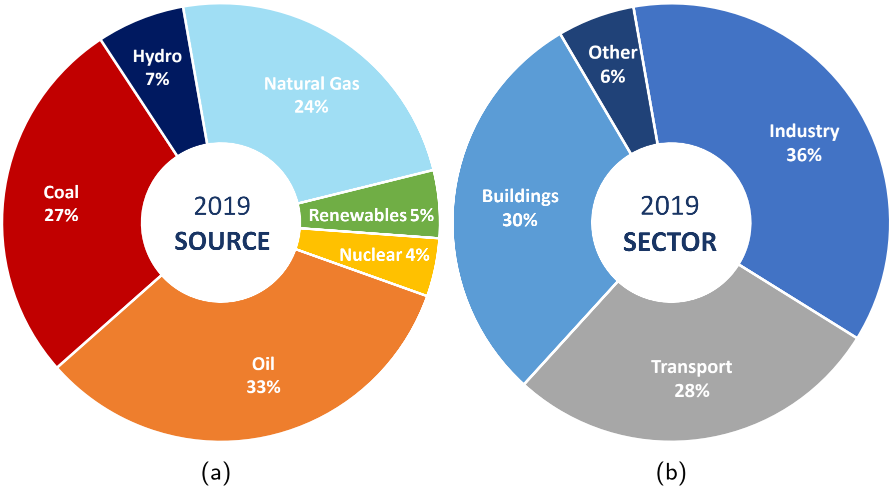

(a) (b)

Figure 1.2: Worldwide consumption of primary energy by fuel and sector in 2019 [3, 7]

Analysing 2019 data to avoid distortion due to the pandemic, fossil fuels, with natural gas at the top, were the primary energy that registered the highest growth. They covered 45% of the global energy demand increase in 2019, as shown in Fig. 1.1. The previous year, 2018, natural gas alone accounted for almost 60% of the primary energy demand increase. Renewables represented the 41% and 44% of the growth in energy demand in 2019 and 2018, respectively. Fossil fuels are primarily used in transportation, industrial and building sectors [5], as shown in Fig. 1.2 (a) in 2019.

The CO_2 emissions from these non-renewable resources are the main contributors to climate change. Furthermore, global CO_2 emissions have risen constantly for many decades due to world economic growth, which encourages energy consumption. Despite the drop in emissions during the pandemic, the global CO_2 is close to the historic 2018-2019 peak [3, 19]. In 2020 the global CO_2 emissions decreased by 5.8% (2 Gt CO_2), which was the largest ever drop and almost five times bigger than the decline produced by the global financial crises in 2009 [19]. In 2021 the global CO_2 emissions reached 33.8 Gt CO_2 0.6% lower than in 2019 [3].

Despite the increase of CO_2 emissions, the efficiency enhancement of energy systems has been one of the most successful measures for emission mitigation during the last decade. Although the rate of improvement has slowed down in the last couple of years due to technology limitations, almost half of the avoided emissions during 2018 were due to energy efficiency enhancement [8], as shown in Fig. 1.3 (a). In 2019, renewable energy sources were the most successful methods, followed by energy efficiency improvements as shown in Fig. 1.3 [7]. Therefore, it is essential to find ways to further reduce the environmental impact of fossil fuels in each sector by making the energy systems that still use these energetic sources more efficient.

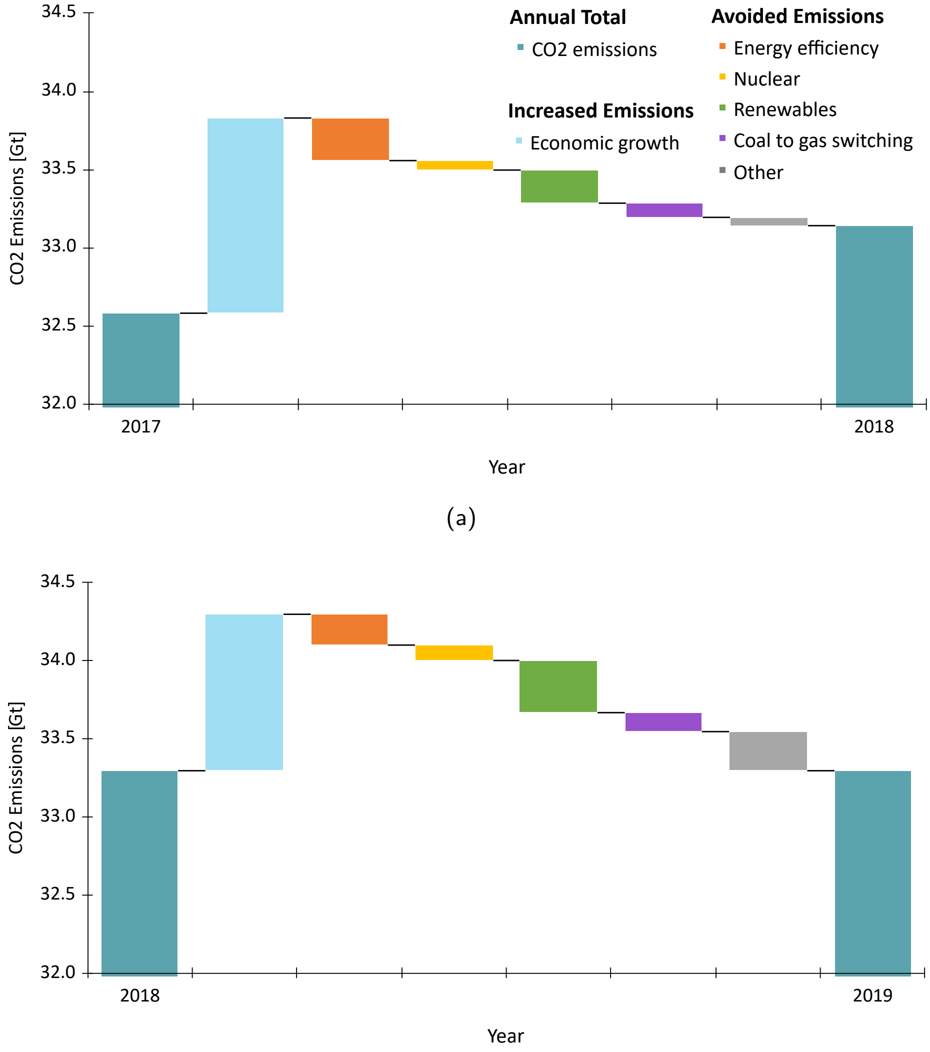

(a)

(b)

Figure 1.3: Change in global energy-related CO_2 emissions and avoided emissions between the periods (a) 2017 to 2018 and (b) 2018 to 2019 [7, 8]

One way to mitigate the impact of fossil fuels in the environment is the implementation of waste heat recovery (WHR) technologies. In this way, electrical energy is generated from waste heat streams currently released to the environment in existing processes. Although WHR has the limitation that there is no technology available today able to recover all the energy in a waste heat stream, it will play an essential role in the decarbonisation of the industry and the transition to renewable energy [20].

WHR technologies have been used in a wide variety of applications that are currently powered by fossil fuels, such as heat-demanding metal, paper pulp, chemical industries [21], transportation [22, 23], electricity generation via fossil fuels, nuclear, thermosolar, biomass, geothermal energy [24–27], natural gas compression stations [28] or refineries [29]. Some of these applications are based on renewable energy, such as geothermal and thermosolar energy generation, thus, research and development of these technologies are in the general interest. One of the areas which are more complicated to decarbonise is the oil and gas industry, the next section introduces the growing environmental footprint of the sector as well as the main challenges of WHR in these applications.

1.2 Oil and Gas Industry Environmental Footprint

The oil and gas sector has a major environmental footprint due to pollutants in discharged process water, seabed effects in the case of offshore fields and greenhouse gas (GHG) emissions. Although CO_2 is the main GHG considered, other gases such as N_2O, CO and unburned hydrocarbons (UHC) must be taken into account due to their high Global Warming Potential (GWP). This means that the greenhouse effect of these other gases is greater than that produced by the same amount of CO_2.

For instance, Norway, which was the 14th oil and gas producer in 2016 [30], has recorded historically the CO_2 emissions from oil and gas industry, which has been the largest CO_2 source sector of the country. In 1990, the offshore oil and gas upstream industry generated 18% of the GHG emissions and in 2016, 25% of the national emissions. Norway's oil and gas production only accounts for 2% of the global energy demand, so it is easy to realise the large GHG footprint of global oil and gas production.

In the upstream industry, the largest source of GHG usually comes from the gas compression substations as well as from the gas turbines and diesel systems producing mechanical, electrical energy and heat to support the processes of the off-shore platform. In addition, flaring, venting and methane leakages also contribute to GHG emissions without producing any power, since these streams are currently being released into the atmosphere.

Nowadays, countries, institutions and oil and gas companies are strongly committed to reducing the carbon footprint of the upstream industry. Initiatives like the Zero Routine Flaring by 2030 introduced by the World Bank have been adopted by companies such as BP or Petronas in their sustainability plans [30, 31].

Furthermore, these plans include strategies such as the use of natural gas as a cleaner option for power generation within the fields, improving energy efficiency and exploring innovative energy solutions like WHR technologies. These technologies can harvest energy from the power system exhausts as well as use the heat in the non-routine flaring when available. This energy solution becomes extremely important in off-shore platforms, where electrical grids, which may transport renewable electrical energy from the mainland, can not reach the fields.

1.3 Waste Heat Recovery in Off-shore Platforms

Low-grade waste heat from industrial processes represents 50% of the total heat generated according to the literature [32]. Commonly, low-grade heat is released into the environment due to the lack of cost-effective and thermally efficient technology. The growing environmental concern about greenhouse gas emissions needs to be focused on the recovery of waste heat to reduce the fuel consumed in industrial processes and mitigate the environmental footprint.

This situation is of significant importance in the offshore oil and gas industry. Offshore facilities are often isolated from the mainland power grid and cannot take advantage of the energy transition to renewables. In addition, these types of platforms have physical space and weight limitations, which is why compact and simple solutions are needed. Maintenance is a complicated and costly task due to the difficulty of reaching offshore platforms, thus, robustness and reliability are essential characteristics of the machinery installed in the facilities.

Nguyen et al. [33] carried out an exergy analysis of offshore platforms in the North Sea and found that the major contributor to exergy destruction is the power system, due to the high temperature of the gas turbines exhaust. Gas turbines often run at partial load to reduce the risk of failure, which means lower performance and more waste heat in the exhaust. They highlight the potential of the waste heat recovery to increase the overall platform efficiency and suggest the use of steam cycles or ORC [34].

The literature on waste heat recovery literature on offshore oil and gas platforms is limited, however, the most relevant studies focused on ORC implementation are reviewed below.

Pierobon et al. [35, 36] carried out a multi-objective optimisation to obtain the maximum thermal efficiency, minimum volumetric footprint and maximum net present value. The calculations were made for two different working fluids, acetone and cyclopenthane and the maximum temperature of the ORC cycle was around 225$°C$. Steam and air cycles were also considered for comparison. The conclusion was the ORC system had higher performance compared to the steam cycle, while the air bottoming cycle was not ideal from an economic and environmental point of view. The heat exchanger was found to be the heaviest component, while the turbine had the highest cost.

Bhargava et al. [37] studied the waste heat recovery of the gas turbine exhaust typically used in offshore applications. This kind of turbine is focused on reliability and compactness due to space limitations, so the thermal efficiency is usually below 35%. Two different thermal connections between the exhaust of four gas turbines and the ORC were investigated, with and without an intermediate heat transfer fluid. Four different power sizes for the gas turbines are selected between 2MW to 30MW each. The chosen working fluid was cyclopentane and the intermediate heat transfer fluid was fixed in a mixture of biphenyl and diphenyl oxide. The researchers found that smaller gas turbines, which tend to be of lower efficiency, had a higher potential for waste heat recovery. An additional 140% of electric power production was achieved for each gas turbine unit, which means that partial load operation of some units could be scrapped, resulting in fuel savings. The use of an intermediate heat transfer fluid did not show benefits in the thermal efficiency of the cycle, but it is interesting for safety considerations. The recuperative cycles had higher thermal efficiency, which translates into lower

GHG emissions and reduced fuel consumption, but increases the space footprint in the platform.

Barrera et al. [38] studied the implementation of an ORC system in a floating product storage offloading (FPSO) in Brazil. These facilities allow the exploration and extraction of deep-sea petroleum products and are usually derived from oil tankers. A model was developed to simulate the impact of ORC systems on the energy and exergetic efficiency of the entire platform, as well as on fuel consumption. The waste heat flow considered for the calculations was the exhaust from two gas turbines working under partial load conditions. Cyclopentane was the selected working fluid and the maximum temperature reached before the expansion stage was 300$^{\circ}C$. In conclusion, the energy consumption saving was calculated at 15-20%.

Veloso et al. [39] continued the ORC research of their colleagues of an FPSO [38]. A multi-objective optimisation was carried out with power output and heat transfer area as objective functions. The ORC footprint is directly related to the heat transfer area of the heat exchangers in the system. The waste heat under study was the exhaust from the gas turbines of the compressor units. The optimal cycle was found to recover up to 4.22% of the energy needed to run the compressor units and was able to significantly reduce the GHG emissions.

Reis et al. [40] conducted similar research focused on off-design performance on an FPSO. ORC provides flexibility in the dynamic demand conditions of the application. Toluene was chosen as the working fluid and the maximum temperature of the cycle was set between 300 and 330 $^{\circ}C$. The resulting thermal efficiency of the ORC system was 24.6 and 28.4% for a simple cycle layout and a regenerative cycle, respectively. The overall efficiency of the electrical systems increased to 11.3% and the reduction in CO2 emissions was around 22.0%. An economic analysis was also carried out, concluding that the implementation of ORC can be very attractive due to the savings in fuel consumption.

1.4 Industrial Project MTJA

The Malaysia-Thailand Joint Authority, MTJA, is the institution that supervises and administers non-living resources, mainly oil and gas, in a shared region of the continental shelf. This 7250 km^2 region, known as Joint Developing Area (JDA), is located in the Gulf of Thailand, as shown in Fig. 1.4. The purpose of MTJA is to manage the exploration and exploitation of these fossil fuel resources in order to obtain equal benefits for both Malaysia and Thailand.

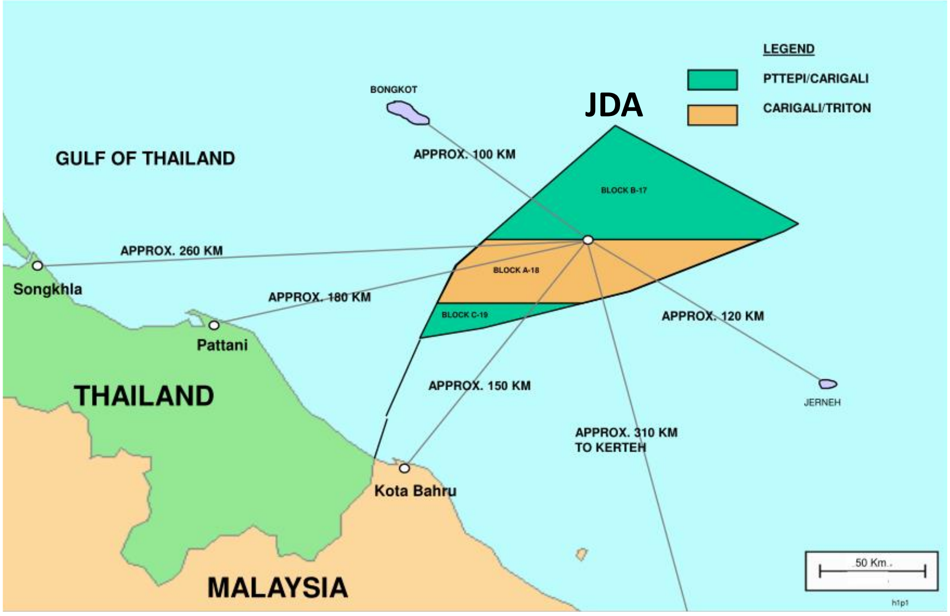

Figure 1.4: Joint development area of MTJA.

In addition, MTJA has a Research Fund for the support of research and development of science and technology related to the exploration and exploitation of its resources. Committed to energy and environmental targets, MTJA has funded the project: Energy Recovery in Petroleum Processes via Integrated High-Performance Technologies, being the framework of this research. This is a collaborative project among academic and research institutions of Malaysia (UTM), Thailand (KMUTT) and the United Kingdom (Imperial College London).

The industrial project consists of the development and optimisation of three WHR technologies and their combination at pilot plant level. The pilot plant, currently under construction at UTM premises, replicates the conditions of the waste heat streams available in off-shore oil and gas platforms. The industrial project will assess the power generation potential from the use of the waste heat streams present in an offshore oil and gas platform. The benefits of these WHR technologies applied to upstream and midstream oil and gas processes are explored in this project. This will allow a more environmentally conscious use of fossil resources during the energy transition and decarbonisation of the oil and gas industry.

There are three mature WHR technologies that are currently under further development and have been also used in some industrial and automotive applications: organic Rankine cycle, ORC, thermoelectric generation, TEG and electric turbo-compound, ETC. These three technologies, ORC, ETC and TEG are the WHR technologies investigated in this project. The impact and contribution of the industrial project are summarised in the following points:

- Use of the energy resources efficiently, enhancing the efficiency of the whole platform, reducing fuel consumption and CO_2 related to power generation.
- Reduction of the environmental impact of flare gas, recovering part of the energy that is, otherwise, released to the atmosphere.
- Maximisation waste heat recovered by implementing a combination of waste heat recovery technologies (ORC, ETC and TEG), while minimising integration cost.

1.5 Waste Heat Recovery Technologies

Although ORC and ETC are more mature WHR technologies, TEG is developing fast due to ongoing research in new materials. The principle behind these WHR technologies can be summarised as follows:

- **ORC** is a thermodynamic cycle that uses an organic fluid in a closed loop. The fluid evaporates in a heat exchanger due to the heat absorbed from the waste heat stream and then it expands in a turbine, a generator then transforms the mechanical energy into electrical energy. Finally, the remaining heat in the fluid is rejected in a condenser and the fluid is pumped again towards the evaporator, as shown in Fig.1.5.

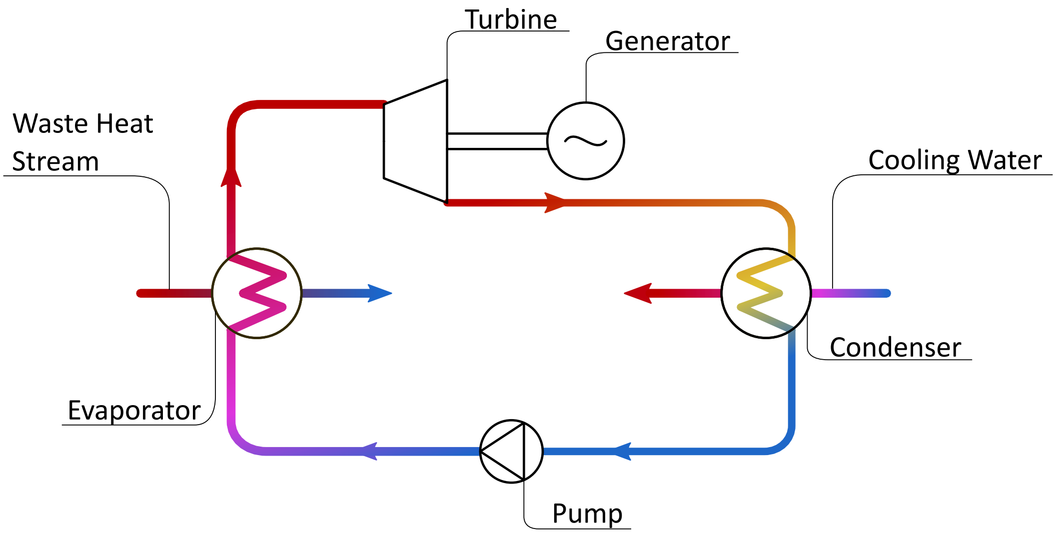

Figure 1.5: Basic outline of an ORC system.

- **ETC** consists of a turbine coupled to a generator as shown in Fig.1.6. The turbine harvests energy from a gaseous waste heat stream.

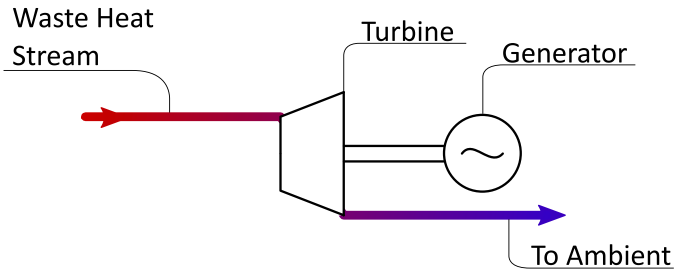

Figure 1.6: Basic outline of the ETC system.

- **TEG** consists of thermoelectric modules which convert directly heat energy into electrical energy making use of the Seebeck effect. The temperature difference occurs between the waste heat stream and an available heat sink. A diagram of this technology is shown in Fig.1.7.

There are significant differences among these three WHR technologies that make each of them more appropriate for a certain application over another, these are discuss here and are summaries in Table 1.1.

- **ORC** can provide a large amount of power, but its footprint, which is a limiting factor for offshore applications, may be large in comparison to ETC and TEG, which are considered rather compact technologies. ORC can be fully non-invasive

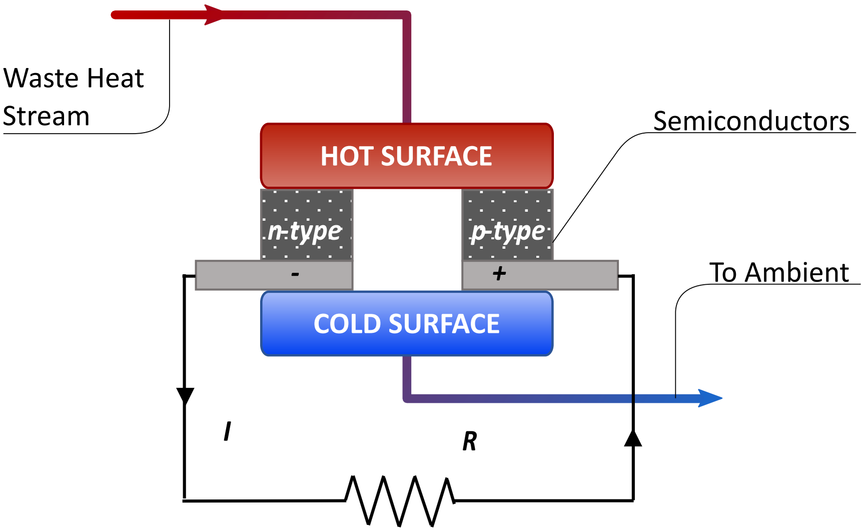

Figure 1.7: Basic outline of the TEG system.

using a secondary loop for evaporation, which means that the waste heat recovery system does not affect the actual platform processes. ORC has rotating components (a turbine, a pump and a generator), which are susceptible to wear and need frequent maintenance (increasing the operating costs), particularly in harsh environments occurring in offshore applications. The initial investment for ORC is moderate.

- **ETC** is a compact non-invasive technology since it is placed downstream of the waste heat stream. However, an ETC causes a back-pressure effect on the upstream system (the engine). ETC relies on well established turbomachinery design methods. ETC has the lowest implementation costs.

- **TEG** does not have any rotating components in contrast to ETC and ORC, therefore this technology is less susceptible to wear. Nevertheless, TEG efficiency is significantly low, experimental results show efficiency lower than 10% [41, 42]. Despite promising research in nanotechnology and semiconductor materials, TEGs remain in their infancy. Furthermore, the implementation costs of TEG technology are large compared to the initial investment required for ORC and ETC.

The current research project is framed in the industrial project, being the main focus of the current research the expander design for ETC and ORC technologies.

Variable	**ORC**	**ETC**	**TEG**
Footprint	High	Medium	Low
Capacity	High	Medium	Low
Invasive	Low	Low	Low
Rotating components	High	High	None
Implementation cost	High	Low	High
Maintenance cost	High	Low	Low

Table 1.1: Differences among WHR technologies

1.6 Research Aim and Objectives

The overarching aim of this thesis can be stated by the following research question:

What is the effect of 3D blade features and non-radial blading on the performance of low pressure turbines and ORC turbines when compared to the commonly used radial fibre design?

This question can be broken down into several objectives:

1. Development of a low order turbine model based on physical principles accounting for real-gas effects.
2. Investigation of the accuracy of the low order model in terms of loss distribution, mass flow and efficiency with air and organic fluids.
3. Proposal of a 3D parametric blading model that enables the generation of designs exploring a wide design space of radial and non-radial blading designs.
4. Understanding the effects of non-radial blading and other 3D geometry modifications on turbine design and exploration of the flow field with an experimentally validated CFD method.

1.7 Thesis Outline

This thesis consists of six main chapters, as outlined below:

- **Chapter 1: Introduction** This chapter is an introduction to the background of the project as well as the aim. Concise research questions and objectives are presented in this chapter.
- **Chapter 2: Literature Review** This chapter shows the literature review of the topics related to this research, highlighting the research gaps and contribution to the current knowledge. Literature on waste heat recovery technologies and their application in industry and off-shore platforms are reviewed. Moreover, the state-of-the-art of radial turbine design is introduced in this chapter.
- **Chapter 3: Methodology** This chapter introduces and explains in detail the methodology used in design and analysis of radial turbomachinery used to carry out the research. First, the meanline model is developed followed by the automated 3D parametric model. The optimisation and calibration strategies applied to the design tools are also explained. The experimental facilities at Imperial College used for cold testing for ETC applications are also explained.
- **Chapter 4: ORC** This chapter shows the application of the methodology developed in this work to ORC expander design. Sensitivity analysis and comparison were carried out with the meanline and 3D parametric approaches using the methodology described in Chapter 3. Loss breakdown was analysed in CFD and the meanline model recalibrating taking into account the loss distribution in order to improve the fidelity of the low order model. The meridional profile shape, hub and shroud contours were modified to assess the impact on efficiency of 3D geometry variations. Finally, optimised geometries are suggested for the operating conditions of the pilot plant built in the frame industrial project.
- **Chapter 5: ETC** This chapter shows the application of the methodology developed in this work to ETC expander design. The comparison of both the meanline and 3D parametric methodologies are compared with sensitivity studies of the main design parameters. Recalibration of the meanline model is carried out with information on the loss breakdown obtained by CFD analysis. New loss coefficients are suggested to improve the meanline model accuracy. Non-radial fibre blading is investigated using meanline and 3D parametric approaches. Finally,

optimum radial and non-radial fibre rotor designs are obtained and compared. Experimental results of both geometries are obtained using the cold facilities at Imperial College and were used to validate and further compared the two designs.

- **Chapter 6: Conclusions** This chapter presents the conclusions reached from this research, particularly regarding the thesis aims and objectives introduced in Chapter 1. The main contribution of the work is also summarised.

1.8 Scholarly Output

The work carried out during the course of this PhD has led to the publication of articles in journals and conferences. These are listed below with a brief synopsis of each one.

- **Alvarez-Regueiro, E, Barrera-Medrano, E, Martinez-Botas, R, and Rajoo, S. "Numerical Analysis of Non-Radial Blading in a Low Speed and Low Pressure Turbine for Electric Turbocompounding Applications." Proceedings of the ASME Turbo Expo 2021: Turbomachinery Technical Conference and Exposition. Volume 2D: Turbomachinery — Multidisciplinary Design Approaches, Optimization, and Uncertainty Quantification; Radial Turbomachinery Aerodynamics; Unsteady Flows in Turbomachinery. Virtual, Online. June 7–11, 2021. V02DT37A017. ASME. [43].**

  This conference paper was authored by Alvarez-Regueiro, while Barrera-Medrano, Martinez-Botas and Rajoo acted in supervisory roles. This paper presents a CFD-based numerical analysis of the potential benefits of non-radial blading turbine for low speed-low pressure applications. The baseline design consisted of a vaneless radial fibre turbine, operating at 1.2 pressure ratio and 28,000rpm. Experimental low temperature tests were carried out with the baseline radial blading turbine at nominal, lower and higher pressure ratio operating conditions to validate numerical simulations. The baseline turbine incidence angle effect was studied and positive inlet blade angle impact was assessed with four different turbine rotor designs of 20, 30, 40 and 50° of positive inlet blade angle. Total-to-static efficiency improved in all the non-radial blading designs at all operating points considered, by maximum of 1.5% at design conditions and 5% at off-design conditions, particularly at low pressure ratio. This paper is the preliminary work of the automated 3D parametric investigation of non-radial fibre blading in Chapter 5. The secondary flow analysis in this paper can be also extrapolated to the analysis carried out in Chapter 4 and 5.

- **Alvarez-Regueiro, E., Yang, B., Barrera-Medrano, M. E., Martinez-Botas, R. F., and Rajoo, S. (August 26, 2022). "Optimisation of an ORC Radial Turbine Using a Reduced-Order Model Coupled With CFD." ASME. J. Eng. Gas Turbines Power. [44].**

  For this article Alvarez-Regueiro was the main author carrying out all the modelling, simulations and writing. Yang assisted with CFD analysis and technical discussion, whilst Barrera-Medrano, Martinez-Botas and Rajoo acted in supervisory roles. The paper presents the geometry optimisation of a single stage radial turbine for an Organic Ranking Cycle system operating over a pressure ratio of 9, corresponding to the pilot plant application. The specific fluid used in this investigation is R1233zd (E). The methodology explained in Chapter 3 corresponds to the one developed in this paper.

  The geometry is optimised for the highest total-to-static efficiency using non gradient based algorithms to allow for wide design space. Firstly, a 1D meanline geometry is optimised, which is followed by a Computational Fluid Dynamics (CFD) optimisation in 3D using a parameterised model. CFD is used to validate and calibrate the meanline model, as well as to understand the flow and the sensitivity of the design parameters not captured by the low-order model. Moreover, the flow field of the successful designs is analysed by CFD to identify the main flow structures that explain the difference in performance among the designs. These results form the majority of Chapter 4.

- **Alvarez-Regueiro, E., Yang, B., Barrera-Medrano, M. E., Martinez-Botas, R. F., and Rajoo, S. (February, 2023). "Design, optimisation and analysis of non-radial fibre turbines for electric turbocompounding applications." Manuscript submitted for publication [45]**

Alvarez-Regueiro was the main author carrying out all the modelling, simulations and writing. Yang assisted with CFD analysis and technical discussion, whilst Barrera-Medrano, Martinez-Botas and Rajoo acted in supervisory roles. This paper presents the analysis and results of the implementation non-radial fibre blading radial turbines for electric turbo-compounding applications.

The design methodology presented in this paper (explained in Chapter 3) consists of a 3D parametric model coupled with Computational Fluid Dynamic (CFD). The 3D parametric model generated a sampling of about a hundred geometries and predicted the efficiency using single blade passage simulations. The sensitivity analysis showed the effect of each design parameter on efficiency. A radial fibre turbine geometry was optimised for maximum efficiency.

The optimum radial fibre geometry was set as the baseline for further non-radial blading optimisation, based on a parametric-CFD approach. The efficiency improvement between the optimum non-radial fibred design and the optimum radial fibre design was found to be +2.0pp experimentally at the Imperial College turbocharger facility. These results are part of Chapter 5.

Chapter 2

Literature Review

The literature review of this thesis is introduced in this chapter, including the basics and state-of-the-art of the following areas, from broader to more specific topics:

- Electric turbocompounding: this explains the basic principles of electric turbocompounding and reviews the traditional applications where this waste heat recovery technology has been used so far.

- Organic Rankine cycle: this introduces the possibilities of the thermodynamic configurations of the cycle, then review the main organic fluid for medium heat applications and the selection criteria. Characteristics of the components in an ORC system are also introduced briefly.

- Expander design: a detailed review of meanline modeling and loss correlations is introduced, as well as the latest progress in non-ideal gas effects and non-radial fibre blading in radial turbines.

- Experimental testing: this includes a brief review of experimental facilities for ORC and ETC testing and introduces the pilot plant that sets the boundary conditions for the turbine design.

2.1 Electric Turbocompounding

Turbocompounding systems have been widely used in the heavy-duty automotive industry since the 1990s and more recently in passenger vehicles to recover the energy contained in the engine exhaust and transform it into mechanical or electrical energy [46]. Mechanical turbocompounding systems are coupled to the main shaft so that the energy recovered increases the engine power output. Electric turbocompounding is a simpler technology, since no mechanical linkage is needed between the shaft and the turbine, requiring fewer parts. In the automotive industry, two different electric turbocompounding systems are currently used:

- The first transforms the surplus energy harvested by the turbocharger turbine, which is not used to power the compressor, into electrical energy via a generator connected to the same shaft.
- The second consists of an additional turbine downstream of the turbocharger turbine coupled to a generator

The electrical energy obtained by both systems is then used to power auxiliaries or battery storage [47].

Turbocompounding systems have been recently applied to power generation for additional shaft power or electricity. Bowman's turbocompounding system was able to extract 1.5% additional energy from a 9 MW gas internal combustion engine [9]. ETC has also been explored in marine engine applications successfully [9, 48–50]. A clear picture of the ETC system of Bowman is shown in Fig. 2.1.

ETC implemented in oil and gas applications has not been found in the literature. However, the potential for energy recovery on offshore platforms is quite significant from waste heat streams currently being released into the atmosphere. Similar to the automotive or power generation industries, ETC could be used to recover energy from power units operating in offshore fields. In addition, flare gas could be another source of waste heat stream for ETC, particularly interesting under intermittent flaring conditions,

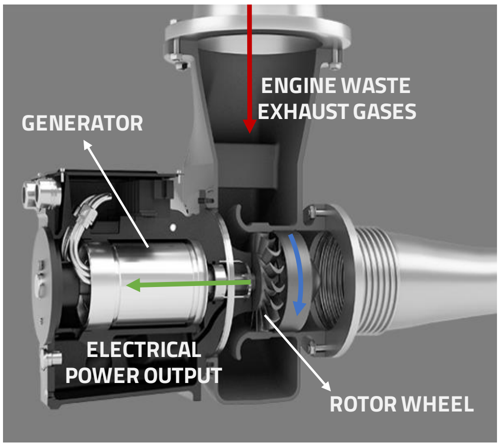

Figure 2.1: Bowman's electrical turbocompounding system [9]

as ETC is a flexible technology and its good unsteady response and performance have been demonstrated in automotive applications.

The turbine is the driver of the efficiency in turbocompounding systems, because the generator always maintains a high efficiency value above 95%. Therefore, an accurate turbine model is essential to obtain an efficient turbocompounding system. The expander design methodology must be application-focused and coupled to an optimisation routine, ensuring the best performance at nominal operating conditions. Furthermore, the prediction of actual turbine performance at off-design points is very important for a realistic assessment of the overall benefits of the designed turbocompounding system.

Conventional radial turbines used in more traditional applications, such as turbocharging, are designed for higher pressure ratios than the operating conditions found in the current electric turbocompounding application. Conventional turbines show poor performance at the low pressure ratios of an electric turbocompounding system (1.1-1.3 at design speed) if run at nominal rotational speed[51]. However, at low rotational speed, the performance of these radial turbines at 1.1-1.3 pressure ratio is acceptable, despite operating at low mass flow conditions. In addition, the low rotational speed (below 50,000 rpm) makes the coupling between the turbine and the high-speed generator easier without the need for intermediate components such as a gearbox.

ETC is therefore a suitable WHR technology, but special attention needs to be paid at the design stage since oil and gas applications are rather new for this technology. More details about the expander design are discussed later in this chapter.

2.2 Organic Rankine Cycle

Organic Rankine cycle fills the gap in power applications with relatively low temperature sources in which traditional steam cycles or Brayton cycles had a poor overall performance. Macchi et al. [10] collected information on the applications where ORC is a technically and economically feasible solution, depending on the temperature of the heat source and the power output. Figure 2.2 shows a diagram of the most common ORC applications depending on the waste heat temperature and power output. The pilot plant and offshore platform applications are highlighted in the diagram, corresponding to small WHR and medium WHR.

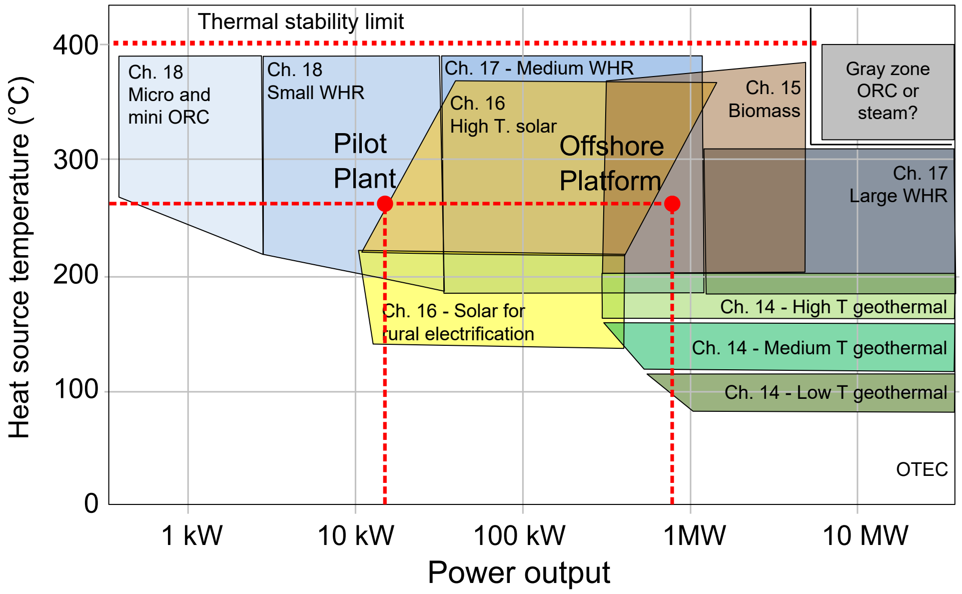

Figure 2.2: ORC applications depending on the heat source temperature and power output [10], highlighting the application of study as red dots

2.2.1 Thermodynamic and Cycle Configuration

As introduced in the first chapter, Organic Rankine cycle is a waste heat recovery technology that consists of a thermodynamic Rankine cycle operating with a refrigerant as working fluid. The fluid is pumped at liquid state up to the maximum operating pressure, then it is heated at constant pressure in the evaporator due to waste heat until superheated vapour conditions are reached. Figure 2.3 shows the flow diagram of and ORC system:

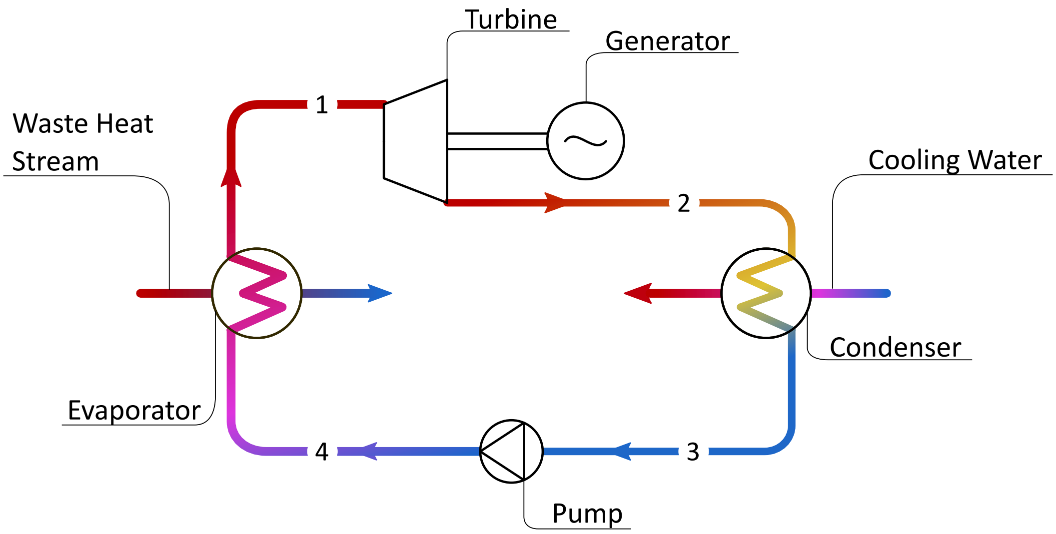

Figure 2.3: Basic outline of the simple ORC system.

The fluid at high pressure and temperature expands to the minimum pressure of the cycle through the turbine, generating power, which can then be transformed into electrical energy with a generator. The residual heat after the expansion stage is rejected at constant pressure to the cold source (usually ambient) until the fluid is totally condensed and pumped again. T-s diagram of the cycle can be seen in Fig. 2.4:

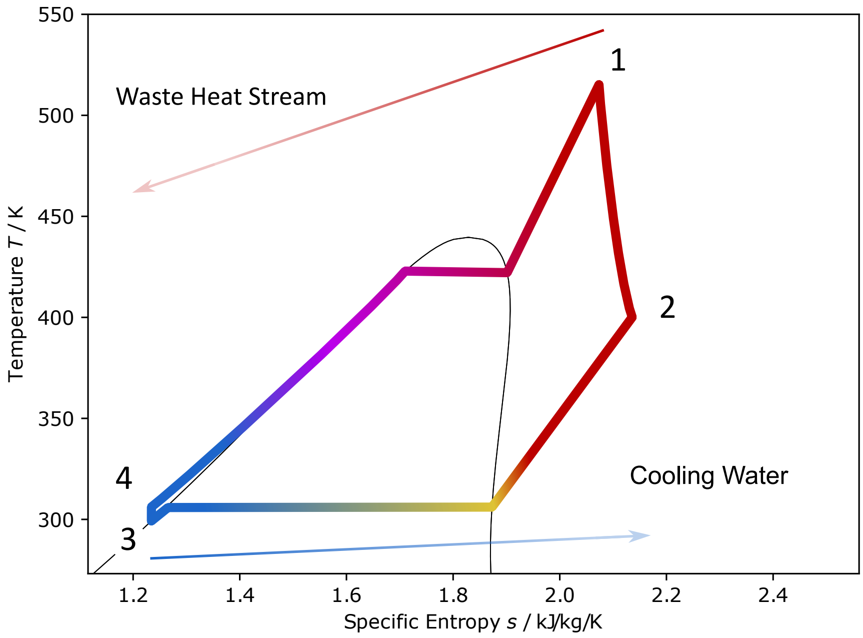

Figure 2.4: T-s diagram of a simple ORC system.

It is possible to increase the efficiency of ORC if recuperation is included. Recuperation consists of circulating the fluid at the expander outlet to preheat the stream coming from the pump outlet. The internal heat transfer in the recuperator recovers part of the thermal energy of the turbine outlet, which otherwise is rejected to ambient in the condenser. In addition, the amount of heat needed in the evaporator is less in a recuperated cycle. The recuperator is often known as regenerator or economizer in the literature. Other strategies to increase cycle efficiency include reheating, adding extra heat between expansion stages, although that is not ideal in small-scale applications [10]. Figures 2.5 and 2.6 show the flow and T-s diagram of a recuperative ORC system.

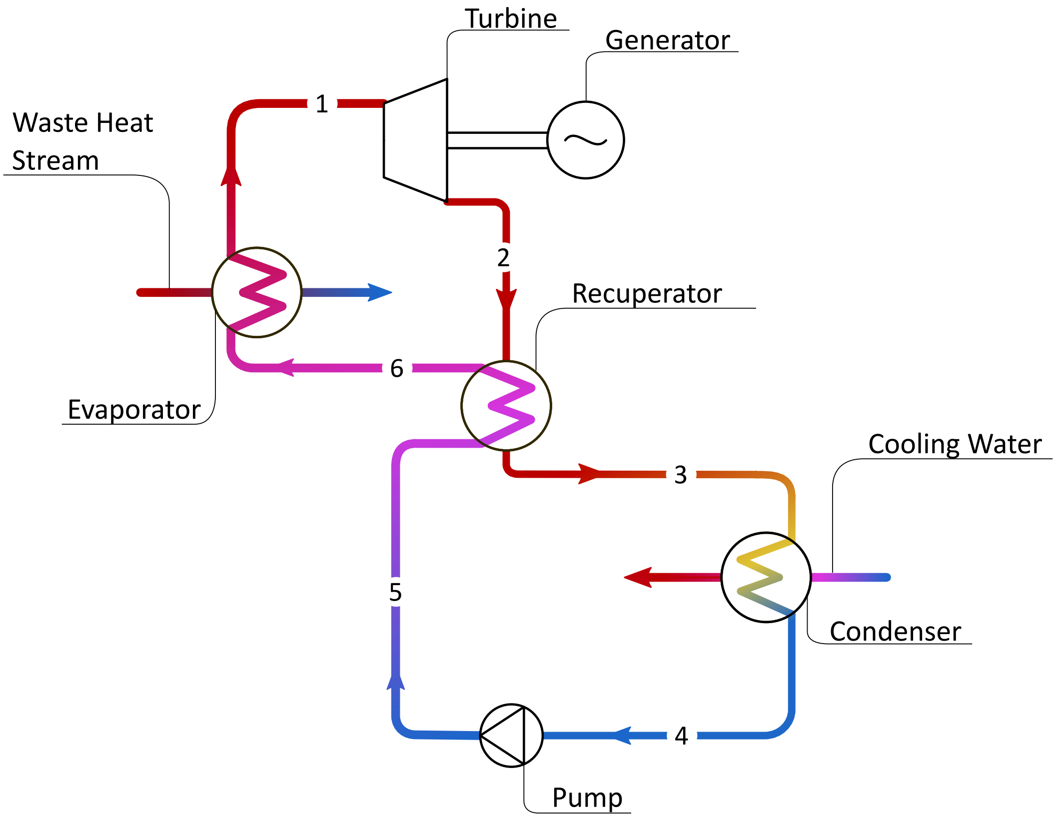

Figure 2.5: Flow diagram of a recuperative ORC system.

ORC becomes the only sensible option when the temperature of the heat source is low, especially below 250 $^{\circ}C$. Brayton cycles register negative efficiency up to this temperature, achieving only 8% cycle efficiency when the temperature of the heat source is as high as 400$^{\circ}C$, according to preliminary cycle calculations [10]. Rankine cycles, on the other hand, show much better performance, between 15% and 30% depending on the fluid used, as calculated in the literature [10]. Recuperative cycles show increased performance up to around 30% for all fluids analysed.

Rankine cycles involve both traditional steam cycles and Organic Rankine cycles. Al-

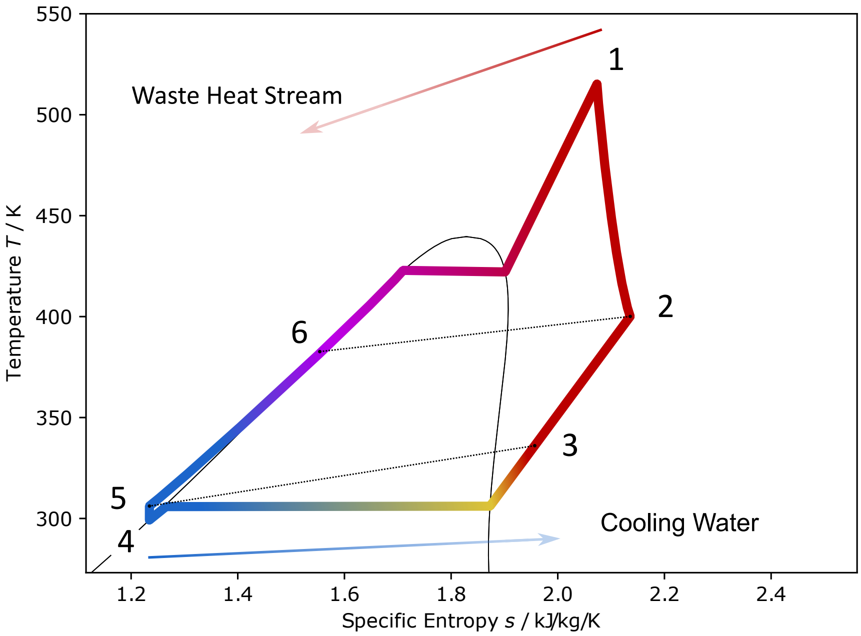

Figure 2.6: T-s diagram of a recuperative ORC system.

though water can be used as working fluid showing reasonable cycle efficiency after preliminary calculations, in practice turbomachinery limitations lead to poor overall performance. Highly supersonic flow, high blade speed and liquid formation during the expansion process are some of the aspects that make steam cycles not feasible for low temperature applications. More details on the characteristics and advantages of organic fluids are explained below.

2.2.2 Organic Fluids

Organic fluids have high molecular complexity, which increases the heat capacity of the fluid. This leads to variation in the traditional shape of the saturation curve. This particular shape makes possible expansion in dry conditions from saturated vapour state. Fluids with less molecular complexity, which have a regular saturation curve such as water, need significant superheating to ensure expansion occurs in dry conditions.

This behaviour can be seen in Fig. 2.7 (a) showing the traditional shape of the saturation curve of water and Fig. 2.7, (b) shows the saturation curve of R1233zd(E). Water shows a "humid" expansion from state 1, on the saturation line to 2, inside the saturation region, as shown in Fig. 2.7 (a). However, the organic fluid in Fig. 2.7 (b) shows a "dry" expansion, since state 2 is outside the saturation region.

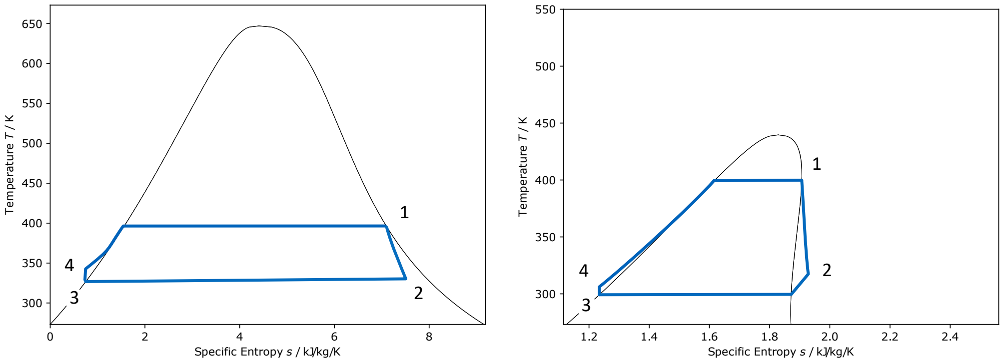

(a) (b)

Figure 2.7: Saturation curves of different fluids: water (a) and refrigerant (b)

Using a refrigerant with "dry" expansion characteristics as working fluid has the advantage of requiring less superheat. On the other hand, the disadvantage is that the final state after the expansion, 2 in Fig. 2.7 (b) is more superheated than the same state using water as working fluid. Part of the heat rejection process occurs outside of the saturation region.

The thermodynamic nature of steam is the reason why traditional Rankine cycles with water as working fluid show low efficiency with low-temperature heat sources. Moreover, steam cycles are not an option for small scale applications due to the high cost of the multi-stage turbine required as well as the technical complexity of the plant and the turbine design itself. ORC instead, makes feasible the implementation of energy recovery at small scale low-temperature waste heat sources. The molecular complexity, low critical pressure and temperature of organic fluids make possible a single stage turbine design for this type of application.

The selection of the specific organic fluid is highly sensitive to the operating conditions of the given application, but other considerations need to be taken into account too. The fluid has to fulfill the following requirements:

- **Low global warming potential**, which accounts for the amount of heat trapped by a certain mass of the working fluid compared to the heat trapped by an equal mass of CO2.

- **Low ozone depletion potential**, which accounts for the ratio of global loss of the ozone layer due to a certain mass of the working fluid over the global loss of the ozone layer produced by an equal mass of CFC-11.
- **Nonflammable, noncorrosive and nontoxic** to ensure safety and material durability. Some applications adopt the use of flammable working fluids, such as hydrocarbons (propane, butane, cyclopentane, among others) or toxic fluids, such as ammonia.
- **Chemical stability** to prevent degradation with temperature.
- **Commercially available**, especially for large scale plants where the cost of the working fluid is a large share of the total investment.
- **Appropriate critical temperature and pressure** for the application.
- **Suitable molecular complexity and molecular mass** to ensure dry expansion and reduced number of turbine stages. However, these features have also negative effects related to the size and cost of the heat exchangers.

Working fluids that meet all the requirements explained above are scarce. Nowadays, chlorofluorocarbons, known as CFC, are banned in many applications due to their environmental impact. Hydrochlorofluorocarbons, HCFC, and hydrofluorocarbons, HFC are also in the process to be removed from operating systems.

After a preliminary study on the efficiency of the organic Rankine cycle with different working fluids, R1233zd(E) was selected as working fluid for the application under study. This organic fluid belongs to the family of the hydrochlorofluoroolefin (HCFO) and is a new generation fluid replacing R11 (CFC), R123 (HCFC) and R245fa (HFC) which were found to be not environmentally friendly. Tables 2.1 and 2.2 summarise the properties of R1233zd(E) compared to the properties of working fluids to be replaced. R1233zd(E) shows similar properties to the other three fluids, but no impact on global warming showing a GWP of zero [2]. The ODP is not zero, but close enough, compared to the ODP of 1 and 0.02 of R11 and R123, respectively.

Property	Value
Chemical Name	Trans-1-chloro-3,3,3-trifluoropropane
Chemical Notation	(E)CF3-CH=CClH
Critical Temperature $[°C]$	165.5
Critical Pressure $[bar]$	35.7
Relative Molar Mass $[g/mol]$	120.5
Liquid Density 0°C $[kg/m^3]$	1321.3
Vapour Density 25°C $[kg/m^3]$	7.2

Table 2.1: R1233zd(E) thermophysical properties [1]

Property	R11	R123	R245fa	R1233zd(E)
Molar Mass $[g/mol]$	137	153	134	131
Critical Temperature $[°C]$	197.6	183.7	154.01	165.5
Normal Boiling Point $[°C]$	23.71	27.82	15.14	19.00
GWP	5160	807	880	1
ODP	1.00	0.02	0.00	0.00034

Table 2.2: Comparison of basic thermophysical properties and environmental index of R11, R123, R245fa and R1233zd(E) [2]

2.2.3 Components of an ORC System

As discussed previously, ORC systems show simpler layout and less components than equivalent steam Rankine cycles. The four main components of ORC systems are: pump, evaporator, condenser and expander. If the cycle is recuperative, a fifth component needs to be included, the recuperator.

The **pump** raises the pressure of the fluid after the condenser and before the evaporator. Variable speed centrifugal pumps are typically used in ORC applications. If the pressure ratio is sufficiently high multi-stage configuration is adopted. This component may need a large proportion of the power generated in the expander depending on the application, cycle configuration and fluid selection. In those situations special attention is required for the pump design.

Heat exchangers are used in the evaporation, condensation and recuperation stages. Similar considerations apply to the heat exchangers used in each stage. Careful selection

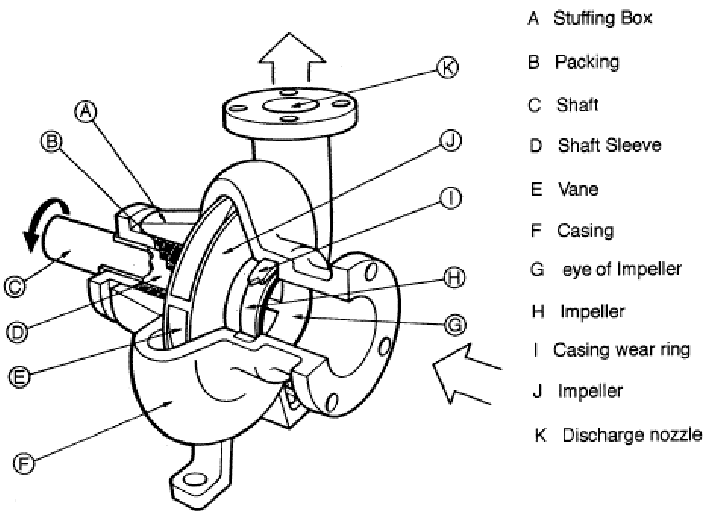

Figure 2.8: Centrifugal pump

and design of the heat exchangers is paramount because of the relative low efficiency of ORC cycles. This means that a large proportion of the heat absorbed is then rejected in the condensation stage,leading to large heat transfer areas and large fraction of the total cost of the ORC plant. Higher heat transfer areas improve the efficiency of the cycle, but increase the equipment cost.

The fluid absorbs the waste heat from the source through the **evaporator** until saturation or even superheated conditions are achieved. The type of heat exchanger for this stage varies depending on the operating conditions and constraints of the application as well as on the type of fluids used. In subcritical cycles the primary heat exchanger consists of the economiser, the evaporator and the superheater. Shell and tubes are the most common heat exchanger for the economiser and superheater if the heat source is liquid. For the evaporator, kettle reboiler type is preferred.

The heat rejection happens in the **condenser**. Condensers typically have a similar configuration to kettle reboiler heat exchangers when cold water is available or when a heat transfer fluid is used for cogeneration applications. Cold water from natural resources cannot return to the environment at a high temperature, introducing cooling towers can reduce the condensation temperature and the mass flow or water used.

If water is not available, air cooled condensers are used instead. The equipment consists of finned tubes and fans often of large size due to the poor heat transfer coefficient of air. This can impact negatively the ORC plant, since the weight, footprint and cost could increase significantly. Recently, water sparkling systems have been introduced in this type of heat exchangers to improve the heat transfer, especially when the ambient temperature is high.

The **recuperator** uses heat in the stream at the turbine outlet to preheat the fluid leaving the pump. Finned tube heat exchangers are usually chosen for this stage. This component helps increasing the cycle efficiency, especially at high temperature applications. The working fluids of these applications show high molecular complexity, leading to small temperature drop across the expander stage. The high thermal power available can be then transferred to the cold fluid coming from the pump.

For small size applications brazed plate, plate-finned and plate-shell heat exchangers, can replace shell and tubes as well as kettle re-boiler heat exchangers. Figure 2.9 shows a few examples of heat exchangers.

The **expander** takes the fluid at high temperature and pressure after the evaporator and extracts the power. Both volumetric or positive displacement machines and turbomachinery can be used, the choice depends on the size of the ORC system and the working fluid selection.

Volumetric or positive displacement devices expand the fluid by increasing its volume and they are often found in small scale applications (below 100kW of power output). Scroll, screw and piston expanders have been used in ORC applications and are cost-effective [11, 13, 52, 53]. They can also cope with two-phase expansion. However there are some limitations related to the reduced volume ratio they can operate, difficulty for multistage configuration and maximum temperature materials can stand due to thermal expansion [10, 54]. Figure 2.10 show examples of screw, piston and scroll expanders.

Most of the ORC applications, especially in large scale, use turbines as expanders. The different types of turbines are axial, radial inflow and radial outflow and their application in ORC systems mainly depend on the size. More details on each type are provided in the next section.

Turbines allow for much bigger expansion ratios than volumetric devices, however their

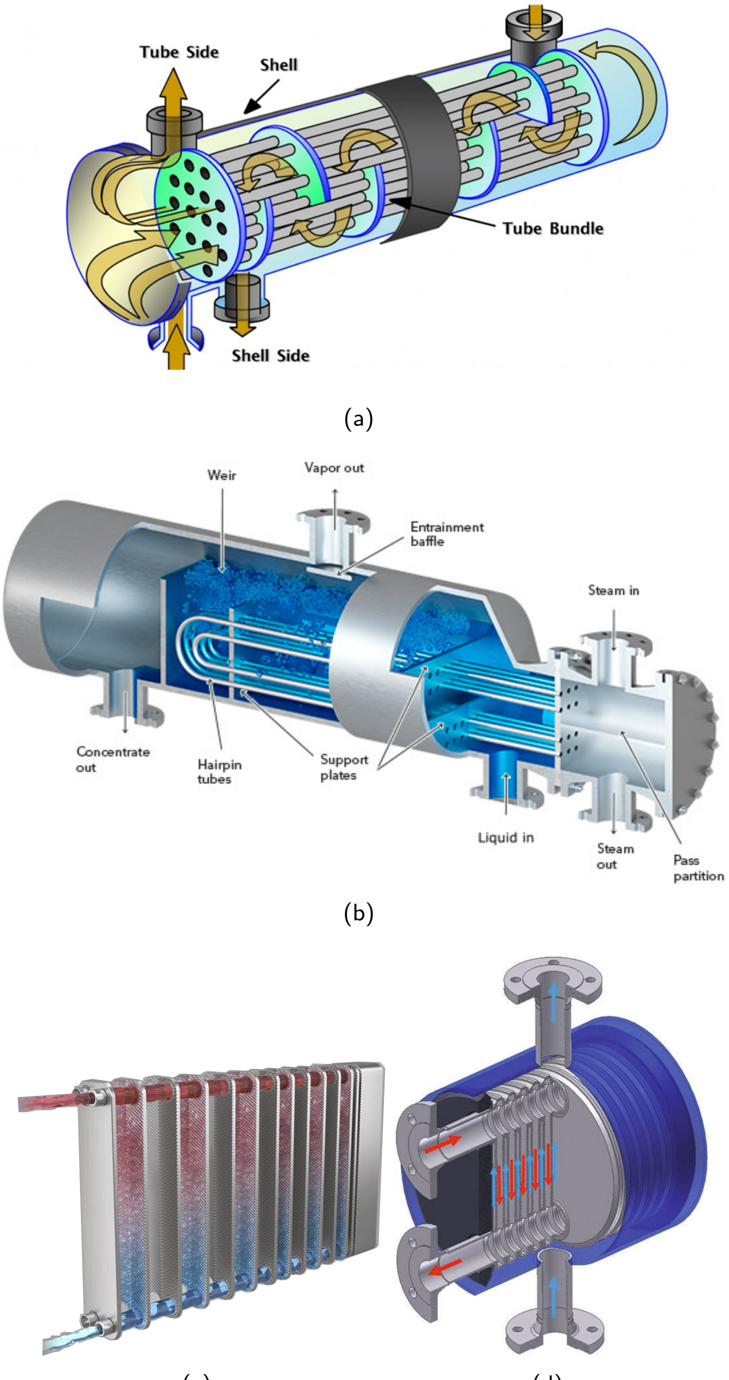

(a)

(b)

(c) (d)

Figure 2.9: Heat exchangers: (a) shell and tube, (b) kettle boiler (c) brazed plate and (d) shell and plate types

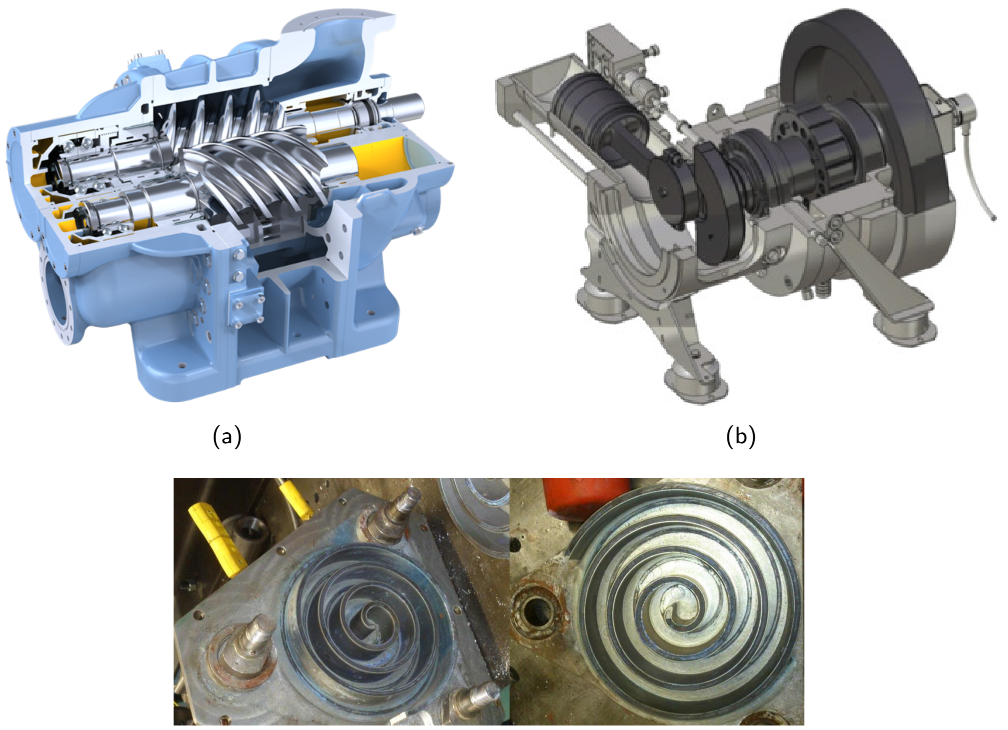
(a) (b)

(c)

Figure 2.10: Volumetric expanders: (a) Screw expander, (b) piston expander and (c) scroll expander [11–13]

efficiency is heavily penalised in small scale ORC plants if they are not carefully designed. Therefore, it is important for ORC designers to have the appropriate tools for high efficiency turbine design, which will enhance the efficiency of the overall system. A more detailed literature review is summarised below on expander design for ORC and ETC applications.

2.3 Expander Design

Turbine modelling has been explored during the last decades for many diverse applications such as, steam and gas turbines for power generation, aircraft engines, turbochargers and wind turbines among others, with the aim of obtaining more efficient turbine designs. Traditionally, the common modelling strategies relied on iterative adjustments of some parameters that affect the turbine geometry and performance. New automated approaches, based on physical models coupled to optimisation routines, have been developed to make the design process more automated [55].

Several aspects must be taken into account when designing a turbine for a given application. Figure 2.11 shows a brief summary of the main aspects to be considered in this process: topology, boundary conditions and modelling approaches. Typically, different modelling techniques have been applied for each turbine topology (axial, radial, mixed-flow), due to the different geometry of each topology, leading to different assumptions and simplifications of the turbomachinery equations. For instance, the blade speed in axial turbines is assumed to be constant throughout the rotor, since the radius in the inlet and the outlet of the rotor has almost the same value. However, in radial and mixed flow turbines, the large variation in radius between the inlet and the outlet of the rotor makes this assumption invalid when modelling this type of turbine designs.

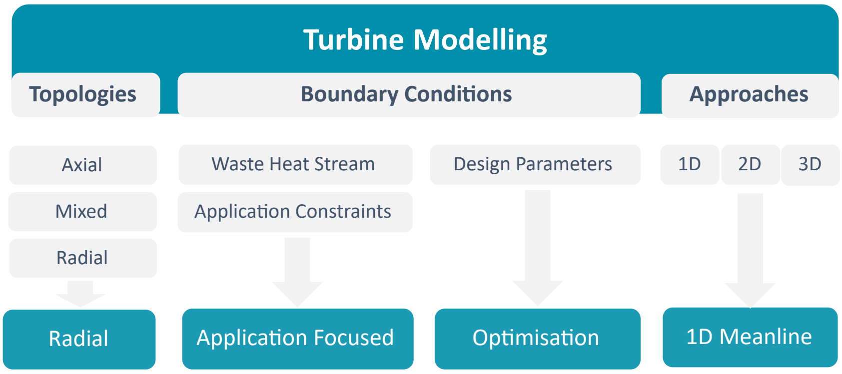

Figure 2.11: Different approaches in turbine modelling

The design of a turbine is strongly influenced by the boundary conditions in which the turbine will operate. Some of boundary conditions are given by the waste heat stream, but also by the application constraints and design parameters of choice. The design parameters can be chosen within a range defined by upper and lower boundaries to ensure a realistic and feasible outcome.

The third aspect to consider in turbine modelling and design is the modelling approach. Commonly, there are different modelling approaches which provide higher or lower levels of accuracy and computational cost. 3D and 2D-axisymmetric approaches, developed by means of computational fluid dynamics are complex, time-consuming and the optimisation of these models is usually limited. However, a reduced or low-order modelling approach, such as the one-dimensional mean-line modelling, simplifies high-fidelity complex models but still provides enough accuracy compared to the small amount of time required to compute.

Considering the different approaches in turbine modelling, the aim of this thesis is to develop a general one dimensional model for radial inflow turbines which also considers different working fluids. The outcome of the model will be a radial turbine design, optimised for maximum performance for a given application. The modelling approach considered to be optimum for this research corresponds to 1D meanline modelling. This approach is widely used in preliminary turbine design due to its compromise between low computational cost and decent accuracy.

2.3.1 Expander Topology

Typically, every turbine stage has a stationary component, the stator, generating swirl to the flow; and a rotor, through which the fluid expands and turns to give tangential velocity, generating power [56]. However, there are fundamental differences between each topology, both in their geometry and design features as well as in the application and boundary conditions.

In **axial turbines**, the inflow and outflow follow predominantly the axial direction. The manufacturing process of this type of expander is rather complex since blades and disks are usually manufactured separately and assembled later on. [56]. Axial turbines are more appropriate for large power applications. A picture of an axial turbine is shown in Fig. 2.12.

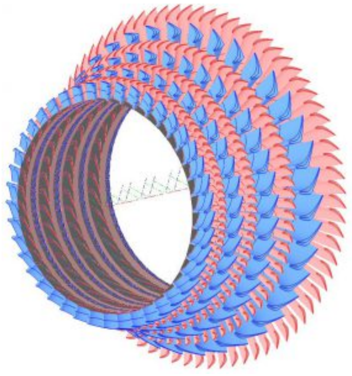

Figure 2.12: Axial turbine.

In **radial inflow turbines**, the flow approaches the rotor blade in the radial direction and leaves it mainly axially. This type of turbine has higher specific power than the axial design due to the contribution of the change in blade speed since the radius is not constant throughout the stage. Therefore, for the same power output, radial expanders can be smaller in size or have fewer stages when compared to axial turbines. Being more compact than axial turbines, the rotor wheel of a radial turbine can be a single casting, making the manufacturing process easier and cheaper [56].

(a)

(b)

Figure 2.13: Radial inflow turbine: volute (a) and rotor (b).

Radial inflow turbines usually consist of a volute, shown in Fig. 2.13(a) and nozzle vanes which distribute the flow in the circumferential plane and turn it to the correct angle as it approaches the rotor blades. The rotor, Fig. 2.13(b), harvests the energy of the flow coming from the volute outlet. However, some radial-inflow turbine designs avoid the use of nozzle vanes. Nozzleless radial inflow turbines are more compact and the manufacturing cost is smaller compared to nozzled turbines, but they have lower peak efficiencies, due to the lack of pre-swirl, commonly given by the nozzle. On the other hand, nozzleless turbines show better performance in off-design conditions compared to nozzled turbines. A diffuser is sometimes placed in the rotor outlet so that the static pressure is recovered, usually allowing a higher pressure ratio across the turbine.

Radial outflow turbines have a similar configuration to radial inflow turbines, but the flow approaches the rotor axially and leaves it in the radial direction instead. Moreover, in this turbine topology, the radius of the turbine increases towards the outlet. This feature is particularly interesting for fluids that show a high expansion ratio, like organic fluids [57]. Figure 2.14 shows a radial outflow turbine, indicating the direction of the flow.

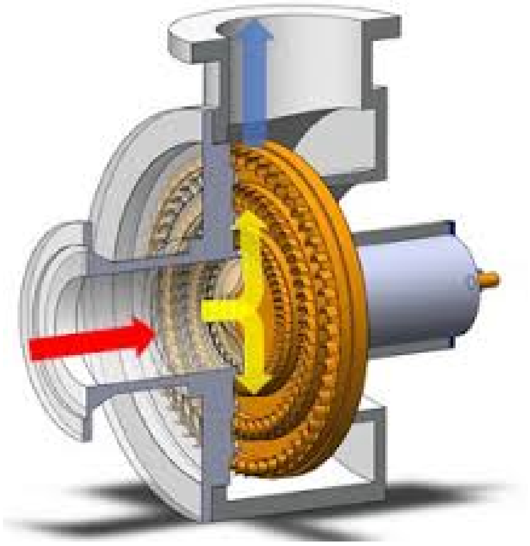

Figure 2.14: Radial outflow turbine [14]

The **mixed-flow turbine** is a variation of the radial inflow turbine, where the rotor leading edge radius is not constant and the flow at the rotor inlet has radial and axial components. Figure 2.15 shows the main differences in the blade shape and the flow direction of both radial and mixed-flow turbines. The main advantage of mixed flow turbines is that the radius ratio between the exit tip radius and the inlet radius can be larger while the blades maintain low curvature. The low blade curvature reduces the centrifugal pressure that develops against the flow direction, smooths the flow across it, allowing less flow separation and increasing the swallowing capacity of the turbine, which defines the turbine performance range [58]. The lower blade curvature also provides a shorter and more compact passage. Therefore, the rotor exducer and throat area can be bigger, making the mixed-flow turbine good for large flow capacity applications [56].

The cone angle, defined as the angle between the blade span and the radial direction in a mixed-flow turbine (see Fig. 2.15) adds an extra degree of freedom to the design process, since different cone angles will lead to different turbine geometries. The mixed

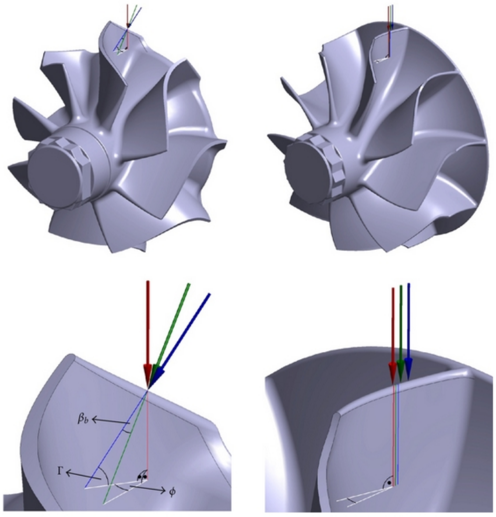

Figure 2.15: Comparison between mixed-flow (right) and radial (left) turbine rotors [15]

flow configuration allows the use of non-zero blade angles at the same time that the radial blade fibre requirement is satisfied. In radial turbines, the zero-blade angle is the main limitation since it is required to keep the blade load purely tensile [59]. Baines et al. (1979) [60] conducted an experimental test of mixed flow turbines with positive blade angles obtaining higher efficiency and at lower velocity ratios, as well as higher swallowing capacity than equivalent radial-inflow turbines.

Authors started investigating mixed flow turbines for turbocharger applications [60]. Maximum efficiency and flat response of the pressure ratio with the swallowing capacity of the turbine were the main targets of turbocharger designers. The swallowing capacity of a radial turbine increases with decreasing turbine speed, which leads to a sudden decrease in pressure ratio and boosting capacity of the turbocharger. In addition, the inherent zero inlet blade angle of radial inflow turbines, to keep the radial fibre, set the velocity ratio for maximum efficiency at 0.7. The velocity ratio is defined as the ratio of the blade speed in the rotor inlet, U_4, over the isentropic or spouting velocity, C_{is}, the equivalent ideal velocity that the fluid would have in an isentropic expansion from the turbine inlet conditions with the designed pressure ratio, Eq. 2.1, where the subindex 4 indicates the rotor inlet and β and α, the relative and absolute flow angles, respectively. If zero-incidence is assumed, then the velocity ratio is fixed to $1/\sqrt{2}$, which is around 0.707.

$$VR = \frac{U_4}{C_{is}} = \frac{1}{\sqrt{2}}\sqrt{1 - \frac{tan\beta_4}{tan\alpha_4}} \tag{2.1}$$

In radial turbines, decreasing the degree of reaction will move the optimum velocity ratio towards lower values. That would require, however, to sweep the blade in a forward direction at the inlet, breaking the radial fibre condition. However, mixed-flow turbines can achieve this lower optimum velocity ratio while keeping the radial fibres of the blades; they show a flatter pressure ratio response and a higher swallowing capacity.

Due to the different geometry and features between axial and radial turbines, the simplifications used to model each topology are not the same. This has led to multiple different models depending on the turbine topology. The mixed-flow turbine has common characteristics with both axial and radial designs, since the flow entering the turbine rotor has both radial and axial components. Although the first models for mixed-flow turbines used an axial turbine approach [61], the radial approach was preferred by authors to model mixed-flow turbines, because of the geometrical and flow similarities between both topologies.

2.3.2 Meanline Modelling for Radial Inflow Turbines

The real flow through a turbine is rather complex, 3D, viscous and compressible, even supersonic in some regions. There are modelling strategies that try to reduce complexity, one such method is known as the mean-line model approach. It has been shown to provide a good preliminary design and performance prediction at off-design conditions. Radial and mixed-flow turbine modelling have been a research topic of interest for more than 50 years, in which many authors have been involved, as can be seen in Fig, 2.16. Upon completion of the meanline design methodology, 2D and 3D modelling is needed to analyse the flow through the turbine.

Mean-line modelling is a one-dimensional modelling approach which assumes that the flow behaviour (thermodynamics and aerodynamics) through the turbine can be represented only from the flow along the mean-line, the streamline at mid-span [55]. The mean-line model is usually the first step in the design process. Stations are chosen

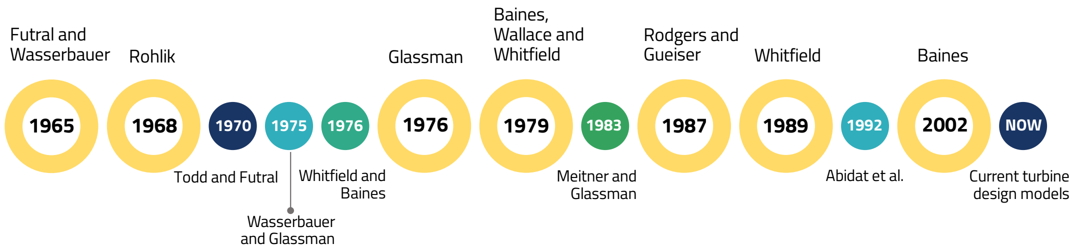

Figure 2.16: Radial and mixed-flow turbine mean-line models in the literature.

at the inlet and outlet of each component, as shown in Fig. 2.17. Thermodynamic and fluid dynamic conservation principles (mass, momentum and energy) are applied at each station. The outcome of this analysis is the main geometrical parameters and estimated performance of a turbine [56].

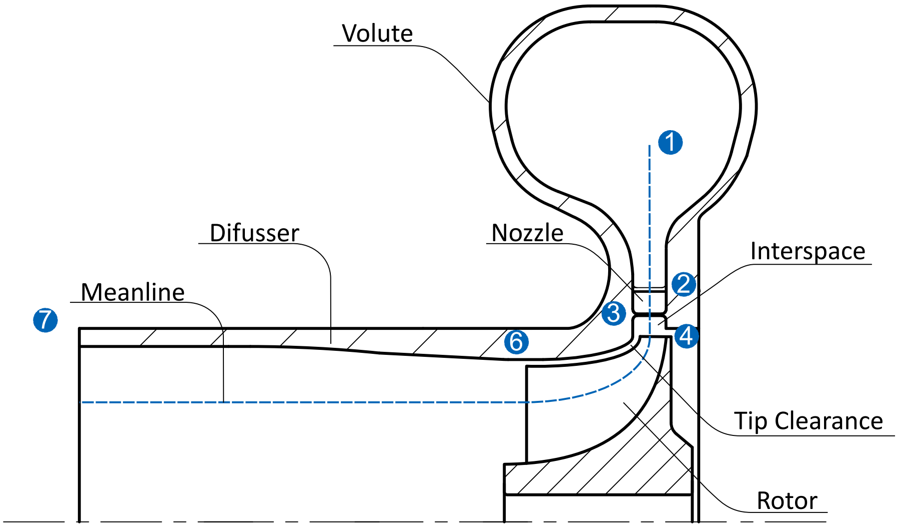

Figure 2.17: Turbine stations considered in mean-line modelling.

Futral and Wasserbauer (1965) developed one of the first methodologies for design and performance prediction of radial-inflow turbines [62]. This turbine model was based on the one-dimensional solution along the mean streamline of the blade, a mean-line model. Perfect gas conditions were assumed and the turbine performance was computed only for subsonic conditions, as choking was not expected for the turbines they considered. Later, Todd and Futral (1970) used this mean-line model to create a code in FORTRAN IV for automated turbine calculations for both design and off-design conditions [63]. The code was used for off-design performance prediction of an existing turbine, and also as design guide for the development of new ones.

At the same time, **Rohlik (1968)** developed the first analytical method for high efficiency radial turbine design [16]. The aim of the study was to carry out a comprehensive analysis of the preliminary turbine design process to provide a quick guide to selecting the turbine geometry for optimum efficiency depending on the turbine specific speed. Assuming zero-swirl at the rotor outlet and a good rotor reaction, Rohlik developed a mean-line model with three independent variables to find the turbine design with the highest efficiency. These variables were the stator exit flow angle, stator blade height-to-rotor exit diameter ratio and outlet to inlet diameter ratio.

Rohlik analysed the effect of the independent variables on the turbine performance (efficiency, geometry and velocity ratio, among others) for a range of specific speeds from 0.12 to 1.34 $rad \cdot m^{-\frac{3}{2}} \cdot kg^{-\frac{3}{4}} \cdot s^{-\frac{3}{2}} \cdot J^{-\frac{3}{4}}$ [16]. Although the maximum static and total efficiencies were found at different values of specific speed (0.58 and 0.93, respectively), the geometry was the same for the optimum of both efficiencies. The pressure ratio had a small influence on the turbine geometry, except on the stator blade height-to-rotor inlet diameter ratio. The density change between the rotor inlet and outlet depends on the pressure ratio and is directly related to this geometrical relation. Results also indicated that the static efficiency decreased significantly at low specific speeds due to large passage, windage and clearance losses. Similarly, the efficiency decreased at high specific speed due to the high flow and exit losses. Finally, Rohlik found that the presence of the diffuser enhanced the total to static efficiency except at high specific speeds.

Wasserbauer and Glassman (1975), 5 years later, reviewed Futral and Wasserbauer's procedure [62] and Todd and Futral's code [63], because poor agreement of their results with experimental data [64]. A subroutine to account for choked conditions was included in the new code. The loss correlations included in the former code were reviewed and updated, and additional losses, such as windage losses, were implemented in the new version of the code. Experimental results of two radial turbines were used for validation. Wasserbauer and Glassman found a better agreement with the new version of the code, particularly regarding the total efficiency, where maximum deviation were as high as 10% in Todd and Furtral's code and negligible with the new version. An improved correlation was found between the mass flow rate and the turbine performance with the experimental data suggesting that new loss models were more accurate.

The following year, **Glassman (1976)** developed a computer program for radial-inflow turbine design [65] based on Rholik's mean-line model [16]. From the flow conditions (inlet temperature, pressure and mass flow), the turbine power output and speed at the design point, a preliminary design of the turbine geometry and its performance could be obtained. Some examples were included in Glassman's study, but no validation was discussed in the paper.

Parallely, **Whitfield and Baines (1976)** derived a general one-dimensional performance prediction method for radial turbomachinery [65]. The aim of the study was not to develop a new mean-line model for turbine design and analysis like the previous approaches already mentioned [62, 63, 65], which required the designer to become familiar with each methodology. Instead, their objective was to separate the fundamental one-dimensional gas theory used on the mean-line approach from the empirical loss correlations and the assumptions that must be considered to apply the basic theory to a real three-dimensional flow through a turbine. Whitfield and Baines came up with a single general equation for all duct configurations and explained the different considerations that must be taken into account for each duct (volute, nozzle, rotor and diffuser). Thus, the authors provided an open-ended methodology for turbine design and analysis, an alternative to previous mean-line models, which showed certain limitations to new designers.

At the same time radial turbine modelling was being developed, mixed-flow turbines awakened interest. **Baines, Wallace and Whitfield (1979)** investigated the use of mixed-flow turbines for turbocharger applications [60]. They developed a computer program that accounts for all the cone angles of mixed-flow turbines. They used previous approaches of design and off-design mean-line models [65, 66]. 3D methods were used to generate the blades and the complete geometry of the turbine. Two mixed-flow turbines were designed using this procedure, manufactured and tested in a dynamometer rig. In addition, an equivalent radial turbine was also tested to check the advantages of mixed-flow turbines. The mixed-flow turbines showed improved efficiency and swallowing capacity compared to the radial turbine, as well as lower blade tip speeds for the same overall dimensions.

Meitner and Glassman (1983) [17] updated the previous mean-line models for radial turbines [64, 65], reviewing loss correlations and accounting for new losses and variable area nozzle turbines. Named RTOD, Radial Turbine Off-Design, the computer program predicted the performance of an existing turbine depending on its operating point. The code was validated with a radial turbine for space applications tested by Wassenbauer in 1966 with air and argon [67]. A thorough comparison between this code and Wasserbauer and Glassman's [64] was discussed, showing that both computer programs provided a good efficiency prediction, in agreement with the experimental data. The more accurate geometry inputs and flow modelling in the rotor trailing edge made the Meitner and Glassman's code predict mass flow rate more closely to the experimental data than Wasserbauer and Glassman's program. However, the new version of the code still underpredicted the mass flow rate under choking conditions, which was attributed to the inaccuracies of the loss models.

Rodgers and Gueiser (1987) carried out the design and experimental test of a radial-axial two stage turbine [68]. They correlated the flow coefficient and the velocity ratio with the efficiency in a similar way to the Smith chart for axial turbines [69], as it can be seen in Fig. 2.18(a) and 2.18(b), respectively. They found that the flow coefficient range for the highest efficiency in radial turbines was between 0.2 and 0.3, and the velocity ratio, around 0.7.

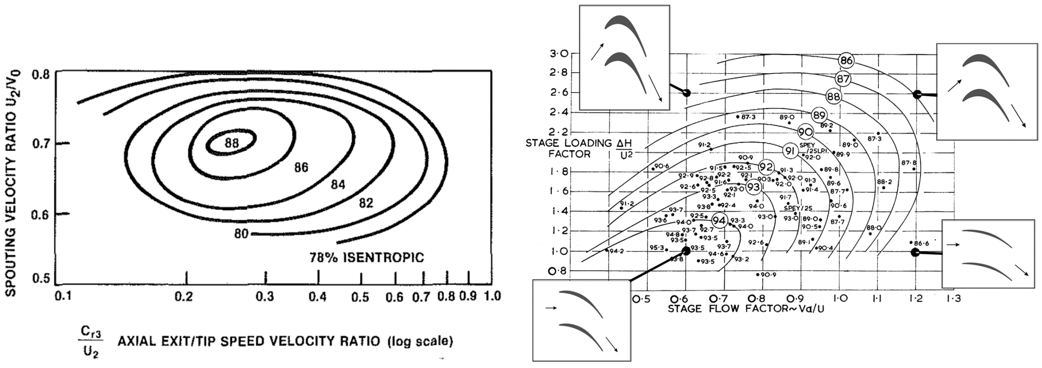

(a) Rodgers and Gueiser chart [68]

(b) Smith chart [69]

Figure 2.18: Turbine performance contours for radial (right) and axial turbines (left).

Later, **Whitfield (1989)** [70] developed a non-dimensional methodology for radial inflow turbine design looking for maximum efficiency. A non-dimensional turbine design could be obtained by specifying the power ratio and an optimum incidence angle, between -30 and -20 *deg*, as well as by estimating the efficiency. The efficiency was recalculated with empirical loss correlation models and updated in the preliminary design. The final non-dimensional design could be transformed into actual dimensions by setting the power output or the mass flow rate at design conditions.

Abidat et al. (1992) [71] designed and tested two mixed flow turbines using the correlations and loss prediction of previous authors [16, 68, 72]. They generated different designs depending on the stator outlet flow angle, the cone angle, the inlet blade angle, the rotor pressure ratio and the volute area-to-radius ratio. After checking the off-design performance, two different turbine geometries were chosen, one with constant blade inlet angle, rotor A, and the other with constant incidence along the span of the blade, rotor B. Experimental results showed that the assumed optimum incidence was close to the real incidence. Rotor A had a higher efficiency, whereas rotor B showed a larger swallowing capacity.

Baines (2002) suggested a design method based on the selection of the flow and load coefficients, which are strongly related to the efficiency [56]. This methodology is similar to the design approach for axial turbines and it has been implemented recently by some authors successfully [73–75] when a preliminary design is needed. For off-design performance prediction, Baines improved the meanline model for high-pressure ratio conditions. After choking the throat area, the parameter which controls the mass flow, is reduced due to blockage. This phenomenon was accounted for by adjusting the deviation angle. Nozzle tip clearance losses were also accounted for variable area nozzles. These developments in the code were reported in a series of papers led by the author and in collaboration with others [76, 77]

Romagnoli (2010) [78] introduced modifications to meanline model to predict the performance of twin entry, mixed flow turbines. The model was successful when predicting the turbine performance at full and partial admission conditions. The model was validated with experimental data of a wide operating range, unlike the previous meanline model, which relied on limited range experimental data.

More recently, **Hohenberg (2020)** [79] developed a meanline model and carried out an extensive loss correlation comparison and calibration with a design space CFD data and experimental data in a wide range of operating conditions. Efficiency and mass flow predicted by meanline model deviate an average of 3% in efficiency and mass flow in the calibration dataset.

2.3.3 Loss Modelling

The complex 3D flow through a turbine leads to energy losses that can not be captured by reduced order modelling approaches, like meanline modelling. Therefore, semi-empirical correlations were developed by different authors to account for the losses in the preliminary turbine design and performance prediction methodologies. Volute and nozzle loss correlations are used in turbine modelling to account for the complexity of loss sources and types. In the rotor, the different loss mechanisms have been identified and, although they are all interrelated, a physical-based loss breakdown is sensible, as Rohlik [16] showed in Fig. 2.19. The loss sources usually considered in the rotor are the following and are discussed below:

- Incidence losses
- Passage losses
- Tip clearance losses
- Trailing edge losses
- Disk friction losses
- Exit losses

There are different ways to define loss coefficients: in terms of enthalpy [80], stagnation pressure [81] or head loss [82]. Although Horlok showed the relation between the enthalpy loss coefficient and the pressure loss coefficient [81], this can only be applied in nozzles, because in the case of rotors of radial inflow turbines, the relative stagnation pressure through the rotor is not constant, even in ideal conditions. Therefore, the loss correlations need to be carefully chosen and their coefficients calibrated for a given application so the model is highly accurate.

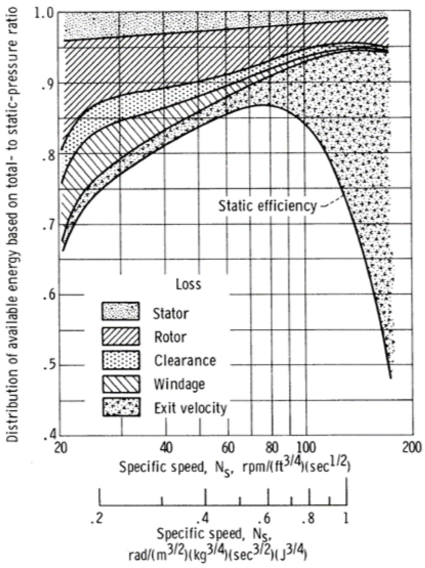

Figure 2.19: Loss distribution of a turbine with the rotational speed [16].

Incidence Losses The incidence loss occurs as a consequence of turning the flow from the free stream direction to the blade direction, it is also related to the circulation needed for a flow to turn around a body [56]. The first formulation of the incidence loss was based on a stagnation pressure loss coefficient, assuming that the process occurs at constant static pressure, by Wallace [66]. Later, Futral and Wasserbauer modelled the incidence loss as a change in tangential kinetic energy [62]. This formulation was updated by Wasserbauer and Glassman for non-zero optimum incidence [64] and has been used in some of the most recent mean-line models [74, 83], although others preferred previous models [73, 75].

Passage Losses Passage loss is the main blade loss related to friction (profile loss) at the wall as well as the effects of secondary flow motion that ensues due to pressure gradients caused mainly by Coriolis forces and centrifugal forces. Note that in this thesis the tip leakage loss has a specific entry although it clearly interacts with passage loss. In addition, flow separations can occur, contributing to the flow disturbance in the passage and enhancing the passage loss. Therefore, conventional analysis of friction in a duct is not an accurate approach for passage loss modelling. Correlating experimental results of passage losses for turbine performance prediction is a rather complex problem because incidence conditions have an important influence on the flow through the passage [84].

The tip speed, the mass flow rate and the number of blades are some of the most influencing parameters in passage losses [80]. Unlike in axial machines, passage losses in radial turbines include both profile (friction) and secondary losses and its breakdown does not seem very sensible in this case [56].

In 1970, Benson reviewed some of the earliest passage loss correlations of that time, comparing the results with experimental data [80], but found a small numerical difference among them. The correlation of Bridle and Boulter [85], which used the Aienly and Mathieson [86] approach for modelling the secondary flows, had three empirical constants. Balje [82] used the convectional skin factor to model passage losses, including an empirical loss factor to account for secondary losses. Futral and Wasserbauer [62] developed a simple correlation considering the mean kinetic energy of the flow through the passage, but it lacked physical basis. Benson developed a correlation based on the inlet relative velocity [87]. Later, Wasserbauer and Glassman in 1975 further developed the passage loss correlation from Futral and Wasserbauer [62] based on an evaluation of the boundary layer thickness development. They defined it as kinetic energy loss, a fraction of the ideal velocity of the flow through the blade passage [64].

Glassman in 1976 [65] used correlations based on the enthalpy loss coefficient proposed by Rohlik [16]. First reported by Benson [80] and then by Baines [56], the loss model proposed by Futral and Wassenbauer [62] and later improved [64] is the most widely used correlation in current radial turbine models [74, 75, 78, 83, 88, 89], as it is simple and provide the same accuracy than other models. Nevertheless, Baines [56] discussed that this approach does not predict losses properly when dealing with a wide variety of radial turbines. Therefore, an updated correlation to model friction losses and secondary flow more accurately was provided by Baines [56].

Disk Friction Losses These losses relate to the rotating back surface of the rotor, they are always present and are enhanced flow leakage. They are usually modelled as a power loss [56, 80]. The analysis of Daily and Nece [90] considered enclosed rotating disks in 1960, setting the basis for the disk friction correlation, which is the most commonly used [56, 80].

Tip Clearance Losses The radial and axial clearance between the rotor and the shroud is a source of losses due to leakage over the tip of the blade. Futral and Wasserbauer modelled this loss as a fraction of the mean kinetic energy [62]. Rodgers defined clearance losses as an empirical efficiency drop coefficient [68]. Then, Glassman [65] suggested that the tip clearance losses were a fractional loss equal to the clearance-to-blade height ratio, based on the analysis by Rohlik [16]. Reported by Baines [56], the tip clearance loss model from Dambach et al. [91] includes the effects of radial and axial clearances and a cross-coupling coefficient. This loss can become quite large and become the dominant loss mechanism for high pressure ratio turbines, especially when the clearance-to-blade height ratio is also high. This is particularly relevant in the case of ORC turbines, which operate at high pressure ratio and have small blade heights.

Trailing Edge Losses Trailing edge losses account for the losses generated from the rotor throat to the trailing edge plane, which the passage losses reported by Baines [56] do not include. Thus, Baines suggested a pressure loss coefficient based on a sudden expansion between the throat and the trailing edge. Glassman, instead developed a more complex expression [92] that is widely used in turbine modelling [74].

Exit Losses The exit loss is related to the kinetic energy of the flow that leaves the rotor, in other words, the rotor was not able to recover this energy and thus it can be seen as a loss. The use of an exit diffuser is often used to allow the turbine to extract greater power by increasing turbine pressure ratio and reducing exit kinetic energy.

Some of the loss correlations above explained are included in the meanline model developed for the current project. Specific details in the loss models chosen are in the following chapter.

2.3.4 Non-ideal Gas Effects and Modelling

All turbine models described above were developed under the ideal gas assumption. However, the matching between mean-line model predictions and experimental data for turbines used in other applications, such as ORC, was not satisfactory. The meanline model developed by Baines [18] is the most widely used in recent studies on radial inflow turbines. These studies attempted to solve the limitations of the ideal gas assumption by using the compressibility factor or the equations of state of different fluids.

The behaviour of the fluids of high molecular complexity and the fluids that operate around the critical point need to use equations of state that describe more accurately their non-ideal properties. Van der Waals introduced the first equation of state and set the basis for the family of cubic equations of state such as Peng-Robinson (PR) [93] or Soave-Redlich-Kwong (SRK) [94, 95] equations. These are frequently used due to their computational efficiency and the limited amount of factors needed to perform calculations.

Although many types of equations were developed in the early 1900s, with the improvement of computational resources and optimisation strategies, more sophisticated equations of state were derived. These are multiparameter equations of state based on the Helmholtz free energy methods. Nowadays, multiparameter equations of state are the most accurate methodology for property calculation [96]. Thermophysical property data of several fluids are available in databases such as CoolProp [97] or REFPROP [98].

Multiparameter equations of state are empirical correlations of experimental data. Therefore, different equations apply to each fluid or family of fluids. R1233zd(E) equation of state used in the databases was developed by Mondejar et al. in 2015 [1]. Most of the meanline models in the literature have used these databases to carry out the calculations for radial turbine design for ORC applications [55, 73–75, 99–101].

2.3.5 Non-Radial Fibre Blading

Turbine blades are commonly designed to be oriented in the radial section in planes normal to the axis of rotation, this is known are radial fibre rotors [18]. This design feature results in low stresses in the blades. High temperatures and the centrifugal loading at high rotational speeds, induce large stresses that may compromise the structure if the radial-fibre design constraint is not followed. Departing from the radial fibre constraint introduces additional degrees of freedom in the design process, allowing the possibility of different camberline and blade angle distributions along the span.

From an aerodynamic point of view, the incidence angle deviates from the optimum value, which lies between -20 and -40 degrees [18], when operating at off-design conditions, particularly at low velocity ratios, at which the incidence angle increases. This effect has motivated the positive inlet angle, or backswept rotor designs, seeking to decrease the incidence angle.

Discussion on non-radial blading designs can be found in the literature as early as 1982. Mulloy et al. [102] carried out an experimental assessment of different configurations of a 40 degree backswept rotor compared to a radial design. The results showed performance improvement in the non-radial blading design due to the swirl reduction of the flow leaving the rotor. A smaller degree of separation and recirculation was found in the optimised rotor, explaining this lower exit swirl. A large recirculation formed at the rotor inlet was found at low mass flow and low speed operating conditions, which is explained as a similar effect to non-zero incidence.

Barr et al. [103] carried out an experimental and numerical investigation on a 25 degree inlet blade angle backswept rotor reporting an efficiency improvement of 1.76% at low velocity ratios (high pressure ratio) compared to a radial baseline design. It was argued that the performance improvement corresponded to mass flow increase at these points. However, the efficiency was penalised at design point for the optimised rotor. The analysis of the secondary flow features showed a reduction on the vortex forming at the leading edge due to separation on the suction surface. This vortex was also found to have less influence on the flow at the trailing edge in the backswept design. In addition, structural and modal analyses carried out showed good structural and vibrational behaviour.

Walkingshaw et al. [104] investigated the effect of inlet blade angle on different designs with constant backsweep and one design with a variable inlet blade angle along the span. The results suggested flow separation at the pressure surface with increasing blade inlet angle. Moreover, the simulations showed a decrease in blade loading at the leading edge in designs with high backswept angle which reduced the suction surface separation and tip leakage at high velocity ratio conditions. This explained the performance improvement found when increasing inlet blade angle. However, the stress constraints made some of the designs inadequate for high-speed, high-temperature turbocharging applications.

The literature on non-radial blading summarised above focused on turbocharger applications. These applications are characterised by high pressures, temperatures and rotational speeds. The high centrifugal and thermal stresses in these applications mean that only small deviations from the radial fibre constraint are possible in order to keep the structural integrity of the rotor.

2.4 Experimental Testing

A larger database on experimental measurements of axial turbines is available in the literature, compared to radial turbine experimental data. Most of the experimental data available in the literature has been obtained by cold air testing. Although cold tests do not replicate the real hot conditions, non-dimensional analysis allows finding equivalent cold conditions to simulate an operating point in hot conditions. This a good way to directly compare the results from the mean-line model, since the adiabatic conditions in the calculations are close to the cold test conditions since little heat transfer occurs.

Test rigs for cold tests usually consist of a compressor that blows pressurised air into the turbine. Two different ways of measuring the actual power output can be found:

- The actual power of the turbine can be measured from the power consumption of the compressor [67].
- A dynamometer can measure the actual torque of the turbine with a load cell.

The first way uses a compressor as a loading device and thus relies on thermodynamic quantities (i.e. temperature rise) and includes mechanical efficiency losses, it is thus less accurate. Imperial College facilities include an eddy-current dynamometer that removes the difficulties of using a compressor to evaluate turbine power. Additionally, it measures directly the turbine power. Many radial and mixed-flow turbines have been experimentally tested in this facility [58, 78, 79, 88, 88, 105]. Figure 2.20 shows a schematic representation of Imperial College test facilities. More details about the testing facilities are provided in the next section.

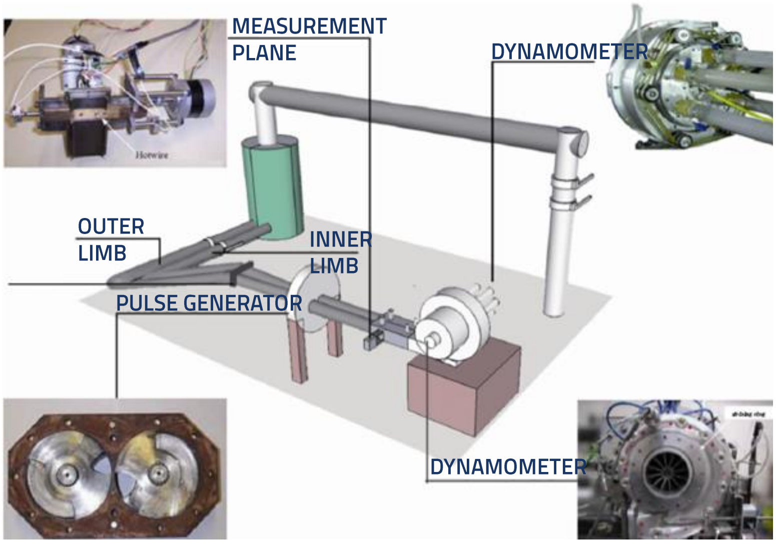

Figure 2.20: Eddy-current dynamometer test rig at Imperial College.

ORC experimental facilities have been developed in many locations worldwide, but those focused in radial inflow turbines testing are limited. In Korea, a simple 42 kW ORC experimental test bench was built to test single and two stage radial turbines [106, 107], the working fluid was R245fa. In the same country, another R245fa ORC experimental facility was designed for the same purpose [108], the power output was 200kW. A 40kW ORC-heat pump unit working with R134a was developed in Switzerland, radial turbines were successfully tested experimentally [109]. In Finland a 10 kW recuperative ORC experimental rig was designed running with siloxane as working fluid [110]. A 2kW simple ORC rig with radial turbomachinery was built in China [111], the working fluid was R123. A comparison between the performance of R245fa and R1233zd(E) of a radial turbine was carried out in a 3.5 kW ORC research facilities built in Belgium [112]. In the United Kingdom, a 20kW ORC rig was built coupled with radial turbine [113].

No experimental facilities combining different waste heat recovery technologies were found in the literature. Since this research is part of a bigger collaboration, Universiti

Teknologi Malaysia (UTM), as one of the partners in this global program, has developed a pilot plant replicating the conditions of the waste heat streams in an oil and gas offshore platform. The pilot plant will integrate the waste heat recovery technologies considered, ORC, ETC and TEG. Figure 2.21 shows the layout of the pilot plant. An engine provides exhaust gases of similar characteristics as the identified waste heat sources in the offshore plant. An eddy-current dynamometer will measure the torque for the test of radial and mixed-flow turbines in real conditions.

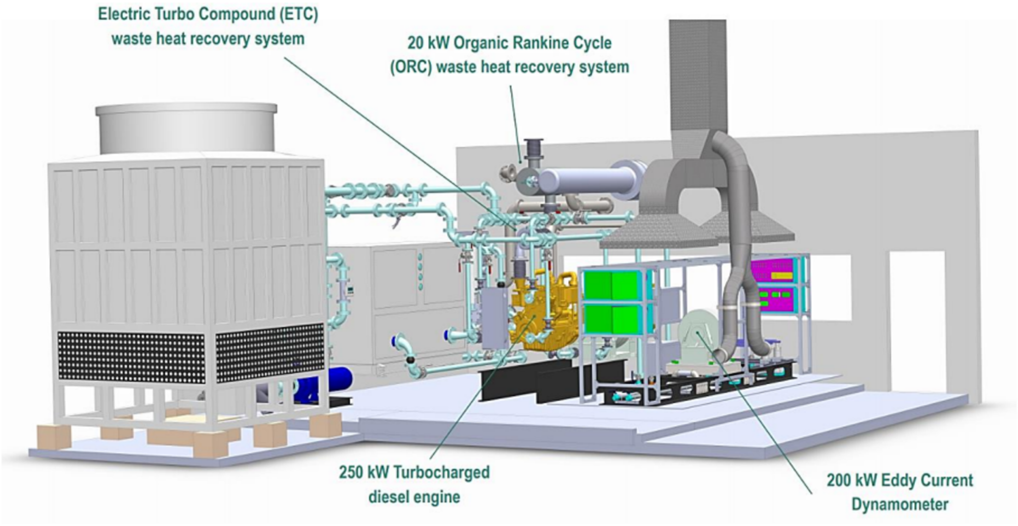

Figure 2.21: Pilot plant layout at UTM.

The engine used in the pilot plant as the waste heat source is a CAT C9.3 (see Fig. 2.22). The design power output is 224 kW, 300 HP and their design speed is 2100 RPM. The selection of the engine size has been based on the organic Rankine cycle boundary conditions that will run on the pilot plant. The engine will be coupled to a 415V 3-phase AC generator delivering 200 kW of electrical power. The electricity produced will be used for the power-consuming components in the pilot plant. While ensuring the pilot plant is self-sustaining, without the need for an external power supply, it also maintains the engine at fully loaded condition, so that the exhaust gas is at a constant temperature.

Figure 2.23 shows the process flow diagram of the pilot plant. The electric turbocompounding turbine will be installed downstream of the engine (stage (a) in Fig. 2.23). The exhaust gas stream of the engine sets the inlet conditions for the ETC turbine, 1.2

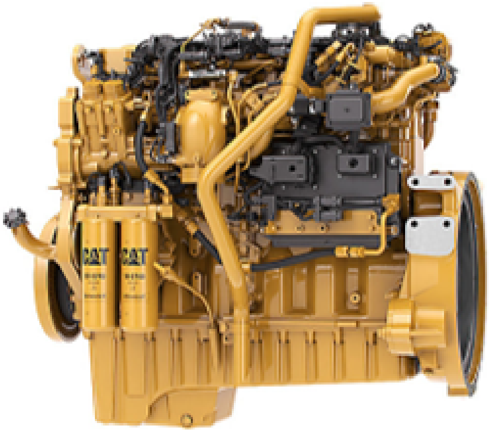

Figure 2.22: CAT C9.3 engine of the pilot plant at UTM.

bar and 470 $^{\circ}C$. The ETC outlet gas (stage b) still at a high temperature, 455 $^{\circ}C$ will be recirculated to the ORC heat exchanger to raise the temperature of the organic fluid before entering the ORC turbine (stage 1). The exhaust gases after the super-heater (stage c) will be recirculated through the TEG system, which is not included in the diagram for clarity.

After the turbine expansion (stage 2) the pressure drops from 27 bar to 3 bar and the organic fluid flows through the regenerator to preheat the fluid after the pump. The fluid goes to the condenser (stage 3) until saturation conditions are achieved (stage 4). The pump raises the pressure from 1.6 bar up to almost 28 bar (stage 5), then temperature rises in the regenerator up to 113 $^{\circ}C$ (stage 6). The flow enters the super-heater where the fluid will evaporate due to the waste heat reaching 250 $^{\circ}C$.

The conditions and efficiency of the components shown in Fig. 2.23 were the values assumed for the system optimisation carried out at UTM. Table 2.3 summarises the boundary conditions for the ETC and ORC turbine design by using the expander design approach, explained in the next section.

Parameter	**ETC**	**ORC**
Mass flow [$kg \cdot s^{-1}$]	0.3	0.9
Inlet Pressure [bar]	1.1-1.3	27.0
Outlet Pressure [bar]	1.0	3.0
Inlet Temperature [C]	470	250

Table 2.3: Turbine inlet conditions for ETC and ORC applications.

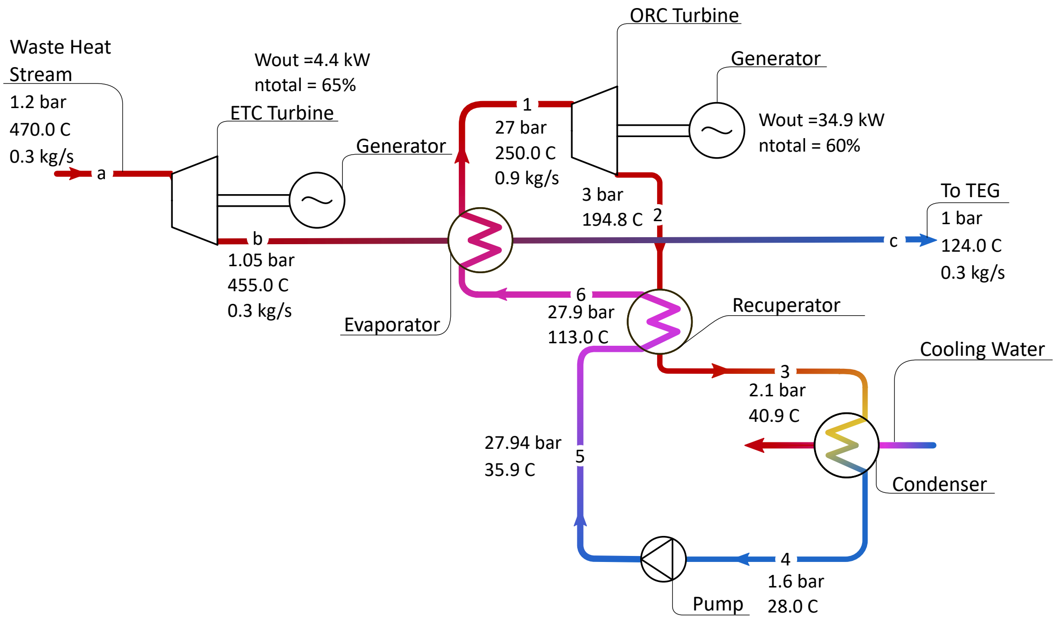

Figure 2.23: Pilot plant diagram at UTM.

2.5 Gaps of Knowledge

This chapter gathers the literature review and the state-of-the-art on the relevant areas of this research:

- Lack of investigation on combination of WHR technologies.
- Lack of accuracy of meanline modelling loss coefficients for unconventional boundary conditions, typically found in ORC and ETC applications.
- Lack of understanding of the effect of 3D geometry modifications of the blades on turbine performance and flow field.

There is a high potential for waste heat recovery in oil and gas offshore platforms. However, only a few studies have investigated the implementation of ORC systems and no study has been found on the combination of ORC with ETC technologies for waste heat recovery. In both technologies, the turbine represents one of the main components that drive the system efficiency. Therefore special attention needs to be paid to its design to ensure high efficiency, particularly considering the unconventional boundary conditions under which the turbines for these applications operate.

Several authors have developed meanline models for radial inflow turbine design and performance prediction over the last 80 years, using physically based equations but also empirical correlations for loss prediction for turbocharger applications. Recently, efforts have focused on the implementation of the equations of state to predict the behaviour of non-ideal gases for other applications such as ORC applications. One of the main limitations of meanline methods lies in the empirical models for loss prediction on radial turbomachinery, which provide a loss breakdown that may not be entirely realistic. Moreover, the empirical models rely on calibration coefficients, which are specific to the application. Therefore, the unconventional boundary conditions of the applications, low pressure, for ETC and the opposite, high pressure for ORC make the loss coefficients available in the literature inaccurate. Objectives 1 and 2 of this work address this research gap and assess how significant these limitations in meanline modelling are. The meanline model developed in Chapter 3 is used to evaluate the performance and loss breakdown of several geometries for ORC and ETC applications in the first part of Chapters 4 and 5.

In addition, low-order models also show limitations when predicting the impact on the performance of certain geometry modifications. Therefore more detailed approaches are essential to come up with designs that may be out of the meanline design space and understand the flow physics. There is a gap in understanding the effect of 3D geometry modifications and non-radial fibre that is addressed in the final parts of Chapters 4 and 5 and relate to Objectives 3 and 4.

ORC experimental facilities to test radial turbomachinery are available in the literature, however, no test rig capable of integrating different waste heat recovery technologies was found. UTM, one of the main collaborators in this project, is currently building an experimental facility replicating the waste heat stream conditions to test the combination of WHR technologies. Although this is not part of this thesis, it is important to highlight the research gap in experimental ORC turbine data, which will be addressed in the main project in which this thesis is framed.

The next chapter introduces the methodology used in this study to overcome the gap in knowledge of the topics above, to answer the main research question in this work:

What is the effect of 3D blade features and non-radial blading on the performance of low pressure turbines and ORC turbines when compared to the commonly used radial fibre design?

Chapter 3

Expander Design Methodology

The methodology used in this study consists of low-order modelling and 3D modelling. The low-order model developed in this research is based on meanline modelling, widely used for preliminary turbine design. The 3D model consisted of a 3D parametric model of the nozzle and the rotor coupled with CFD software, also widely used in turbomachinery flow analysis.

Both methodologies predict the turbine performance using operating conditions and geometrical key parameters as main inputs to the solver. Meanline modelling has a low computational cost and reduced number of geometrical inputs, but cannot predict the effect of certain geometric changes related to the 3D geometry on the resulting efficiency. The parametric-CFD based approach, however, is able to assess the impact of 3D geometric features, such as non-radial blading, on the resulting efficiency, but it comes at a higher computational cost. The structural analysis methodology for ETC rotors is introduced in this chapter.

3.1 Meanline Modelling

The meanline approach consists of a set of physics-based equations to calculate the thermodynamic properties and flow velocity at each turbine stage. Figure 3.1 shows the components and stages of the meanline model, where each stage refers to:

1. Volute inlet
2. Volute outlet and nozzle inlet
3. Nozzle outlet and interspace inlet
4. Interspace outlet and rotor inlet
5. Rotor outlet and diffuser inlet
6. Diffuser outlet

The subscripts of thermophysical properties and velocities in the meanline model refer to the turbine stages introduced above. This study is focused on the rotor performance (4 and 6); hence the volute (1), interspace (3) and diffuser (7) are not considered. These three components introduce an efficiency penalty in the whole turbine performance, however, the main drivers of the efficiency are the nozzle and the rotor, since most of the losses occur there.

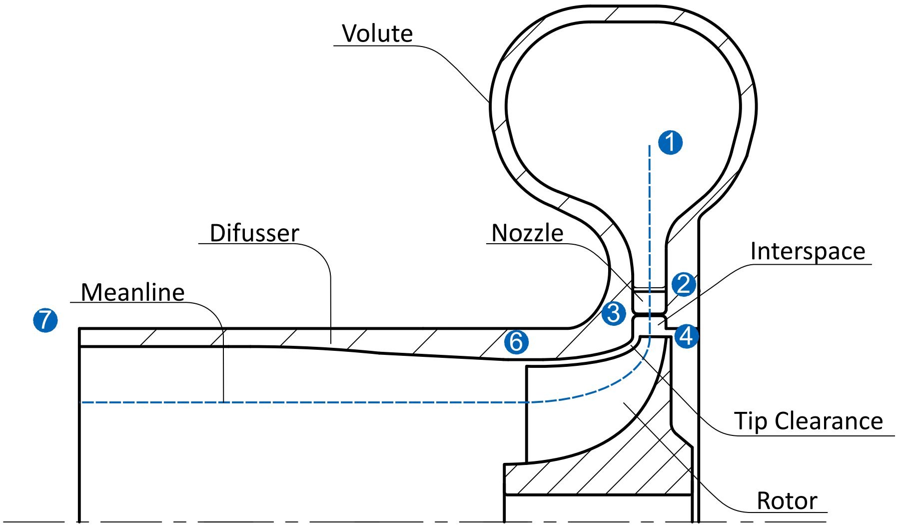

Figure 3.1: Meanline turbine components and stages

3.1.1 Meanline Equations

Meanline equations ensure continuity, momentum and energy conservation across the turbine domain. Mass conservation equation, 3.1, is applied at each station i, where $\dot{m}$ is the mass flow across the turbine, $A_{eff,i}$ is the effective area, C_i is the absolute velocity, ρ_i is the density and B the blockage factor due to blade thickness, boundary layer thickness and separation, among other effects.

$$\dot{m}_i = A_{eff,i}\, C_i\, \rho_i\, B_i \tag{3.1}$$

The blockage factor value is found by calibrating the model against experimental or high fidelity turbine performance data, being this a common practice in meanline modelling approach [18]. The effective area is calculated according to Eq. 3.2, where A_i is the geometric area of the flow path at the nozzle or rotor and $\alpha_{flow,i}$, $\beta_{flow,i}$ the flow angle in the absolute and relative frame of reference, respectively.

$$A_{eff,i} = A_i \;\; cos\,(\alpha_{flow,i} \quad or \quad \beta_{flow,i}) \tag{3.2}$$

Euler's equation is derived from momentum and energy conservation, and it is applied across the rotor stage, shown in Eq. 3.3, where $\dot{W}_{act}$ is the actual power output, subscripts $_4$ and $_6$ stand for the rotor inlet and outlet, respectively, U is the blade rotational speed and Ct is the circumferential component of the absolute velocity.

$$\frac{\dot{W}_{act}}{\dot{m}} = U_4\, Ct_4 - U_6\, Ct_6 \tag{3.3}$$

The turbine performance maps consist of mass flow rate and efficiency at each operating point, which is defined by rotational speed, inlet temperature and pressure ratio.

The total-to-static efficiency, η_{ts}, defined in Eq. 3.4, measures the ratio of actual power recovered by the turbine, $\dot{W}_{act}$, out of the isentropic power available, $\dot{W}_{iso}$. Since power is equal to specific enthalpy drop by mass flow, η_{ts} can be simplified into the ratio of actual total specific enthalpy drop, $\Delta h_{0,act}$, and isentropic specific enthalpy drop, Δh_{iso}. At the same time, Δh_{iso} is equal to the sum of the actual enthalpy drop, the specific enthalpy drop due to losses in the nozzle and rotor, Δh_{loss}, and the specific enthalpy drop due to exit losses, Δh_{exit}.

$$\eta_{ts} = \frac{\dot{W}_{act}}{\dot{W}_{iso}} = \frac{\dot{m}\Delta h_{0,act}}{\dot{m}\Delta h_{iso}} = \frac{\Delta h_{0,act}}{\Delta h_{0,act} + \Delta h_{loss} + \Delta h_{exit}} \tag{3.4}$$

CoolProp [97] database was used to calculate the thermophysical properties of the ORC working fluid, R1233zd(E) [1], at each state. Although this increases the computational time of the meanline algorithm, it is deemed to be essential to capture the non-ideal effects of the organic fluid. For ETC expander, a perfect gas assumption was used to model air as working fluid.

3.1.2 Loss Correlations

The loss correlations used in this study are semi-empirical equations that estimate the pressure or enthalpy drop due to the different loss mechanisms across the turbine. These consist of pressure losses across the nozzle (stage 4 in Fig. 3.1) and incidence, passage, tip clearance, trailing edge, post-expansion losses across the rotor (stage 6 in Fig. 3.1). While these correlations are based on physical models, they include coefficients that require calibration against experimental or high-fidelity computational data.

Incidence loss modelling assumes that the kinetic energy resulting from the change in direction of the relative circumferential velocity at the leading edge is converted into internal energy. This increase in internal energy contributes to the entropy increase in the flow. This formulation accounts for non-zero optimum incidence and it is used in some of the most recent meanline models, as shown in Eq. 3.5 [64], where Δh_{inc} stands for specific enthalpy incidence losses, K_{inc} is the incidence calibration coefficient, W_4 and β_4 are the velocity and the flow angle in the relative frame of reference at the rotor inlet, respectively.

$$\Delta h_{inc} = K_{inc}\frac{1}{2}W_4^2 \; sin^2(\beta_4 - \beta_{opt}) \tag{3.5}$$

The optimum relative flow angle, β_{opt}, represents the flow angle for optimum incidence, i_{opt}, calculated using a semi-empirical correlation, Eq. 3.6, where $\beta_{blade,4}$ is the metal blade angle at the rotor leading edge. The optimum incidence angle, i_{opt}, is the incidence angle that results in the highest efficiency and depends on the turbine design. This work used a correlation derived from experimental results, as shown in Eq. 3.7 [18], where N_r is the number of rotor blades and α_4 is the absolute flow angle at the rotor inlet. Experimentally, the optimum incidence has shown to be between $-20°$ and $-40°$ [18].

$$\beta_{opt} = \beta_{blade,4} - i_{opt} \tag{3.6}$$

$$i_{opt} = tan^{-1}\left(\frac{-1.98\ tan\,\alpha_4}{N_r - 1.98}\right) - \beta_{blade,4} \tag{3.7}$$

The losses generated due to boundary layers and secondary flows across the passages are denoted as passage losses. Low momentum fluid adhering to the surface of the rotor blades and walls forms the boundary layers. The boundary layers are affected by the pressure gradient, centrifugal, and Coriolis forces. As a result, secondary flows originate from the low momentum boundary layers, develop and distort the main flow. This results in increased entropy, and the corresponding loss is proportional to the main flow kinetic energy. Equation 3.8 [64] shows the formulation chosen for these losses, where Δh_p stands for specific enthalpy passage losses, K_p is the incidence calibration coefficient and W_6 is the velocity in the relative frame of reference at the rotor outlet,

$$\Delta h_p = K_p\frac{1}{2}(W_4^2\ sin^2\left(\beta_{blade,4} - \beta_4\right) + W_6^2) \tag{3.8}$$

The radial and axial clearance between the rotor and the shroud, known as tip clearance (shown in Fig. 3.1) is a source of losses due to leakage and corresponding mixing. The loss model used suggests that the tip clearance losses are proportional to the clearance-to-blade height ratio, as shown in Eq. 3.9 [114], where Δh_{cl} represents specific enthalpy drop due to tip clearance losses, ϵ_r is the tip clearance, Z_r is the rotor length and N_r is the number of rotor blades:

$$\Delta h_{cl} = K_{cl} \frac{1}{4} \frac{U_4^3 \, \rho_4 \, Z_r \, N_r \, \epsilon_r}{\dot{m}} \tag{3.9}$$

Trailing edge losses account for the losses generated from the rotor throat to the trailing edge plane. Equation 3.10 [92] shows the expression for the trailing edge losses calculation, Δh_{te}, where Nr corresponds to the number of rotor blades, r_{6s} and r_{6h} to the rotor shroud and hub radius, respectively, β_6 is the relative flow angle, W_{6s} is the relative velocity, γ_6 is the adiabatic coefficient and Ma_{6r} is the relative Mach number. Subscript $_6$ refers to the rotor trailing edge, stage 6 in Fig. 3.1.

$$\Delta h_{te} = \left(\frac{N_r \, t_6}{\pi \, (r_{6s} + r_{6h}) \; cos \, \beta_6} \right)^2 \frac{1}{2} \, W_{6s}^2 \left(1 + \frac{n-1}{2} \, Ma_{6r}^2 \right)^{\frac{n}{1-n}} \tag{3.10}$$

The flow has a certain kinetic energy when leaving the rotor that is wasted unless a diffuser is used. In those cases where there is not a diffuser, like in the present work, exit losses, Δh_e, are modelled as the kinetic energy at the rotor outlet, Eq. 3.11 where C_6 is the absolute velocity at the rotor exit:

$$\Delta h_e = \frac{1}{2} \, C_6^2 \tag{3.11}$$

Losses across the nozzle are simply modelled as pressure losses, as shown in Eq. 3.12 [92], where K_n is the pressure loss coefficient, P_{02} and P_{04} refers to total pressure at the nozzle inlet and nozzle outlet, respectively, and P_4 refers to static pressure at the nozzle outlet.

$$K_n = \frac{P_{02} - P_{04}}{P_{04} - P_4} \tag{3.12}$$

Finally, blockage factor coefficients B_i were applied to the continuity equation at each station, Eq. 3.1 to account for the reduction of the effective area due to blade thickness and boundary layer separations. Equation 3.1 shows how this coefficient is applied in the meanline model.

The equations and empirical correlations of the meanline model introduced above were used to define an algorithm to predict the turbine performance in an automated way. The performance algorithms were written in Python and their structure and resolution are explained in the next section.

3.1.3 Code Structure

The structure of the algorithm is explained below, covering the inputs, main code and subroutines, as well as the iterating parameters and convergence criteria used.

Among the meanline algorithm inputs are the operating conditions and geometric data of the turbine. The operating conditions include temperature, pressure and mass flow of the waste heat stream, as well as the pressure ratio fixed by the application and the rotational speed. The geometrical data involve blade angles, radii of the nozzle and the rotor, blade thickness, tip clearance and rotor length. Some of these geometrical parameters are used as variables for the optimisation of the design, these are so-called design geometrical inputs.

Other geometrical parameters were fixed for all designs to limit the number of design parameters. Each turbine design is defined by 7 parameters, 6 related to the geometry design; and 1 to the rotational speed. The summary of the operating conditions and input parameters related to the geometry are shown in Table 3.1.

Once the geometry is fully defined, meanline equations can be applied to solve the thermodynamic and velocity characteristics across all stages of the turbine. The flowchart describing the iterative method for the main algorithm can be found in Fig. 3.2. As it can be seen in this flowchart, two different subroutines may apply depending on the nozzle and rotor choke state defining 4 situations: both nozzle and rotor unchoked, nozzle chokes first but the rotor is unchoked, both nozzle and rotor choked and rotor chokes first. The routine defining the component that chokes first depends on the location of the minimum effective throat area.

The main algorithm, shown in Fig. 3.2, consists of one overall loop over the density at the nozzle inlet, ρ_2, and two inner loops over the nozzle outlet (coincident with the

Table 3.1: Operating conditions and input geometric parameters of the meanline performance algorithm

Type	Parameter	Expression
Operating conditions	Inlet total temperature	T_{02}
	Inlet total pressure	P_{02}
	Pressure ratio	PR
	Rotational speed	$Nrpm$
Design geometric inputs	Nozzle metal angle	α_4
	Wheel radius	r_4
	Blade height	b_4
	Shroud exit radius to inlet radius ratio	$\frac{r_{6s}}{r_4}$
	Hub exit radius to inlet radius ratio	$\frac{r_{6h}}{r_4}$
	Rotor blade metal angle at exit	β_6
Other geometric inputs	Rotor length to inlet radius ratio	$\frac{Z_r}{r_4}$
	Nozzle inlet radius to rotor inlet radius ratio	$\frac{r_2}{r_4}$
	Tip clearance	tc
	Rotor trailing edge thickness	$t6$

rotor inlet), iterating ρ_4, and the rotor outlet, iterating ρ_6. The density is iterated until a residual value lower than 10^{-5} is achieved. The residual value for ρ_2 is defined as the error between in the input pressure ratio and the pressure ratio resultant from the calculations (iterations), based on the initial guess of ρ_2.

If a feasible solution is reached for the inner loops based on ρ_4 and ρ_6, the operation of the turbine is subsonic, and both components are unchoked. When a solution is not reached for ρ_4, then the nozzle is considered as choked and the subroutine shown in Fig. 3.3 is applied. After choking of the nozzle, the conditions at inlet are kept constant, ρ_2, and mass flow is fixed to $\dot{m}_{choke}$. In subsonic operation, the flow is assumed to follow the nozzle vanes and rotor blades angle at the trailing edge, with no deviation, $\delta_{4,6} = 0°$. However, after the choking point, deviation is assumed to increase allowing post-expansion as if the passage had a convergent-divergent shape [18]. Therefore, the parameter for iteration of the outer overall loop is the absolute flow angle at the trailing edge of the nozzle, α_4, defined as shown in Eq. 3.13.

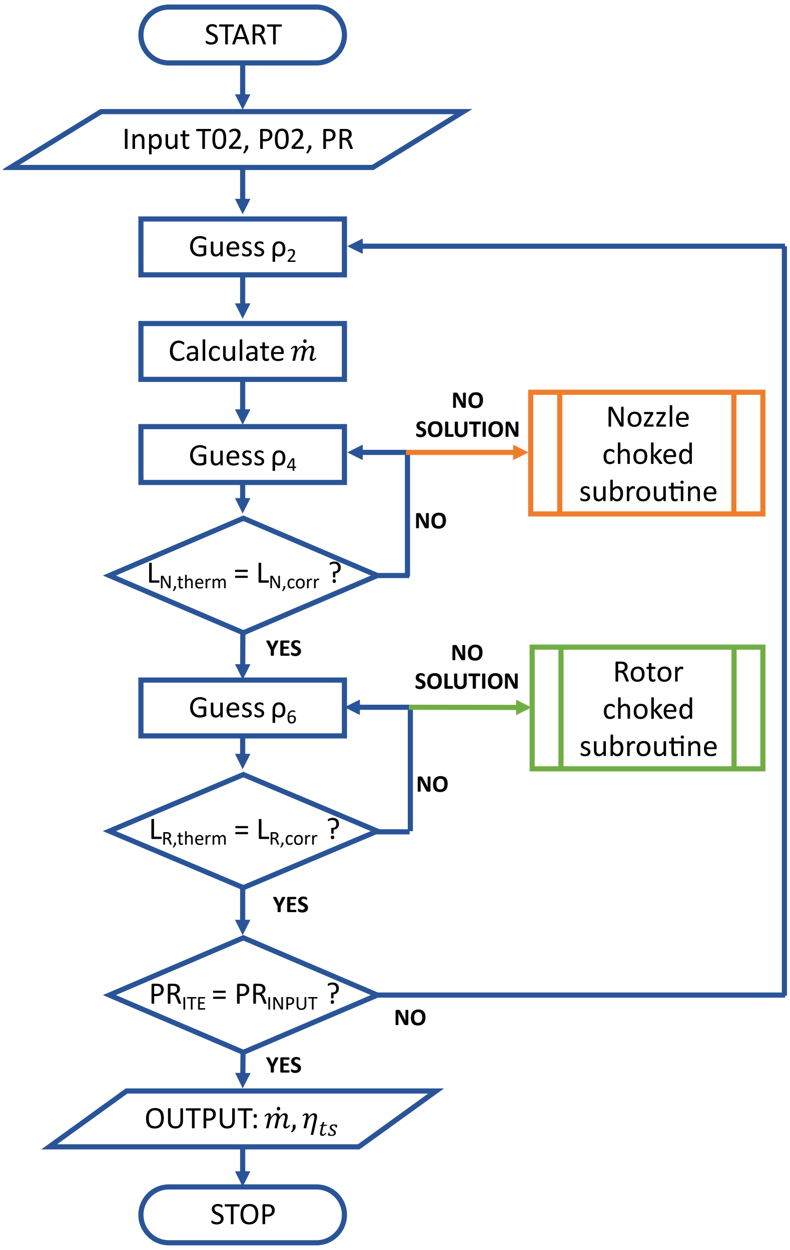

Figure 3.2: Performance algorithm

$$\alpha_4 = \alpha_{4,nozzle} - \delta_4 \tag{3.13}$$

This effect consisting of the flow deflection due to post-expansion after the shock wave is illustrated in Fig. 3.4. The flow angle at the trailing edge of both the nozzle and rotor deviates from the blade angle due to the shock waves allowing for a supersonic expansion.

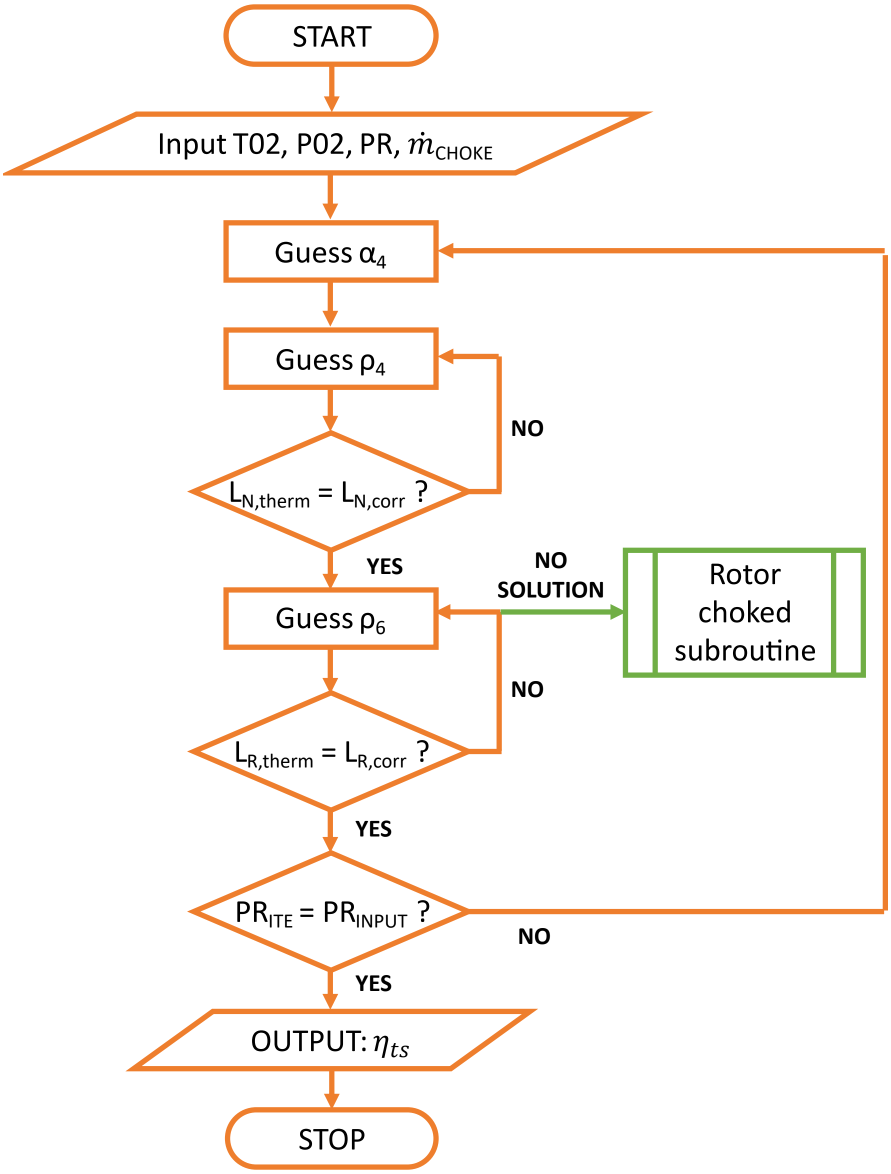

Figure 3.3: Nozzle choked algorithm subroutine

The algorithm in Fig. 3.3 decreases α_4 from the subsonic value where deviation was set to zero, $\delta_4 = 0°$. This allows for a higher expansion ratio across the nozzle, until the pressure ratio calculated matches the application pressure ratio.

Similarly, if there is no solution available for the inner loop based on ρ_6, the rotor is assumed to be choked and conditions upstream are fixed, as shown in Fig.3.5. If the nozzle was already choked, that sets the absolute flow angle at the nozzle outlet fixed to $\alpha_4 = \alpha_{4,choke}$. Otherwise, deviation at the outlet of the nozzle is assumed to zero, and thus, the flow angle is equal to the metal angle, $\alpha_4 = \alpha_{4,nozzle}$ and conditions at

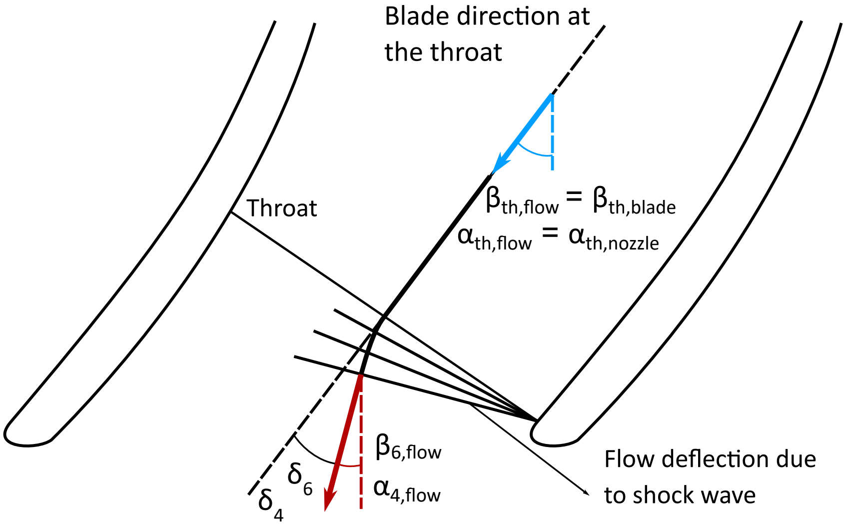

Figure 3.4: Flow deviation at the nozzle and rotor throat after shock waves in supersonic flows [17, 18]

nozzle outlet are calculated with the ρ_4 loop. The rotor choked subroutine increases β_6 (towards $0°$), assuming that the flow deviates at the trailing edge from the metal angle in Eq. 3.14, to allow for a higher expansion ratio across the rotor (Fig. 3.4), until both the calculated and application pressure ratios matches.

$$\beta_6 = \beta_{6,blade} - \delta_6 \tag{3.14}$$

For ρ_4 and ρ_6, the residual value is calculated as the error between the thermodynamic losses, L_{therm}, and the losses from empirical correlations, L_{corr}, in the nozzle and rotor, respectively, as described in Eq. 3.15. It has to be noted that thermodynamic losses, L_{therm}, are calculated as the difference between the static enthalpy, h and the isentropic enthalpy, h_s for the corresponding stage.

$$Residuals = L_{therm} - L_{corr} = h - h_s - L_{corr} \tag{3.15}$$

The root of the residual function is then the solution for ρ_4 and ρ_6 at the nozzle outlet and rotor outlet, respectively. The characteristic function is plotted in Fig. 3.6, showing three different mathematical scenarios: two possible roots, one single root and no root.

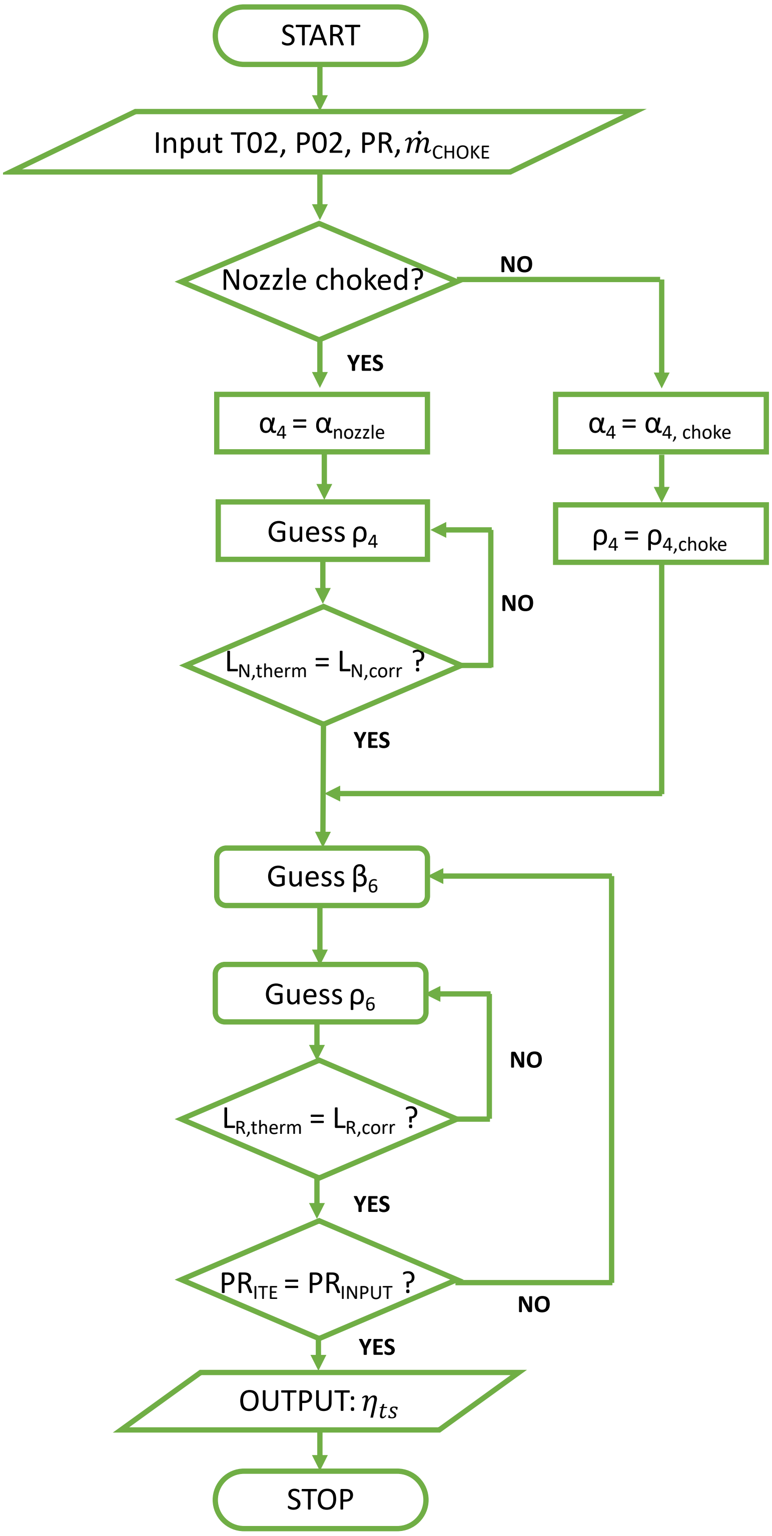

Figure 3.5: Rotor choked algorithm subroutine

The red solid dot indicates the minimum value of the function. When the value of the function at the minimum, res_{min} is negative, the characteristic function, which has a parabolic behaviour, results in two roots. The right hand side root, represented by purple solid dot, corresponds to the subsonic-unchoked solution. The left hand side root, represented by solid green dot, corresponds to the supersonic solution, obtained using the choke subroutines for the nozzle or rotor. If the unchoked subroutine is applied and ρ_2 is increased (or α_4 if the nozzle is choked), the characteristic curve moves upwards, as indicated by Fig. 3.6, until the minimum is coincident with the root, providing a single solution. This corresponds to the choking point of the component.

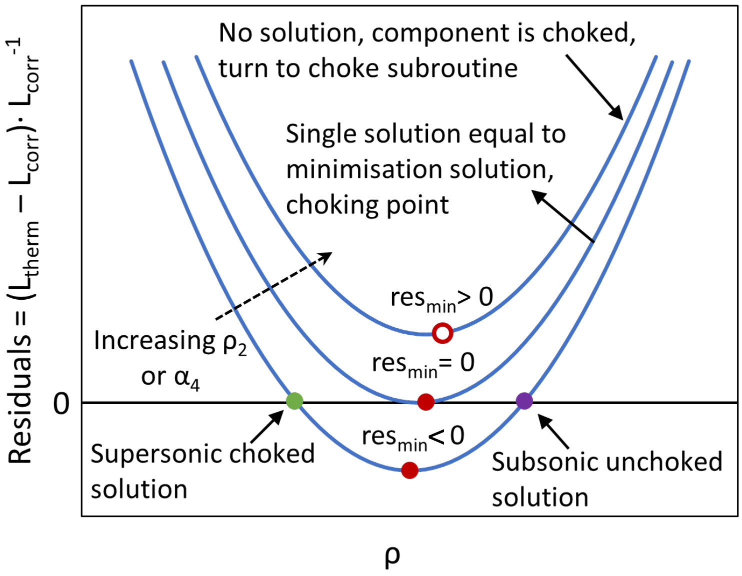

Figure 3.6: Characteristic function for component calculation indicating different modes

The minimum of the function can be easily computed allowing a quick calculation of the choking point of each component. The density at choking conditions can thus be found, as well as the pressure ratio at which the component chokes. For any operating conditions above the choking pressure ratio, the characteristic curve lays above the x-axis with no solution available, indicating that the component is choked and the appropriate supersonic subroutine is required to find the supersonic solution (green solid dot in Fig. 3.6).

3.1.4 Calibration and Validation

While the main equations in meanline modelling are based on physical models, losses are based on semi-empirical equations. Loss correlations have been validated in the literature against experimental results for a fix set of geometries, operating conditions and working fluids. However, the loss coefficients need to be calibrated for each particular application. The calibration requires the use of data from the literature, experimental results from preliminary designs or high fidelity CFD data of similar operating conditions and geometries to the actual application.

In this work, high fidelity CFD data is used for calibration of the meanline model. The CFD data is obtained from a sampling of 3D geometries at design conditions. The calibration algorithm consists of the prediction of the efficiency and mass flow of each geometry using the meanline model and calculate the relative RMS (root mean square) error between the meanline and CFD efficiency and mass flow. The sum of the accumulated relative error in efficiency and mass flow for all designs is the objective function to be minimised during calibration, as shown in Eq.3.16:

$$RRMSE = \sum \frac{\eta_{ts,MEANLINE} - \eta_{ts,CFD}}{\eta_{ts,CFD}} + \sum \frac{\dot{m}_{MEANLINE} - \dot{m}_{CFD}}{\dot{m}_{CFD}} \tag{3.16}$$

A differential evolutionary algorithm is used for the minimisation of the objective function by varying the loss coefficients within a certain range. Although calibrating against CFD data have some limitations, the meanline model predicts accurately the trend in performance, validating the low order model. Specific data of the calibration for ETC and ORC is provided in the results chapters.

3.1.5 Meanline Design Optimisation

The meridional geometry, nozzle and rotor blade angles, and rotational speed are optimised using the meanline modelling approach. In this case, the design operating point is defined by the inlet temperature, mass flow and pressure ratio of the ORC or ETC systems. These come from the waste heat stream conditions identified on the real offshore platform for the implementation of waste heat recovery technologies, as discussed in Chapter 1. The design conditions are summarised in Table 3.2:

Table 3.2: Design operating conditions for ETC and ORC expanders

Parameter	ETC	ORC
Inlet temperature, $T_{01}[K]$	743	523
Pressure ratio, $PR[-]$	1.2	9
Mass flow $\dot{m}, [kg/s]$	0.1	0.833

The total-to-static efficiency at design operating point is the main output of the performance algorithm, as shown in Fig. 3.2 and it is set as objective function for the optimisation. Moreover, mass flow is also an output parameter of the performance algorithm and it does not necessarily need to be the same as the mass flow at design conditions fixed by the application, $\dot{m}_{design}$. In order to match the design mass flow during the optimisation process, a constraint in the mass flow was added. The relative error between the predicted mass flow by the performance algorithm and the design mass flow was set to be below 1%. By doing so, designs that did not meet the constraint were discarded.

The objective function is evaluated for each set of parameters defining the turbine geometry and the rotational speed, as summarised above in Table 3.1. The geometric parameters are varied according to a single objective optimisation algorithm for maximum efficiency meeting the constraint. Once the optimisation algorithm converges, the output of the process is the optimum set of geometrical parameters, performance and error between the design mass flow and the mass flow predicted by meanline, which is expected to be less than 1%. Figure 3.7 shows a flow diagram summarising the optimisation process.

The optimisation maximises efficiency while keeping the mass flow deviation to a minimum, however, the extra calculations to apply the mass flow constrain increases the computational time. A simplification of the process is possible when the nozzle is designed to be choked:

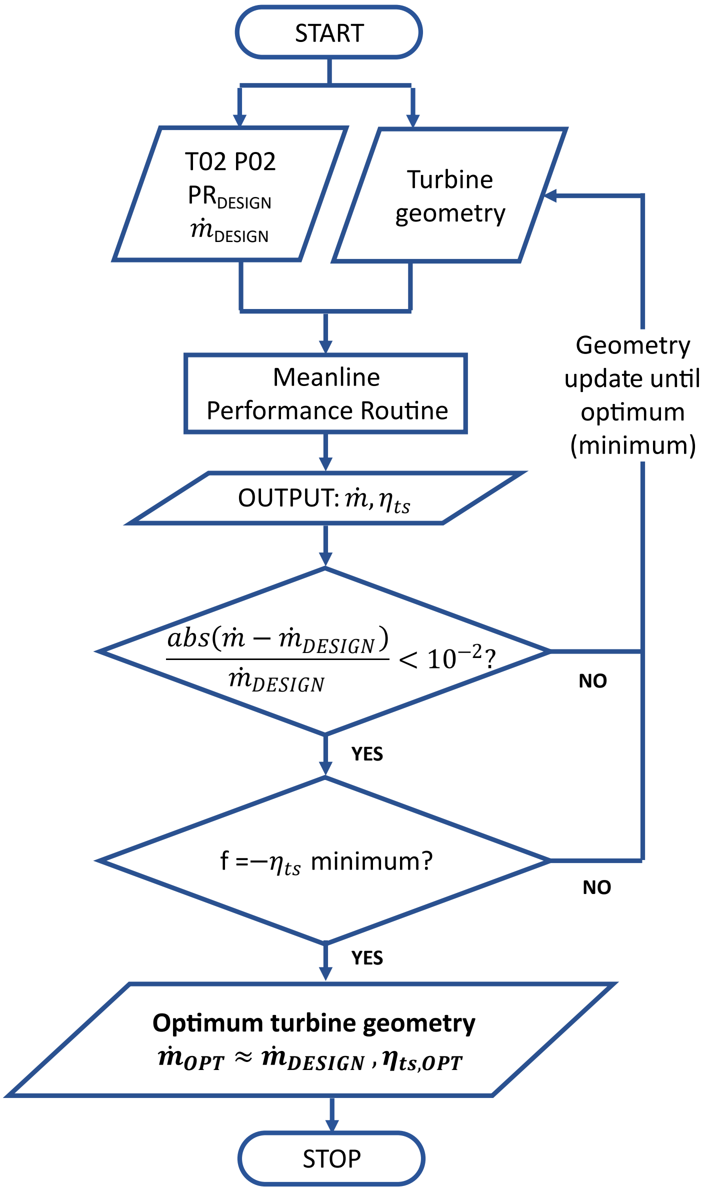

Figure 3.7: Meanline optimisation flow diagram

- Nozzle choking condition fixes mass flow and upstream conditions. In this case, the effective area at nozzle outlet can be calculated only from the inlet conditions under the premise that the nozzle is choked.

- The blade height at the nozzle outlet and rotor inlet is calculated according to Eq. 3.17, instead of being specified:

$$b_4 = \frac{A_{4,eff}}{2\,\pi\,r_4\,cos(\alpha 4, nozzle)} \tag{3.17}$$

Subsequently, the choked nozzle subroutine is applied to calculate the efficiency. This function is evaluated for several turbine geometries until the optimum solution is achieved. Choking is likely to happen in ORC turbine designs, where the pressure ratio is sufficiently high to keep the nozzle choked during normal operation at design conditions ($PR = 9$ in the ORC application under study). The process is summarised in the flow diagram of Fig. 3.8.

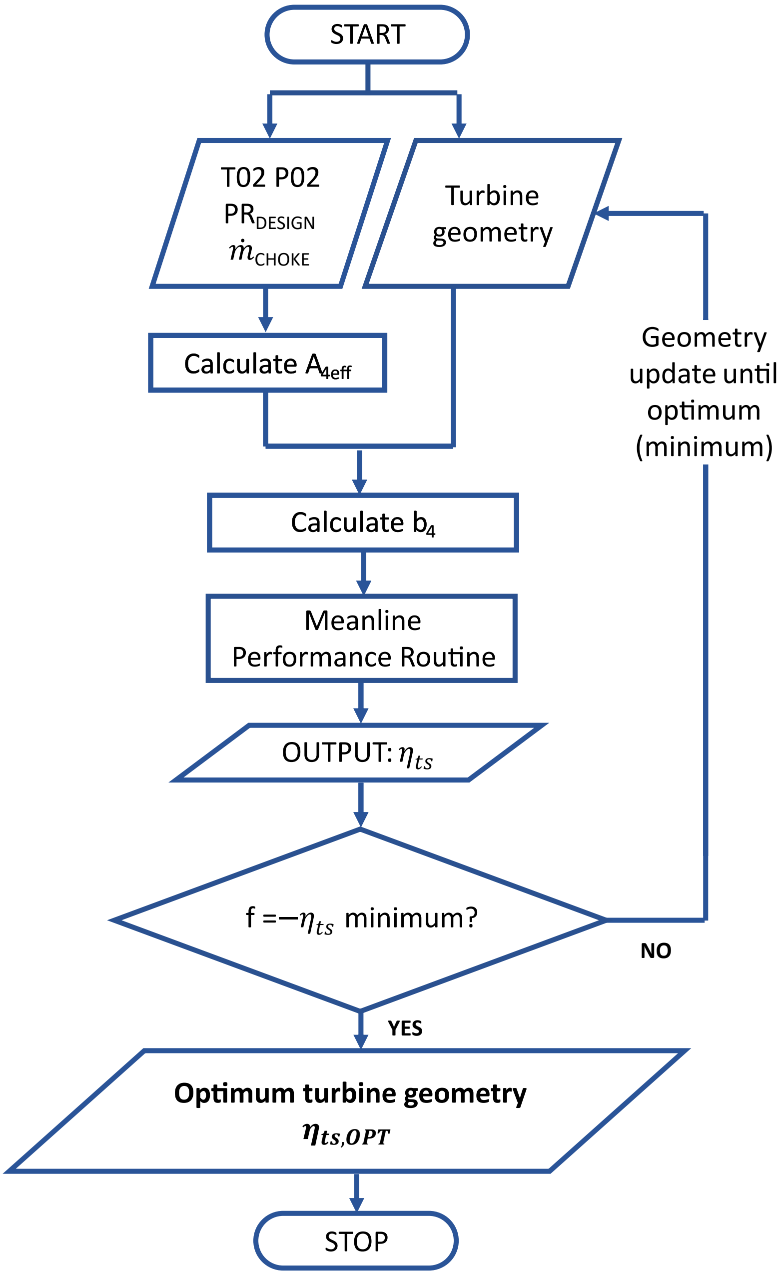

Figure 3.8: Meanline optimisation flow diagram for choked nozzle

Since this is a complex problem with non-linear equations and many variables, a non-gradient based differential evolutionary algorithm was chosen in order to increase the possibility of finding the global minimum of the objective function in a wide design space [115].

The fact that this type of algorithm is non-gradient based means that it does not require the objective function to be differentiable. This meta-heuristic optimisation method builds a population of candidates and by mutation, recombination and selection, the method is able to find the optimum of the objective function based on vector differentiation.

The number of control parameters is reduced to the population size, the number of generations, the differential weight and the crossover rate. These parameters are kept constant during the whole optimisation process:

- Population size, NP: number of designs in each generation. It is particularly important for the first population, which is usually created randomly, trying to cover as much design space as possible. The design space is usually defined by the boundaries of the variables of the objective function. A typical setting for the population size is usually ten times the dimension of the problem (number of variables on the objective function).
- Number of generations, G: number of generations over which the entire population is evolved following the whole process of mutation, recombination and selection of the best candidates.
- Differential weight, F: probability that mutation occurs. Mutation ensures design diversity since the 'child' design will not get the characteristics of the 'parents' design exclusively, but also these characteristics will mute to some extent. Mutation prevents the algorithm to fall onto local minima.
- Crossover rate, CR: probability that recombination occurs. Recombination or crossover consists of taking the features of more than one 'parent' design onto a 'child' design of the next generation. By combining characteristics of the best

designs of one generation it is more likely the algorithm finds the optimum design in the next generation.

The selection of these parameters is important for convergence, computational time, and even the quality of the optimum solution. Guidance on the selection of these parameters was followed according to the literature [115]. In addition, a tolerance parameter was set to define the stopping condition. The stopping condition is actually that all the individuals (parameter sets) have approximately the same objective function value. Then, the parameter set giving the lowest function value is returned as a solution.

3.2 Parametric CFD-based Modelling

The 3D parametric model of the turbine was developed in CAESES, a software for parametric CAE and integration platform that allows automated evaluation of designs in CFD [116]. The following subsections describe the main features of the definition of the full turbine geometry for all the turbine designs considered in this study.

3.2.1 3D Geometry Definition

The 3D geometry of the nozzle vanes and rotor blades are based on the parametrisation of the meridional profile, camberline and blade thickness distribution. Some parameters defining the geometry are also modelled by the meanline methodology, while others have exclusively a 3D effect and cannot be modelled in meanline or other low fidelity approaches in the literature. For the ETC, the number of nozzle vanes and rotor blades was fixed to 19 and 11; while the ORC number of nozzle vanes was set to 13 and the blade number to 11. The selection of number of blades and vanes was made based on the flow field analysis from CFD, ensuring enough guidance to prevent separation while minimising friction losses.

Nozzle Definition

The nozzle meridional geometry was set in the radial direction and constant blade height, matching the rotor inlet blade height, b_4, as shown in Fig. 3.1. Two lines were set as hub and shroud contours defined by the blade height and nozzle inlet and outlet radius, as shown in Fig. 3.9.

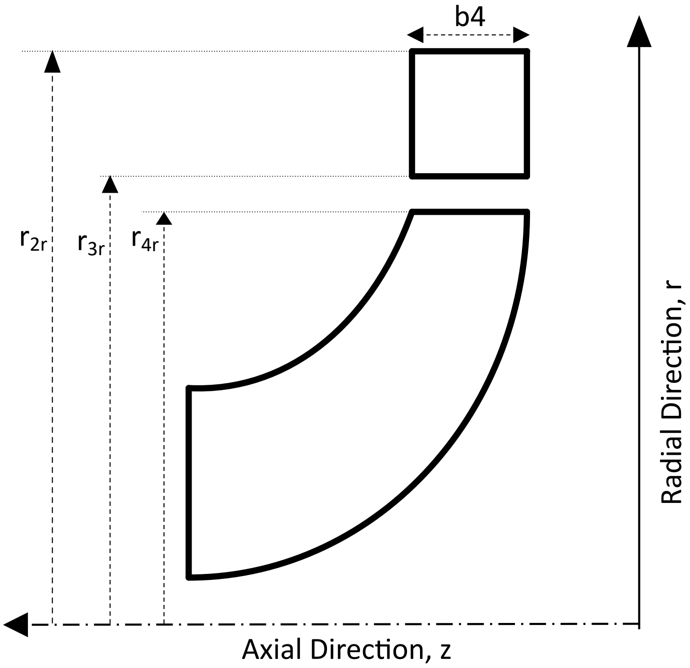

Figure 3.9: 3D parametrisation of the meridional profile of the nozzle

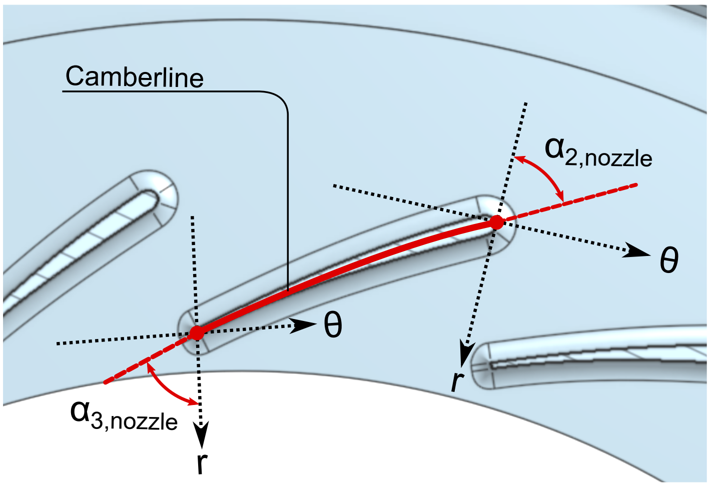

Figure 3.10: 3D parametrisation of the nozzle camberline

The nozzle metal angle, α_{nozzle} was used for vane camberline definition, which was set to be the same at nozzle inlet and outlet, $\alpha_{2,nozzle} = \alpha_{4,nozzle}$. Figure 3.10 shows an axial section of the nozzle where the camberline is highlighted in red. The nozzle angles are defined as the angles of the camberline with the radial direction.

Radial Fibre Blading

The rotor meridional curves are quadratic Bezier polynomials defined at the hub and shroud. Figure 3.11 shows the meridional contour definition with the relevant parameters. Their definition consists of the two end points based on inlet and outlet radii and axial position. The third point of the polynomial was set by the cone angles, ψ of the hub and shroud curves at the two ends.

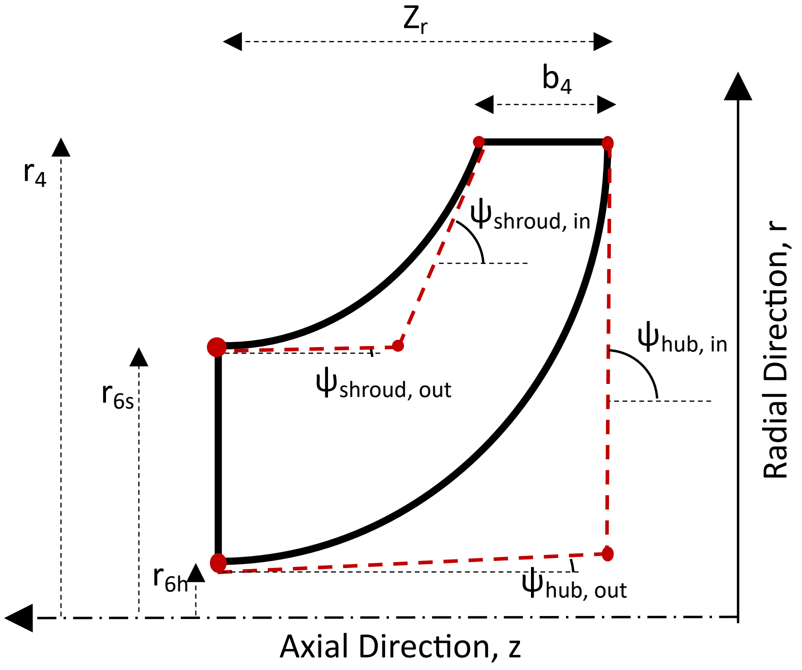

Figure 3.11: 3D parametrisation of the meridional profile of the rotor

The cone angle is defined as the angle between the hub, shroud or any streamline projected onto the meridional plane, and the z-axis at any point [18], as shown in Eq. 3.18. In this study the cone angle is a parameter exclusively used in 3D geometry and its effect on the performance of the turbine is not predicted using meanline approach. For the same radii and blade height, different meridional profiles can be created by varying the cone angle. The effect of this variation in efficiency can only be measured using CFD.

$$cos\psi = \frac{dz}{\sqrt{dr^2 + dz^2}} \tag{3.18}$$

The design of the rotor blades for the ETC baseline and ORC application was set to radial fibre. This means that the section of the blade in each axial plane is aligned radially with the axis of rotation. Figure 3.12 shows the section of a radial fibre rotor at different axial locations.

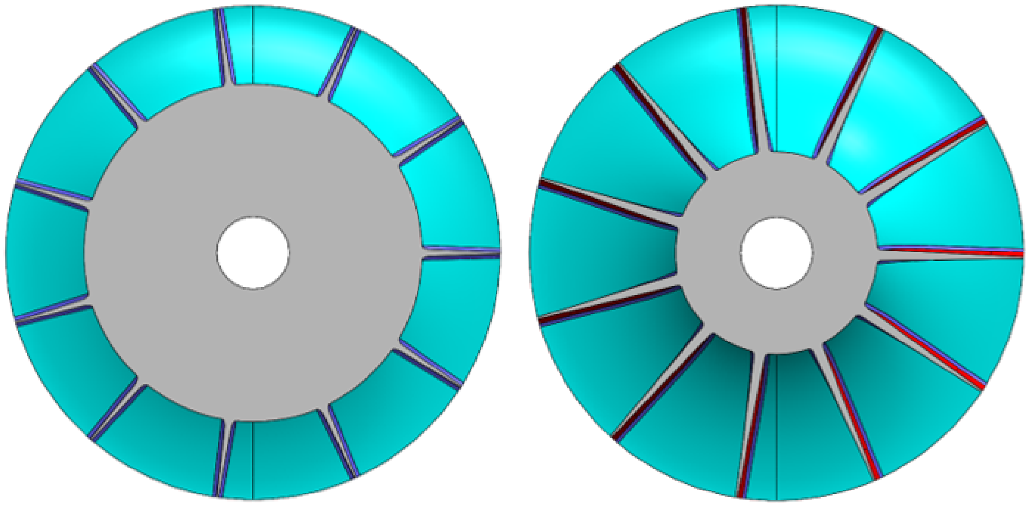

(a) $z = 3\,mm$ (b) $z = 13\,mm$

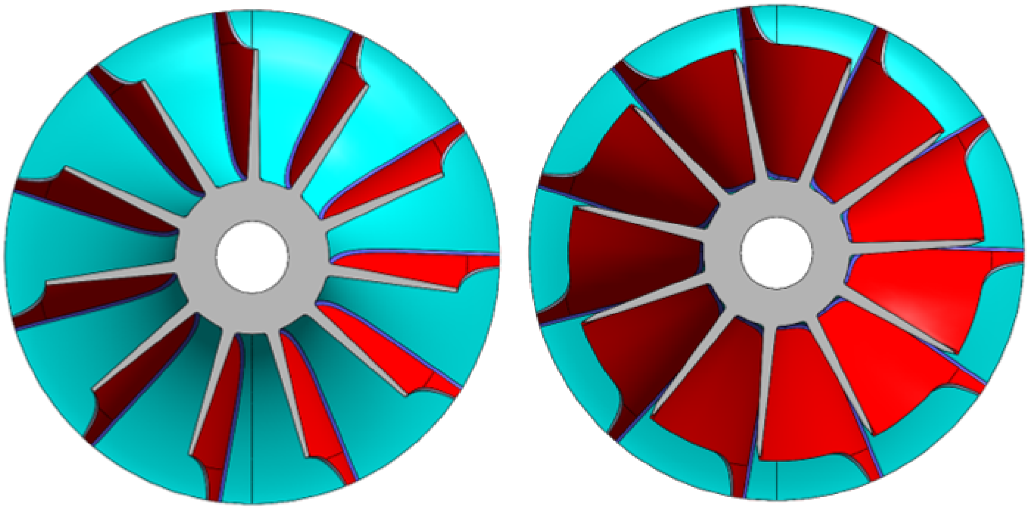

(c) $z = 23\,mm$ (d) $z = 33\,mm$

Figure 3.12: Sections of a radial fibre rotor at different axial locations

The rotor camberline is defined by the wrap angle, θ, at a reference radius and the axial position. Since the rotor is radial fibre, a single camberline defines the blade shape entirely. The curve consists of a quadratic Bezier polynomial, the two ends are defined by the leading edge and trailing edge wrap angle, θ, while the inner point is set by tangential angles at the both edges, as shown in Fig. 3.13

The relation of blade angle, β_{blade}, camber angle, ϕ and cone angle, ψ at any point of the blade is shown in Eq. 3.19 [18]. The tangent of the camber angle is defined as the derivative of the camberline, $\frac{d\theta}{dz}$.

$$tan\,\beta_{blade} = tan\,\phi\;\;cos\,\psi = \frac{r}{r_{ref}}\frac{\mathrm{d}\theta}{\mathrm{d}z} cos\,\psi \tag{3.19}$$

Therefore, the blade angle at the inlet was set to zero, $\beta_{blade,4} = 0°$, since the camber angle was set to zero too, $\phi_4 = 0°$. The blade angle at the trailing edge, $\beta_{6,blade}$, was determined by the cone and camber angles. In case of a cone angle equal to zero at the trailing edge of the blade, $\phi_6 = 0°$, the blade angle and the camber angle are assumed equivalent, as indicated in Eq. 3.20:

$$tan\,\beta_{blade,6} = tan\,\phi_6 \;\; = \frac{r}{r_{ref}}\frac{\mathrm{d}\theta}{\mathrm{d}z}_6 \tag{3.20}$$

The rotor blade was built by taking the radial fibre at each axial location turning them the corresponding wrap angle, θ, indicated by the camberline. Figure 3.14 shows a different view of the axial sections of the rotor indicating the radial fibre and the wrap angle.

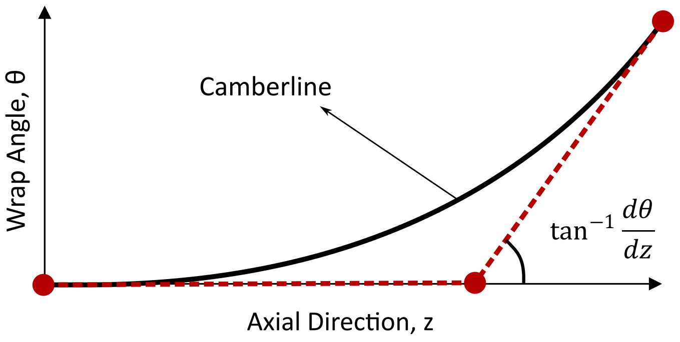

Figure 3.13: 3D parametrisation of the camberline of the radial fibre rotor

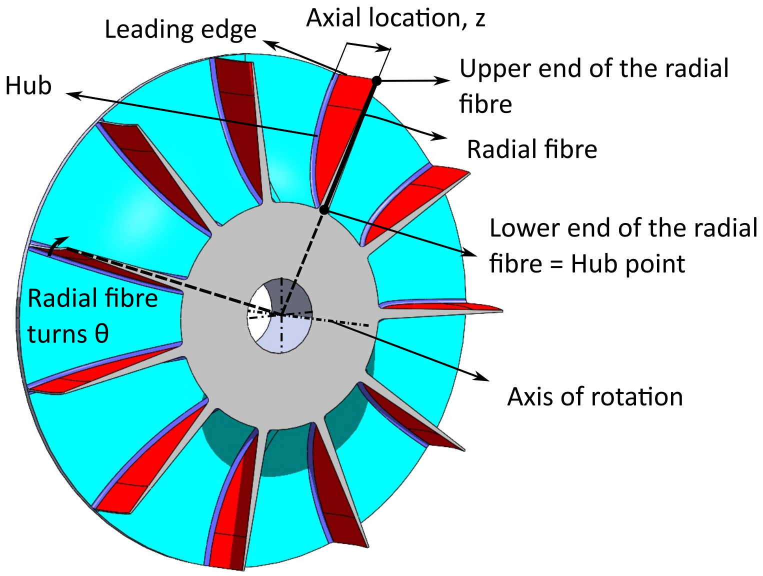

(a) $z = 13\,mm$

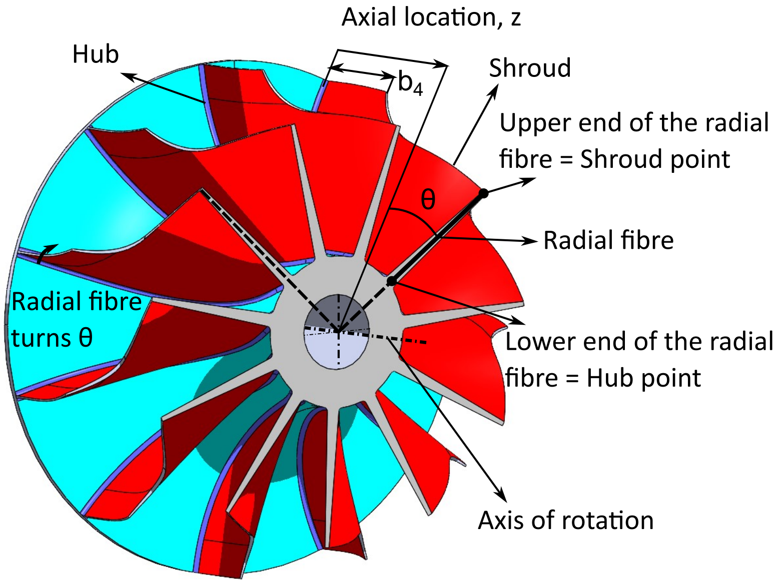

(b) $z = 33\,mm$

Figure 3.14: Radial fibre and wrap angle of the rotor at two axial locations

In the rotor section at low z shown in Fig. 3.14 (a), the radial fibre can be identified very clearly as the thick black line. The fibre, which is aligned with the axis of rotation, has an upper end, which lays on the leading edge of the blade and a lower end, which corresponds to the hub point.

When the axial location, z, increases beyond the blade height, b_4, the upper end of the radial fibre shown in Fig. 3.14 (b) corresponds to the shroud point. The blade of radial fibre designs was built based on the fibres at each axial location, from $z = 0$ to $z = Z_r$. For the parametrisation of non-radial fibre blades, extra parameters have to be introduced to define the blade geometry. Non-radial fibre parametrisation is explained in the next section.

Non-radial Fibre Blading

Departing from the radial fibre constraint introduces additional degrees of freedom in the design process, allowing the possibility of varying camberline and blade angle distribution along the span. However, non-radial fibre blading can lead to high centrifugal stresses in the blade, specially at the blade root. Therefore, only applications in which the rotational speed is sufficiently low are structurally safe when introducing non-radial fibre blading. In this study, non-radial fibre designs were only explored for the ETC application since the optimal rotational speed is low. The results are discussed in the next chapter.

The design flexibility allowed by the non-radial fibre design introduces more variables in the parametrisation of the blade geometry. Figure 3.15 shows the overlapping sections of a radial rotor a the non-radial fibre modification at the same axial location. The non-radial fibre rotor is built from the radial fibre rotor, so the modifications introduced corresponds to blade fibres. The parametrisation of the non-radial fibre is also shown in the figure and consisted of 3 steps, highlighted in black, blue and red in the figure. Each of the parametrisation steps is described as follows:

1. A radial fibre (black) was built according to the wrap angle, θ, distribution for that axial location.
2. The radial fibre was transformed by changing its angular position according to the lean angle, ν, with the hub location of the radial fibre as centre of the transformation. This leaned, straight fibre (blue) is non-radially arranged, therefore the lower end of the fibre is not coincident with the axis of rotation anymore. When $\nu = 0^\circ$ the leaned fibre is coincident with the radial fibre.

3. The non-radial fibre (red) was built as a quadratic Bezier polynomial with the upper end and the lower end of the leaned straight fibre as outer nodes. The inner node was set by the tangential angles at the ends of the bspline, named as γ_{lower} and γ_{upper}. These two angles were defined as the angle between the tangential line and the leaned straight fibre. This means a non-radial fibre with tangential angles set to zero, $\gamma_{lower} = \gamma_{upper} = 0^\circ$ corresponds to the leaned straight fibre itself.

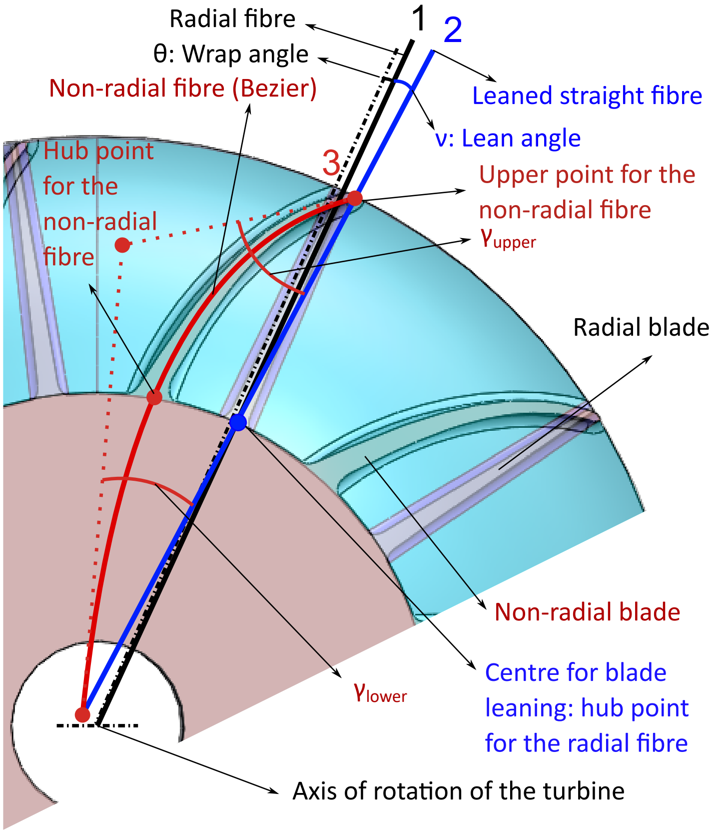

Figure 3.15: Non-radial fibre blading parametrisation showing the radial fibre (black), the leaned straight fibre (blue) and the non-radial fibre (red) on top of overlapping sections of the radial and non-radial rotors

The number of parameters required to build the non-radial fibre of the blade located at a certain axial position, z is four: the wrap angle, θ, the lean angle, ν, and the two tangential angles of the non-radial fibre, γ_{lower} and γ_{upper}. Consequently, the distribution of each of the four parameters with the axial location, z, needs to be defined to build the full blade, all the fibres from $z = 0$ to $z = Z_r$.

Any distribution could be used to define non-radial blades to different levels of complexity, but, for simplicity, the following distributions were applied. The wrap angle distribution with the axial position is defined by the camberline, as shown in Fig. 3.13. The distribution of ν and γ_{lower} is shown in Fig. 3.16. A quadratic distribution was specified for ν, where the lean angle at the leading edge was set to zero, $\nu_{LE} = 0$, and ν_{TE} was set as a variable, as shown in Fig. 3.16(a). A linear distribution was specified for γ_{lower}, which both $\gamma_{lower,LE}$ and $\gamma_{lower,TE}$ set as variables, as shown in Fig. 3.16(b). The distribution of, γ_{upper} was parametrised as a horizontal line when $z < b_4$ (effectively keeping the value of γ_{upper} constant at the first part of the rotor) and as a straight line when $z > b_4$, shown in Fig. 3.16(c).

The reason for setting a constant $\gamma_{upper,LE}$ is that the upper end of the blade fibre (radial or non-radial) corresponds to the leading edge when the axial location is lower than the blade height, $z < b_4$, as shown above in Fig. 3.14 (a). The blade angle at the leading edge, $\beta_{blade,4}$, is the angle between the tangential direction of the blade at the leading edge (upper point of fibre when $z < b_4$) and the radial direction at the same point. In the radial fibre configuration, the blade angle at the leading edge, $\beta_{blade,4}$ is set to zero, the leading edge of the blade is aligned with the radial direction. However, the non-radial fibre is allowed to have a non-zero $\beta_{blade,4}$. At the leading edge of the non-radial fibre, $\nu \approx 0$ when $z < b_4$, as shown in Fig. 3.16(a). This means that the radial fibre and the leaned fibre are almost coincident, therefore the upper point of the non-radial fibre is aligned with the radial direction. As a result, the blade angle at the leading edge, $\beta_{blade,4}$ can be approximated to γ_{upper} at the leading edge.

To prove that $\beta_{blade,4}$ can be approximated to γ_{upper} at the leading edge, the relation between the different angles involved in the non-radial fibre definition is explained in Fig. 3.17. In addition to the angles already defined: wrap angle, θ (black), the lean angle, ν (blue) and the tangential angles of the radial fibre at the lower and upper ends, γ_{lower} and γ_{upper} (red), θ'_{upper} angle is defined in grey. θ'_{upper} is the angle between the tangent of the non-radial fibre at the upper end (red line) and the radial direction at the upper end of the non-radial fibre (grey line). It is calculated as the arc tangent of the x coordinate of the upper end of the non-radial fibre (coincident with the upper end

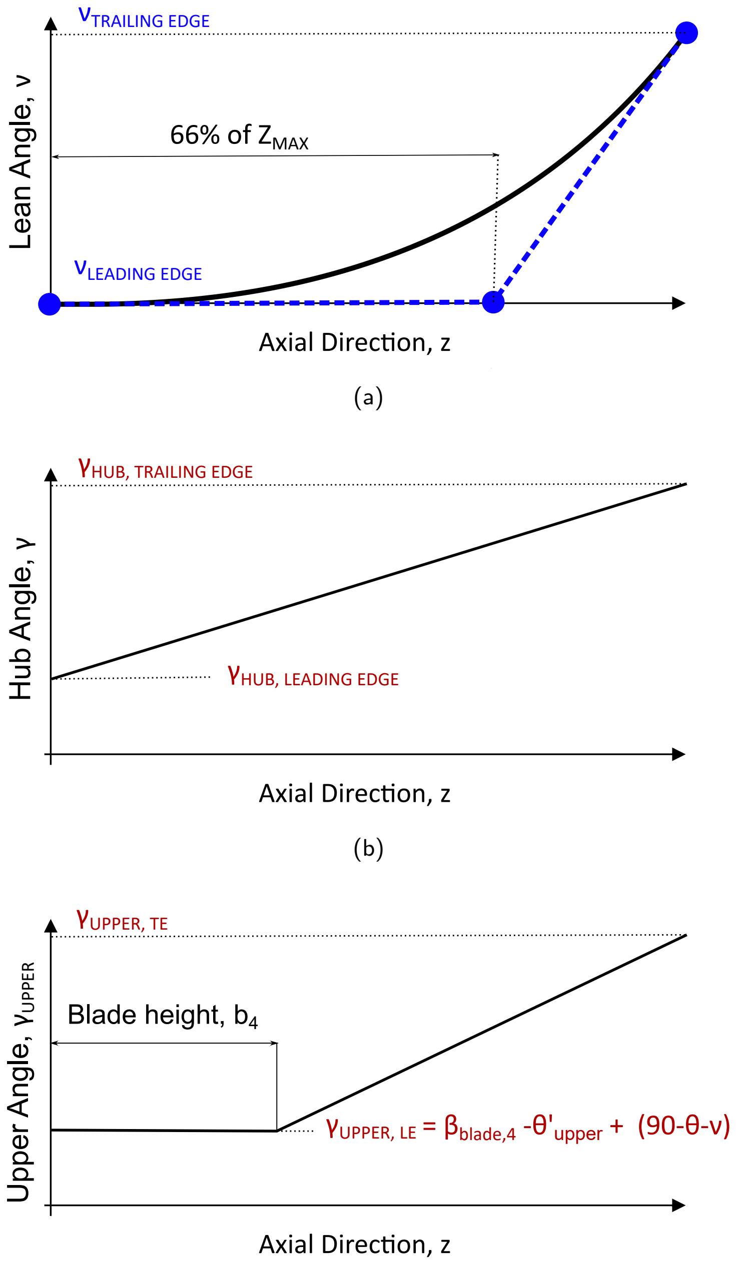

(a)

(b)

(c)

Figure 3.16: Distribution of: (a) lean angle, ν, (b) tangential angle of the non-radial fibre at the lower end with the leaned straight fibre, γ_{lower} and (c) tangential angle of the non-radial fibre at the upper end with the leaned straight fibre, γ_{upper}, which can be expressed as a function of the inlet blade angle, $\beta_{blade,4}$ when $z > b_4$

of the leaned straight fibre), x_{upper} divided by its y-coordinate, y_{upper} (Eq. 3.21):

$$\theta'_{upper} = tan^{-1}\frac{x_{upper}}{y_{upper}} \tag{3.21}$$

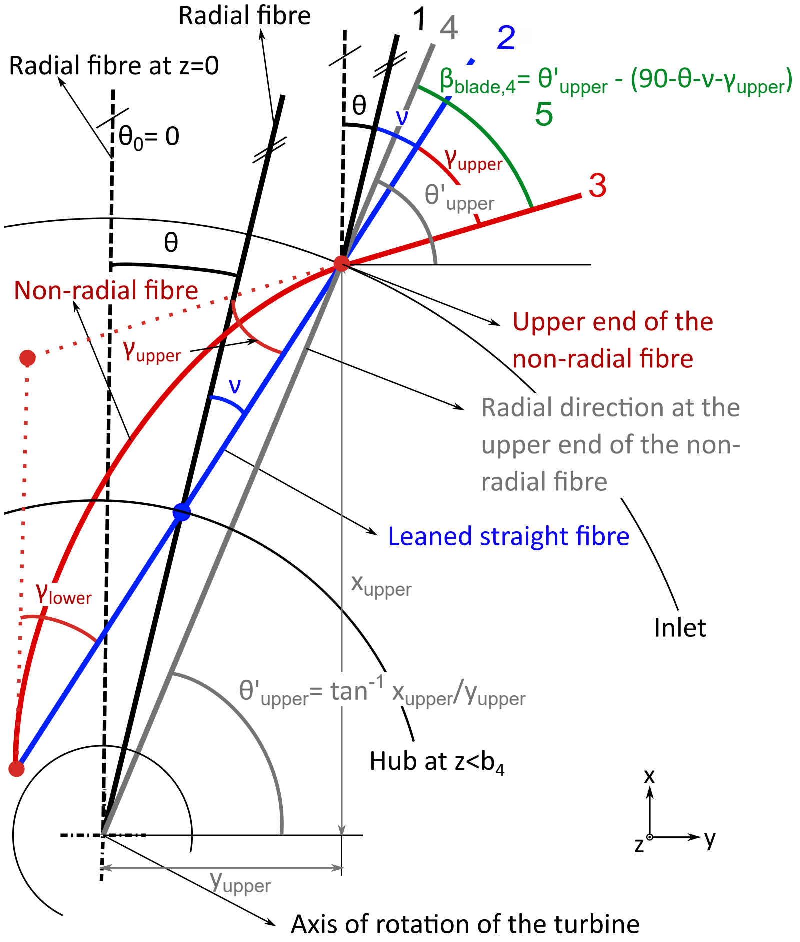

Figure 3.17: Blade inlet angle, $\beta_{blade,4}$, parametrisation showing the relation with the other angles, the wrap angle, θ, the lean angle, ν and the circumferential angle of the shroud of the non-radial fibre with the horizontal, θ'_{upper}, for a section at $z < b_4$

On the upper right corner of Fig. 3.17 all the angles are superimposed forming a 90° sector. The blade angle at the leading edge, $\beta_{blade,4}$ (in green) is shown as the combination of these angles. By construction, the blade inlet angle, $\beta_{blade,4}$ can be expressed as Eq. 3.22 shows:

$$\beta_{blade,4} = \theta'_{upper} - (90^\circ - \theta - \nu - \gamma_{upper}) \tag{3.22}$$

At the leading edge when $z < b_4$, $\theta \approx 0^\circ$ and $\nu \approx 0^\circ$, which means that the radial fibre and the lean fibre are aligned, therefore $\theta'_{upper} \approx 0^\circ$. As a result, $\beta_{blade,4} \approx \gamma_{upper}$. This parametrisation gives full control of $\beta_{blade,4}$ of the non-radial fibre blade and therefore on the incidence angle which has a big effect on losses across the rotor and overall efficiency.

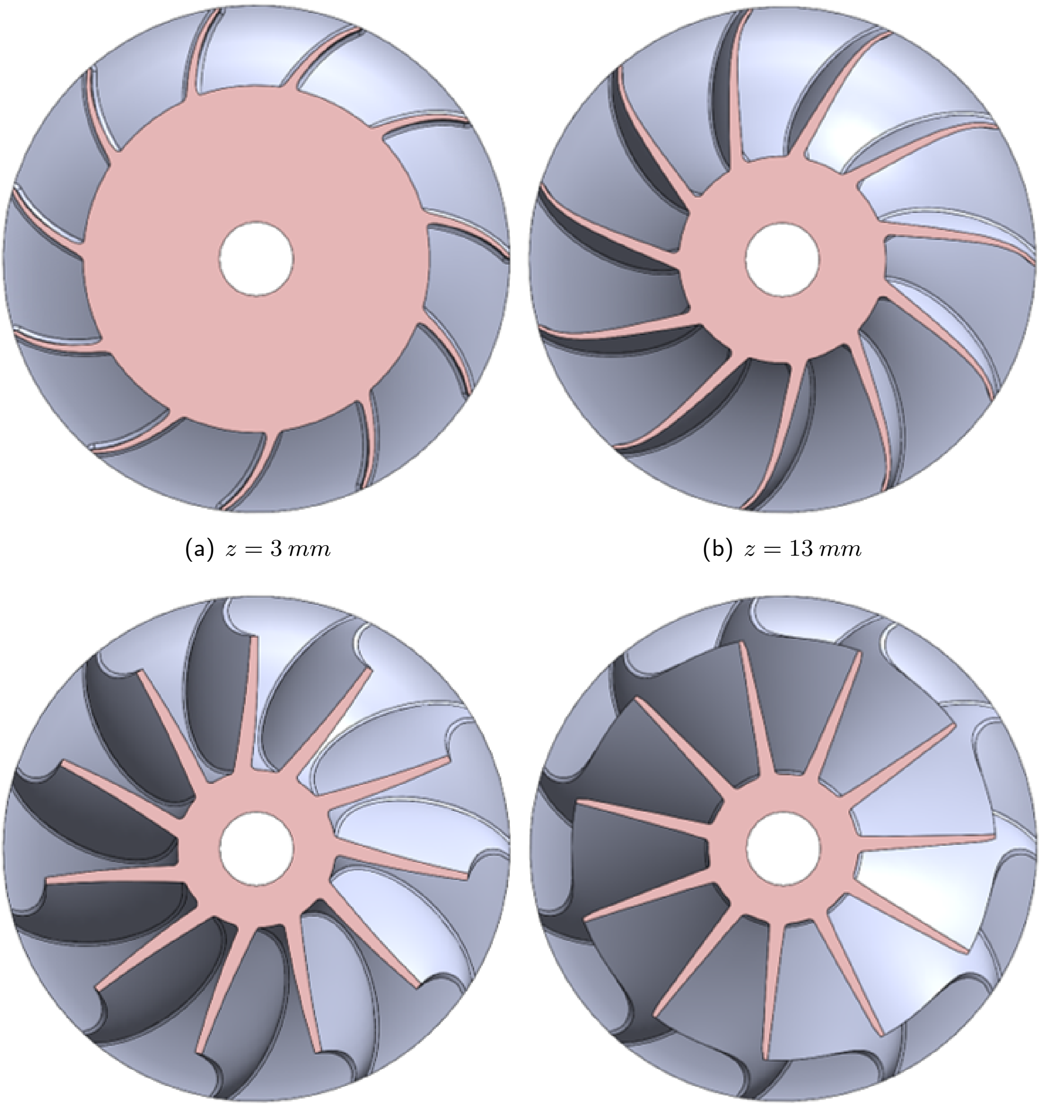

(a) $z = 3\,mm$

(b) $z = 13\,mm$

(c) $z = 23\,mm$

(d) $z = 33\,mm$

Figure 3.18: Sections of a non-radial fibre rotor at different axial locations

As a result of the application of the presented parametrisation method, a non-radial fibre rotor is build. Figure 3.18 shows the section of the non-radial fibre blades at different axial planes. When comparing with the radial fibre rotor in Fig. 3.12, this blades are clearly non-radial, particularly at the low z, as shown in Fig. 3.18 (a) and (b). Then the blade becomes straight, but leaned, (c), and finally recovers the radial alignment at the trailing edge, shown in (d). This results in different camberlines at different span locations (hub, midspan and shroud) for a non-radial fibre blade, whereas the radial fibre blade is defined by a single camberline.

3.2.2 Other 3D Design Considerations

Nozzle and rotor blade thicknesses were defined by polynomials at leading edge, middle section and trailing edge thicknesses. The thickness distribution for both the nozzle and the rotor was kept constant in every design. The rotor tip clearance was set to $\epsilon_r = 0.5mm$ for all ETC geometries and $\epsilon_r = 0.3mm$ for all ORC geometries. In this way the 3D geometry of the nozzle vane and rotor blade is completely defined. Flow domains were then created from the geometries and exported to external software for CFD simulation.

The parametrisation explained in this section is used for the generation of the nozzle and rotor full 3D geometries. A detailed evaluation of the performance of the geometries was carried out using numerical simulations. The next section presents the specifics of the CFD evaluation.

3.2.3 CFD Setup

Single passage nozzle and rotor simulations were set to run the geometry optimisation. Double passage simulations were preferred for detailed flow analysis of the selected designs. ANSYS CFX 19.4v was the CFD software used for meshing, solver and data post-processing, integrated in CAESES platform.

The flow domain for the nozzle and rotor consisted of extended hub and shroud contours (2 times the wheel diameter for the exit pipe) and blade curves, as shown in Fig. 3.19. The curves and contours were imported to TurboGrid to build the structured mesh.

A grid convergence study was carried out to ensure mesh-independent results and enough boundary layer resolution for y+. Table 3.3 summarises the number of elements, first element offset and y^+ in each component for both ETC and ORC simulations.

To achieve grid independent results two parameters of the mesh were varied, the number of elements and the first element offset. First, the number of elements was increased

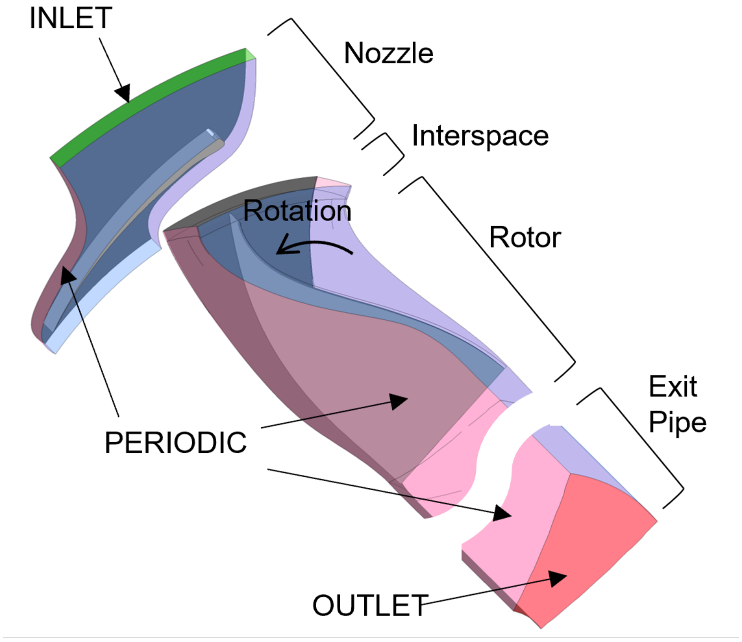

Figure 3.19: CFD domain

while keeping the first element offset constant. After the first element offset was reduced while keeping the element number fixed to the value that provided grid-independent results from the previous step. Figure 3.20 shows an example of the convergence of total-to-static efficiency with the number of elements at the rotor and outlet passage (a) and first element offset (b) for the ETC single passage simulations. This process was repeated for the nozzle for the ETC and ORC turbines.

The CFD simulations were set to steady state and the turbulence model used was $k-\epsilon$. The change of frame of reference between the nozzle-rotor and rotor-outlet interfaces was set to mixing plane, based on the circumferential averaging of the flow field. While this coupling approach has some limitations regarding local flow interactions, it is representative of a nozzled turbine, which provides a highly uniform flow at the nozzle outlet.

Total temperature and pressure were imposed at the nozzle inlet and static pressure was set at the outlet boundary of the exit pipe, placed at 2 wheel diameter length of the rotor trailing edge. Periodic interfaces were set at lateral boundaries of the nozzle, rotor and exit pipe domains. Figure 3.19 shows a picture of the CFD domain highlighting the components and main boundaries.

Table 3.3: Mesh details after mesh sensitivity study for ETC and ORC single passage simulations

Parameter	ETC		ORC	
Component	Nozzle	Rotor + Outlet	Nozzle	Rotor + Outlet
Element number	50k	170k	70k	160k
First element offset	0.075mm	0.075mm	0.075mm	0.075mm
y^+_{ave} blade surface	30	33	32	39
y^+_{ave} shroud surface	30	50	32	81
y^+_{max} blade surface	36	67	44	130
y^+_{max} shroud surface	36	106	44	280

Peng-Robinson equation of state was used to calculate the thermopyshical properties of the working fluid, R1233zd(E), for ORC simulations, whereas the ideal gas assumption was preferred for ETC simulations with air. The standard deviation of the calculated total-to-static efficiency over 20 iterations was set to $\sigma_{\eta,20it} = 0.001pp$, meaning that the efficiency computed by CFD was $\eta_{ts,CFD} \pm 0.002pp$ with a 95% confidence. This convergence criteria ensures geometries can be compared based on small efficiency difference.

Full stage simulations were carried out to compare the efficiency and flow features with those obtained with single passage simulations. Same trends were found in efficiency and flow features at the rotor passage in the single stage simulation were representative enough of the flow features found in the full simulation, for ORC and ETC simulations. Results of the full rotor evaluation are discussed in the corresponding chapters 5 and 4 Frozen rotor was set as change of frame of reference model in the full stage simulations.

3.2.4 Geometry Sampling for Meanline Calibration and Optimisation

CAESES provides an integration platform for automated geometry design and CFD computations with optimisation algorithms. Figure 3.21 shows a screenshot of the software integration platform provided by CAESES, where different files can be added to call external software, mesh the geometries, pre and post-process the simulations

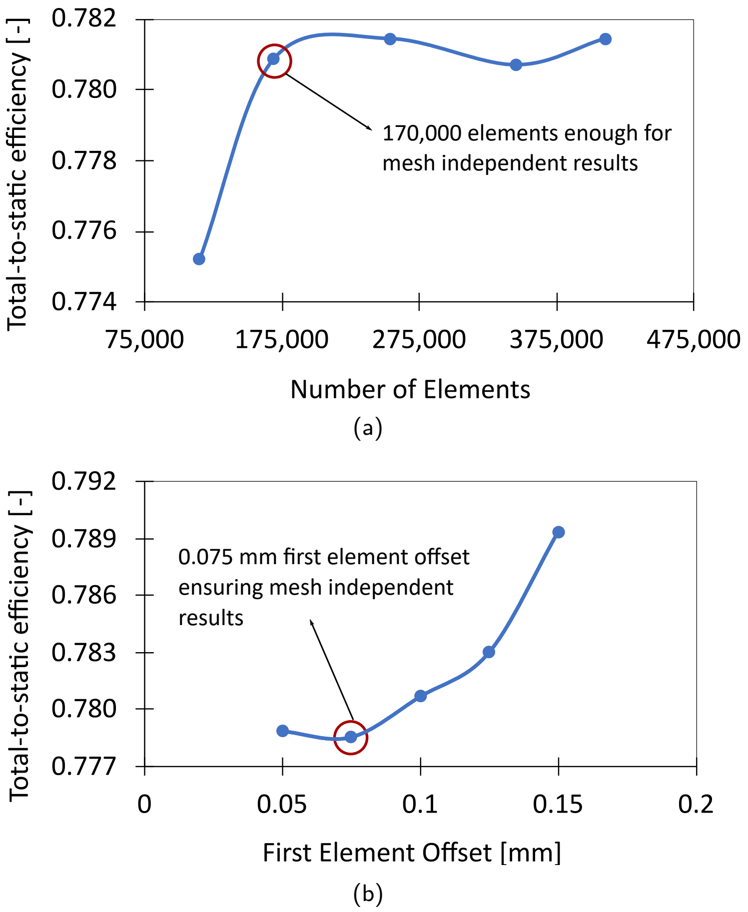

Figure 3.20: Total-to-static efficiency as function of number of elements at the rotor and outlet passage (a) and first element offset (b) for ETC simulations as part of the mesh sensitivity study

and extract the results.

Latin Hypercube Sampling, LHS, was used to get a near-random set of geometry evaluations based on the meridional profile, nozzle and blade angles and rotational speed for the ETC and ORC cases. This statistical method explores the design space determined by the range of the parameters in a near-random way ensuring that the sampling is a set of data representative enough of the whole design space [117]. The results were used for the calibration of the meanline model loss coefficients using the calibration routine explained in the previous section. Geometric data of the designs generated by the LHS, as well as the efficiency and mass flow obtained in the CFD evaluation were used to find the values of the loss coefficient which minimise the error between meanline and CFD.

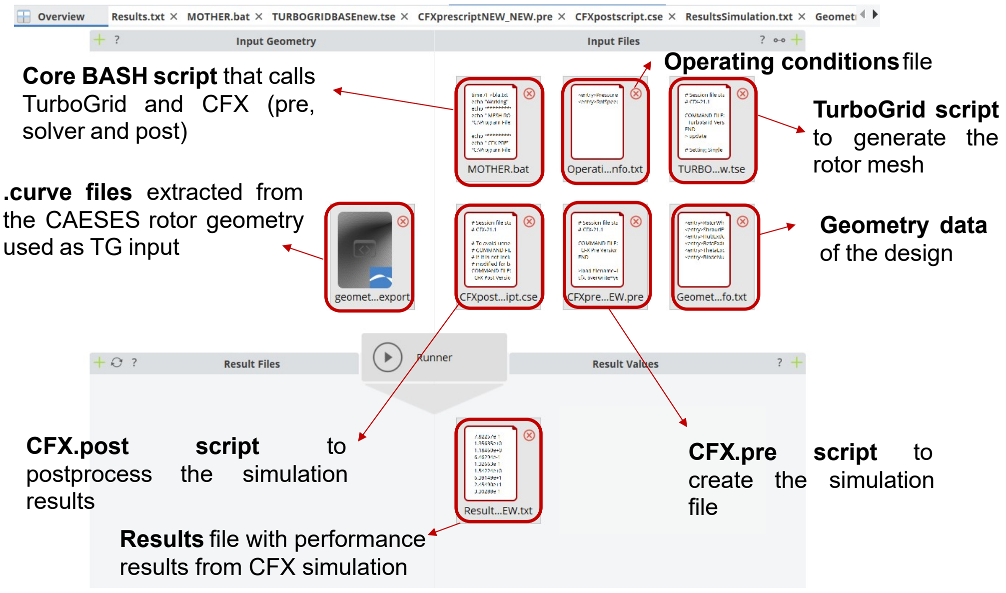

Operating conditions file

Core BASH script that calls TurboGrid and CFX (pre, solver and post)

TurboGrid script to generate the rotor mesh

.curve files extracted from the CAESES rotor geometry used as TG input

Geometry data of the design

CFX.post script to postprocess the simulation results

CFX.pre script to create the simulation file

Results file with performance results from CFX simulation

Figure 3.21: Integration platform in CAESES

Figure 3.22 shows an example of the sampling and optimsation interface in CAESES. The screenshot shows the sampling of 15 geometries using LHS with $\alpha_{nozzle,4}$ as designs variable and efficiency, mass flow parameters and power output as objective functions. During the sampling, these objectives are set to "observers", which means the parameters are only monitored, while during an optimisation they could be set to "min" or "max", depending on what the objective is.

Rotor design optimisations based on the parametric model coupled with CFD were carried out using non-gradient based algorithms allowing for global optimisation available in CAESES software. Genetic algorithms or differential evolution (used for in meanline optimisation, as explained above) are, to some extent, inefficient algorithms for optimisation, since they take a large number of evaluation functions to converge into an optimum solution.

The parametric optimisation described in this study involves CFD calculations, which implies a high computational cost compared to other methods. Therefore, a global optimisation on a response surface was chosen as optimisation strategy for the CFD-parametric model.

A response surface is a statistical model built based on the relationship between the

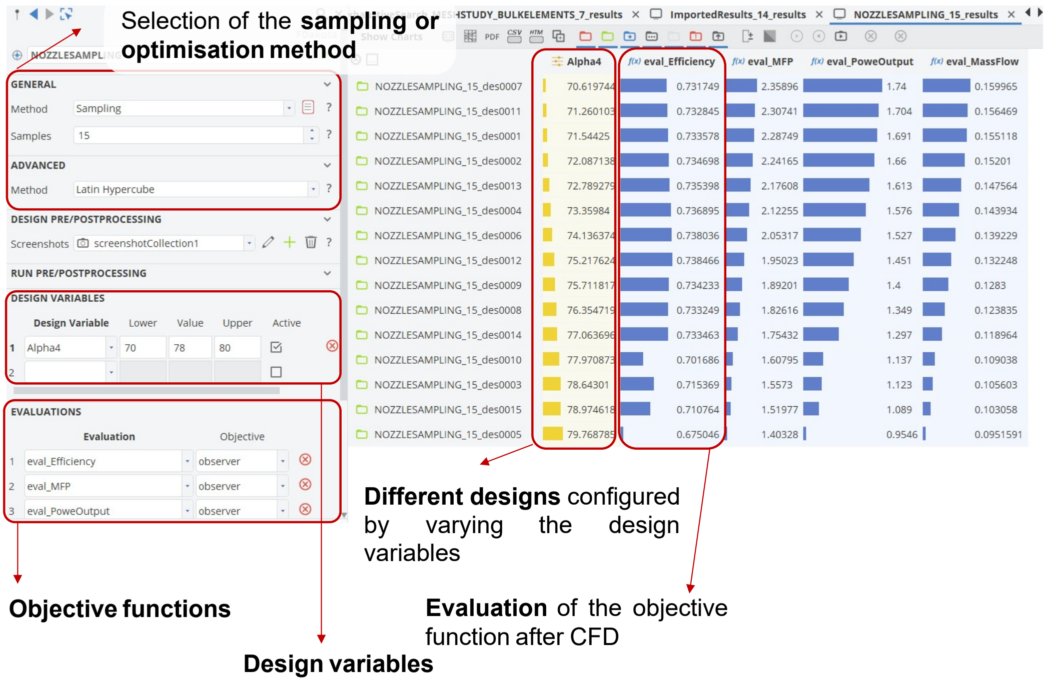

Selection of the **sampling or optimisation method**

GENERAL
Method: Sampling
Samples: 15

ADVANCED
Method: Latin Hypercube

DESIGN PRE/POSTPROCESSING
Screenshots: screenshotCollection1

RUN PRE/POSTPROCESSING

DESIGN VARIABLES

	Design Variable	Lower	Value	Upper	Active
1	Alpha4	70	78	80	☑
2					☐

EVALUATIONS

	Evaluation	Objective
1	eval_Efficiency	observer
2	eval_MFP	observer
3	eval_PoweOutput	observer

	Alpha4	f(x) eval_Efficiency	f(x) eval_MFP	f(x) eval_PoweOutput	f(x) eval_MassFlow
NOZZLESAMPLING_15_des0007	70.619744	0.731749	2.35896	1.74	0.159965
NOZZLESAMPLING_15_des0011	71.260103	0.732845	2.30741	1.704	0.156469
NOZZLESAMPLING_15_des0001	71.54425	0.733578	2.28749	1.691	0.155118
NOZZLESAMPLING_15_des0002	72.087138	0.734698	2.24165	1.66	0.15201
NOZZLESAMPLING_15_des0013	72.789279	0.735398	2.17608	1.613	0.147564
NOZZLESAMPLING_15_des0004	73.35984	0.736895	2.12255	1.576	0.143934
NOZZLESAMPLING_15_des0006	74.136374	0.738036	2.05317	1.527	0.139229
NOZZLESAMPLING_15_des0012	75.217624	0.738466	1.95023	1.451	0.132248
NOZZLESAMPLING_15_des0009	75.711817	0.734233	1.89201	1.4	0.1283
NOZZLESAMPLING_15_des0008	76.354719	0.733249	1.82616	1.349	0.123835
NOZZLESAMPLING_15_des0014	77.063696	0.733463	1.75432	1.297	0.118964
NOZZLESAMPLING_15_des0010	77.970873	0.701686	1.60795	1.137	0.109038
NOZZLESAMPLING_15_des0003	78.64301	0.715369	1.5573	1.123	0.105603
NOZZLESAMPLING_15_des0015	78.974618	0.710764	1.51977	1.089	0.103058
NOZZLESAMPLING_15_des0005	79.768785	0.675046	1.40328	0.9546	0.0951591

Different designs configured by varying the design variables

Objective functions

Evaluation of the objective function after CFD

Design variables

Figure 3.22: Example of the sampling and optimisation interface in CAESES

variables and the objective function [118]. In this method, a genetic algorithm is conducted on a response surface that is iteratively build-up. For the initial response surface, the LHS carried out for the meanline calibration can be used. The best designs of each generation are evaluated and added to the response surface. This updates and improves the response surface in each iteration. With this approach, the algorithm aims to reduce the number of computationally costly evaluations. A similar stopping condition to the meanline optimisation was followed, based on a tolerance value.

Two optimisations based on the parametric model coupled with CFD were carried out for both ORC and ETC using a differential evolution algorithm. Different parameters were optimised in each stage, but the total-to-static efficiency was the objective function in both applications:

1. Optimisation of the meridional profile, nozzle and rotor blade angles and rotational speed for ORC and ETC. This can be compared to the optimisation of the turbine geometry using the meanline code.
2. Optimisation of the 3D geometry features on the blade shape from the best meridional configuration optimised in the previous step. In ORC, the hub and

shroud contour shapes defined by the cone angles at leading and trailing edge were optimised. For the ETC application, the parameters optimised in this stage were those related to the non-radial fibre blade definition.

The set up for numerical simulations explained above allows the prediction of the performance of turbine designs and provides detailed information on the flow field. This helps understanding the impact of geometry modifications on the performance of the turbine and the physics behind.

3.3 FEA Numerical Simulations

Static Structural package from ANSYS was used for the structural calculations of the rotor for ETC applications to ensure that non-radial fibre blades were structurally safe. In ORC applications the rotor designs explored were only radial fibre, therefore there was no concern for their structural integrity and no stress analysis was carried out for these rotors.

The FEA model consists of the full rotor with some holes on the front face of the rotor that simulate the rigid attachment of the rotor to the shaft, as shown in Fig. 3.23. An unstructured tetrahedral mesh was built for the rotor. A mesh sensitivity analysis carried out considering the equivalent stress and deformation of the rotor showed that there selected nodes number to ensure the results were grid independent. The selected mesh size was 712k nodes. The size of the elements was set to 1mm and mesh refinement was set to a minimum size of 0.25 mm at the blade fillets.

Second-order elements were used for the simulations. Fixed supports limiting all degrees of freedom were set as boundary conditions at the screw holes of the rotor front face as indicated in Fig. 3.23. Alternative supports were tested to ensure the results did not depend on the specific support chosen and that stresses artificially computed next to the supports would not affect the resulting stress distribution on the rotor blades.

The material chosen was Al7075 T76 an aluminum alloy with zinc, magnesium, and copper among other metals. This alloy has high strength and it is widely used in aircraft

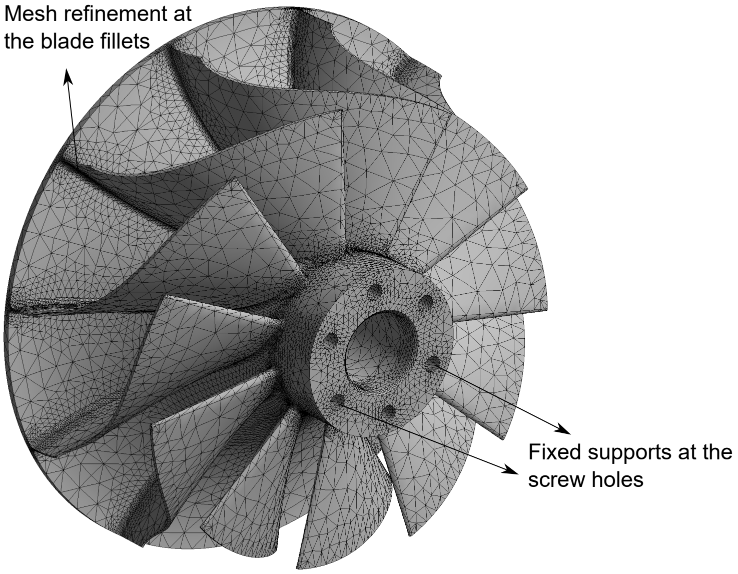

Figure 3.23: FEA domain and mesh

structural parts. Since the experimental campaign is carried out at low temperature conditions, this material can be used. Table 3.4 summarises the main mechanical properties of Al7075 T76:

Table 3.4: Al7075 T76 mechanical properties

Property	Value
Density $[gcm^{-3}]$	3.0
Yield strength $[MPa]$	480
Ultimate yield strength $[MPa]$	560
Young's modulus $[GPa]$	70
Poisson's ratio [-]	0.32
Coefficient of thermal expansion $[K^{-1}]$	2.36E-05

However, for the real application, where the temperature can be as high as 470°, aluminum alloys are not suitable since their strength drops significantly with temperature. Instead, a nickel-based super-alloy, Inconel 718, widely used in turbomachinery applications will be used. The yield strength of Inconel 718 is substantially higher than Al7075 T76 even at high temperatures, therefore structural calculations were not carried out with Inconel as the rotor material.

The most extreme conditions that could be achieved experimentally were chosen as boundary conditions in order to ensure the structural integrity of the designs during operation, the rotational speed was set to $50,000rpm$ and the body temperature was set to $40°$. The centrifugal load was set by the rotational speed. The pressure distribution on the rotor surface was loaded from the CFD results. The equivalent stress, maximum principal stress and displacement in the different directions were computed and compared to the material yield strength and with the design tolerances for displacement.

Designs that did not meet the stress and displacement requirements were discarded to ensure that the final optimised geometries are structurally safe for the considered application.

3.4 Experimental Methodology

The experimental data of this study was obtained only for electric turbo-compounding (ETC) turbines. This was done using the turbine test facility at Imperial College London. A detailed description of this experimental facility can be found in the literature [119], but general information about the experimental set up is explained in the forthcoming section. Moreover, the equations to calculate the turbine performance as well as the related uncertainty can be fond in the next sections.

3.4.1 Experimental Facilities

This experimental facility has been used to collect a large amount of performance data of radial turbines under steady and pulsating conditions [79, 105, 120]. The main feature of the test rig is the eddy-current dynamometer used as a loading device. The torque generated by the turbine is measured directly by a load cell. The experiments were performed under cold flow conditions. Therefore, heat losses to the environment are negligible, and the expansion process across the turbine is assumed to be adiabatic.

The layout of the test rig is shown in Fig. 3.24. Air is supplied by 3 screw compressors centrally housed. The working pressure is set to 4 bar and the maximum mass flow rate is 1.2 kg/s. The air flow enters the laboratory through a 4 inch pipe and pass through the heater. The 72kW heater warms the air flow up to 30 - 50 $^{\circ}C$ at the turbine inlet. The purpose of the heating stage is to avoid condensation at the outlet of the turbine, after the expansion.

After the heater, the flow goes trough the 4 inch main valve and the 1 inch secondary, bypass valve in parallel. Both are electrical actuated ball valves, which are used to regulate the mass flow trough the turbine during experiments. The flow is then divided in two limbs to allow testing of double entry turbines. Each of the limbs have control valves that were kept fully opened during the testing to ensure identical conditions in both limbs. The mass flow through each limb is measured with V-cones differential pressure type flow meters.

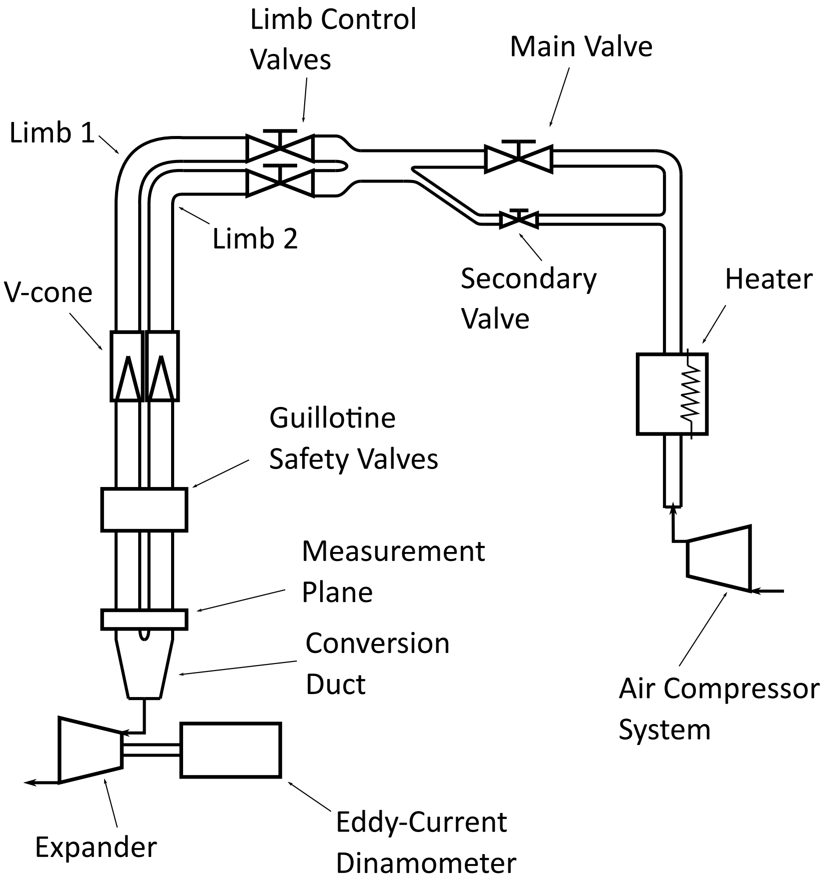

Figure 3.24: Turbine experimental facility at ICL - Platform layout

Guillotine safety valves are placed downstream in each limb to protect the rig. If any of the operating parameters of the rig goes off limit the spring loaded cut-off valves are activated interrupting the flow immediately. Pressure and temperature measurements are taken at the measurement plane, just before the flow goes through the conversion duct. The conversion duct adapts the pipes of the two limbs to the inlet cross section of the volute. Since the turbines tested in this study are single entry, the conversion duct join the two limbs into a single duct. The air then flows through the volute, scroll, rotor and outlet pipe. An additional static pressure measurement is taken at the exit of the outlet pipe and the air is then released to the atmosphere.

The rotor is connected to the high speed eddy-current dynamometer which sets the load of the turbine. The maximum speed is 60krpm and the maximum load is 60kW. The load is the result of the magnetic forces induced by the eddy currents generated in the two metallic stator plates and due to rotation of the magnetic rotor. The stator plates can be placed closer or further apart from the magnetic rotor setting higher or lower load to the turbine. Figure 3.25 shows the stator plates and magnetic rotor of the eddy-current dynamometer with the wheel assembled on the other end of the shaft.

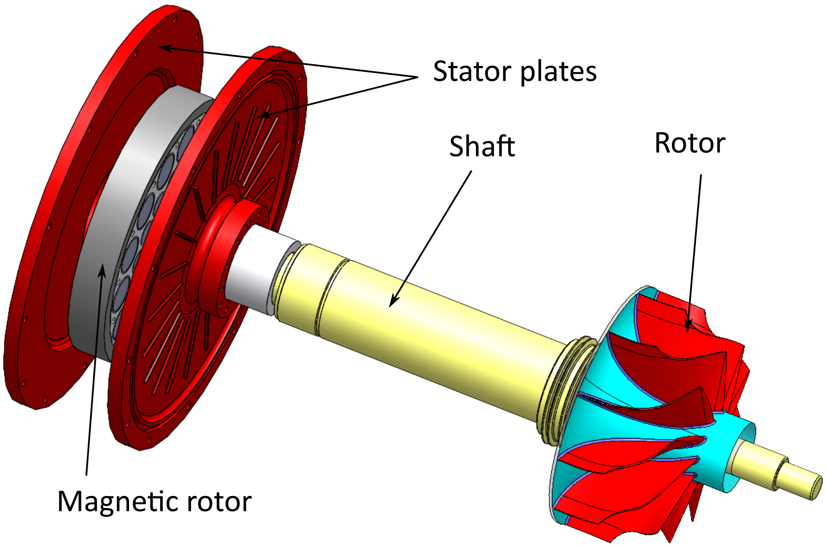

Figure 3.25: Eddy-current dynanometer stator plates and magnetic rotor on the shaft with the turbine wheel

The whole eddy current dynamometer is mounted on a gimbal bearing system including the bearings of the shaft. This allows the direct measurement of the turbine torque as the reaction force against a load cell. The measurement includes the bearing losses, therefore the true aerodynamic performance of the turbine can be obtained.

Vibrations are monitored during the rig operation by a velomiter attached onto the casing of the eddy-current dynamometer. Excessive vibrations due to an unbalanced rotor-shaft assembly could result on a rig failure, therefore, the rig should operate below a certain vibration threshold [105, 119]. Balancing of the turbine wheel, shaft and magnetic rotor assembly is done before testing. The balancing is carried out at medium speed, around 2,500 rpm adding weights on the turbine wheel and magnetic rotor side. Figure 3.26 shows a real image of the rig highlighting some of the components mentioned above.

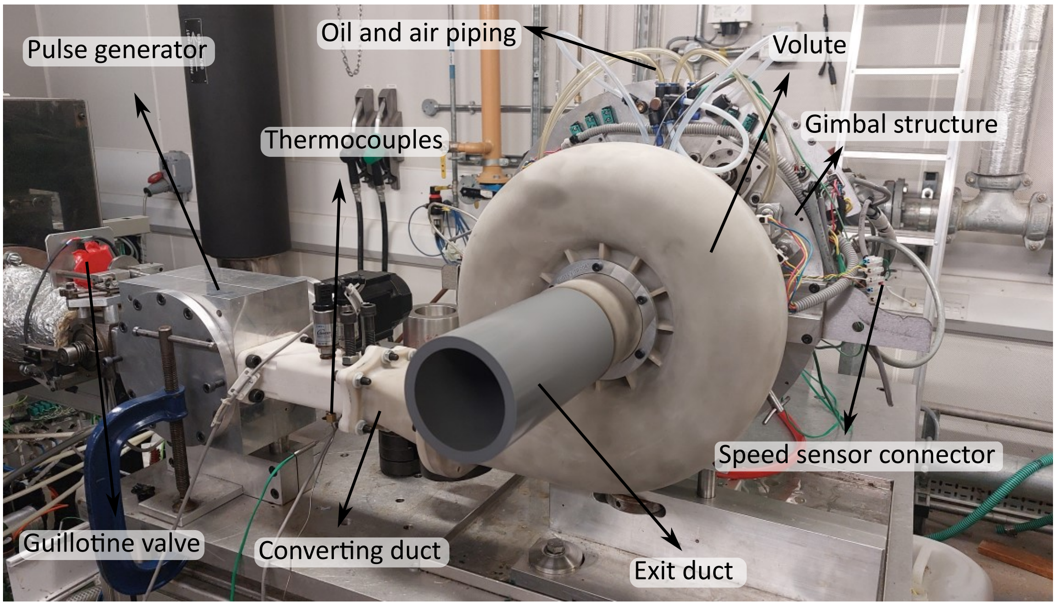

Figure 3.26: Turbine rig set up

Auxiliaries consisting of a water loop, oil loop and air supply allow the correct operation of the rig and prevents failure of the materials. Water cooling is available for the dissipation of the heat released by the stator plates due to the current induced by the magnetic field. A small pump feeds oil to the bearing systems and air is supplied at high pressure to prevent oil leakage from the bearings.

3.4.2 Experimental Performance Calculation

The temperature, pressure, mass flow, torque and rotational speed measurements taken at different locations of the rig are the essential magnitudes that allow the calculation of the performance of the turbine. A brief summary of the measuring devices can be found below, but the reader is referred to previous literature on the rig for more detailed information and specification sheets of each device [105]

Temperature measurements are taken with T-type thermocouples. The acquired temperature of the flow, T_a, is somewhat between the stagnation, T_0, and static temperature, T. They are related through the recovery coefficient,r, as shown in Eq. 3.23:

$$T_a = T + r(T_0 - T) \tag{3.23}$$

The static and stagnation temperature for an ideal gas are related through the Mach number, M, indicated in Eq. 3.24. After an iterative process, the static and stagnation temperature of the flow can be obtained.

$$\frac{T}{T_0} = 1 + \frac{\gamma - 1}{2} M^2 \tag{3.24}$$

Static pressure is measured with 24 channel Scanivalve system. Two high accuracy strain gauge pressure sensors are used, a Druck PDCR 22 for low pressure measurements ($< 350mbar$) and a Druck PDCR 23D for higher pressures ($< 3.5bar$).

Mass flow is measured with McCrometer v-cone flow meter, based on differential pressure. The differential pressure is measured by Siemens Sitrans P DSIII differential pressure transducer and the Scanivalve measured the absolute pressure. The temperature is measured by an E-type thermocouple. The differential pressure, absolute pressure and temperature was used to calculate the mass flow according to Eq. 3.25:

$$\dot{m} = \sqrt{\rho} F_a C_d k_1 Y \sqrt{\Delta P} \tag{3.25}$$

Where ρ is the density, ΔP is the differential pressure, and F_a, C_d, k_1, Y are the material thermal expansion, the discharge coefficient, the flow coefficient and the gas expansion factor, respectively. These factors are related to the mass flow meter and the flow conditions.

Torque is measured as the reaction force of the dynamometer on the gimballed system with an Interface miniature beam load cell transducer and the known arm length of the position of the load cell. The load cell transducer has a linear response between the voltage and the force and it is calibrated before experimental tests. The calibration consists of hanging 4 weights of known mass at 250 mm of the axis and correlating the force with the registered voltage.

Speed measurement is taken with an optical speed sensor, Omron EE-SX4101 type infra-red transmissive optical switch with an integrated amplifier. The optical signal is interrupted every time one of the 20 teeth of the encoder located at the shaft of the turbine passes between the sensor. 20 of the pulses created by this signal interruption correspond to one revolution.

Total-to-static efficiency is then calculated with the magnitudes measured as the ratio between the actual power and the isentropic power, as shown in Eq. 3.26. The actual power of the turbine is derived from the torque, τ, and rotational speed in revolutions per second, n_s. The isentropic power is calculated from the mass flow, $\dot{m}$, inlet temperature, T_{01} pressure ratio, PR and specific heat at constant pressure, C_p:

$$\eta_{ts} = \frac{\dot{W}_{act}}{\dot{W}_{isen}} = \frac{\tau n_s}{\dot{m} C_p T_{01} \left(1 - PR^{\frac{\gamma-1}{\gamma}}\right)} \tag{3.26}$$

3.4.3 Uncertainty Analysis

A thorough explanation of uncertainty analysis was carried out by previous users of the experimental facilities and it is not in the scope of this study to give all the details. The methodology followed to estimate the uncertainty on mass flow and total-to-static efficiency can be found in the literature, [79, 105]. This uncertainty is calculated based on the principle of the propagation of error in the measured quantities (temperature, static pressure, torque, rotational speed).

The uncertainty of total-to-static efficiency, $\Delta\eta_{ts}$, is estimated based on the uncertainty of the mass flow, inlet total temperature, pressure ratio, torque and rotational speed, as shown in Eq. 3.27:

$$\Delta\eta_{ts} = \sqrt{\Delta\dot{m}\frac{\partial\eta_{ts}}{\partial\dot{m}} + \Delta T_{01}\frac{\partial\eta_{ts}}{\partial T_{01}} + \Delta PR\frac{\partial\eta_{ts}}{\partial PR} + \Delta\tau\frac{\partial\eta_{ts}}{\partial\tau} + \Delta n_s\frac{\partial\eta_{ts}}{\partial n_s}} \tag{3.27}$$

The dominant factor in efficiency uncertainty is torque. Torque uncertainty was calculated as two times the standard deviation of the difference between the reading provided by the linear response of the load cell and the real force generated by the weights used for calibration. The torque uncertainty was found to be $\pm 0.002\,Nm$ after several calibration runs.

The torque uncertainty is an absolute uncertainty, meaning that the impact on efficiency uncertainty at low torque will be very high compared to high torque conditions. As a result, efficiency uncertainty was between 2.3 pp and 0.5 pp for low torque and high torque operating conditions. The average uncertainty in total-to-static efficiency was found to be 1.31 pp.

The uncertainty of the mass flow, $\Delta\dot{m}$, is calculated based on the uncertainty of the density, the gas expansion factor and the differential pressure. The uncertainty of the material thermal expansion, discharge coefficient and flow coefficient were considered negligible adding no uncertainty to the mass flow. Equation 3.28 shows the expression for the mass flow uncertainty:

$$\Delta\dot{m} = \sqrt{\Delta\rho\frac{\partial\dot{m}}{\partial\rho} + \Delta Y\frac{\partial\dot{m}}{\partial Y} + \Delta\left(\Delta P\right)\frac{\partial\dot{m}}{\partial\Delta P}} \tag{3.28}$$

Mass flow uncertainty ranged between 0.92% and 2.50%. Uncertainty is shown as error bars in the charts of the experimental results included in Appendix B.

3.5 Chapter Summary

This chapter introduced the methodology used in this investigation. The expander design methodology consisting of the meanline model and the 3D parametric model was described. The meanline model was developed to predict the turbine performance working with ideal and non-ideal fluids. The code implements different subroutines to predict the choking point of the nozzle and the rotor and allows performance map generation and design optimisation. The meanline model is calibrated using CFD data generated for the applications of study.

The 3D parametric model was developed to overcome the limitations of meanline modelling when predicting the impact on efficiency of certain geometry modifications including the meridional profile and non-radial blading. The model can generate radial and non-radial fibre geometries and it is coupled to a CFD solver. Automated sampling and optimisation can be carried out using this methodology. This method, although computationally costly, provides more accurate performance prediction and more understanding of the impact of geometry modification on the flow field.

Finally, the experimental methodology using Imperial College turbine test rig was explained. Performance calculation and uncertainty were also introduced. Widely used in previous research, the test rig provided experimental results for the validation of the methodology with air as working fluid.

The next two chapters introduce the results of the application of this methodology on the design of turbines for ORC and ETC applications. Both methodologies are compared and the effect of design parameters on the performance of radial and non-radial fibre rotors is investigated.

Chapter 4

Organic Rankine Cycle Turbine Design

The meanline model introduced in Chapter 3 was implemented for organic fluids. The application requires unconventional operating conditions for these turbines, operating at high pressure at the design point. While meanline model provides good design guidance for conventional radial turbomachinery, limitations are expected in predicting the performance of turbines for ORC (or non-ideal fluids) applications.

The parametric model coupled with CFD was used to investigate the detailed flow field of different designs and to obtain high-fidelity data to compare and calibrate the meanline model. The next sections describe the calibration, sensitivity study and optimisation using the two methodologies, meanline and parametric modelling. Finally, 3D blading designs are explored using the CFD parametric model by modifying the meridional shape of the hub and shroud contours.

4.1 Meanline Model Calibration

While the main equations in meanline modelling are based on physical models, losses are based on semi-empirical equations. Loss correlations have being validated in the literature against experimental data for a fixed set of geometries, operating conditions and working fluids. However, it is advised that the loss coefficients are calibrated for each particular application. Calibration requires the use data from the literature, experimental results from preliminary designs or high fidelity CFD data of similar application conditions and geometries to the actual application.

CAESES provides an integration platform for automated geometry design and CFD computations with optimisation algorithms. Latin Hypercube Sampling, LHS, was used to obtain a near-random set of 20 geometry evaluations based on the meridional profile, nozzle and blade angles, and rotational speed. This methodology tries to explore all the design space determined by the range of the parameters, defining the meanline geometry, the blade angles and the rotational speed. Five designs were selected to calibrate the meanline model loss coefficients, while the rest of the generated designs was used to evaluate the deviation between the meanline predicted performance and the CFD performance.

The calibration algorithm consists on predicting the efficiency and mass flow of each geometry using the meanline model and calculate the relative RMS error (RRMSE) between the meanline and CFD efficiency and mass flow values. The efficiency RRMSE and the mass flow RRMSE are part of the objective function to minimise during calibration. A multiobjective genetic algorithm is used for the minimisation of the objective function by varying the loss coefficients within a certain range. The number of generations was set to 40 and the population in each generation was set to 80 iterations. The convergence of the algorithm is monitored using the hypervolume indicator shown in Fig. 4.1. The hypervolume indicator measures the proximity of the function evaluations to the Pareto front and how evenly distributed and spread are [121]. The advantage of this metric is that the Pareto front does not need to be known in advance to assess the performance and convergence of the optimiser. The asymptotic behaviour of the hypervolume indicates that the calibration has converged [122].

After 3200 iterations, the Pareto front of the multi-objective calibration was obtained. The Pareto front shows potential solutions that minimise the error between the meanline and CFD efficiency and mass flow. Weights, w_i, are applied to each of the components of the objective function to assess the overall error and get a single solution for the loss

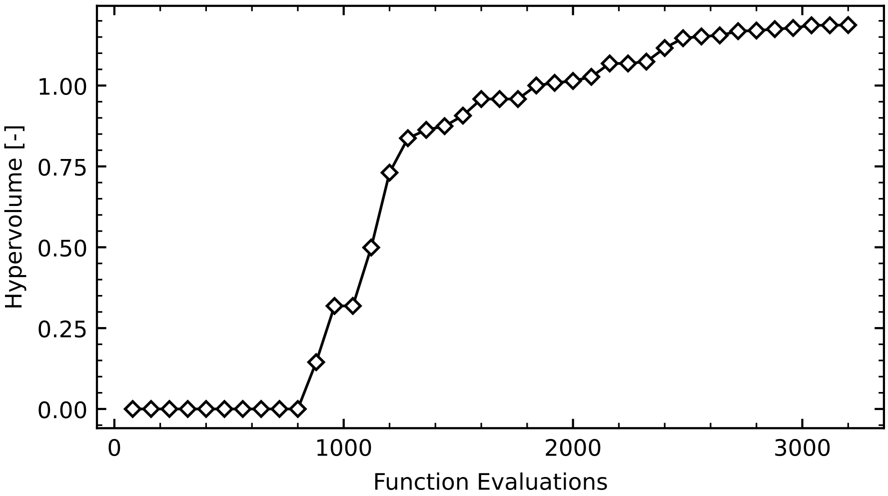

Figure 4.1: Hypervolume indicator monitoring with calibration iterations for the first calibration with efficiency and mass flow.

coefficients, according to Eq. 4.1. Efficiency and mass flow RRMSE were assigned the same weights, 0.5 and the set of loss coefficients that returns the lowest overall RRMSE was chosen as the solution of the calibration.

$$F_{solution} = min\{w_{\eta_{ts}} RRMSE_{\eta_{ts}} + w_{\dot{m}} RRMSE_{\dot{m}}\} \tag{4.1}$$

The RRMSE in efficiency and mass flow after calibration was 0.82% and 0.3%, respectively. This resulted in an average deviation of 1.2 pp in efficiency and 0.4% in mass flow. Figure 4.3 shows the total-to-static efficiency and mass flow comparison between the CFD data used (x-axis) and the data predicted by the meanline model (y-axis) of the calibration points.

When analysing the full set of CFD data, the total-to-static efficiency and mass flow deviation measured in percentage points difference, pp, and relative deviation, were found to be 3.2 pp and 3.9%, with an RRMSE of 2.6% and 2.8%, respectively. Figure 4.4 shows the comparison of the efficiency and mass flow of the full set of CFD data and their meanline predicted results. The loss coefficients after calibration are summarised in Table 4.1.

Table 4.1: Loss coefficients after the first calibration

K_n	K_{inc}	K_p	K_{cl}	B_2	B_4	B_6
0.7	0.63	0.12	0.7	0.97	1.0	0.9

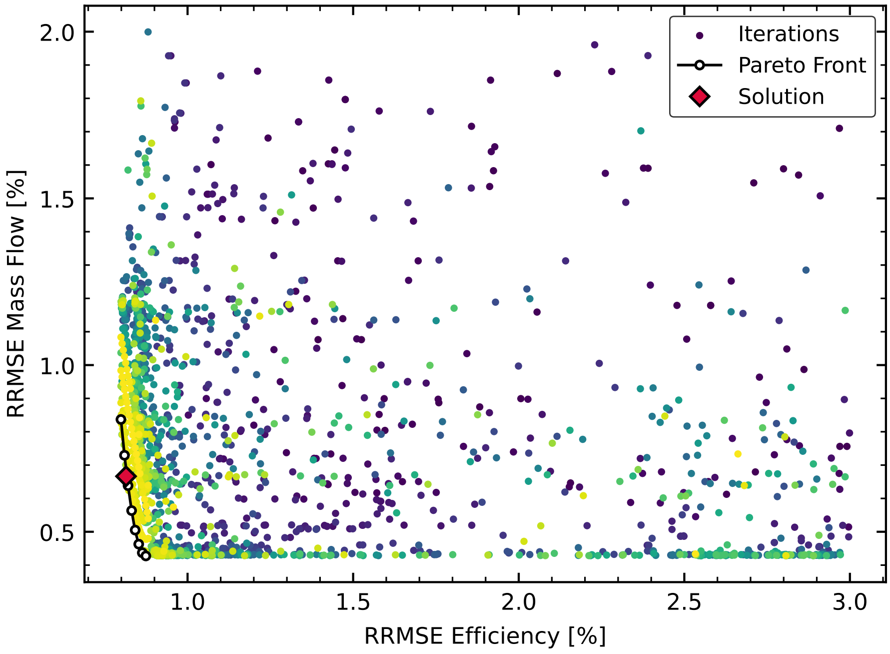

(a)

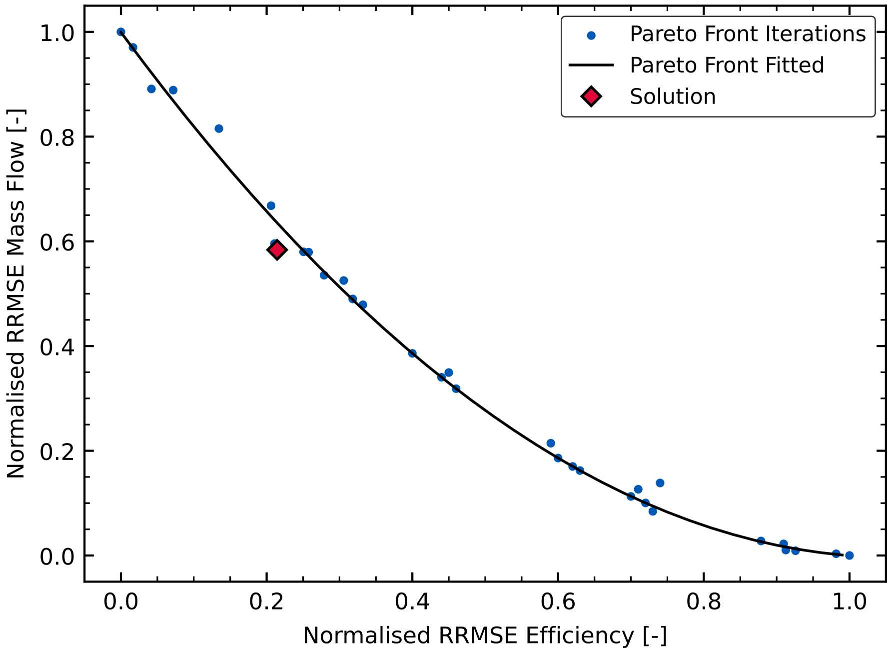

(b)

Figure 4.2: (a) Multi-objective calibration showing iterations, the Pareto front and the solution obtained (colour map from blue to yellow indicates older to newer iterations, respectively) and (b) normalised Pareto front showing the calibration solution

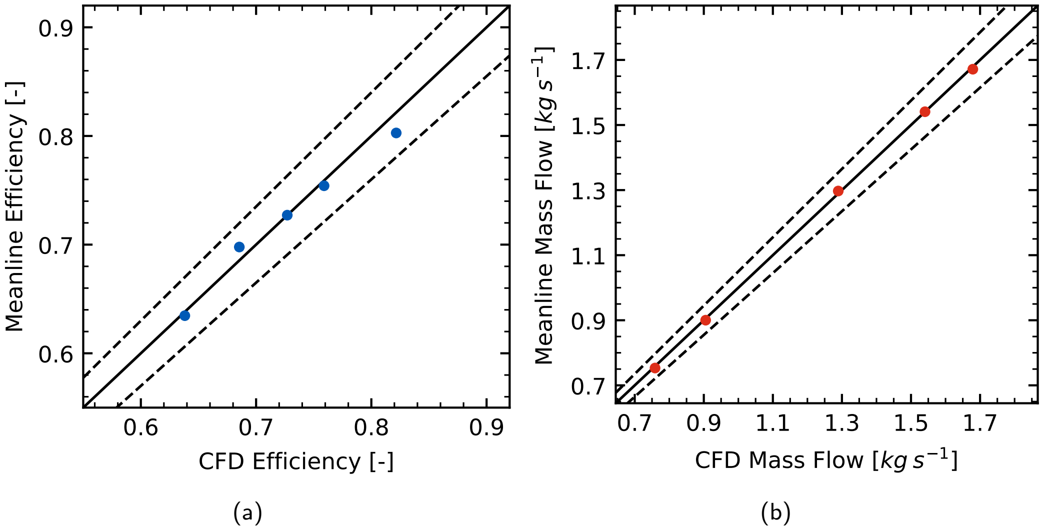

(a)

(b)

Figure 4.3: Comparison between meanline and CFD efficiency after meanline model calibration for the selected designs

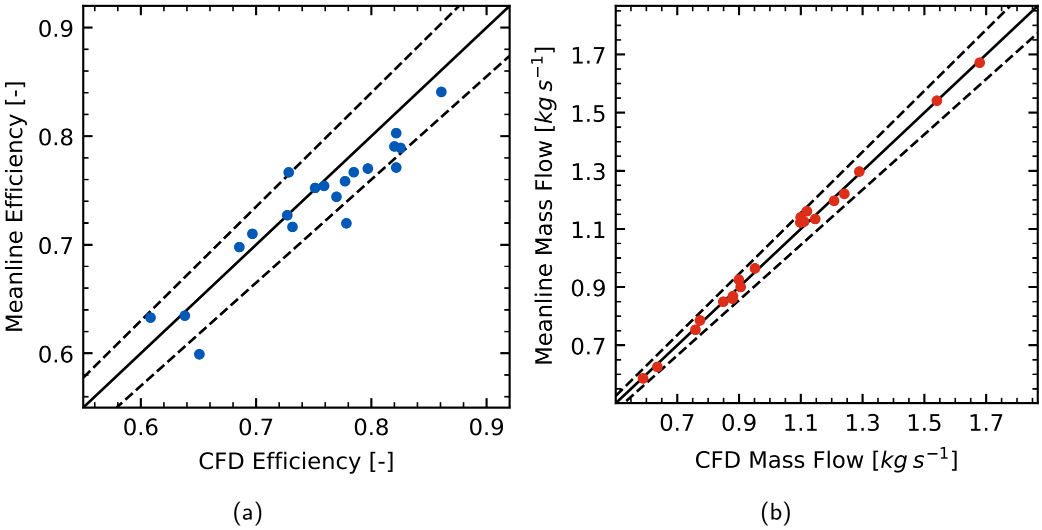

(a)

(b)

Figure 4.4: Comparison between meanline and CFD (a) efficiency and (b) mass flow after meanline model calibration for the whole sample. Dashed lines indicate $\pm 5\%$ deviation

The meanline model predicts accurately trends in performance (efficiency and mass flow) compared to the CFD data available. This confirms the use of the low order model. In the next subsection the loss breakdown is analysed to determine if the meanline model is physically representative of the actual loss mechanisms in a radial ORC turbine.

4.1.1 Loss Breakdown for Calibration

To compare the loss breakdown predicted by the meanline model and the loss breakdown provided by CFD results, 5 geometries out of the sampling were chosen and analysed in more detail. The CFD domain was divided into several regions and the entropy generation calculated in each region was assigned to one loss mechanism.

Losses are proportional to the entropy change, Δs, across the turbine. The entropy generation of an adiabatic process, is a function of the entropy change across the turbine boundaries, according to Eqn. (4.2) [123]:

$$d\dot{W}_{loss} = Td\dot{S}_{gen} = T\left((sd\dot{m})_{out} - (sd\dot{m})_{in}\right) \tag{4.2}$$

The fluid domain was divided into regions according to Fig. 4.5 to calculate the entropy increase across them and link them to specific loss mechanisms across the rotor [124, 125]. The interspace region was set at the inlet and the leading edge of the blade, extending up to 2% of the blade chord. Pressure surface and suction surface regions were located in the passage adjacent to each blade surface and extended up to 67% span.

The tip region extended from 67% up to 100% span at both sides of the blade. Pressure surface, suction surface and tip regions extended from 2% to 95% blade chord. The trailing edge domain extended from 95% to 110% (after the trailing edge) blade chord and it is divided into two regions at 67% span. Finally, the exit pipe region consists of the domain from 110% blade chord up to the outlet boundary.

The four loss mechanisms analysed were incidence losses accounting for the entropy generation in the interspace and the first part of the blade, including the leading edge, shown in Fig. 4.5; passage losses, linked to the blade surface region including the passage and surface regions; tip leakage losses including the tip and the trailing edge tip regions, and trailing edge losses including the trailing edge blade region. The entropy generation across each region was divided by the mass flow of each design to allow for a fair comparison.

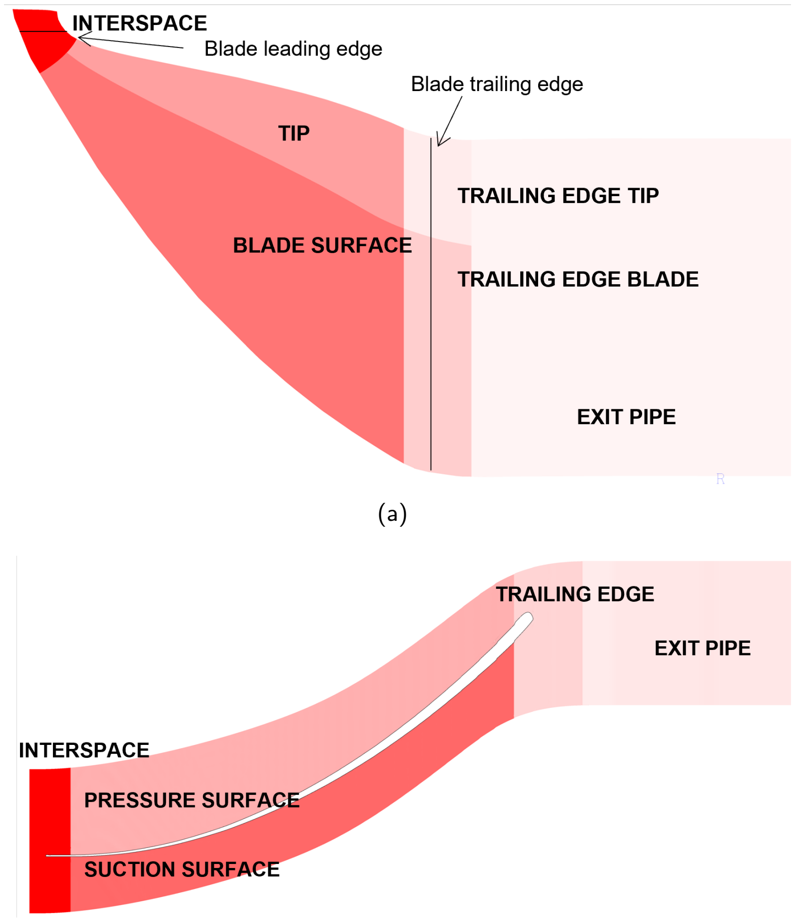

(b)

Figure 4.5: Regions for loss breakdown in the rotor domain: meridional view (a), blade to blade view (b)

Figure 4.6 shows the entropy generation per unit mass flow in each region of 5 different nozzle-rotor designs. Total-to-static efficiency is also shown in the graph. A good correlation between efficiency and entropy generation is observed, design E shows the lowest entropy generation (losses) across all components, therefore the highest efficiency. Contrarily, design D has the highest entropy generation across all components, excluding the nozzle, leading to the lowest efficiency. The entropy generation across the exit pipe modelled in CFD for convergence and for boundary conditions purposes is not equivalent to the exit losses accounted for in meanline. Exit losses in meanline are purely kinetic energy losses due to the absence of a diffuser to recover this kinetic energy and are excluded from the following analysis.

The loss distribution predicted by meanline after the first calibration was compared to

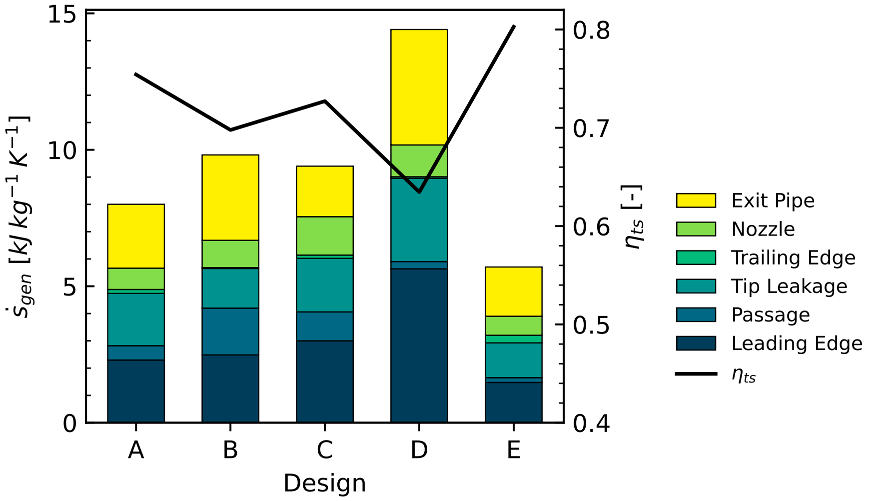

Figure 4.6: Entropy generation per unit mass calculated in each region of the CFD domain and assigned to each loss mechanism (left axis) and total to static efficiency (right axis) for 5 different geometries

the CFD loss distribution. Figure 4.7 shows this comparison. The meanline model predicts accurately the trends in loss distribution across the designs, but fails at estimating the right loss breakdown in each design. The model identifies that the contribution of incidence losses to the overall losses across the rotor is lower in design E compared to the other designs. However, the calibrated meanline model overpredicts the share of incidence losses to the overall losses.

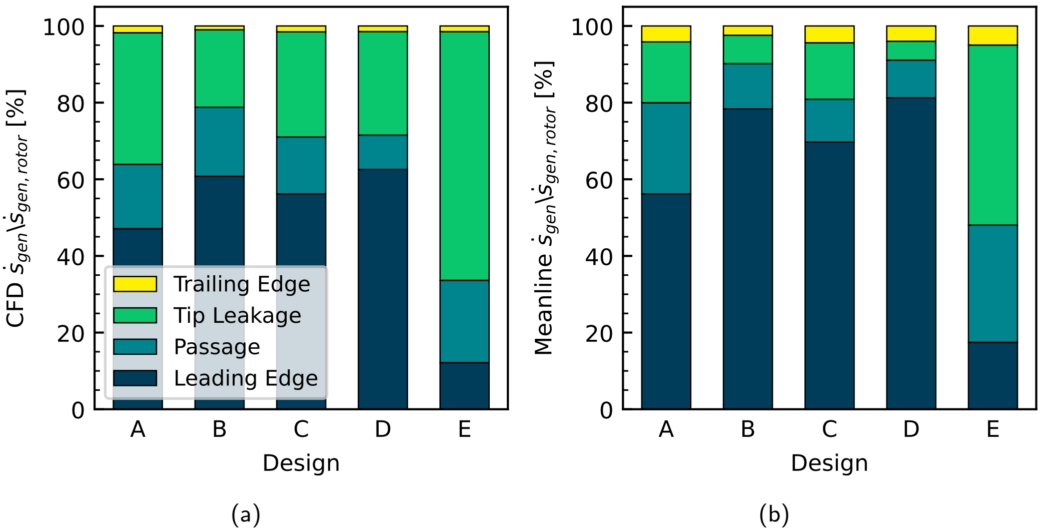

(a)

(b)

Figure 4.7: Loss breakdown in the rotor for 5 different designs calculated via (a) CFD and (b) meanline using the first set of loss coefficients

The CFD results of entropy generation distribution across the rotor were taken as input for a second calibration of the meanline model. Incidence, passage and tip clearance losses were accounted as the percentage of loss contribution to the rotor overall losses, as indicated in Eq. 4.3.

$$\%L_i = \frac{L_i}{L_{rotor}} = \frac{L_i}{L_{inc} + L_{pas} + L_{tc} + L_{te}} \tag{4.3}$$

The relative root mean square error, RRMSE, between the contribution of each loss mechanims (incidence, passage and tip leakage losses) to the rotor overall losses, $\%L_i$, predicted by meanline and the results from CFD was included as objective functions. Equation 4.4 shows the calculation of RRMSE for each loss mechanism and Eq. 4.5 shows the multi-objective function.

$$RRMSE_{\%L_i} = \frac{1}{n}\sum^{n} \frac{\%L_{i,meanline} - \%L_{i,CFD}}{\%L_{i,CFD}} \tag{4.4}$$

$$F_{obj} = \{RRMSE_{\eta_{ts}}, RRMSE_{\dot{m}}, RRMSE_{\%L_{inc}}, RRMSE_{\%L_{pas}}, RRMSE_{\%L_{tc}}\} \tag{4.5}$$

Convergence was monitored using the hypervolume too, as shown in Fig. 4.8, however, it is not possible to visualise the Pareto front since the multi-objective calibration had 5 objective functions, the relative root mean square error, RRMSE in efficiency, mass flow, incidence loss, passage loss and tip clearance loss.

Similarly to the first calibration, equal weighting, w_i, was applied to each term of the objective function to choose the final solution of the calibration, as shown in Eq. 4.6. Efficiency and mass flow RRMSE were assigned the same weights, 0.2 and the set of loss coefficients that returns the lowest overall RRMSE was chosen as the solution of the calibration.

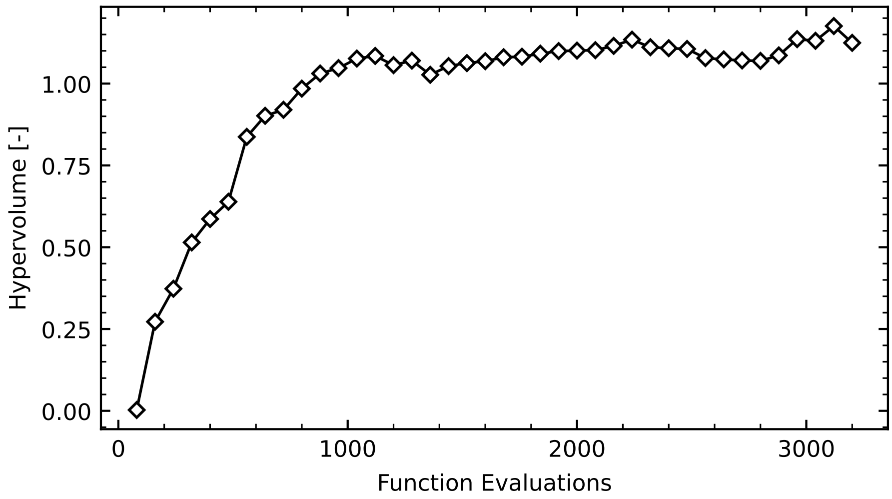

Figure 4.8: Hypervolume monitoring with calibration iterations for the second calibration with efficiency and mass flow and loss distribution

$$F_{solution} = min\{w_{\eta_{ts}}RRMSE_{\eta_{ts}} + w_{\dot{m}}RRMSE_{\dot{m}} + w_{\%Linc}RRMSE_{\%Linc} + \\ + w_{\%Lpas}RRMSE_{\%Lpas} + w_{\%Ltc}RRMSE_{\%Ltc}\} \quad (4.6)$$

The final set of loss coefficients that minimises the RRMSE in performance and loss distribution is summarised in Table. 4.2.

Table 4.2: Loss coefficients after the second calibration

K_n	K_{inc}	K_p	K_{cl}	B_2	B_4	B_6
0.12	0.59	0.21	1.42	0.98	0.98	0.81

Efficiency, mass flow and the loss breakdown predicted by the meanline model after the second calibration is compared to the CFD results in Fig. 4.10. Matching the loss distribution in the rotor penalises the efficiency prediction. Figure 4.10 (a) and (b) show the efficiency and mass flow predicted by meanline after the second calibration and CFD results of the designs used for calibration. The mass flow agreement is quite good across all designs with an average deviation of 0.8% and an RRMSE of 1%. The meanline model predicts accurately the total-to-static efficiency of the first 4 designs, but fails in the last design, leading to an average error of 2.9 pp and the RRMSE of 4.4%

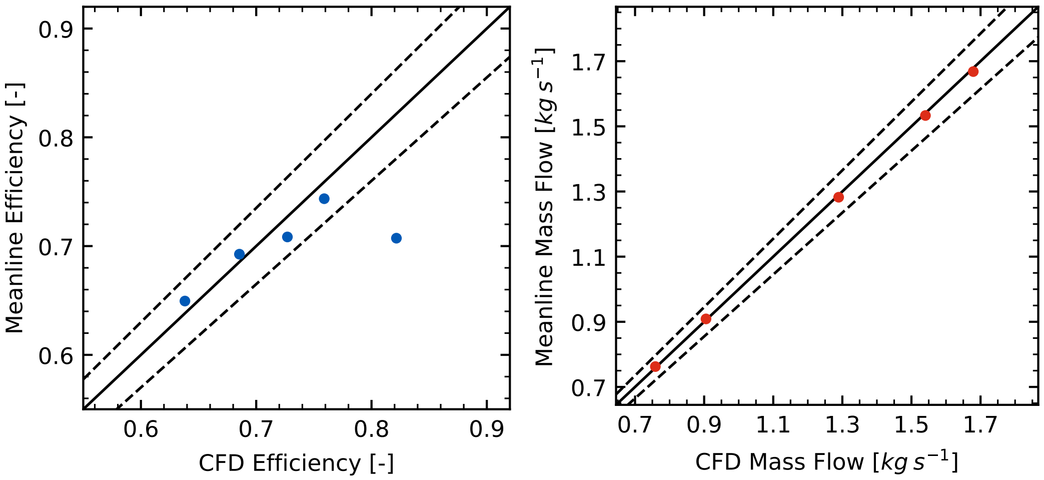

(a) (b)

Figure 4.9: Comparison between meanline and CFD efficiency after the second calibration of the meanline model for the selected designs

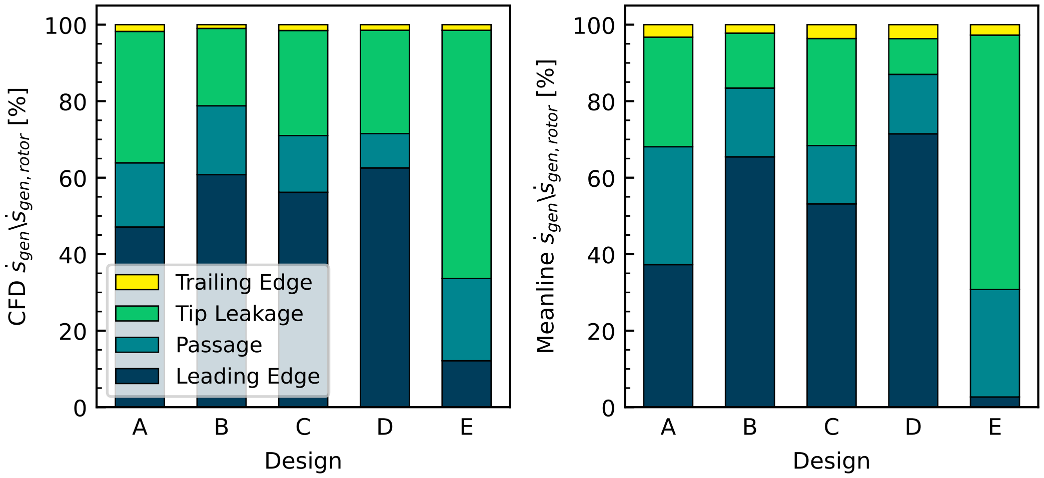

(a) (b)

Figure 4.10: Comparison of the loss breakdown in the rotor domain of the selected designs obtained via (a) CFD and (b) meanline after the second calibration

The loss distribution predicted by the meanline model after the second calibration is closer to the loss distribution found in CFD, shown in Fig. 4.10 (c) and (d), compared to the meanline prediction after the first calibration, Fig. 4.7. The contribution of incidence losses predicted by meanline modelling is very similar to the CFD results.

Passage losses in meanline are slightly higher than CFD results. Tip leakage share in rotor losses is also more similar to CFD results than the prediction after the first calibration. Meanline also predicts that trailing edge losses have a small effect on rotor overall losses, in agreement with CFD results.

To further assess the validity of each calibration, the meanline model was used to calculate the performance of a sample of 500 geometries. Figure 4.11 shows the sensitivity analysis of each of the input parameters of the meanline model with efficiency. The first insight that can be drawn is that the second calibration set overpredicts losses in high performance designs. When looking at the highest efficiency designs obtained with the first calibration set (blue dots) and the second calibration set (red dots) Fig. 4.11 (a), there is a consistent 8pp difference between them regardless of the value of r_4. However, this efficiency shift does not appear to happen in medium to low-efficiency designs. The second insight is that trends are predicted accurately after both calibrations. This leads to the conclusion that accurate loss breakdown in meanline is not that relevant for evaluating efficiency only and overall trends.

A meanline model does not provide an accurate loss breakdown, while CFD has its own limitations due to the nature of losses in radial turbines. Radial turbines show very complex flow structures that interact and merge, making them difficult to isolate and assign to different loss mechanisms. To illustrate this, the vortex core region of design A, corresponding to the set of designs used for calibration purposes, is shown in Fig. 4.12. Figure 4.12 (a) corresponds to the CFD simulation carried out without tip clearance in order to isolate the effects of the other three loss mechanisms acting in the rotor. Figure 4.12 (b) shows the simulation with tip clearance, in which tip leakage plays a significant role.

The flow structures in the core of the passage of both simulations are quite similar. This structure is a big vortex created by boundary layer separation on both the suction and hub surfaces. In the tip clearance case, Fig. 4.12 (b) the tip leakage vortex wraps the suction-hub surface vortex and merges with it, as indicated by the curved arrows. If the two cases were not compared, one can incorrectly conclude that the main flow structure observed within the passage corresponds to the tip leakage vortex, however,

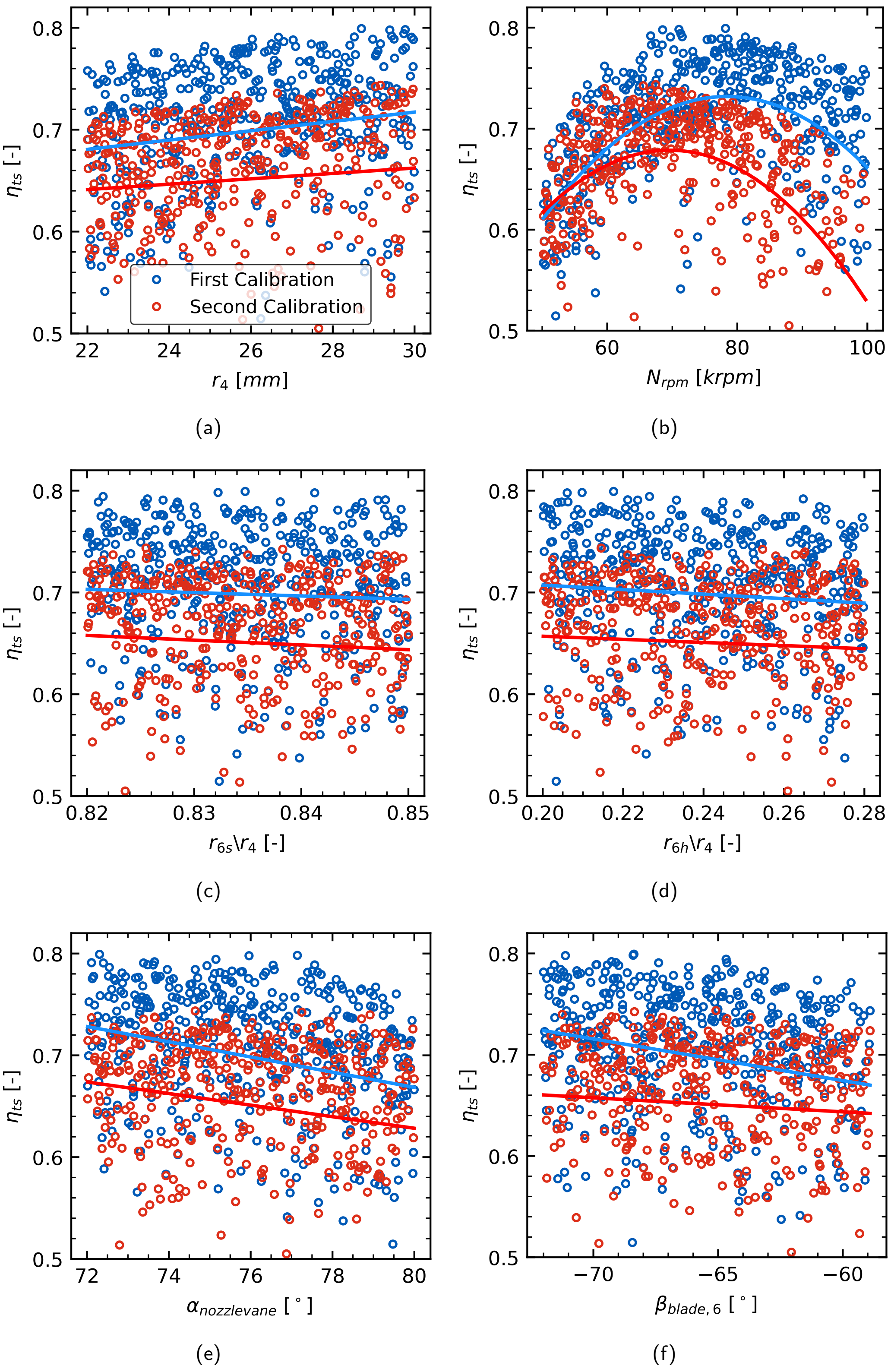

Figure 4.11: Sensitivity analysis of total-to-static efficiency as function of (a) rotor wheel radius,r_4, (b) rotational speed $Nrpm$, (c) rotor shroud radius to wheel radius ratio, $\frac{r_{6s}}{r_4}$, (d) rotor hub radius to wheel radius ratio, $\frac{r_{6h}}{r_4}$ (e) nozzle vane metal angle $\alpha_{nozzlevane}$, (d) rotor blade metal angle at trailing edge, $\beta_{blade,6}$, and fitting curves for the first calibration (blue) and the second calibration (red) sampling

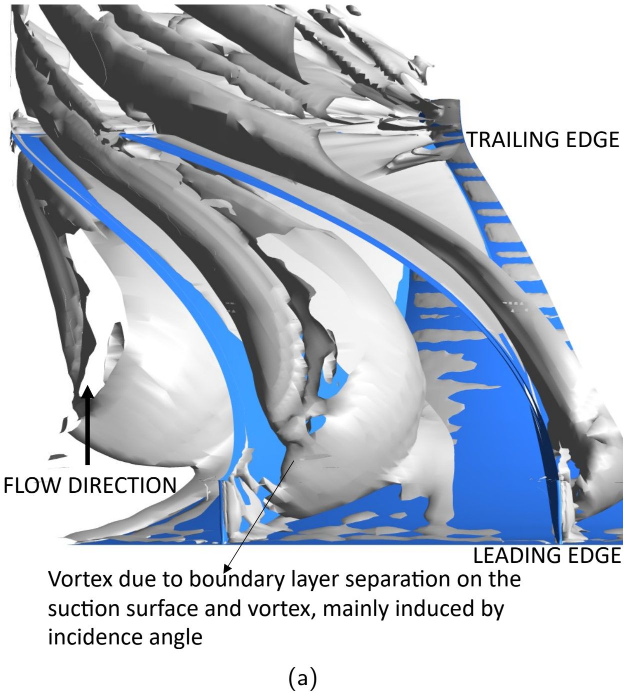

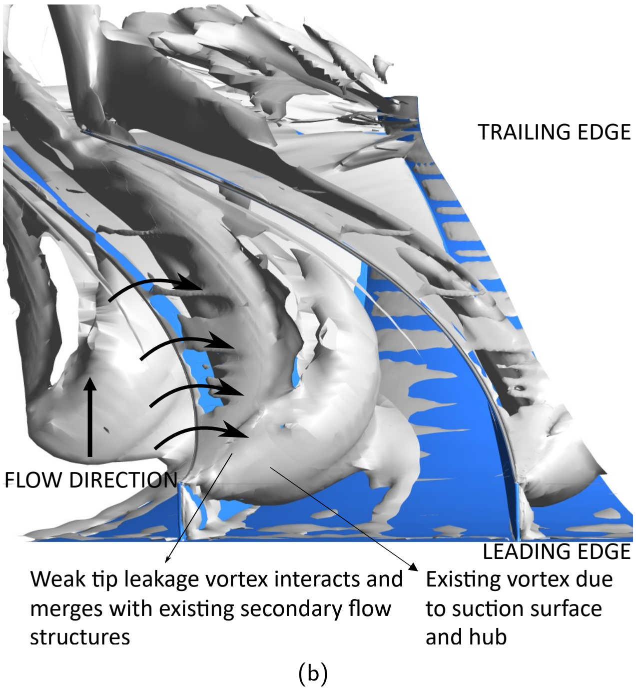

Figure 4.12: Vortex core showing secondary flow structures of design A with (a) no tip clearance and (b) tip clearance

it corresponds to the suction-hub vortex. This could not be easily observed unless the non-tip clearance simulation is considered in the evaluation.

Furthermore, the suction-hub surface vortex starts at a different location due to the tip clearance effect. Figure 4.12 (b) shows an earlier formation of this vortex (closer to the leading edge) than Fig. 4.12 (a) shows. Finally, the suction-hub surface vortex is mainly induced by a sub-optimal incidence angle which promotes the boundary layer separation and the suction surface. In this particular case, it is, therefore, impossible to isolate completely the effect of individual loss mechanisms.

The set of loss coefficients used in the meanline model calculations for the next sections of this chapter corresponds to that obtained after the first calibration, where only the error in efficiency and mass flow was set as objective functions and disregarding the loss breakdown obtained in CFD. Although the second calibration showed a more accurate loss distribution prediction, it heavily penalises the efficiency prediction, which is more relevant for preliminary design.

4.2 Meridional Geometry Optimisation

The sensitivity analysis and optimisation of the meridional geometry and blade angles were carried out using the meanline model and the 3D parametric model coupled with CFD for the highest total-to-static efficiency. First, a Latin hypercube sampling was carried out as part of the sensitivity analysis using both methodologies. Then, the design was optimised using a differential evolutionary algorithm for the meanline model approach. The optimisation with the parametric-CFD approach used a genetic algorithm based on the response surface built from the sampling.

The sensitivity analysis was carried out to assess and compare the influence of each parameter in efficiency during the optimisation process using the meanline and CFD-based approaches, as shown in Fig. 4.13. Fitting curves were plotted to assess the correlation of each parameter with efficiency. Similar levels of correlation were found on the effect of the design parameters on total-to-static efficiency, except from $\alpha_{nozzlevane}$ and β_{blade6}, where the correlation indicates opposite trends.

Analysing the data shown in Fig. 4.13 (a) and (b), the correlation of r_4 and $Nrpm$ with η_{ts} for meanline and CFD-based optimisation is similar, both showing a quadratic relationship. The effect of $\frac{r_{6s}}{r_4}$ and $\frac{r_{6h}}{r_4}$ in efficiency is negligible, as shown in Fig. 4.13 (c) and (d), where the fitting curve are almost horizontal, indicating no correlation.

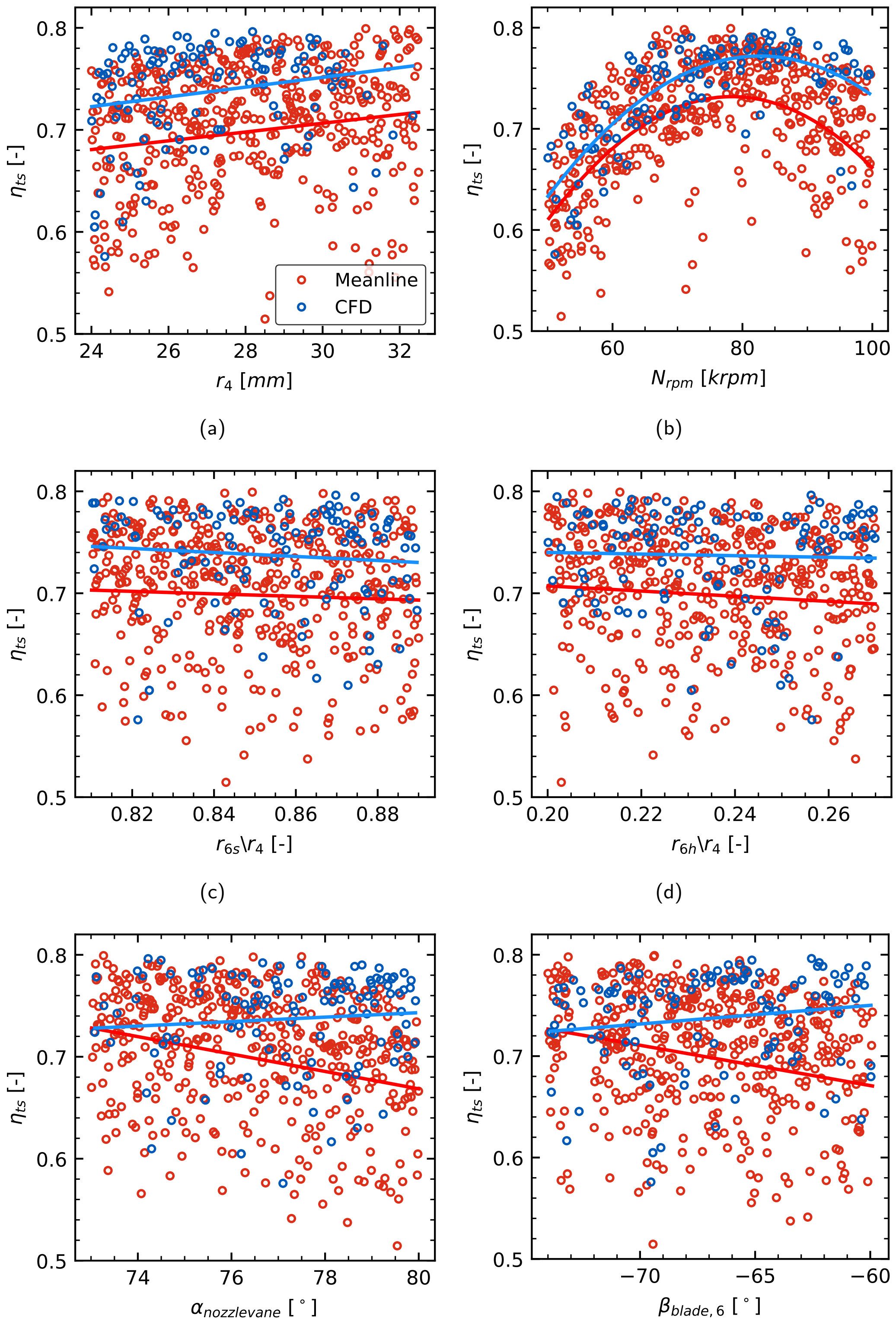

(a) (b)

(c) (d)

(e) (f)

Figure 4.13: Sensitivity analysis of total-to-static efficiency as function of (a) rotor wheel radius,r_4, (b) rotational speed $Nrpm$, (c) rotor shroud radius to wheel radius ratio, $\frac{r_{6s}}{r_4}$, (d) rotor hub radius to wheel radius ratio, $\frac{r_{6h}}{r_4}$ (e) nozzle vane metal angle $\alpha_{nozzlevane}$, (d) rotor blade metal angle at trailing edge, $\beta_{blade,6}$, and fitting curves for meanline (red) and CFD-based (blue) sampling

The meanline model predicts higher efficiency for designs with lower nozzle and rotor angles, α_{nozzle}, β_{blade6} for higher efficiency, as shown in Fig. 4.13 (e) and (f), respectively. The CFD model shows a weak correlation of the efficiency with the nozzle angles since high efficiency designs are possible with any value of α_{nozzle}. The correlation of efficiency with β_{blade6} is also weak but the efficiency slightly increases with higher values of β_{blade6}. These different trends between the meanline model and the parametric-CFD model could be explained due to losses due to excess turning and losses due to choked conditions that are not accurately captured by meanline modelling.

The optimised variables are shown in Table 4.3, with the optimum value and range defining the design space. Table 4.3 also shows the geometrical parameters that were kept constant in every design during the sampling and the optimisation(including the cone angles that were optimised in the next section, but were kept constant in this first geometry optimisation). Efficiency, blade height and mass flow for the optimum geometry of each methodology are also reported in Table 4.3.

The number of candidates assessed in each methodology was different, 450 for meanline and 115 for CFD sampling, to reduce the computational cost. During the optimisation, 980 geometries were generated using meanline. The CFD based optimisation assessed 30 geometries, in addition to the 115 samples which were built the response surface. Designs with blade height lower than 2mm, $b_4 < 2.00mm$, were discarded and not included in this analysis in the CFD methodology. This constraint was set to $1.2mm$ in the meanline approach.

While the efficiency obtained from the optimum designs of each methodology is very close, $\eta_{ts,meanline} = 79.98\%$ and $\eta_{ts,CFD} = 81.29\%$, the meridional geometry and blade angles are significantly different. The meanline optimisation led to higher values (equal to the higher bound) of r_4 and $\alpha_{nozzlevane}$ compared to the CFD-based optimisation. $Nrpm$, $\frac{r_{6h}}{r_4}$ and β_{blade6} were lower in the meanline-optimum geometry than in the CFD-based geometry. Only one parameter, $\frac{r_{6s}}{r_4}$, converged to the same value after both optimisations.

Table 4.3: Optimised meridional geometry and design space for meanline and CFD.

Parameter	Meanline	CFD-based
Optimisation Variables		
r_4 $[mm]$	32.5 [24.0-32.5]	28.6 [24.0-32.5]
$Nrpm$ $[krpm]$	76 [50-100]	93 [50-100]
$\frac{r_{6s}}{r_4}$ $[-]$	0.81 [0.81-0.89]	0.81 [0.81-0.89]
$\frac{r_{6h}}{r_4}$ $[-]$	0.20 [0.20-0.27]	0.27 [0.20-0.27]
$\alpha_{nozzlevane}$ $[°]$	80.0 [73.0-80.0]	74.9 [73.0-80.0]
β_{blade6} $[°]$	-73.6 [-74.0- -59.0]	-59.9 [-74.0- -59.0]
Fixed Parameters		
Number of blades	11	11
Number of vanes	13	13
Tip clearance $[mm]$	0.3	0.3
Z_r $[mm]$	19.2	19.2
$A_{eff,4}$ $[mm^2]$	97.67	97.67
$\psi_{hub,in}$ $[°]$	-	90.0
$\psi_{hub,out}$ $[°]$	-	0.0
$\psi_{shroud,in}$ $[°]$	-	85.0
$\psi_{shroud,out}$ $[°]$	-	0.0
Results		
η_{ts} $[\%]$	79.98	81.29
b_4 $[mm]$	2.75 [>1.20]	2.08 [>2.00]
$\dot{m}$ $[kgs^{-1}]$	0.90	0.89
$N_{designs}$ (sampling)	450	115
$N_{designs}$ (optimisation)	980	115+30

Many factors can affect the different optimum designs, but the main source of discrepancy may be:

1. Less number of geometries to cover the entire design space.
2. CFD-based geometries which are similar to the meanline optimum design show low deviation in efficiency, which means they are good candidate designs.
3. CFD-based optimisation allows for finer cross-over of candidates between generations due to the more detailed effect of each parameter on efficiency, resulting

in an optimum geometry with higher efficiency than the meanline optimisation.

4.3 Hub and Shroud Contour Sensitivity

Once the meridional profile, nozzle vanes and rotor blade angles, as well as rotational speed were optimised, the influence on efficiency of 3D geometry features that can not be captured by the meanline model was investigated. The meridional profile, nozzle and rotor blade angles and rotational speed were kept constant based on the best configuration of the previous CFD-based optimisation shown above (data shown in Table 4.3). The camberline, shown in Fig. 4.14, was also constant for all designs considered in the optimisation of the hub and shroud contours. The cone angle at the leading edge and trailing edge of the rotor hub and shroud (see Fig. 3.11 as reference) were optimised for highest efficiency.

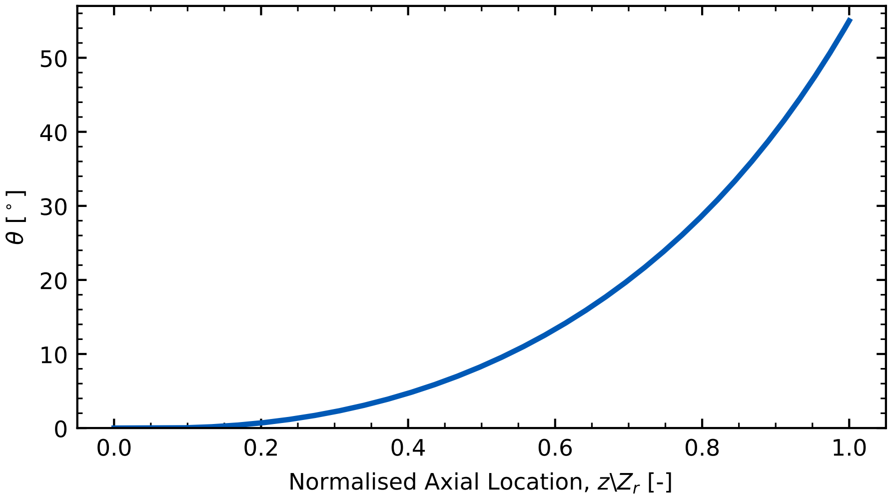

Figure 4.14: Common camberline for the three designs

The lowest efficiency design and a mid efficiency design obtained during the sampling were chosen to analise and compare the flow field in more detail. Geometrical data and total-to-static efficiency results of the three designs can be found in Table 4.4, along with the design space considered in the optimisation.

70 candidates were computed during the CFD-based optimisation of the 3D parameters defining the hub and shroud contours. A 2.1 pp difference between the high η_{ts} and the low η_{ts} was found and it is attributed to the effects of the different 3D shape of

Table 4.4: Optimised hub and shroud contours and design space for 3D-CFD-based optimistation

Parameter	Design Space	Low η_{ts}	Medium η_{ts}	High η_{ts}
Optimisation Variables				
$\psi_{hub,in}$ [°]	[60.0-90.0]	86.0	64.2	63.3
$\psi_{hub,out}$ [°]	[0.0-30.0]	9.0	7.6	26.5
$\psi_{shroud,in}$ [°]	[60.0-85.0]	82.0	68.7	73.8
$\psi_{shroud,out}$ [°]	[0.0-30.0]	2.0	15.0	26.9
Results				
η_{ts} [%]	-	79.19	80.01	81.29
Number of geometries	70	-	-	-

the blade on the flow. Note that, since the meridional contour and nozzle and rotor blade angles were kept constant for all geometries during the optimisation, the efficiency predicted by meanline modelling is the same, not capturing the impact of local geometry modifications.

A sensitivity analysis was carried out based on the efficiency of the different geometries calculated by CFD during the optimisation. Figure 4.15 shows the total-to-static efficiency as function of the 4 variables in the optimisation and their correlations. The hub cone angle at the leading edge, $\psi_{hub,in}$, and the shroud cone angle at the trailing edge, $\psi_{shroud,out}$, are the parameters which have the biggest impact on efficiency. Higher $\psi_{hub,in}$ and lower $\psi_{shroud,out}$ values lead to higher efficiency, as shown in Fig. 4.15 (a) and (d), respectively. No significant correlation with efficiency was found for $\psi_{hub,out}$ and $\psi_{shroud,in}$, as the flat fitting curves show in Fig. 4.15 (b) and (c), indicate no correlation.

Entropy generation and loss breakdown analysis was carried out to explain the difference in efficiency obtained among the three geometries. The entropy generation rate is calculated in each region according to Fig. 4.5 and assigned to the appropriate loss mechanisms for the three geometries, as shown in Fig. 4.16. The entropy generation in the suction surface and pressure surface regions was calculated separately for a more detailed analysis. The high efficiency design shows lower entropy generation across

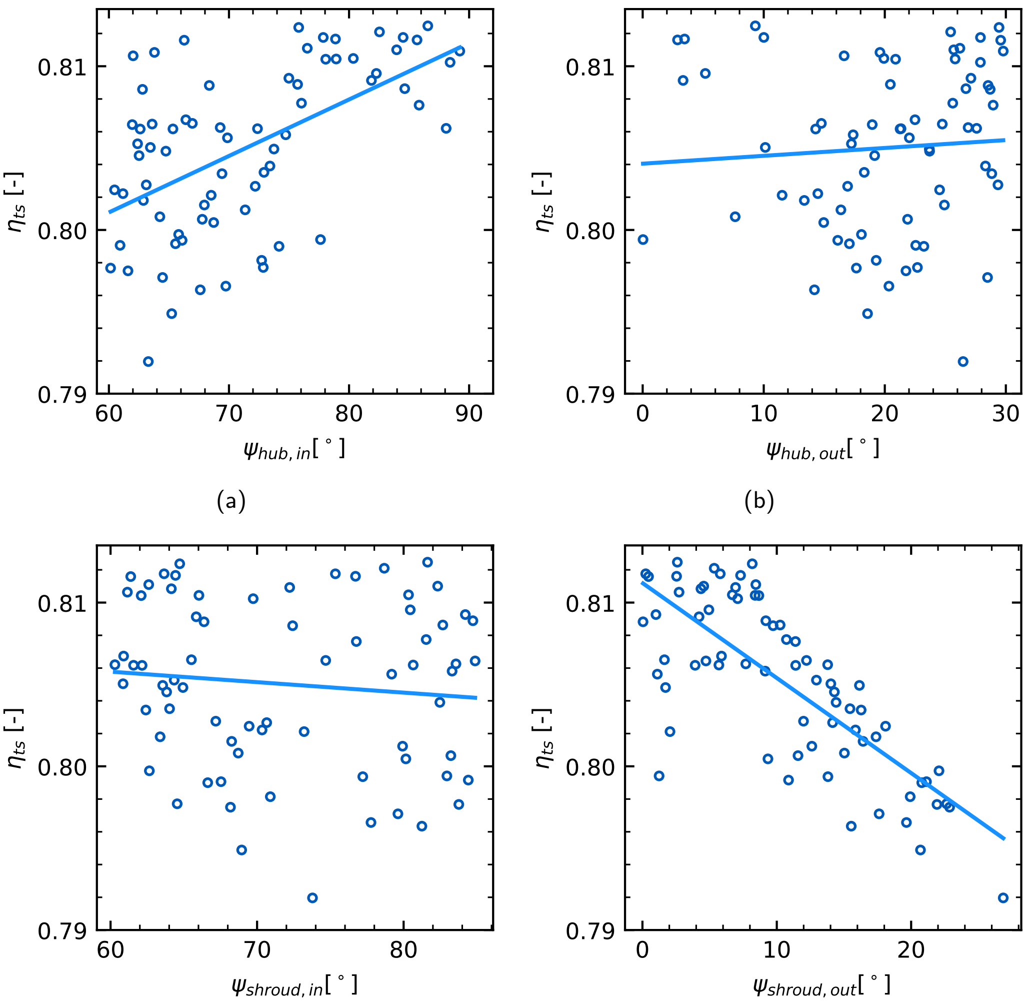

(a) (b)

(c) (d)

Figure 4.15: Sensitivity analysis of the 3D parameters studied in the optimisation:total-to-static efficiency as a function of (a) hub cone angle at inlet , $\psi_{hub,in}$, (b) hub cone angle at outlet , $\psi_{hub,out}$, (c) shroud cone angle at inlet , $\psi_{shroud,in}$, (d) shroud cone angle at outlet, $\psi_{shroud,out}$, and fitting curves

the whole rotor, suggesting lower losses than the other two designs. The difference in overall entropy generation between the high and mid efficiency designs is small, leading to 1.28 pp difference in total-to-static efficiency. The comparison is therefore focused on the high and low efficiency designs, which show a 5.5% difference in overall entropy generation and 2.1 pp efficiency difference.

Evaluating in more detail the loss breakdown between the high and low efficiency designs, it was found that entropy generation across the passage (including interspace, tip, pressure and suction surface regions) is similar (1.2% lower entropy generation in the low efficiency design compared to the high efficiency design), but there is a redistribution

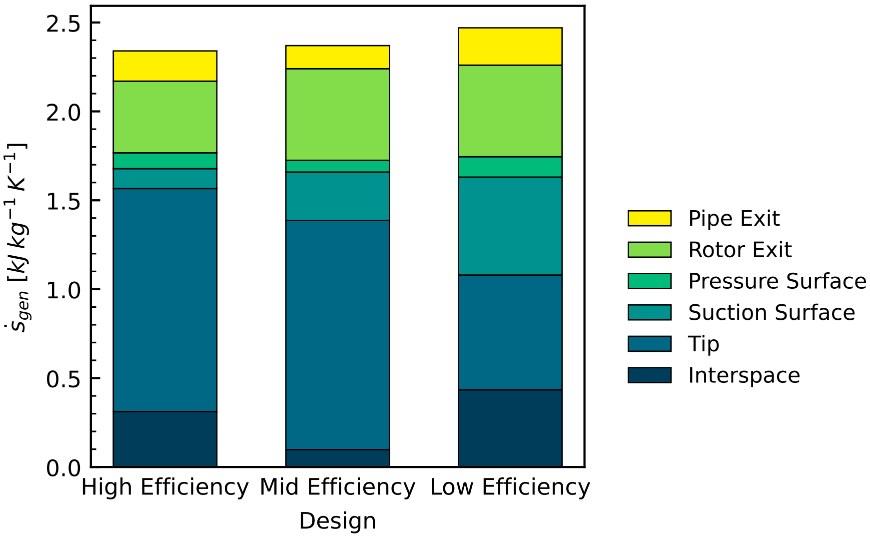

Figure 4.16: Entropy generation rate comparison and loss breakdown between 3 designs of different hub and shroud contours but common meridional profile and blade angles.

of losses. This redistribution can be linked to secondary flow structures, as source of entropy generation.

Interspace losses, suction surface losses and pressure surface losses are 39%, 400% and 28% higher in the low efficiency case compared to the high efficiency one, respectively. However, tip clearance losses are 48% lower in the low efficiency geometry compared to the high efficiency design.

Figure 4.17 shows the blade streamlines at the suction surface for the high efficiency and low efficiency designs. Tip clearance is the dominant loss mechanism in the high efficiency design, leading to a big tip vortex created from the leading to the trailing edge of the blade, as shown in Fig. 4.17 (a). This keeps the entropy generation in the interspace, suction and pressure surface to a minimum in the high efficiency design.

In the low efficiency design, however, the main tip leakage vortex is smaller, as it can be seen in Fig. 4.17 (b). The flow separates at a previous location, mainly at the suction surface, but also at the interspace and pressure surface to a small extent. The suction surface separation also drags low momentum material from the leading edge tip and the hub, forming a vortex that travels upwards up to 60% span and detaching from the suction surface as it heads to the trailing edge.

Figure 4.16 shows higher rotor and pipe exit losses in the low efficiency design. Rotor

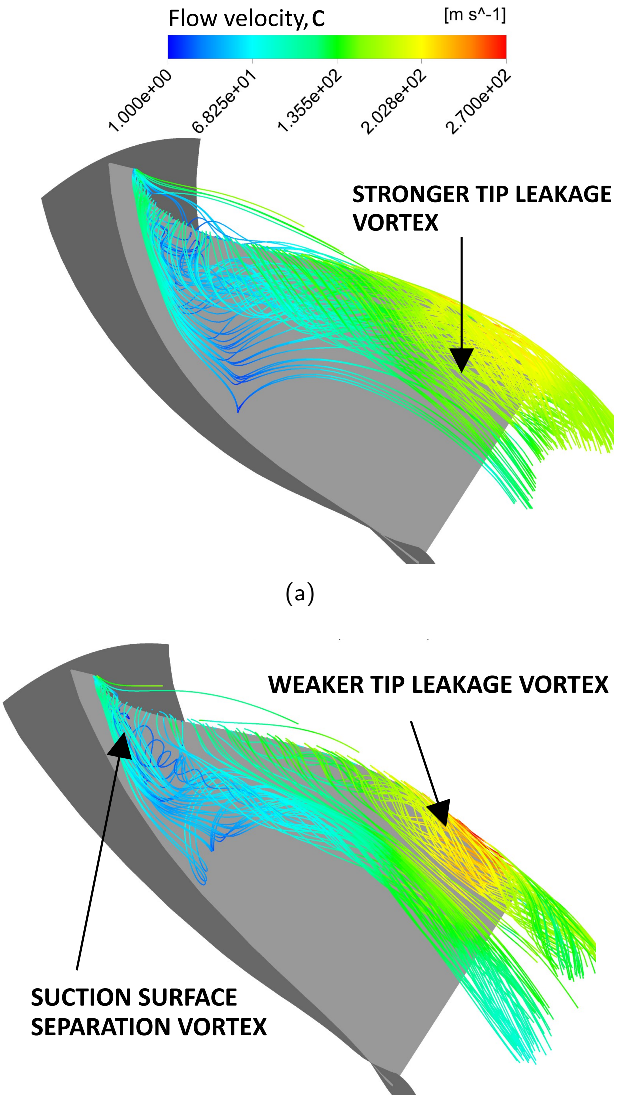

(a)

(b)

Figure 4.17: Blade streamlines in (a) high efficiency design (b) low efficiency design

exit and pipe exit losses are 28% and 24% higher in the low efficiency design compared to high efficiency one, due to the effect of the vortices created upstream, explaining the increased entropy generation in these regions.

Entropy is generated by different mechanisms according to the literature [123, 126–128]. One of the mechanisms is the entropy generation due to turbulence dissipation, $\dot{S}_{gen,d}$, which is the main contributor to the overall entropy generation. Entropy is generated as a result of the dissipation of useful kinetic energy into internal energy. Equation 4.7 shows that $\dot{S}_{gen,d}$ is dependent on the turbulence eddy dissipation rate, ϵ, the rate at which the energy of larger eddies dissipates into smaller eddies until it is fully converted to thermal internal energy.

$$\dot{S}_{gen,d} = \frac{\rho\epsilon}{T} \tag{4.7}$$

Figure 4.18 shows the contour plots of the entropy generation due to turbulence dissipation, $\dot{S}_{gen,d}$ at 8 different streamwise locations for the high efficiency and low efficiency designs. The flow structures discussed in Fig. 4.17 correspond in Fig. 4.18 to the high $\dot{S}_{gen,d}$ regions, highlighted with dotted lines.

Tip leakage results in high $\dot{S}_{gen,d}$ at the region close to the suction surface tip in both designs. In the high efficiency design, all the tip leakage flow forms a strong vortex from the leading to the trailing edge and it is the main contributor to entropy generation due to turbulence dissipation, as shown in Fig.4.18 (a).

The low efficiency design, the tip leakage vortex is weaker as it only takes leakage flow from around 30% chord to the trailing edge, as shown in Fig. 4.17 (b). This translates into smaller area of high entropy generation at the suction surface tip compared to the high efficiency design, as shown in contours in Fig. 4.18. This agrees with the finding that the overall entropy generation rate at the tip is lower in the low efficiency design, shown in Fig. 4.16. Suction surface separation and tip leakage flow from the leading edge up to 30% chord results in entropy generation corresponding to the suction surface vortex. $\dot{S}_{gen,d}$ contours in 4.18 (b) suggest that the suction surface vortex dissipates around 75% chord length. This has a huge impact on suction surface overall entropy generation in the low efficiency design, as discussed earlier in Fig. 4.16.

Entropy generation and flow field analysis give an insight into the difference in performance between designs. Moreover, the quantitative CFD loss breakdown helps focus the design efforts on those regions that lead to higher losses.

4.4 Chapter Summary

This chapter investigates different aspects of turbine design ORC application with a focus on rotor geometry. The design process was based on two strategies applying

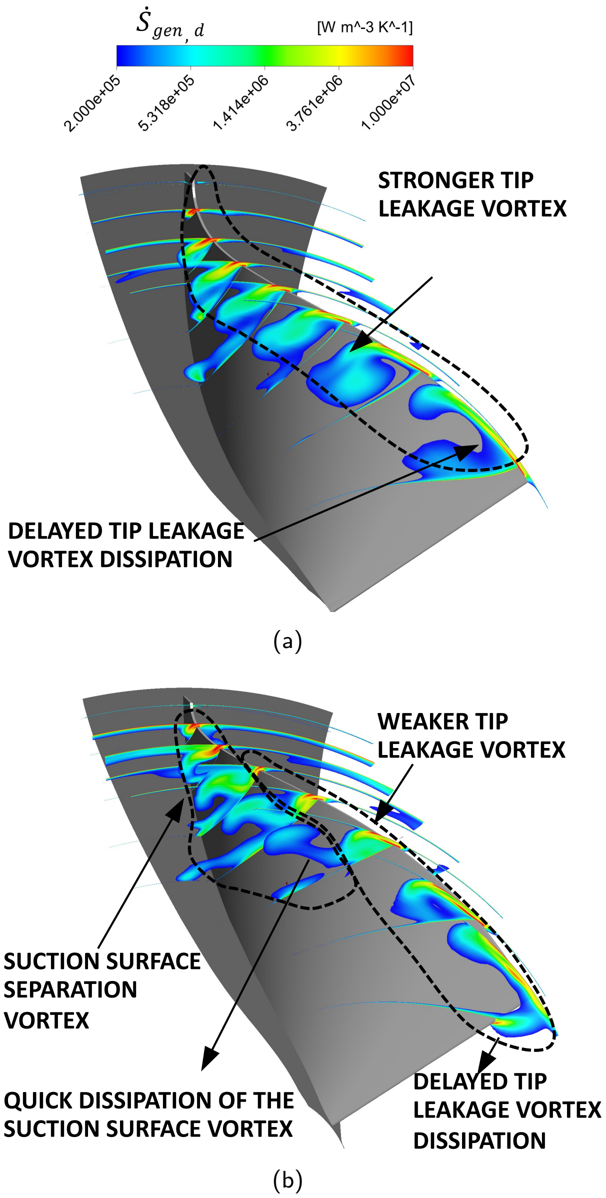

Figure 4.18: Turbulent dissipation rate contours at different streamwise locations in (a) high efficiency design (b) low efficiency design

differential evolution single-objective optimisation: meanline model and 3D parametric model with CFD evaluation.

The meanline model was successfully calibrated with high fidelity CFD data. The average deviation in efficiency was found to be 3.8 pp.

A first optimisation of the meridional geometry, nozzle and rotor blade angles and rotational speed was carried out with total-to-static efficiency as the objective function using the meanline and CFD-based approaches separately. The low order model provided an optimised geometry with lower efficiency ($\eta_{ts,meanline} = 79.98\%$) than the CFD-based optimum configuration ($\eta_{ts,CFD} = 81.29\%$). The optimum geometries obtained with the two approaches were different, as well as the correlation of some design parameters with efficiency. This suggests some limitations on low-order modelling, specially on loss correlations. Future comparison of the meanline loss distribution with the CFD loss breakdown may be helpful to overcome this limitation.

A second CFD-based optimisation of the hub and shroud cone angles at the rotor leading and trailing edge was carried out to determine the effect of 3D geometry modifications while keeping the same meridional geometry, nozzle and rotor blade angles and rotational speed. The efficiency difference between the best and worst designs during the optimisation was as high as 2.1 pp, while the efficiency predicted by the meanline model is the same (due to the same meridional profile, angles and rotational speed). This highlights the limitations of meanline modelling in predicting efficiency of different configurations, when the geometry modifications are outside the meanline design parameters.

Entropy generation and loss breakdown analysis was carried out for two geometries with different hub and shroud contours. The flow field was also analysed, explaining the efficiency difference between the two geometries analysed in more detail.

The same methodology and analysis were carried out for the design of the ETC turbine, looking in more detail at non-radial fibre parameters. This is explained in the following chapter.

Chapter 5

Electric Turbocompunding Turbine Design

This chapter presents the sensitivity analysis and optimisation of the radial fibre and non-radial fibre rotor geometries following the methodology outlined in Chapter 3 applied to electric turbo-compounding (ETC). The meanline model is calibrated with CFD results. The accuracy of the meanline model when predicting turbine efficiency and mass flow is targeted first, whilst a second calibration is carried out to improve the prediction of loss distribution across the rotor.

The sensitivity of the calibrated meanline model and the parametric CFD-based methodology is analysed to evaluate the influence of the design parameters on the efficiency of radial fibre turbines. Optimised ETC turbine designs for the application of study were obtained with both approaches.

Once an optimised baseline radial fibre design is obtained, the effect of additional 3D parameters that allow for non-radial fibre blading design is investigated. The parametric model coupled with CFD computations allow for a detailed analysis of the performance and flow field of non-radial fibre designs.

In addition, an experimental evaluation of the optimised geometries was carried out and compared with the CFD analysis of the losses and flow structures, for complementary validation.

5.1 Meanline Model Calibration

Similar to the previous chapter, the meanline model was also calibrated for the ETC application. ETC operating conditions are substantially different from ORC, since the working fluid is air and the pressure ratio is set to 1.2. A near-random set of 20 different geometries was generated using the Latin Hypercube Algorithm (LHA) in CAESES.

The calibration algorithm aims to improve the accuracy of the meanline model when predicting efficiency and mass flow values. This is done by calculating the difference, or error, between the predictions obtained by the meanline model and those obtained using computational fluid dynamics (CFD).

The algorithm seeks to minimise this error, defined as the relative root mean squared error (RRMSE), for both efficiency and mass flow. To achieve this, the algorithm employs a multi-objective genetic algorithm, which adjusts the values of the loss coefficients through an iterative process. The algorithm runs for a total of 80 generations, considering a population of 160 designs. Once this iterative process finishes, the pareto front is obtained, as shown in Fig. 5.1 (a). The convergence of the algorithm is tracked using a metric called hypervolume, shown in Fig. 5.1 (b). This parameter, explained in more detail during the ORC calibration of Chapter 4, measures the convergence and the quality of the optimisation result in terms of proximity of the function evaluations to the Pareto front and how evenly distributed and spread the data is.

The Pareto front is a visual representation of the multiple possible solutions that show a minimal difference between efficiency and mass flow predictions using meanline modelling and CFD. To determine a single solution, weights can be applied to evaluate the overall error using the equation introduced in Chapter 4 and repeated here for clarity in Eq. 5.1.

$$F_{solution} = min\{w_{\eta_{ts}} RRMSE_{\eta_{ts}} + w_{\dot{m}} RRMSE_{\dot{m}}\} \tag{5.1}$$

In this case, equal weights of 0.5 were assigned to both efficiency and mass flow root mean squared error (RRMSE). The set of loss coefficients that resulted in the lowest overall RRMSE was then selected as the solution for the calibration process and is summarised in Table 5.1.

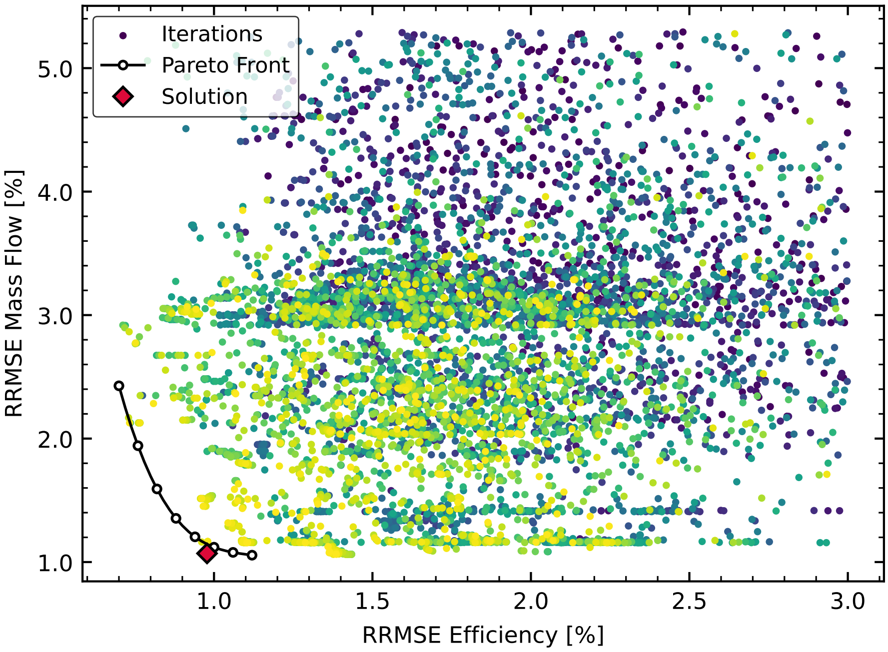

(a)

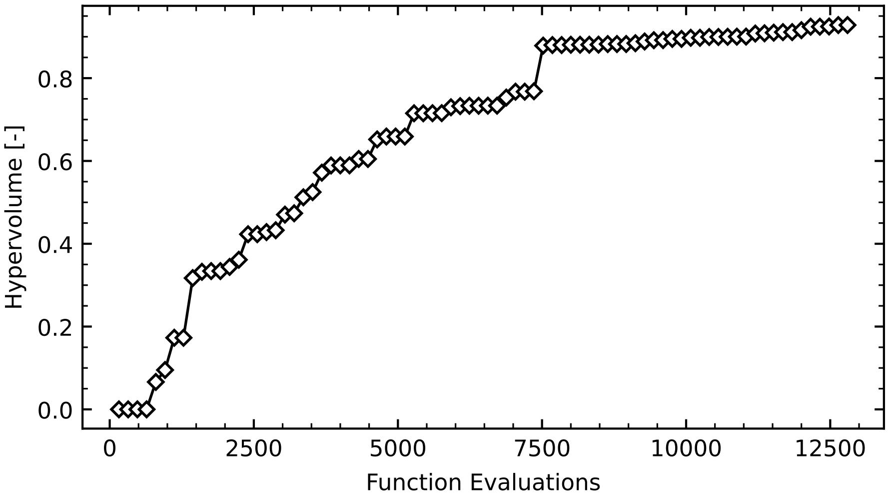

(b)

Figure 5.1: (a) Multi-objective calibration showing: (a) calibration iterations and the Pareto front and the solution obtained (colour map from blue to yellow indicates older to newer iterations, respectively) and (b) hypervolume monitoring with calibration iterations for the first calibration with efficiency and mass flow

The RRMSE in efficiency and mass flow after calibration was 0.98% and 1.09%, respectively. This corresponded to an average deviation of 1.3 pp in efficiency and 1.2% in mass flow of the set of data taken for calibration. Analysing the full set of CFD data, total-to-static efficiency and mass flow deviation measured in percentage points difference, pp, and relative deviation, were found to be 3.6 pp and 3.8%, respectively. The efficiency RRMSE was 2.9%, while the mass flow RRMSE was 3.1%. Figure 5.2 shows the comparison of efficiency and mass flow results for the full set of CFD data (x-axis) and the corresponding meanline prediction (y-axis).

Table 5.1: Loss coefficients after the first calibration

K_n	K_{inc}	K_p	K_{cl}	B_2	B_4	B_6
0.4	0.05	0.49	1.03	0.99	1.0	0.98

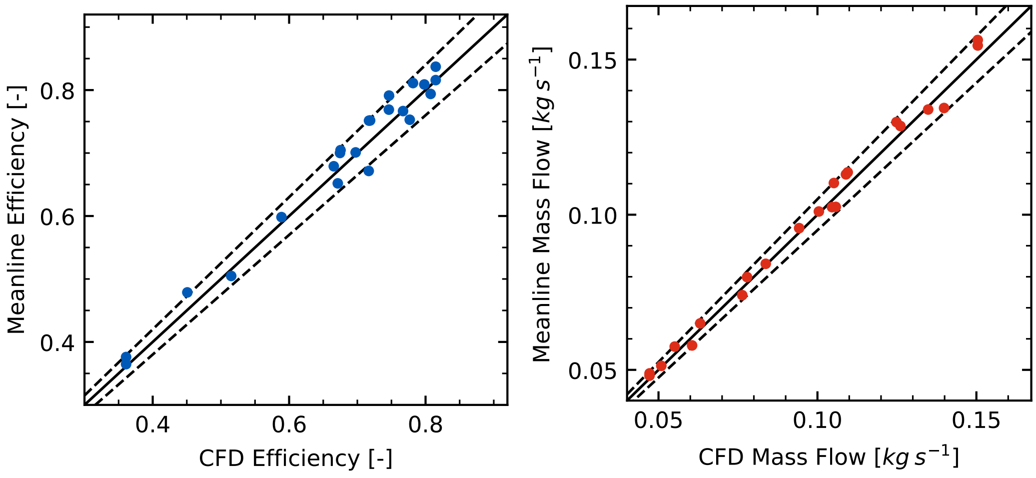

(a) (b)

Figure 5.2: Comparison between meanline and CFD (a) efficiency and (b) mass flow after meanline model calibration for the whole sample

The meanline model is able to predict the trends in performance when compared to CFD data. This supports the accuracy of the low order model. In the following section, the breakdown of losses will be examined to determine if the meanline model accurately reflects the actual loss mechanisms present in a ETC turbine.

5.1.1 Loss Breakdown for Calibration

To assess the accuracy of the loss breakdown of the meanline model, 5 representative geometries from the sample were selected and analysed in more detail. The CFD domain was divided into several regions and entropy generation in each region was attributed to a specific loss mechanism. Similarly to the previous chapter, the loss breakdown from the meanline model and the loss breakdown from the CFD results were compared. The CFD prediction of the loss distribution was taken from the entropy generation across the different regions in which the turbine domain was divided, according to Fig. 4.5.

Figure 5.3 shows the entropy generation breakdown, equivalent to the loss distribution, and the total-to-static efficiency of the 5 selected designs. As expected, higher efficiency designs are associated with lower entropy generation. Design A shows the highest efficiency and lowest entropy generation, while design E shows the opposite, lowest efficiency and higher entropy generation.

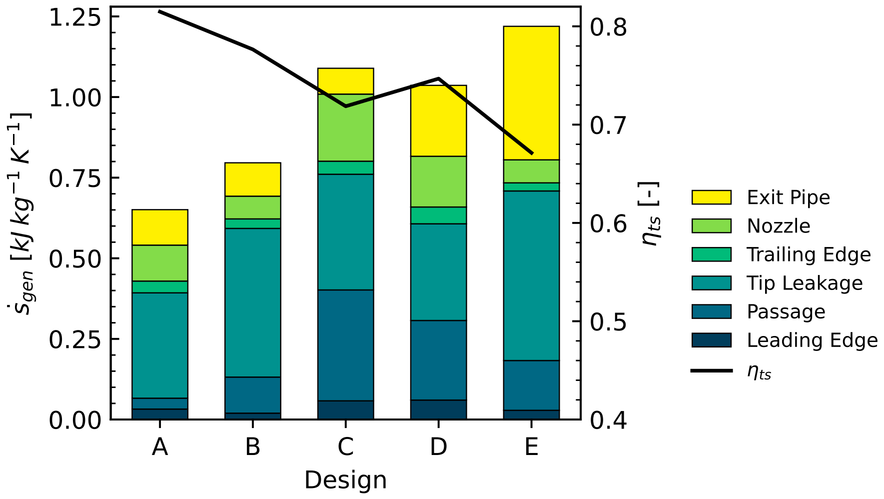

Figure 5.3: Entropy generation per unit mass calculated in each region of the CFD domain and assigned to each loss mechanism (left axis) and total to static efficiency (right axis) for 5 different geometries

Focusing on the rotor only, the comparison between the loss distribution predicted by CFD and calculated by meanline after the first calibration is presented in Fig. 5.4. Incidence and trailing edge losses are accurately predicted by meanline, since the share of these loss mechanisms into the overall losses across the rotor is similar to the CFD results. However, passage losses are significantly overpredicted, while tip leakage losses are severely underpredicted using meanline modelling after the first calibration.

A second calibration taking into account the loss distribution across the rotor was carried out to test if it was possible to improve the physical accuracy of the meanline model. The objective function was defined by the RRMSE for efficiency, mass flow and each

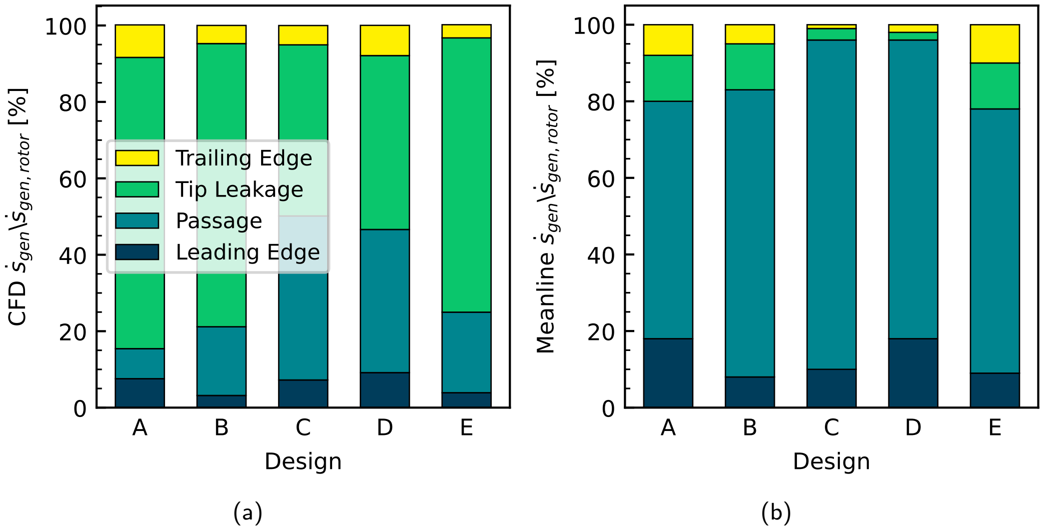

Figure 5.4: Loss breakdown in the rotor for 5 different designs calculated via: (a) CFD and (b) meanline using the first set of loss coefficients

contribution of incidence, passage and tip clearance losses to the rotor loss. The multi-objective function was introduced in Chapter 4 but it is repeated here for clarity, Eq. 5.2.

$$F_{obj} = \{RRMSE_{\eta_{ts}}, RRMSE_{\dot{m}}, RRMSE_{\%L_{inc}}, RRMSE_{\%L_{pas}}, RRMSE_{\%L_{tc}}\} \tag{5.2}$$

During the second calibration, 40 generations with a population size of 80 designs were sufficient to fulfill the convergence criteria, as shown in the hypervolume results in Fig. 5.5. The loss coefficients resulting after the second calibration are summarised in Table 5.2.

Table 5.2: Loss coefficients after the second calibration

K_n	K_{inc}	K_p	K_{cl}	B_2	B_4	B_6
0.42	0.12	0.13	2.15	0.98	1.0	0.97

The comparison of loss distribution across the rotor between the CFD results and the meanline prediction after the second calibration is shown in 5.6. There is a clear improvement in the loss distribution prediction by meanline using the second set of loss coefficients, compared to the prediction using the first calibration (shown in Fig. 5.4).

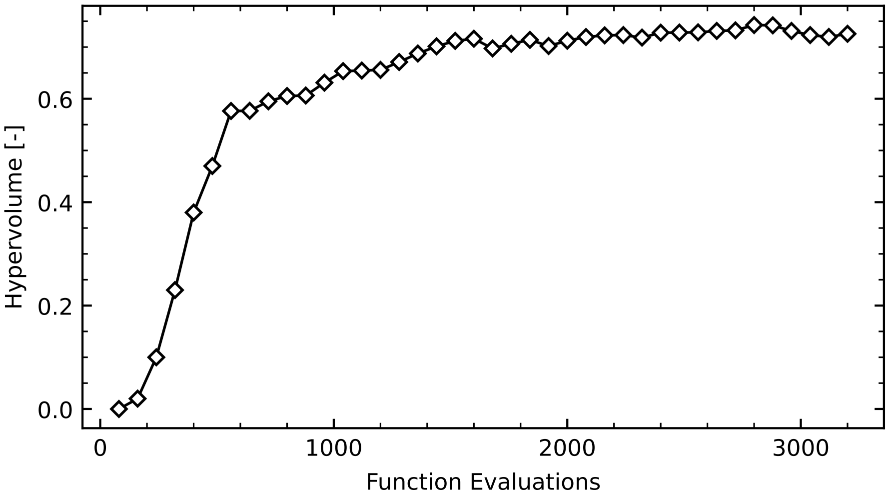

Figure 5.5: Hypervolume monitor of the second calibration showing convergence

Although incidence losses are slightly overpredicted by meanline, the model is able to predict trends in the contribution of this loss mechanisms. For example, CFD results in Fig. 5.6 indicate that design A has higher incidence losses than design B and this trend is captured by meanline shown in Fig. 5.6. The contribution of passage losses predicted by meanline (refer to Fig. 5.6 (b)) is close to the CFD results in Fig. 5.6 (a), particularly in low efficiency designs, design C, design D and design E. However, passage loss contribution is overpredicted by meanline in high efficiency designs, design A and design B. A better loss breakdown prediction comes at the expense of a less accurate prediction of efficiency. The RRMSE of efficiency after the second calibration was found to be 3.6%, higher that the RRMSE of the first calibration. Mass flow RRMSE after the second calibration was 3.2%, a value close to the first calibration.

Due to the impossibility of matching the loss breakdown of the meanline prediction to the loss breakdown provided by CFD without penalising the efficiency prediction, the loss coefficients used in the meanline model calculations for the following sections of this chapter are based on the initial calibration. The first calibration only considered the error in efficiency and mass flow as part of the objective function, without taking into account the loss breakdown obtained through CFD.

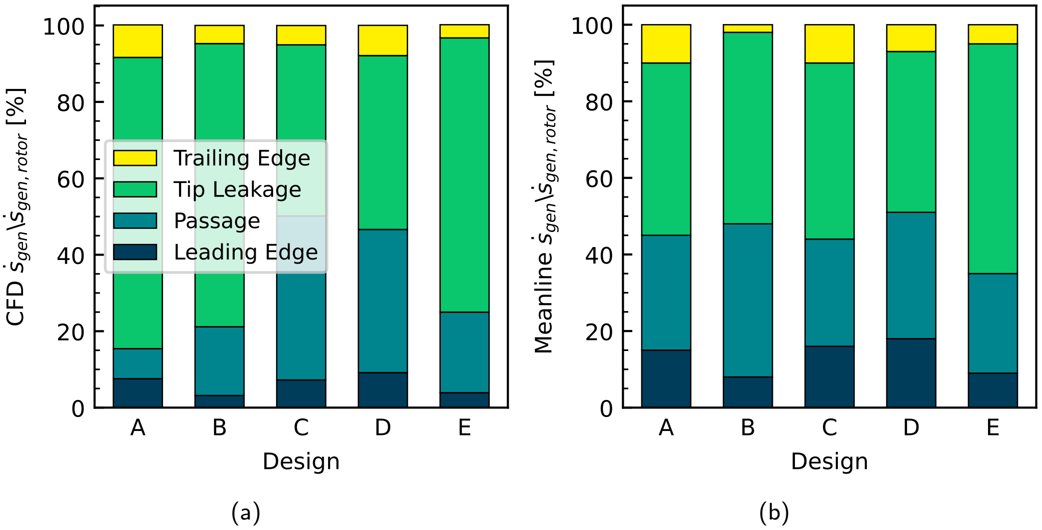

(a) (b)

Figure 5.6: Loss breakdown in the rotor for 5 different designs calculated via: (a) CFD and (b) meanline using the second set of loss coefficients

5.2 Sensitivity Analysis and Optimised Radial Fibre Geometry

The sensitivity study based on the sampling to create the response surface for optimisation shows interesting results. Figure 5.7 summarises the effect of each design parameter on efficiency, Fig. 5.7 (a) shows a clear correlation of increasing efficiency with increasing r_4. Other parameters determining the geometry of the rotor outlet, $\frac{r_{6s}}{r_4}$ and $\frac{r_{6h}}{r_4}$, have only a small effect on efficiency, as shown in Fig. 5.7 (b) and (c), leading to slightly higher performance for high values of $\frac{r_{6s}}{r_4}$.

Figure 5.7 (d) describes the effect of $\alpha_{nozzle,4}$ on efficiency, showing better performance for lower values of $\alpha_{nozzle,4}$. The correlation of $\beta_{blade,6}$ with efficiency, shown in Fig. 5.7 (e), is not as clear as the correlation of other parameters, since high efficiency designs are achieved with a wide range of blade angles at the trailing edge, from $-70°$ to $-50°$. Finally, Fig. 5.7 (f) shows an optimum region of $Nrpm$ for high efficiency, around 30,000 rpm.

The global optimisation carried out from the response surface resulted in the geometry summarised in Table 5.3. This geometry is set as the radial fibre baseline design from which the non-radial fibre blading investigation is carried out.

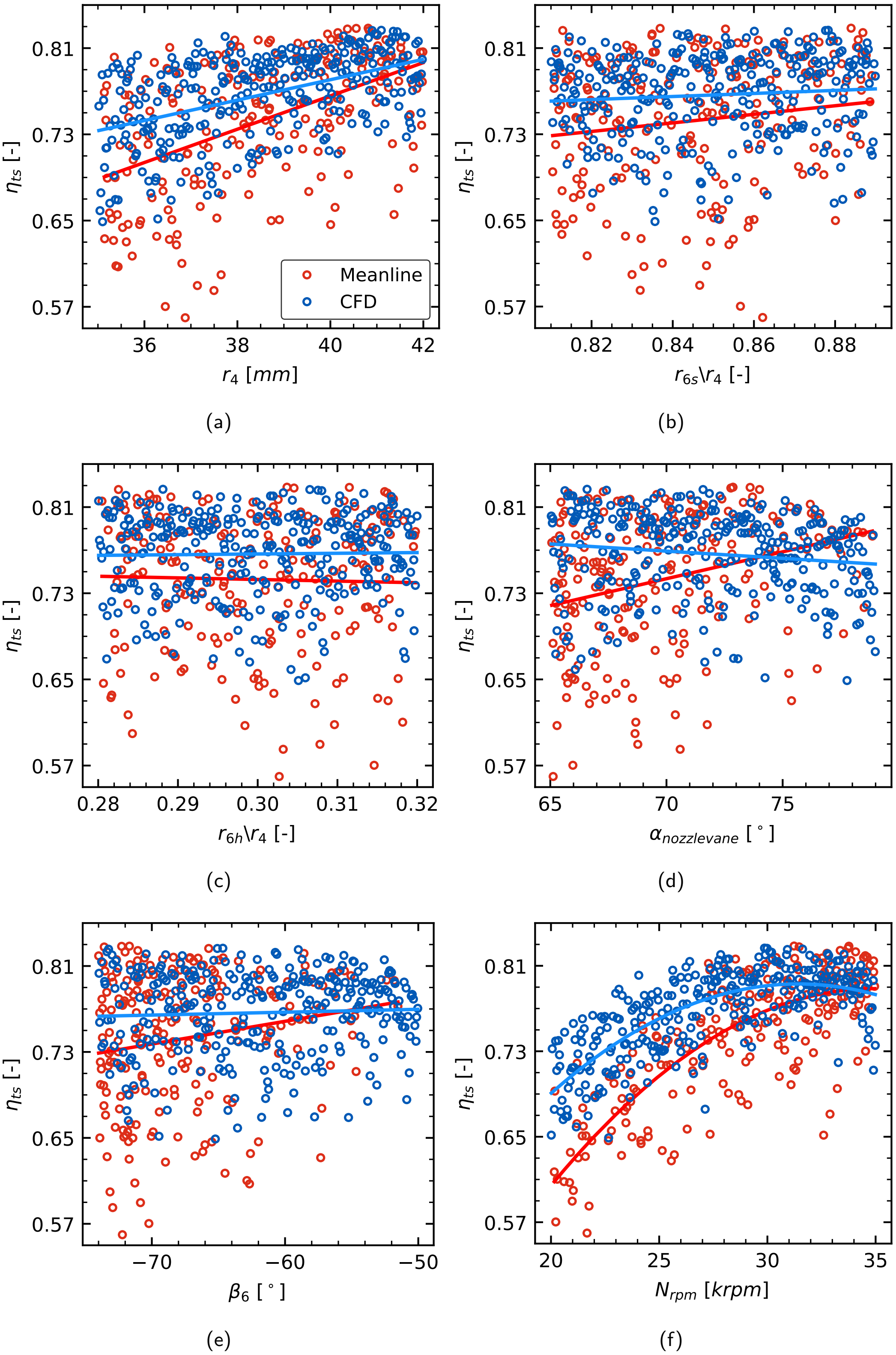

Figure 5.7: Sensitivity analysis of total-to-static efficiency as function of (a) rotor wheel radius,r_4, (b) rotor shroud radius to wheel radius ratio, $\frac{r_{6s}}{r_4}$, (c) rotor hub radius to wheel radius ratio, $\frac{r_{6h}}{r_4}$ (d) nozzle vane metal angle $\alpha_{nozzlevane}$, (e) rotor blade metal angle at trailing edge, $\beta_{blade,6}$, (f) rotational speed $Nrpm$ and fitting curves for meanline (red) and CFD-based (blue) sampling

Table 5.3: Optimised meridional geometry and design space for meanline and CFD.

Parameter	Meanline	CFD-based
Optimisation Variables		
r_4 $[mm]$	40.82 [35.0-42]	40.83 [35.0-42]
$Nrpm$ $[krpm]$	31 [20-50]	30 [20-50]
$\frac{r_{6s}}{r_4}$ $[-]$	0.88 [0.81-0.89]	0.88 [0.81-0.89]
$\frac{r_{6h}}{r_4}$ $[-]$	0.30 [0.28-0.32]	0.31 [0.28-0.32]
$\alpha_{nozzlevane}$ $[°]$	72.86 [65.0-79.0]	65.9 [65.0-79.0]
β_{blade6} $[°]$	-71.6 [-75.0- -50.0]	-66.98 [-75.0- -50.0]
Fixed Parameters		
Number of blades	11	11
Number of vanes	19	19
Tip clearance $[mm]$	0.5	0.5
Z_r $[mm]$	24.2	24.2
Results		
η_{ts} $[\%]$	82.86	82.93
b_4 $[mm]$	8.52	7.39
MFP $[kgs^{-1}K^{0.5}Pa^{-1}]$	1.92e-5	1.93e-5
Number of geometries	800	200

5.3 Sensitivity Analysis and Optimised Non-radial Fibre Geometry

After the radial fibre geometry was optimised, the blade is modified to investigate the effect of non-radial fibre parameters. The radii and rotational speed are kept constant to limit the number of variables for optimisation. A sensitivity study was carried out as part of the surface response for the optimisation of the non-radial fibre parameters, with this the impact of each parameter on efficiency can be assessed.

The results of this analysis are summarised in Fig. 5.8. An optimum $\alpha_{nozzle,3}$ around $68°$ can be guessed from the correlation of this parameter with efficiency, as shown in Fig. 5.8(a). This trend is possibly the result of the effect of $\alpha_{nozzle,3}$ on the incidence angle. The incidence angle, i, is the difference between the flow angle into the rotor in the relative frame of reference, $\beta_{flow,4}$ and the blade angle at the leading edge, $\beta_{blade,4}$.

Optimum incidence, around $-20°$ to $-40°$ as reported in the literature [18], leads to low leading edge losses and high efficiency. Assuming there is no deviation and the free vortex effect in the interspace is negligible, $\alpha_{nozzle,3}$ is equal to the flow angle into the rotor in the absolute frame of reference, $\alpha_{flow,4}$. In this way, the incidence angle can be expressed using velocity triangles [18], as indicated in Eq. 5.3. Contrarily to $\alpha_{nozzle,3}$, $\beta_{blade,4}$ seems to have small correlation with efficiency (Fig. 5.8(b)).

$$i = \beta_{flow,4} - \beta_{blade,4} = \tan^{-1}\left(\frac{C_4 \sin\alpha_{flow,4} - U_4}{C_4 \cos\alpha_{flow,4}}\right) - \beta_{blade,4} \tag{5.3}$$

Other parameters show a strong correlation with efficiency, $\gamma_{upper,TE}$ and ν_{TE}, as shown in Fig. 5.8 (c) and (d), respectively. Lower ν_{TE} and higher $\beta_{shourd,TE}$ lead to high performance. γ_{lower} had minimum impact on efficiency, as the fitting curves are flat for the leading edge and trailing edge shown in Fig. 5.8 (e) and (f).

The results of the sensitivity analysis were used for the optimisation. Table 5.4 summarises the values of the non-radial fibre parameters and the resulting efficiency and MFP of the optimised geometry. The radii and rotational speed were the same as the radial fibre optimised geometry presented in the previous section and summarised in Table 5.3.

The camberline of both the radial design and non-radial fibre design are shown in Fig. 5.9. The radial fibre blade is defined by a single camberline, while the projection of the blade of the non-radial fibre design with planes at different span locations result in different camberline curves.

The achieved η_{ts} of the non-radial fibre design was +0.27 pp higher than the radial fibre design performance. The MFP also increased by 5.18%. In order to understand and validate the small performance improvement of the non-radial fibre blade design compared to the radial fibre baseline, experimental tests were carried out. The analysis and results of this experimental campaign are described in Section 5.5.

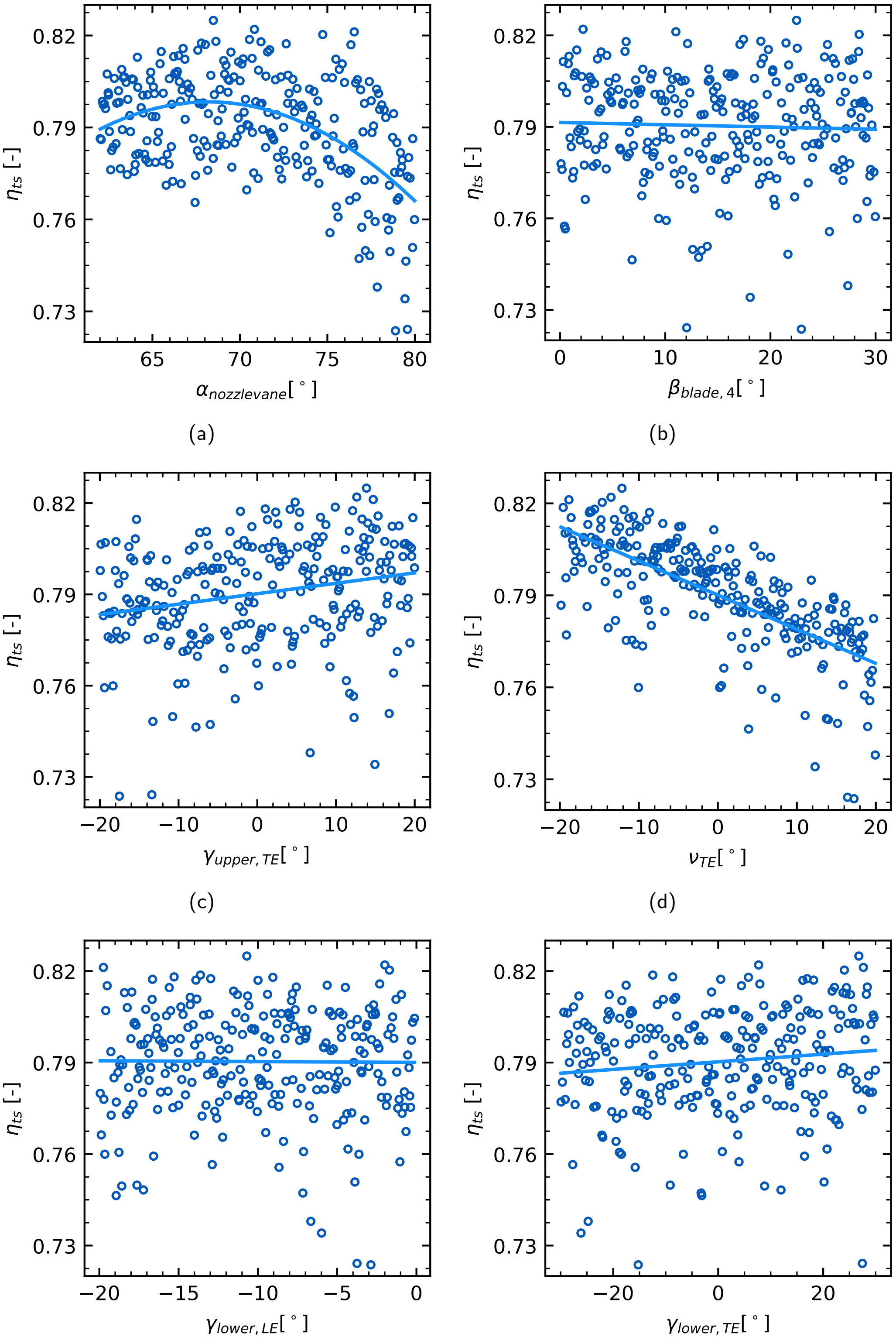

(a) (b)

(c) (d)

(e) (f)

Figure 5.8: Sensitivity analysis of η_{ts} as function of (a) nozzle vane metal angle nozzle vane, $\alpha_{nozzle,4}$, (b) rotor blade metal angle at the leading edge, $\beta_{blade,4}$, (c) tangential angle of the non-radial fibre at the upper end with the leaned straight fibre at trailing edge, $\gamma_{upper,TE}$, (d) lean angle at the trailing edge, ν_{TE} and tangential angle of the non-radial fibre at the lower end with the leaned straight fibre at (e) the leading edge, $\gamma_{lower,LE}$, and (f) the trailing edge, $\gamma_{lower,TE}$ and fitting curves (solid line) for CFD-based sampling

Table 5.4: Optimised non-radial fibre geometry and design space based on the CFD approach

Parameter	CFD-based
Optimisation Variables	
$\alpha_{nozzle,4}$ $[^{\circ}]$	70.23 [62.0-80.0]
β_{blade4} $[krpm]$	24.02 [0.0-30.0]
$\gamma_{upper,TE}$ $[^{\circ}]$	0.29 [-20.0-20.0]
ν_{TE} $[^{\circ}]$	-9.66 [-20.0-20.0]
$\gamma_{lower,LE}$ $[^{\circ}]$	14.05 [-20.0-0.0]
$\gamma_{lower,TE}$ $[^{\circ}]$	19.47 [-30.0-30.0]
Fixed Parameters	
Number of blades	11
Number of vanes	13
Tip clearance $[mm]$	0.5
Z_r $[mm]$	24.2
Results	
η_{ts} $[\%]$	83.20
b_4 $[mm]$	8.93 [>2.00]
MFP $[kgs^{-1}K^{0.5}Pa^{-1}]$	2.03e-5
Number of geometries	200

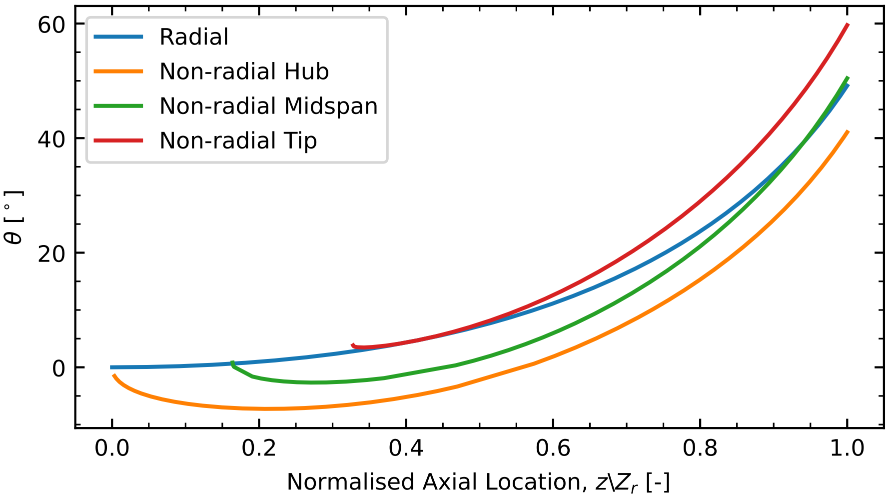

Figure 5.9: Comparison of the camberlines for the radial fibre blade and non-radial fibre blade at three different span locations

5.4 Losses and CFD Analysis

In order to further analyse and explain the difference in performance between the two designs, the entropy generation across the different components was calculated, as an indication of energy losses. The losses at the turbine stage, Δh_{loss}, are proportional to the entropy change, Δs, across the turbine [128]. The entropy generation of an adiabatic process, such as a fluid expansion in a turbine, can be regarded as the entropy change across the turbine, according to Eq. 5.4 [123]:

$$dW_{loss} = Td\dot{S}_{gen} = T\left((sd\dot{m})_{out} - (sd\dot{m})_{in}\right) \tag{5.4}$$

Total-to-total efficiency, unlike total-to-static, assumes by definition that all the exit energy is recovered; therefore this efficiency definition is more useful when comparing designs in a complete stage [18]. The expansion process of a perfect gas between two states is shown in the T-s chart of Fig. 5.10. The blue line describes the actual expansion process, while the green line shows the ideal, isentropic process.

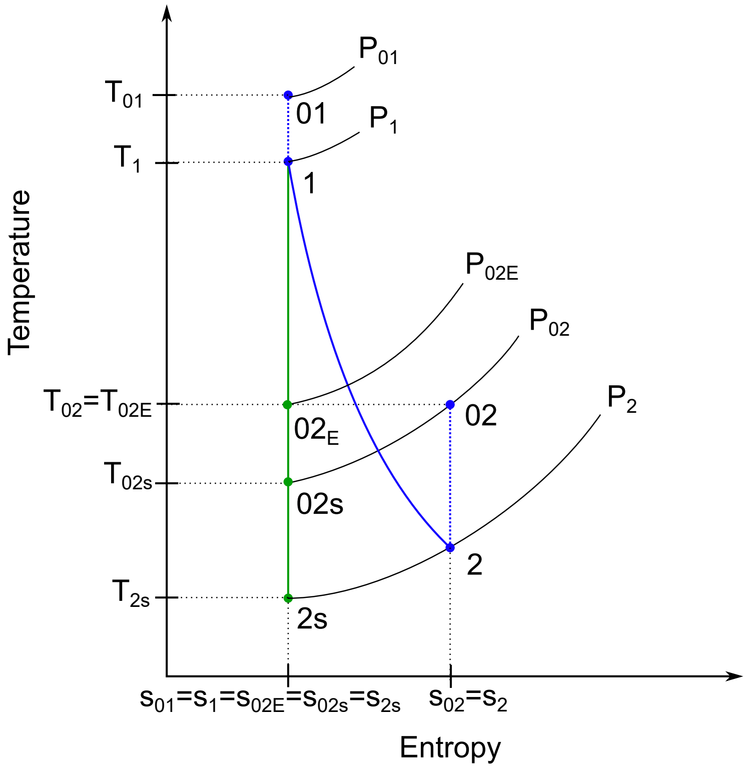

Figure 5.10: Thermodynamic T-s chart of an expansion process

The total-to-total efficiency depends exponentially on the entropy increase across the stage, the derivation of the equation is as follows. Considering the adiabatic expansion of a perfect gas between states 1 and 2, the entropy generated can be calculated from Eq. 5.5:

$$\dot{S}_{gen} = \dot{m} s_{gen} = \dot{m}\Delta s = \dot{m}\left(s_2 - s_1\right) = \dot{m}\left(c_p \cdot ln\left(\frac{T_2}{T_1}\right) - Rln\left(\frac{P_2}{P_1}\right)\right) \tag{5.5}$$

Looking at the T-s chart in Fig. 5.10, $s_2 - s_1$ is equal to $s_{02} - s_{01}$, which leads to Eq. 5.6. In the same chart, the entropy change in the isentropic process between 01 and 02E, can be modelled according to Eq. 5.7. State 02E is the equivalent isentropic state at the same temperature as state 02. This state is defined only for derivation purposes and does not correspond to a real physical state during the expansion process.

$$s_2 - s_1 = s_{02} - s_{01} = c_p \cdot ln\left(\frac{T_{02}}{T_{01}}\right) - Rln\left(\frac{P_{02}}{P_{01}}\right) \tag{5.6}$$

$$s_{02E} - s_{01} = c_p \cdot ln\left(\frac{T_{02E}}{T_{01}}\right) - Rln\left(\frac{P_{02E}}{P_{01}}\right) = 0 \tag{5.7}$$

Considering that $T_{02E} = T_{02}$, $s_{02E} = s_{01}$ and combining Eq. 5.6 and Eq. 5.7,

$$s_2 - s_1 = s_{02} - s_{01} = Rln\left(\frac{P_{02E}}{P_{02}}\right) \rightarrow \frac{P_{02E}}{P_{02}} = e^{\frac{\Delta s}{R}} \tag{5.8}$$

The total-to-total efficiency can be defined as the ratio between the actual and isentropic total-to-total power, which is equal to the ratio of the total temperature difference for a perfect gas. Dividing this equation by T_{02s} and combining using the isentropic relation and $T_{02E} = T_{02}$, gives Eq. 5.9:

$$\eta_{tt} = \frac{\dot{W}_{act}}{\dot{W}_{iso,tt}} = \frac{T_{01} - T_{02}}{T_{01} - T_{02s}} = \frac{\frac{T_{01}}{T_{02s}} - \frac{T_{02E}}{T_{02s}}}{\frac{T_{01}}{T_{02s}} - 1} = \frac{\left(\frac{P_{01}}{P_{02}}\right)^{\frac{n-1}{n}} - \left(\frac{P_{02E}}{P_{02}}\right)^{\frac{n-1}{n}}}{\left(\frac{P_{01}}{P_{02}}\right)^{\frac{n-1}{n}} - 1} \tag{5.9}$$

Combining Eq. 5.8 and Eq. 5.9 leads to the final expression relating the η_{tt} and the

Δs in Eq. 5.10, where PR_{tt} is the total-to-total pressure ratio across the expansion process.

$$\eta_{tt} = \frac{(\frac{P_{01}}{P_{02}})^{\frac{n-1}{n}} - e^{\frac{\Delta s}{R}\frac{n-1}{n}}}{(\frac{P_{01}}{P_{02}})^{\frac{n-1}{n}} - 1} = \frac{PR_{tt}^{\frac{n-1}{n}} - e^{\frac{\Delta s}{R}\frac{n-1}{n}}}{PR_{tt}^{\frac{n-1}{n}} - 1} \tag{5.10}$$

Furthermore, the rotor domain was divided into several regions and the entropy generation across each of them was assigned to a different loss mechanism, the regions were summarised in Chapter 4 and highlighted in Fig. 4.5. The loss breakdown, as entropy generated per unit mass flow, across the rotor and the other components is shown in Fig. 5.11.

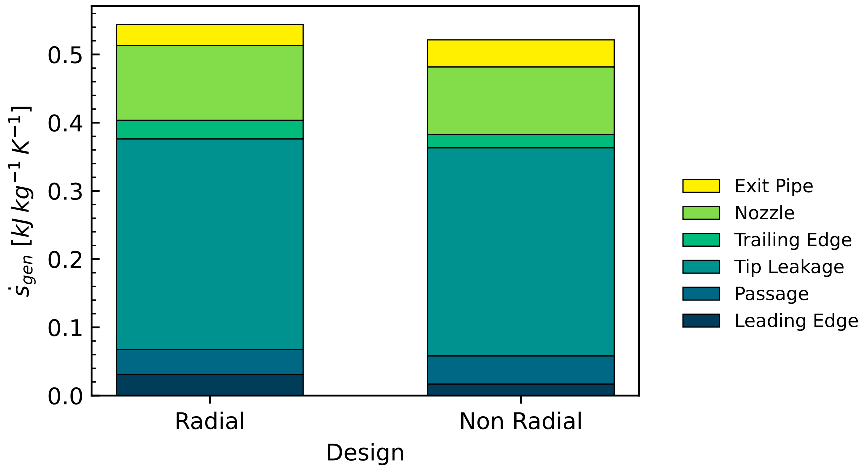

Figure 5.11: Distribution of the entropy generation per unit mass flow for the radial fibre and non-radial fibre designs

Overall, the entropy generation across the whole turbine was lower for the non-radial fibre design, Fig. 5.11, in agreement with the resulting higher efficiency. When comparing the non-radial fibre design to the radial fibre design, exit duct and passage losses increased 22% and 11%, respectively; tip leakage losses remain the same and nozzle, trailing edge and leading edge losses decreased by 11%, 39% and 80% respectively.

The decrease in the leading edge losses is possibly the results of to a better alignment of the flow with optimum incidence angle. From an aerodynamic point of view, the optimum incidence angle lies between -20 and -40 degrees [18]. Figure 5.12 shows the incidence angle at the rotor inlet for the radial fibre and non-radial fibre designs.

As described in Eq. 5.3, incidence depends on the relative angle of the flow when approaching the leading edge and the blade angle at the leading edge. Figure 5.12 (b) shows a lower (more negative) incidence angle for the non-radial fibre design compared to the radial fibre design shown in Fig. 5.12 (a). The average incidence for the radial fibre design was $i_{radialf} = -20.45^{\circ}$ and the non-radial fibre design had an average incidence of $i_{non-radialf} = -46.73^{\circ}$. Lower incidence (more negative) seemed to reduce the entropy generation at the rotor leading edge and limit the flow separation in this region.

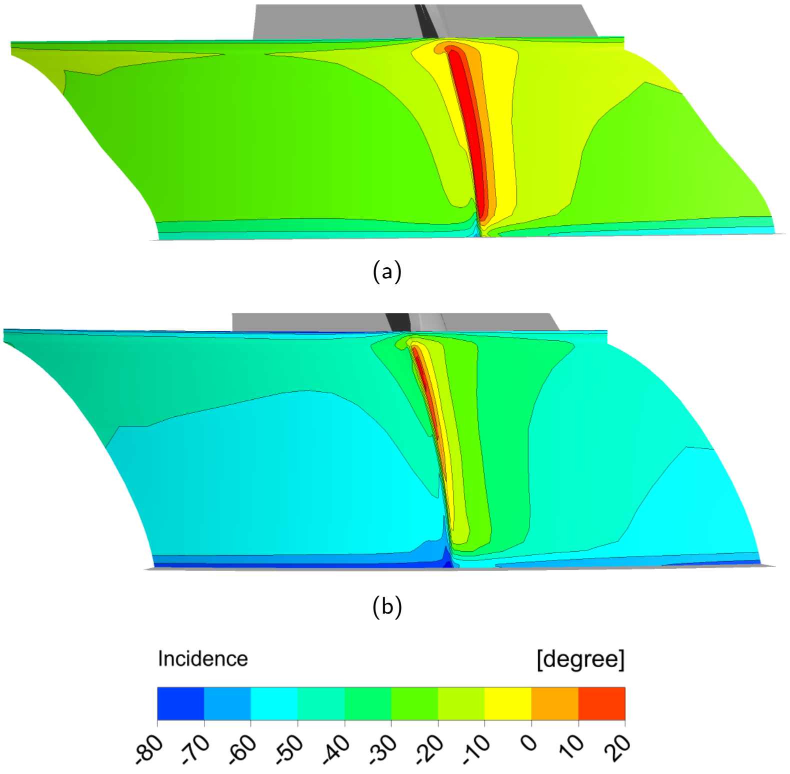

(a)

(b)

(c)

Figure 5.12: Incidence angle at the leading edge of the (a) radial fibre and (b) non-radial fibre designs

As indicated in Eq. 5.10, η_{tt} can be linked to the entropy change. If applied to rotor only, Eq. 5.11 shows the relation between the $\eta_{tt,rotor}$ with the total-to-total pressure ratio across the rotor, $\frac{P_{04}}{P_{06}}$, and the specific entropy change across the rotor, Δs_{rotor}, which corresponds to the entropy generation per unit mass for adiabatic processes discussed in Fig. 5.11(b). Comparing the total-to-total efficiency of the two designs, the non-radial fibre rotor achieved a $\eta_{tt,rotor} = 90.07\%$, 0.3pp higher than the radial fibre rotor. Since the pressure ratio across the rotor remained constant for the two geometries, the reduction in entropy generation was the only factor explaining the increase in $\eta_{tt,rotor}$.

$$\eta_{tt,rotor} = \frac{\dot{W}_{act}}{\dot{W}_{iso,tt,rotor}} = 1 - \frac{\Delta h_{ROTOR}}{c_p T_{04}\left(1 - \frac{P_{04}}{P_{06}}^{-\frac{n-1}{n}}\right)} = \frac{\frac{P_{04}}{P_{06}}^{\frac{n-1}{n}} - {e^{\frac{\Delta s_{rotor}}{R}}}^{\frac{n-1}{n}}}{\frac{P_{04}}{P_{06}}^{\frac{n-1}{n}} - 1} \tag{5.11}$$

Reduction in entropy generation implies reduction in losses and therefore, higher actual power recovered in the rotor. The increase in actual power in the non-radial fibre design can also be observed when compared to the blade loading as shown in Fig. 5.13. The blade loading of the non-radial fibre improves at the midspan and tip, as indicated by the arrows in Fig. 5.13(b) and (c). The blade loading increase occurs at the leading edge and at the middle of the passage. Higher loading means higher power recovered which increases the efficiency of the turbine.

The flow field analysis of the two optimum designs with radial and non-radial blading, was explained based on CFD results. These numerical results are supported by experimental data obtained from the actual designs. A summary of the experimental results is included in the next section.

5.5 Experiments Results

The experimental results of this study were obtained in the turbine test facility at Imperial College London, Fig. 5.14 (a). A detailed description of this experimental facility can be found in Chapter 3 and in the literature [129]. The turbine geoemtries were scaled down to fit in the test rig. The scaled-down wheel radius, r_4, was set to $38mm$, which effectively leads to a scale factor of 0.93 for all the linear dimensions. Angles were kept constant.

Total-to-static efficiency is calculated as the ratio between the actual power and the isentropic power, as shown in Eq. 5.12. The actual power of the turbine, $\dot{W}_{act}$ is derived from the torque, τ, and rotational speed in revolutions per second, n_s. The isentropic power, $\dot{W}_{isen}$ is calculated from the mass flow, $\dot{m}$, inlet temperature, T_{01}, pressure ratio, PR and specific heat at constant pressure, C_p.

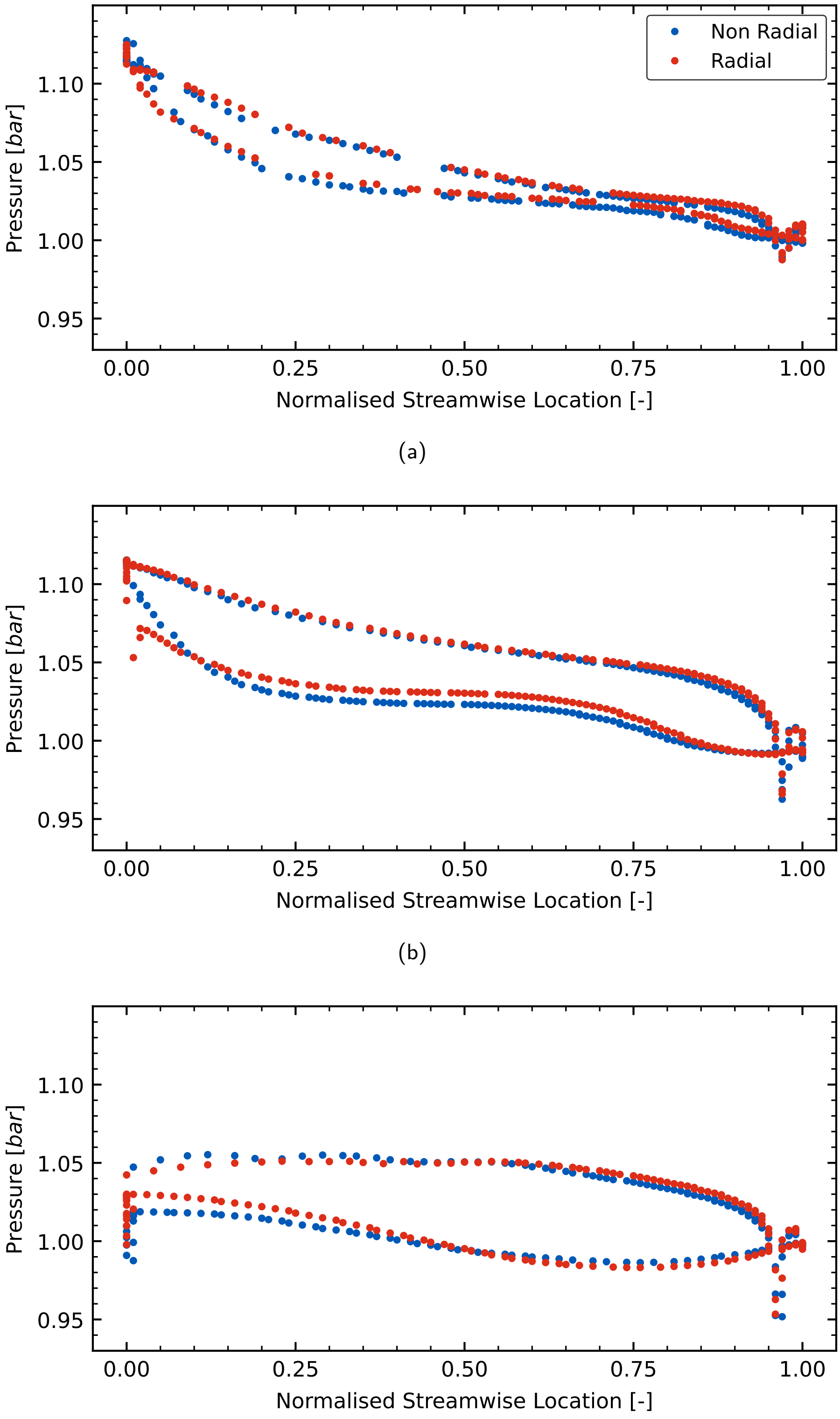

(a)

(b)

(c)

Figure 5.13: Blade loading of the radial and non-radial fibre design at different span locations: (a) hub, (b) midspan and (c) blade tip

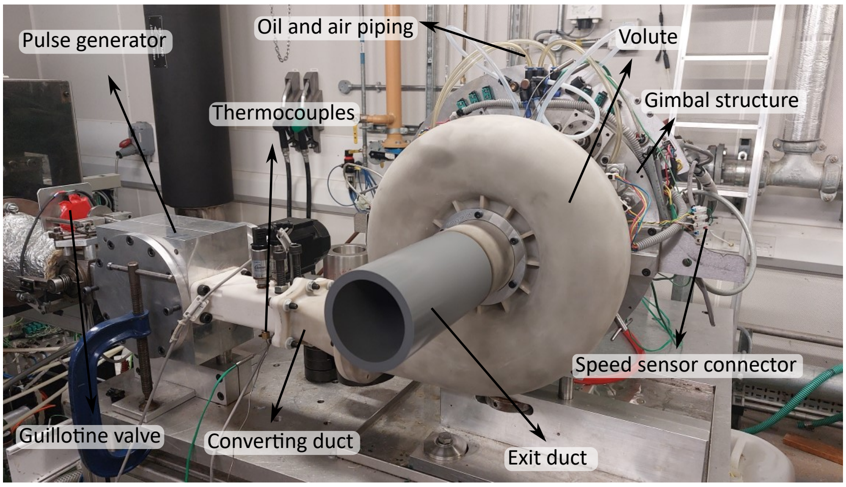

(a)

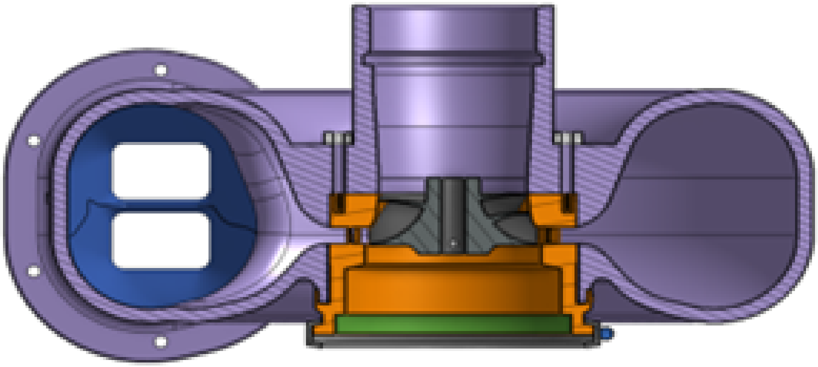

(b)

Figure 5.14: Experimental set up (a)Turbine rig and (b) Section view of the full assembly consisting of common volute (purple), nozzle insert for radial and non-radial fibre designs (orange) and radial and non-radial fibre rotor wheels (grey)

$$\eta_{ts} = \frac{\dot{W}_{act}}{\dot{W}_{isent}} = \frac{\tau n_s}{\dot{m} c_p T_{01}\left(1 - PR_{ts}^{-\frac{n-1}{n}}\right)} \tag{5.12}$$

To minimise the manufacturing cost, a new stator assembly was designed consisting of a single volute and two nozzle inserts, one for the radial fibre rotor and another one for the non-radial fibre rotor, as shown in Fig. 5.14 (b). The volute, which has no area reduction, distributes the flow around the nozzle inlet and was printed using laser sintering in glass fibre nylon polyamide 12, it is shown in Fig. 5.15. The nozzle inserts are secured to the volute by 6 bolts and were metal printed in aluminium, as shown in Fig. 5.16.

Figure 5.15: Front view of the manufactured volute

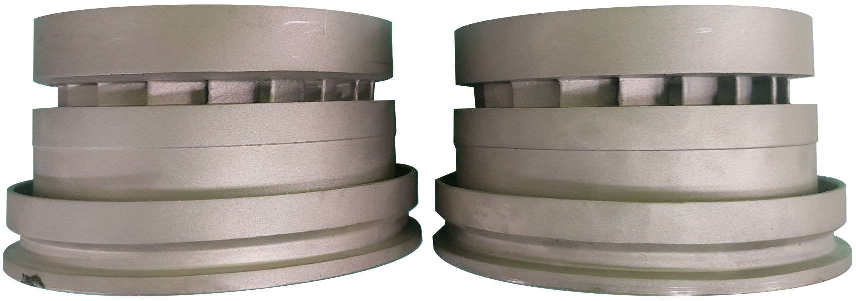

(a) (b)

Figure 5.16: Manufactured nozzle inserts for the: (a) radial fibre rotor (b) non-radial fibre rotor

The rotor wheels of the radial and non-radial fibre designs were manufactured by CNC machining of Al7075, an aluminium alloy with zinc. Figure 5.17 (a) and (c) show front and top views of the radial fibre rotor, while (b) and (d) show the non-radial fibre rotor after manufacturing. More details on the manufactured parts for this experimental campaign can be found in Appendix A

The experimental tests of both designs were carried out at steady state conditions at three different rotational speeds, 20,000, 28,000 and 38,000 rpm, for a range of static pressure ratios, PR, varying from 1.06 to 2.4. Figure 5.18 shows the experimental results of the two designs compared to the CFD results for one speedline, 28,000 rpm.

Efficiency and mass flow parameter results showed good agreement between CFD and experiments (around 2.5- 2.8 pp -percentage points - average deviation), as shown in

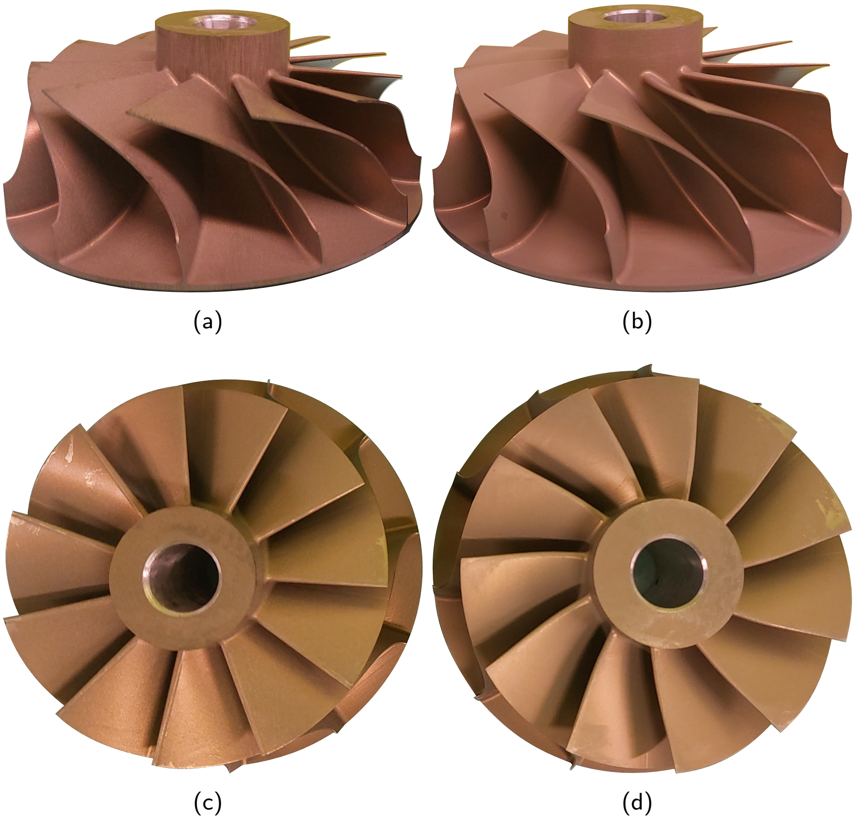
(a) (b) (c) (d)

Figure 5.17: Manufactured rotor wheels: (a) front view and (c) top view of the radial fibre rotor and (b) front view and top view (d) of the non-radial fibre rotor

Fig. 5.18 (a). At low velocity ratios, 0.3 to 0.65, the non-radial fibre design shows a consistent improvement in efficiency of 3.3 pp compared to the radial fibre design. Around peak efficiency point and velocity ratio 0.7, the non-radial fibre design show 2.03 pp higher efficiency than the radial fibre design in experiments. CFD results show smaller difference in performance between the two designs at peak efficiency, only 0.9 pp.

However, at high velocity ratio, above 0.7, the radial fibre design performs better than the non-radial fibre design. The performance improvement between non-radial fibre rotors and equivalent radial fibre rotors was higher at low velocity ratios than at the design point and high velocity ratios. This effect has also been observed by previous studies [43, 103], were non-radial fibre rotors outperformed the radial fibre baselines at the same velocity ranges as the turbines analysed in this chapter.

This effect can be explained by the lower incidence angle of the non-radial fibre design,

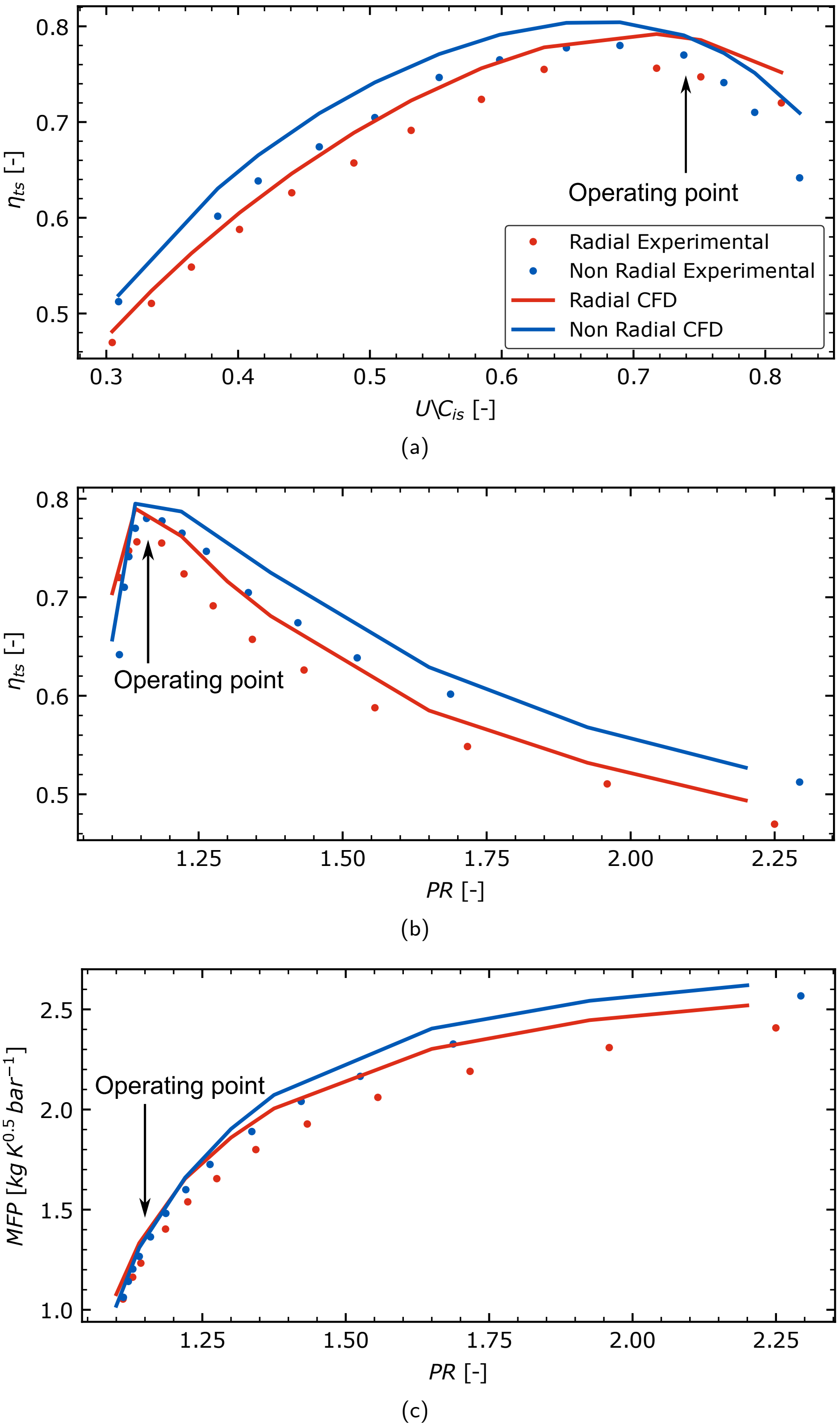

Figure 5.18: Experimental (circle marker) and CFD (solid line) performance results for the radial fibre design (red) and non-radial fibre design (blue) for the design speedline, $28,000rpm$: (a) η_{ts} as function of the velocity ratio, (b) η_{ts} as function of the PR and (c) MFP as function of the PR, with an arrow indicating the operating point

which is closer to the optimum incidence angle at low velocity ratios than the incidence of the radial fibre design. However, at high velocity ratios the incidence angle of the non-radial fibre design is too low, penalising the total-to-static efficiency more than in the radial fibre design. The velocity triangles in Fig. 5.19 show how the incidence angle varies with the operating condition

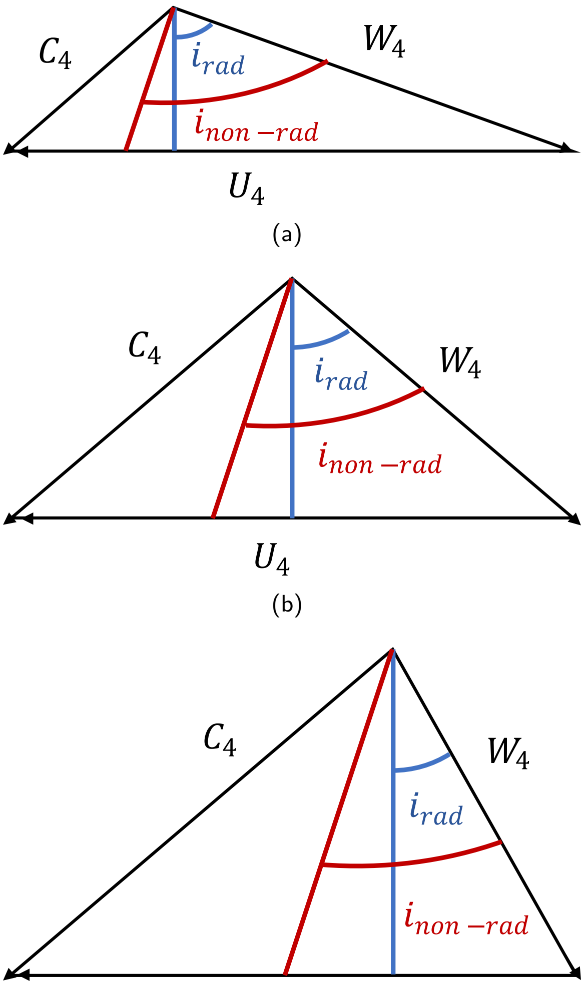

(a)

(b)

(c)

Figure 5.19: Velocity triangles at the rotor inlet showing the incidence angle for the radial and non-radial fibre rotors at a constant rotational speed (constant U_4), but different velocity ratios, U/C_{is}: (a) high U/C_{is}, (b) design point U/C_{is} and (c) low U/C_{is}.

Figure 5.18 (c) shows an increase in the swallowing of the non-radial fibre design, especially at high pressure ratios (equivalent to low velocity ratio) to a maximum of 3.9% increase in MFP at the highest PR.

These experimental results also validate the CFD simulations used for performance prediction in the parametric model calculations. Although the CFD results shown in Figure 5.18 take into account the full assembly of the turbine (volute, nozzle, rotor and outlet pipe), the performance and trend of the single passage simulations for the radial and non-radial fibre designs are in agreement with the full stage simulations and the experiments. This can be seen in Table 5.5, which compares the efficiency at design point predicted by different CFD set up and experiments. Additional experimental and CFD results can be found in Appendix B.

Table 5.5: Predicted efficiency by different CFD set up and experiments for the two optimised geometries, the radial fibre and the non-radial fibre designs

Set up	Radial fibre $\eta_{ts}[\%]$	Non-radial fibre $\eta_{ts}[\%]$
Single passage CFD	82.93	83.20]
Full stage CFD	82.55	83.14
Full stage with volute CFD	79.22	80.18
Experiments	76.09	78.13

5.6 Structural Analysis

Structural analysis of both the radial and non-radial fibre rotor wheels was carried out prior to manufacturing to ensure their structural integrity during the experiments. Using the setup introduced in Chapter 3, the equivalent stress and the maximum principal stress were calculated and compared to the yield strength of the material. The radial displacement was also monitored and compared to the tolerances and the tip clearance of the turbine.

Figure 5.20 shows the equivalent stress distribution in the rotor wheels. The calculations concluded that the non-radial fibre design showed, as expected, higher stresses compared to the radial fibre design, particularly at the blade root. The maximum equivalent stress went from 89.2 MPa at the blade root in the radial fibre design to 129.6 MPa, an increase of 45%. At other locations of the rotor wheel such as the leading edge and the blade surface, the equivalent stress also increased in the non-radial fibre design, as shown in Fig. 5.20.

However, the maximum equivalent stress of the non-radial fibre design (129.6 MPa) remained below the yield strength of the material (480MPa), leading to a safety factor of 3.7, concluding the non-radial fibre designs are structurally safe like the radial fibre design. The highest maximum principal stress was also below the yield strength of the material and was found to be 41 and 68 MPa at the blade root for the radial fibre and non-radial fibre designs, respectively.

Centrifugal loads lead to the deformation of the material, which results in the reduction of the clearances between the rotor and the casing. Figure 5.21 shows the deformation in the radial direction of the radial fibre (a) and non-radial fibre (b) designs.

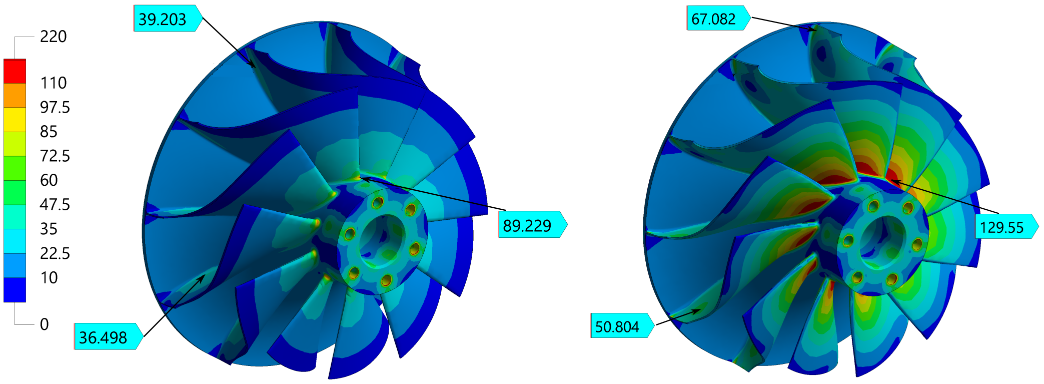

(a) (b)

Figure 5.20: Equivalent stress distribution in (a) the radial fibre rotor and (b) the non-radial fibre rotor. Values are in MPa

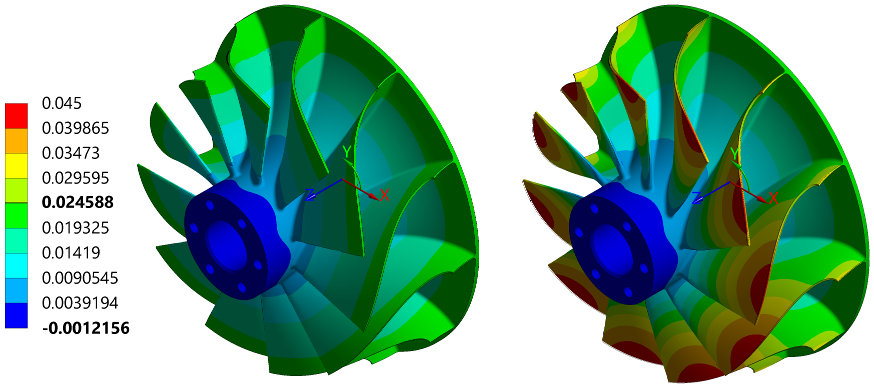

(a) (b)

Figure 5.21: Radial deformation in (a) the radial fibre rotor and (b) the non-radial fibre rotor. Values are in mm

The non-radial fibre rotor shows greater deformation in the radial direction compared to the radial fibre design, particularly in the tip of the blade at the trailing edge. However, this maximum deformation is less than 10% of the tip clearance, not risking the normal operation of the turbine.

5.7 Chapter Summary

A systematic study of the influence of traditional design parameters, but also 3D blading parameters on efficiency of radial turbomachinery for ETC applications was carried out in this paper. A 3D parametric model coupled with CFD was developed to evaluate the effect of each parameter by performing a sensitivity study, but also to optimise a radial fibre and a non-radial fibre geometries.

The two optimised geometries were tested experimentally showing increased efficiency of the non-radial fibre geometry compared to the radial fibre baseline geometry, of 2.03pp at the design operating point. The experimental results also validated the CFD simulations which explained the improved performance. Non-radial fibre blading reduced the entropy generation, especially at the leading edge and improved the blade loading.

Chapter 6

Conclusions

This research focuses on turbine design for waste heat recovery applications in offshore platforms. Waste heat recovery has a high potential in oil and gas offshore platforms, but only a few studies have investigated the use of organic Rankine cycle systems, and no research has looked at combining waste heat recovery technologies. The technology used in automotive applications, known as electric turbocompounding, has different conditions than turbocharger turbines and requires special attention during design to ensure high efficiency at low pressure ratios and low rotational speed, as applications require. ORC technology has been successful at recovering energy from waste heat streams, but designing ORC turbines can be challenging due to the high pressure ratio and the need to consider the non-ideal gas behaviour of refrigerants.

In terms of expander design, meanline models and physically based equations have been used to predict performance, but low-order models do not accurately capture the impact of certain geometry modifications. In addition, loss coefficients from the literature are not accurate for the unconventional boundary conditions of these applications. The boundary conditions for the turbine design carried out in this research for ETC and ORC systems are set based on the pilot plant currently in progress in UTM as part of the main project funded by MTJA.

This chapter summarised the main conclusions that have been obtained from this work, in the areas of the meanline model development and its accuracy, the 3D parametric model development and the understanding of the effects of 3D geometry and non-radial fibre blading modifications on the performance of the turbine. Finally, some ideas for future work are discuss at the end of the chapter, related to the meanline model, the parametrisation of the geometry and the pilot plant.

6.1 Conclusions

In the introduction of this thesis the key objectives were set out. These are answered one by one in this conclusion. .

1. **Development of low order model for turbine design based on physical principles accounting for real-gas effects.**

   This investigation developed the methododology for designing and optimising radial turbine performance. The first approach consisted of a 1D meanline model. The meanline model was used to predict the performance of the turbine consisting of a nozzle and a rotor and was calibrated using computational fluid dynamics (CFD) data.

   Non-ideal gas effects were taken into account by using thermodynamic property database (COOLPROP) which calculated the fluid properties (density, pressure, temperature, enthalpy, entropy) at each station. Different subroutines were developed to calculate the performance of the turbine under different operating modes: rotor and nozzle unchoked; nozzle choked and rotor unchoked; nozzle unchoked and rotor choked, and both nozzle and rotor choked.

   Single passage CFD dataset of 5 designs was used to calibrate the model using a GA multi-objective algorithm for each of the applications, ORC and ETC. The aim of the calibration algorithm was to minimise the efficiency and mass flow relative root mean square error (RRMSE) between the meanline prediction and the CFD results. After the calibration, the efficiency and mass flow RRMSE of the calibration dataset for the ORC application was 0.82% and 0.3%, respectively and the RRMSE of the whole sample was 2.6% for efficiency and 2.8% for mass flow. The same process was repeated for the ETC application, the efficiency and mass flow RRMSE of the calibration dataset was 0.98% and 1.09%, while the efficiency RRMSE of the whole sample was 2.9% and the mass flow RRMSE was 3.1%.

In addition to calculate the performance of a given turbine at different operating conditions the meanline model was coupled to a genetic algorithm optimiser to obtain an optimum turbine geometry for the boundary conditions of the ORC and ETC applications, exploring a wide design space. Optimised designs were obtained for ORC and ETC turbines achieving a total-to-static efficiency predicted by meanline of 79.98% and 82.86%, respectively.

2. **Investigation of the accuracy of the low order model in terms of loss distribution, mass flow and efficiency with air and organic fluids.**

   The meanline model developed was able to accurately predict efficiency and mass flow, however, the loss breakdown prediction was not in agreement with CFD results. This limitation of meanline modelling was observed after comparing the loss breakdown obtained by meanline with the loss breakdown obtained from entropy generation analysis of the CFD results, for the 5 turbine geometries used for calibration.

   Meanline after the first calibration with ORC and ETC configurations was able to predict trends in loss distribution (i.e designs with higher incidence losses in CFD showed also higher incidence losses in meanline compared to other designs). However, the model overpredicted incidence losses in the ORC configuration and passage losses were overpredicted in the ETC configuration.

   To overcome this limitation, a second multi-objective calibration was carried out considering the RRMSE in efficiency, mass flow and the contribution of each loss mechanism to the rotor overall losses (incidence losses, passage losses, tip clearance losses and trailing edge losses). After this second calibration, the loss breakdown prediction improved and was closer to the CFD results. However, while the error in loss distribution decreased, the error in efficiency prediction increased. The RRMSE in efficiency calculated from the calibration dataset for the ORC application was 4.4% and 3.6% for the ETC application.

Meanline model fails to accurately predict the loss breakdown in radial turbines. Instead, CFD can provide a more clear answer by analysing the flow field and identifying high entropy generation regions. On the other hand, the different loss mechanisms in radial turbomachinery (incidence, passage, tip leakage and trailing edge losses) cannot be entirely isolated, since there usually are complex flow structures that induce, interact and merge with other structures. This suggests that modified loss correlations based on radial turbomachinery are needed to account for that complexity.

3. **Proposal of a 3D parametric blading model that enables the generation of designs exploring a wide design space of radial and non-radial blading designs.**

   The 3D parametric model was used to improve upon the predictions of the meanline model and overcome its limitations, particularly for predicting the impact on the efficiency of changes to the geometry of the rotor. This model is more computationally intensive but provides more accurate predictions and better insight into the impact of geometry modifications on the flow field.

   Built using CAESES, the parametric model used the meanline design parameters (radii, blade and vane angles and rotational speed) and additional 3D parameters (blade thickness, tip clearance, among others). This is enough to generate a radial fibre blade rotor and a nozzle.

   Cone angles, ψ, are used to modify the shroud and hub contours without changing the meridional shape or the blade angles. Meanline modelling cannot predict the impact of these 3D modifications on efficiency, therefore is essential to evaluate them using the CFD approach.

   A novel parametrisation of the blade is developed by modifying each blade fibre, introducing extra parameters (ν, γ_{lower}, γ_{upper}) that transform the blade into non-radial fibred rotor and these can control the rotor blade inlet angle, $\beta_{blade,4}$. The fluid domain of the nozzle and the rotor are exported and the performance is calculated using single passage CFD simulations. The automated model was able to generate hundreds of different geometries for sensitivity analysis and optimisation for the different applications.

First, the nozzle and rotor (with a radial fibre blade configuration) were optimised and compared with the meanline optimised designs based only on the same design parameters as the meanline model. The sensitivity analysis of the main design parameters, prior to the optimisation, showed a weak correlation with efficiency, that is, a high-efficiency turbine design is possible with different values of the design parameters. Only the rotational speed showed a clear optimum value for the highest efficiency in both ORC and ETC applications.

The optimised geometries using this design approach achieved an efficiency of 81.29% and 82.93% for the ORC and ETC turbines, respectively. This represents an efficiency improvement of 1.31pp for the ORC turbine compared to the design obtained after the meanline optimisation. The ETC design obtained by both approaches showed essentially the same efficiency. After adding a volute, the ETC radial fibre design was tested experimentally at the Imperial College turbine test rig, which has been widely used in previous research. The good agreement with the CFD data validates the 3D-parametric methodology.

4. **Understanding the effects of non-radial blading and other 3D geometry modifications on turbine design and exploration of the flow field with an experimentally validated CFD method.**

   Once the baseline designs with radial fibre blade configurations were optimised for the ORC and ETC turbines, the rotor blade geometry modifications were introduced to investigate the effects on efficiency.

   For the ORC application, the effect of different cone angles at the leading and trailing edge of the hub and shroud contours was investigated. For the same meridional geometry in terms of radii, blade height and blade angles, a maximum of 2pp efficiency difference was found between the best and the worst design after a sampling varying the cone angles. The hub cone angle at the leading edge, $\psi_{hub,in}$ and the shroud cone angle at the trailing edge $\psi_{shroud,out}$ had a strong correlation with efficiency. Values of $\psi_{hub,in}$ close to 90° lead to high efficiency designs, and the same occur for values of $\psi_{shroud,out}$ close to 0°. The correlation of the other two cone angles, $\psi_{hub,out}$ and $\psi_{shroud,in}$, with efficiency was rather weak. High efficiency was obtained for designs with any value of $\psi_{hub,out}$ and $\psi_{shroud,in}$ within the ranges tested, from $0°$ to $30°$ and from $60°$ to $90°$, respectively.

For the ETC application, non-radial fibre blades were investigated by introducing modifications to the blade shape. After the sensitivity analysis, it was seen that some of the parameters had a strong correlation with efficiency. The highest efficiency was achieved when α_{nozzle} was around $70°$ and at lowest ν_{TE}, around $-20°$. High values of $\gamma_{upper,TE}$ and $\gamma_{lower,TE}$ around $20°$ lead also to high-efficiency designs. Weak efficiency sensitivity was found when varying $\beta_{blade,4}$ and $\gamma_{lower,LE}$.

The optimised non-radial fibre geometry was compared to the radial fibre design, showing an efficiency increase of 0.3pp in single passage simulations and 0.6pp in full-stage simulations. The performance improvement was explained by a lower (more negative) incidence angle of $i = -46.73°$ compared to the incidence of $i = -20.45°$ in radial fibre design. The increased blade loading was also responsible for the better performance of the non-radial fibre design, mainly at the midspan and the tip.

The optimised non-radial fibre geometry was manufactured and tested at Imperial College facilities using the same volute as the radial fibre design. The experimental campaign confirmed the improved performance between the non-radial fibre design and the radial fibre design, with 2pp of efficiency increase at the design point.

6.2 Future Work

6.2.1 Meanline Modelling

The present work highlighted some limitations of meanline modelling. However, more research is needed to investigate different combinations of loss correlations available in the literature to check if there is any additional improvement. Moreover, modifying the current correlations or developing new ones could be useful to overcome meanline limitations.

Highly detailed experiments would be needed to potentially measure the flow velocity in key turbine stations. Volute, interspace and diffuser equations could be added to the meanline model to make it more realistic when comparing to the experiments.

The meanline model developed can work with any ideal or non-ideal fluid, but investigations were only carried out with air and R1233zd(E). In ORC applications, mixtures of organic fluids are getting more attention lately due to the ability to 'tailor' the mixture properties to the application. Implementing mixtures as working fluids in meanline modelling is an essential step if turbines want to be designed for this application.

6.2.2 Geometry Parametrisation

Additional parameters could be introduced to make the 3D-parametric model more flexible and complete. For instance, mixed flow turbine configurations could be parameterise by replacing the radius at the rotor inlet r_4 by two parameters, the hub and the shroud radius at the rotor inlet r_{4h} and r_{4s}.

In addition, the incidence angle could be used as a design or control parameter during the optimisation. Incidence could be evaluated using the CFD results in each iteration and the nozzle angle, α_{nozzle}, the blade angle at the leading edge, $\beta_{blade,4}$ and among other parameters could be adjusted until the desire incidence angle is obtained. In fact, incidence could be set as a distribution rather than a single value if that leads to higher efficiency and a cleaner flow field in the rotor.

Moreover, additional components could be parameterised in order to increase the fidelity of the numerical model. Although that would increase the computational time significantly, it could be useful for the last stage of the optimisation, where small geometry modifications could increase the efficiency slightly. This way, the volute could be parameterised testing different shapes and connections with other components of the system upstream.

In the ORC application, the development of a parametric model of a convergent-divergent nozzle could be an interesting topic to explore supersonic turbine designs. At high pressure ratios choking conditions at the nozzle outlet are common. In fact, all the designs considered in this work, where $PR = 9.0.$, had the nozzle choked. An adequate design of a convergent-divergent nozzle could allow a supersonic expansion without generating high shock wave losses. Nozzle supersonic expansions and the effects on the rotor flow field and the turbine performance are topic worth investigating as part of future work.

6.2.3 Pilot Plant Experiments and Combination of Technologies

While ORC experimental facilities for testing radial turbomachinery are available, there is currently no facility for testing the combination of different WHR technologies. However, one of the academic partners on this project, UTM, is building an experimental facility to replicate waste heat stream conditions and test the combination of WHR technologies. As part of the main project in waste heat recovery technology, both technologies, ETC and ORC will be tested experimentally at the pilot plant. This will provide high-value experimental data of integrated waste heat recovery technologies.

Furthermore, the methodology developed in this thesis will be used to optimise the turbine geometries for a coupled system of ETC and ORC. Since both turbines will be on the same shaft the rotational speed will be a common parameter. Using the same shaft and keeping the rotational speed below $30,000rpm$ eliminates the use of a gearbox when connecting to the high-speed generator and reduces the use of extra components. This will lead to a compact waste heat recovery solution that will maximise the power recovered while minimising the implementation cost and footprint.

Bibliography

[1] Maria E Mondejar, Mark O McLinden, and Eric W Lemmon. Thermodynamic properties of trans-1-chloro-3, 3, 3-trifluoropropene (r1233zd (e)): Vapor pressure,(p, ρ, t) behavior, and speed of sound measurements, and equation of state. *Journal of Chemical & Engineering Data*, 60(8):2477–2489, 2015.

[2] World Meteorological Organization. Scientific Assessment of Ozone Depletion. Technical report, 2008. URL `https://csl.noaa.gov/assessments/ozone/2018/downloads/2018OzoneAssessment.pdf`.

[3] BP. Statistical Review of World Energy 2022. Technical report, 2022. URL `https://www.bp.com/content/dam/bp/business-sites/en/global/corporate/pdfs/energy-economics/statistical-review/bp-stats-review-2022-full-report.pdf`.

[4] BP. Statistical Review of World Energy 2021. Technical report, 2021. URL `https://www.bp.com/content/dam/bp/business-sites/en/global/corporate/pdfs/energy-economics/statistical-review/bp-stats-review-2021-full-report.pdf`.

[5] BP. Statistical Review of World Energy 2020. Technical report, 2020. URL `https://www.bp.com/content/dam/bp/business-sites/en/global/corporate/pdfs/energy-economics/statistical-review/bp-stats-review-2020-full-report.pdf`.

[6] BP. Statistical Review of World Energy 2019. Technical report, 2019. URL `https://www.bp.com/content/dam/bp/business-sites/en/`

global/corporate/pdfs/energy-economics/statistical-review/bp-stats-review-2019-full-report.pdf.

[7] OECD/IEA. Global Energy Review 2019. Technical report, Paris, 2019. URL https://www.iea.org/reports/net-zero-by-2050.

[8] International Energy Agency. Global energy and CO2 status report 2018. Technical report, International Energy Agency, 2019.

[9] Bowman. ETC Case studies. URL https://www.bowmanpower.com/benefits/case-studies/.

[10] Ennio Macchi and Marco Astolfi. *Organic rankine cycle (ORC) power systems: technologies and applications*. Woodhead Publishing, 2016.

[11] R Daccord, J Melis, T Kientz, A Darmedru, R Pireyre, N Brisseau, and E Fonteneau. Exhaust heat recovery with rankine piston expander. *ICE Powertrain electrification & energy recovery*, pages 1–10, 2013.

[12] Jean-Louis Bouvier, Vincent Lemort, Ghislain Michaux, Patrick Salagnac, and Thiebaut Kientz. Experimental study of an oil-free steam piston expander for micro-combined heat and power systems. *Applied Energy*, 169:788–798, 2016.

[13] Zhiwei Ma, Huashan Bao, and Anthony Paul Roskilly. Dynamic modelling and experimental validation of scroll expander for small scale power generation system. *Applied Energy*, 186:262–281, 2017. Sustainable Thermal Energy Management (SusTEM2015).

[14] Claudio Spadacini, Lorenzo Centemeri, Michele Danieli, Dario Rizzi, and Luca Xodo. Geothermal energy exploitation with the organic radial outflow turbine. In *Proceedings World Geothermal Congress*, pages 1–6, 2015.

[15] Bernhardt Lüddecke, Dietmar Filsinger, and Jan Ehrhard. On mixed flow turbines for automotive turbocharger applications. *International Journal of rotating machinery*, 2012, 2012.

[16] Harld E. Rohlik. Analytical determination of radial inflow turbine design geometry

for maximum efficiency. *National Aeronautics and Space Administration, NASA-TN-D-4384*, 1968.

[17] Peter L. Meitner and Arthur J. Glassman. *Computer code for off-design perfromance analysis of radial-inflow turbines with rotor blade sweep.* NASA Technical Note TN D-2199, 1983.

[18] Arnold Whitfield and Nicholas C Baines. *Design of radial turbomachines*. John Wiley and Sons Inc., New York, NY (USA), 1990.

[19] OECD/IEA. Global Energy Review 2021. Technical report, 2021.

[20] International Energy Agency. Energy Technology Perspectives 2017 - Executive Summary. Technical report, 2017. URL `https://webstore.iea.org/download/summary/237?fileName=English-ETP-2017-ES.pdf`.

[21] Rafaela Agathokleous, Giuseppe Bianchi, Gregoris Panayiotou, Lazaros Aresti, Maria C Argyrou, Giorgos S Georgiou, Savvas A Tassou, Hussam Jouhara, Soteris A Kalogirou, Georgios A Florides, et al. Waste heat recovery in the eu industry and proposed new technologies. *Energy Procedia*, 161:489–496, 2019.

[22] Davide Di Battista, Marco Di Bartolomeo, Carlo Villante, and Roberto Cipollone. On the limiting factors of the waste heat recovery via orc-based power units for on-the-road transportation sector. *Energy conversion and management*, 155:68–77, 2018.

[23] Kévin Rosset, Violette Mounier, Eliott Guenat, and Jürg Schiffmann. Multi-objective optimization of turbo-orc systems for waste heat recovery on passenger car engines. *Energy*, 159:751–765, 2018.

[24] Clemens Forman, Ibrahim Kolawole Muritala, Robert Pardemann, and Bernd Meyer. Estimating the global waste heat potential. *Renewable and Sustainable Energy Reviews*, 57:1568–1579, 2016.

[25] Steven Lecompte, Henk Huisseune, Martijn Van Den Broek, Bruno Vanslambrouck, and Michel De Paepe. Review of organic rankine cycle (orc) architectures

for waste heat recovery. *Renewable and sustainable energy reviews*, 47:448–461, 2015.

[26] Hualing Zhang, Xuan Guan, Yang Ding, and Chao Liu. Emergy analysis of organic rankine cycle (orc) for waste heat power generation. *Journal of Cleaner Production*, 183:1207–1215, 2018.

[27] Kiyarash Rahbar, Saad Mahmoud, Raya K Al-Dadah, Nima Moazami, and Seyed A Mirhadizadeh. Review of organic rankine cycle for small-scale applications. *Energy conversion and management*, 134:135–155, 2017.

[28] Sakineh Tavakkoli, Omkar R Lokare, Radisav D Vidic, and Vikas Khanna. Systems-level analysis of waste heat recovery opportunities from natural gas compressor stations in the united states. *ACS Sustainable Chemistry & Engineering*, 4(7):3618–3626, 2016.

[29] Cheng-Liang Chen, Po-Yi Li, and Si Nguyen Tien Le. Organic rankine cycle for waste heat recovery in a refinery. *Industrial & Engineering Chemistry Research*, 55(12):3262–3275, 2016.

[30] BP. BP Annual Report: Growing the business and advancing the energy transition. Technical report, 2018. URL `https://www.bp.com/content/dam/bp/business-sites/en/global/corporate/pdfs/investors/bp-annual-report-and-form-20f-2018.pdf`.

[31] Petronas. Petronas Annual Report 2017. Technical report, 2017. URL `https://www.petronas.com/ws/sites/default/files/2018-08/petronas-annual-report-2017-0.pdf`.

[32] T.C. Hung, T.Y. Shai, and S.K. Wang. A review of organic rankine cycles (orcs) for the recovery of low-grade waste heat. *Energy*, 22(7):661–667, 1997.

[33] Tuong-Van Nguyen, Leonardo Pierobon, Brian Elmegaard, Fredrik Haglind, Peter Breuhaus, and Mari Voldsund. Exergetic assessment of energy systems on north sea oil and gas platforms. *Energy*, 62:23–36, 2013.

[34] Tuong-Van Nguyen, Tamás Gábor Fülöp, Peter Breuhaus, and Brian Elmegaard. Life performance of oil and gas platforms: Site integration and thermodynamic evaluation. *Energy*, 73:282–301, 2014.

[35] Leonardo Pierobon, Tuong-Van Nguyen, Ulrik Larsen, Fredrik Haglind, and Brian Elmegaard. Multi-objective optimization of organic rankine cycles for waste heat recovery: Application in an offshore platform. *Energy*, 58:538–549, 2013.

[36] L. Pierobon, A. Benato, E. Scolari, F. Haglind, and A. Stoppato. Waste heat recovery technologies for offshore platforms. *Applied Energy*, 136:228–241, 2014.

[37] Rakesh K Bhargava, Michele Bianchi, Lisa Branchini, Andrea De Pascale, and Valentina Orlandini. Organic rankine cycle system for effective energy recovery in offshore applications: a parametric investigation with different power rating gas turbines. In *Turbo Expo: Power for Land, Sea, and Air*, volume 56673, page V003T20A004. American Society of Mechanical Engineers, 2015.

[38] Julian Esteban Barrera, Edson Bazzo, and Eduardo Kami. Exergy analysis and energy improvement of a brazilian floating oil platform using organic rankine cycles. *Energy*, 88:67–79, 2015.

[39] Thiago Gotelip Correa Veloso, César Adolfo Rodriguez Sotomonte, Christian J.R. Coronado, and Marco A.R. Nascimento. Multi-objective optimization and exergetic analysis of a low-grade waste heat recovery orc application on a brazilian fpso. *Energy Conversion and Management*, 174:537–551, 2018.

[40] Max Mauro L. Reis, Jorge Alejandro V. Guillen, and Waldyr L.R. Gallo. Off-design performance analysis and optimization of the power production by an organic rankine cycle coupled with a gas turbine in an offshore oil platform. *Energy Conversion and Management*, 196:1037–1050, 2019.

[41] Nicolae Vlad Burnete, Florin Mariasiu, Christopher Depcik, Istvan Barabas, and Dan Moldovanu. Review of thermoelectric generation for internal combustion engine waste heat recovery. *Progress in Energy and Combustion Science*, 91: 101009, 2022.

[42] Tae Young Kim, Jinwoo Kwak, and Byung-wook Kim. Energy harvesting performance of hexagonal shaped thermoelectric generator for passenger vehicle applications: An experimental approach. *Energy Conversion and Management*, 160: 14–21, 2018.

[43] Eva Alvarez-Regueiro, Esperanza Barrera-Medrano, Ricardo Martinez-Botas, and Srithar Rajoo. Numerical analysis of non-radial blading in a low speed and low pressure turbine for electric turbocompounding applications. In *Turbo Expo: Power for Land, Sea, and Air*, volume 84935, page V02DT37A017. American Society of Mechanical Engineers, 2021.

[44] Eva Alvarez-Regueiro, Bijie Yang, Maria Esperanza Barrera-Medrano, Ricardo F. Martinez-Botas, and Srithar Rajoo. Optimisation of an ORC Radial Turbine Using a Reduced-Order Model Coupled With CFD. *Journal of Engineering for Gas Turbines and Power*, 08 2022. URL `https://doi.org/10.1115/1.4055359`.

[45] Eva Alvarez-Regueiro, Bijie Yang, Esperanza Barrera-Medrano, Ricardo Martinez-Botas, and Srithar Rajoo. Design, optimisation and analysis of non-radial fibre turbines for electric turbocompounding applications. under review. In *15th International Conference on Turbochargers and Turbocharging*. CRC Press, 2023.

[46] Legros Arnaud, Guillaume Ludovic, Diny Mouad, Zai¨di Hamid, and Lemort Vincent. Comparison and impact of waste heat recovery technologies on passenger car fuel Zconsumption in a normalized driving cycle. *Energies*, 7(8):5273–5290, 2014.

[47] Manuel Kant, Alessandro Romagnoli, Aman MI Mamat, and Ricardo F. Martinez-Botas. Heavy-duty engine electric turbocompounding. In *Proceedings of the Institution of Mechanical Engineers, Part D: Journal of Automobile Engineering*, volume 229, pages 457–472, 2015.

[48] Mingyang Yang, Chao Hu, Yunlong Bai, Kangyao Deng, Yuncheng Gu, Yuehua Qian, and Bo Liu. Matching method of electric turbo compound for two-stroke low-speed marine diesel engine. *Applied Thermal Engineering*, 158:113752, 2019.

[49] Dig Vijay Singh and Eilif Pedersen. A review of waste heat recovery technologies for maritime applications. *Energy Conversion and Management*, 111:315–328, 2016.

[50] Alias Mohd Noor, Rosnizam Che Puteh, Srithar Rajoo, Uday M Basheer, Muhammad Hanafi Md Sah, and Sheikh Hussain Shaikh Salleh. Simulation study on electric turbo-compound (etc) for thermal energy recovery in turbocharged internal combustion engine. *Applied Mechanics and Materials*, 799:895, 2015.

[51] Aman Mohd and Ihsan Bin. *Design and Development of a High Performance LPT for Electric Turbocompounding Energy Recovery Unit in a Heavily Downsized Engine*. PhD Thesis, Imperial College London, London, UK, November 2012.

[52] Junjiang Bao and Li Zhao. A review of working fluid and expander selections for organic rankine cycle. *Renewable and Sustainable Energy Reviews*, 24:325–342, 2013.

[53] Vincent Lemort, Sylvain Quoilin, Cristian Cuevas, and Jean Lebrun. Testing and modeling a scroll expander integrated into an organic rankine cycle. *Applied Thermal Engineering*, 29(14):3094–3102, 2009.

[54] Andreas P Weiß. Volumetric expander versus turbine–which is the better choice for small orc plants. In *3rd ASME ORC conference, Brussels (Belgium)*, pages 1–10, 2015.

[55] Kiyarash Rahbar, Saad Mahmoud, Raya K. Al-Dadah, and Nima Moazami. Parametric analysis and optimization of a small-scale radial turbine for Organic Rankine Cycle. *Energy*, 83:696–711, 2015.

[56] H. Moustapha, M. F. Zelesky, N. C. Baines, and D. Japikse. *Axial and radial turbines*. Concepts NREC, 2003. ISBN 0-933283-12-0.

[57] C. Spadacini and D. Rizzi. Radial outflow turbines for Organic Rankine Cycle expanders. In *Organic Rankine Cycle (ORC) Power Systems: Technologies and Applications*. 2016. ISBN 9780081005118.

[58] N. Karamanis, R. F. Martinez-Botas, and C. C. Su. Mixed flow turbines: inlet and exit flow under steady and pulsating conditions. *Journal of Turbomachinery*, 123(2):359–371, 2002.

[59] C. Arcoumanis, R. F. Martinez-Botas, J. M. Nouri, and C. C. Su. Inlet and exit flow characteristics of mixed flow turbines. In Anon, editor, *International Gas Turbine & Aeroengine Congress & Exhibition*, number GT, page 8, Stockholm, Sweden, 1998. ASME,Fairfield, NJ, United States.

[60] N. C. Baines, F. J. Wallace, and A. Whitfield. Computer aided design of mixed flow turbines for turbochargers. *Journal of Engineering for Power*, 101(3):440–448, 1979.

[61] Warner L. Stewart. Analytical investigation of flow through high-speed mixed-flow turbine. *National Advisory Committee for Aeronautics, NACA-RM-E51H06*, 1951.

[62] Samuel M Futral and Charles A Wasserbauer. Off-design performance prediction with experimental verification for a radial-inflow turbine. *National Aeronautics and Space Administration, NASA-TN-D-2621*, 1965.

[63] Carroll A. Todd and Samuel M. Futral. A FORTRAN 4 program to estimate the off-design performance of radial-inflow turbines. *National Aeronautics and Space Administration, NASA-TN-D-5059*, 1970.

[64] C A Wasserbauer and A J Glassman. FORTRAN program for predicting off-design performance of radial-inflow turbines. *NASA Technical Note TN D-8063*, (September 1975):55, 1975.

[65] A. Whitfield and N.C. Baines. A general computer solution for radial and mixed flow turbomachine performance prediction. *International Journal of Mechanical Sciences*, 18(4):179–184, 1976.

[66] F. J. Wallace. Theoretical Assessment of the Performance Characteristics of Inward Radial Flow Turbines. *Proceedings of the Institution of Mechanical Engineers, Conference Proceedings*, 12(1):931–952, 1958.

[67] Cold performance evaluation of a 4.59-inch radial-inflow turbine designed for a brayton-cycle space power system. *National Aeronautics and Space Administration NASA-TN-D-3260*, 1966.

[68] C. Rodgers and R. Geiser. Performance of a High-Efficiency Radial/Axial Turbine. *Journal of Turbomachinery*, 109(2):151–154, 04 1987.

[69] S. F. Smith. A Simple Correlation of Turbine Efficiency. *Journal of the Royal Aeronautical Society*, 69(655):467–470, 1965.

[70] A. Whitfield. The preliminary design of radial inflow turbines. *Journal of Turbomachinery*, 112(1):50, 1989.

[71] Miloud Abidat. *Design and testing of a highly loaded mixed flow turbine*. PhD thesis, University of London Imperial College, 1991.

[72] F. J. Wallace, N. C. Baines, and A. Whitfield. A Unified Approach to the One-Dimensional Analysis and Design of Radial and Mixed Flow Turbines. volume 1B: General of *Turbo Expo: Power for Land, Sea, and Air*, 03 1976. V01BT02A035.

[73] Kiyarash Rahbar, Saad Mahmoud, and Raya K. Al-Dadah. Mean-line modeling and CFD analysis of a miniature radial turbine for distributed power generation systems. *International Journal of Low-Carbon Technologies*, 11(2):157–168, 2016.

[74] Andrea Meroni, Miles Robertson, Ricardo Martinez-Botas, and Fredrik Haglind. A methodology for the preliminary design and performance prediction of high-pressure ratio radial-inflow turbines. *Energy*, 164:1062–1078, 2018.

[75] Carlos A.M. Ventura, Peter A. Jacobs, Andrew S. Rowlands, Paul Petrie-Repar, and Emilie Sauret. Preliminary design and performance estimation of radial inflow turbines: An automated approach. *Journal of Fluids Engineering*, 134(3):031102, 2012.

[76] Xuwen Qiu and Nick Baines. Performance prediction for high pressure-ratio radial inflow turbines. In *Turbo Expo: Power for Land, Sea, and Air*, volume 47950, pages 945–956, 2007.

[77] Xuwen Qiu, Mark R Anderson, and Nicholas C Baines. Meanline modeling of radial inflow turbine with variable area nozzle. In *Turbo Expo: Power for Land, Sea, and Air*, volume 48883, pages 1185–1191, 2009.

[78] Alessandro Romagnoli. *Aerodynamic and thermal characterization of turbocharger turbines: experimental and computational evaluation*. PhD thesis, Imperial College London, 2010.

[79] Karl Georg Hohenberg. *Novel methodology for the optimisation of turbocharger turbine design for improved engine performance*. PhD thesis, Imperial College London, 2020.

[80] Rowland S. Benson. A review of methods for assessing loss coefficients in radial gas turbines. *International Journal of Mechanical Sciences*, 12(10):905–932, 1970.

[81] J. H. Horlock. *Axial flow turbines*. Butterworths, 1966. ISBN 0882750976.

[82] O E Balje. A contribution to the problem of designing radial turbomachines. *Trans. ASME*, 74(4):451–472, 1952.

[83] Qing-Hua Deng, Shuai Shao, Lei Fu, Hai-Feng Luan, and Zhen-Ping Feng. An integrated design and optimization approach for radial inflow turbines—part I: automated preliminary design. *Applied Sciences*, 8(11):2038, 2018.

[84] Albert Betz. *Introduction to the theory of flow machines*. Pergamon Press, 1966.

[85] E. A. Bridle and R. A. Boulter. A Simple theory for the prediction of losses in the rotors of inward radial flow turbines. *Proceedings of the Institution of Mechanical Engineers, Conference Proceedings*, 182(8):393–405, 1967.

[86] G.C.R. Ainley and D.G. Mathieson. A method of performance estimation for axial-flow turbines. *Aeronautical Research Council Reports and Memoranda*, 2974 (2974), 1951.

[87] R S Benson, W G Cartwright, and S K Das. An analysis of the losses in the rotor of a radial flow gas turbine at zero incidence. *Proc. L Mech. E*, 182, 1967.

[88] M. Abidat, N. C. Baines, and M. R. Firth. Design of a Highly Loaded Mixed Flow Turbine. *Proceedings of the Institution of Mechanical Engineers, Part A: Journal of Power and Energy*, 206(2):95–107, 1992.

[89] C. Arcoumanis, I. Hakeem, L. Khezzar, R. F. Martinez-Botas, and N. C. Baines. Performance of a Mixed Flow Turbocharger Turbine Under Pulsating Flow Conditions. volume 2: Aircraft Engine; Marine; Microturbines and Small Turbomachinery of *Turbo Expo: Power for Land, Sea, and Air*, June 1995. V002T04A011.

[90] J. W. Daily and R. E. Nece. Chamber dimension effects on induced flow and frictional resistance of enclosed rotating disks. *Journal of Basic Engineering*, 82 (1):217, 1960.

[91] R Dambach, HP Hodson, and I Huntsman. An experimental study of tip clearance flow in a radial inflow turbine. In *Turbo Expo: Power for Land, Sea, and Air*, volume 78620, page V001T01A110. American Society of Mechanical Engineers, 1998.

[92] Arthur J. Glassman. Enhanced analysis and users manual for radial-inflow turbine conceptual design code RTD. *NASA Contractor Report 195454*, (Lewis Research Center), 1995.

[93] Ding-Yu Peng and Donald B Robinson. A new two-constant equation of state. *Industrial & Engineering Chemistry Fundamentals*, 15(1):59–64, 1976.

[94] Giorgio Soave. Equilibrium constants from a modified redlich-kwong equation of state. *Chemical Engineering Science*, 27(6):1197–1203, 1972.

[95] Giorgio S. Soave. Application of the redlich-kwong-soave equation of state to solid-liquid equilibria calculations. *Chemical Engineering Science*, 34(2):225–229, 1979.

[96] Roland Span. *Multiparameter equations of state: an accurate source of thermodynamic property data*. Springer Science & Business Media, 2013.

[97] Ian H Bell, Sylvain Quoilin, Jorrit Wronski, and Vincent Lemort. Coolprop: An

open-source reference-quality thermophysical property library. In *ASME ORC 2nd International Seminar on ORC Power Systems*. sn, 2013.

[98] Eric Lemmon, Marcia L Huber, Mark O Mclinden, et al. Nist standard reference database 23: reference fluid thermodynamic and transport properties-refprop, version 8.0. 2007.

[99] Luca Da Lio, Giovanni Manente, and Andrea Lazzaretto. A mean-line model to predict the design efficiency of radial inflow turbines in organic rankine cycle (orc) systems. *Applied Energy*, 205:187–209, 2017.

[100] Fuhaid Alshammari, Apostolos Karvountzis-Kontakiotis, Apostolos Pesiridis, and Panagiotis Giannakakis. Off-design performance prediction of radial turbines operating with ideal and real working fluids. *Energy Conversion and Management*, 171:1430–1439, 2018.

[101] Marcin Jankowski, Piotr Klonowicz, and Aleksandra Borsukiewicz. Multi-objective optimization of an orc power plant using one-dimensional design of a radial-inflow turbine with backswept rotor blades. *Energy*, 237:121506, 2021.

[102] J M Mulloy and H G Weber. A radial inflow turbine impeller for improved off-design performance. volume 79566, page V001T01A040. American Society of Mechanical Engineers, 1982. ISBN 0791879569.

[103] Liam Barr, Stephen W T Spence, and Paul Eynon. Improved performance of a radial turbine through the implementation of back swept blading. volume 43161, pages 1459–1468, 2008. ISBN 0791843165.

[104] Jason Walkingshaw, Stephen Spence, Jan Ehrhard, and David Thornhill. An investigation into improving off-design performance in a turbocharger turbine utilizing non-radial blading. volume 54679, pages 2023–2032, 2011. ISBN 0791854671.

[105] Peter Newton. *An experimental and computational study of pulsating flow within a double entry turbine with different nozzle settings*. PhD thesis, Imperial College London, 2013.

[106] Seok Hun Kang. Design and experimental study of orc (organic rankine cycle) and radial turbine using r245fa working fluid. *Energy*, 41(1):514–524, 2012.

[107] Seok Hun Kang. Design and preliminary tests of orc (organic rankine cycle) with two-stage radial turbine. *Energy*, 96:142–154, 2016.

[108] Sangjo Han, JongBeom Seo, and Bum-Seog Choi. Development of a 200 kw orc radial turbine for waste heat recovery. *Journal of Mechanical Science and Technology*, 28(12):5231–5241, 2014.

[109] Jonathan Demierre, Daniel Favrat, Jürg Schiffmann, and Johannes Wegele. Experimental investigation of a thermally driven heat pump based on a double organic rankine cycle and an oil-free compressor-turbine unit. *International Journal of Refrigeration*, 44:91–100, 2014.

[110] Teemu Turunen-Saaresti, Antti Uusitalo, and Juha Honkatukia. Design and testing of high temperature micro-orc test stand using siloxane as working fluid. In *Journal of Physics: Conference Series*, volume 821, page 012024. IOP Publishing, 2017.

[111] Long Shao, Jie Zhu, Xiangrui Meng, Xinli Wei, and Xinling Ma. Experimental study of an organic rankine cycle system with radial inflow turbine and r123. *Applied Thermal Engineering*, 124:940–947, 2017.

[112] Ludovic Guillaume, Arnaud Legros, Adriano Desideri, and Vincent Lemort. Performance of a radial-inflow turbine integrated in an orc system and designed for a whr on truck application: An experimental comparison between r245fa and r1233zd. *Applied Energy*, 186:408–422, 2017. Sustainable Thermal Energy Management.

[113] Laura Palagi, Apostolos Pesyridis, Enrico Sciubba, and Lorenzo Tocci. Machine learning for the prediction of the dynamic behavior of a small scale orc system. *Energy*, 166:72–82, 2019.

[114] WA Spraker. Contour clearance losses in radial inflow turbines for turbochargers. *ASME paper*, No. 87-ICE-52, 1987.

[115] Rainer Storn. On the usage of differential evolution for function optimization. In *Proceedings of North American Fuzzy Information Processing*, pages 519–523. Ieee, 1996.

[116] Computer Aided Engineering System Empowering Simulation by FRIENDSHIP SYSTEMS. CAESES ® v.4.4.2, Germany. URL `https://www.caeses.com/`.

[117] M. D. McKay, R. J. Beckman, and W. J. Conover. A comparison of three methods for selecting values of input variables in the analysis of output from a computer code. *Technometrics*, 21(2):239–245, 1979.

[118] George EP Box. The exploration and exploitation of response surfaces: some general considerations and examples. *Biometrics*, 10(1):16–60, 1954.

[119] Shinri Szymko. *The development of an eddy current dynanometer for evaluation of steady and pulsating turbocharger turbine performance*. PhD Thesis, Imperial College London, London, UK, January 2006.

[120] Jose Francisco Cortell Fores. *Effect of inlet configuration and pulsation on turbocharger performance for enhanced energy recovery*. PhD thesis, Imperial College London, 2018.

[121] Carlos M Fonseca, Luís Paquete, and Manuel López-Ibánez. An improved dimension-sweep algorithm for the hypervolume indicator. In *2006 IEEE international conference on evolutionary computation*, pages 1157–1163. IEEE, 2006.

[122] J. Blank and K. Deb. pymoo: Multi-objective optimization in python. *IEEE Access*, 8:89497–89509, 2020.

[123] H Herwig and F Kock. Direct and indirect methods of calculating entropy generation rates in turbulent convective heat transfer problems. *Heat and mass transfer*, 43:207–215, 2007.

[124] Peter Newton, Colin Copeland, Ricardo Martinez-Botas, and Martin Seiler. An audit of aerodynamic loss in a double entry turbine under full and partial admission. *International Journal of Heat and Fluid Flow*, 33(1):70–80, 2012.

[125] Matthew Elliott, Stephen Spence, Martin Seiler, and Marco Geron. Performance improvement of a mixed flow turbine using 3d blading. In *Turbo Expo: Power for Land, Sea, and Air*, volume 84102, page V02ET39A030. American Society of Mechanical Engineers, 2020.

[126] Fabian Kock and Heinz Herwig. Local entropy production in turbulent shear flows: a high-reynolds number model with wall functions. *International journal of heat and mass transfer*, 47(10-11):2205–2215, 2004.

[127] P Newton, T Palenschat, R Martinez-Botas, and M Seiler. Entropy generation rate in a mixed flow turbine passage. In *International Gas Turbine Congress, Tokyo, Japan, Nov*, pages 15–20, 2015.

[128] Bijie Yang, Peter Newton, and Ricardo Martinez-Botas. Understanding of secondary flows and losses in radial and mixed flow turbines. *Journal of Turbomachinery*, 142(8), 2020.

[129] S Szymko. *The development of an eddy current dynamometer for evaluation of steady and pulsating turbocharger turbine performance*. PhD thesis, Imperial College London, 2006.

Appendix A

Manufactured Parts

This Appendix includes the CAD drawings of the parts (volute, nozzles, rotors and exit duct) manufactured for the ETC testing at Imperial College facilities. Key dimensions are included in the drawings in mm units.

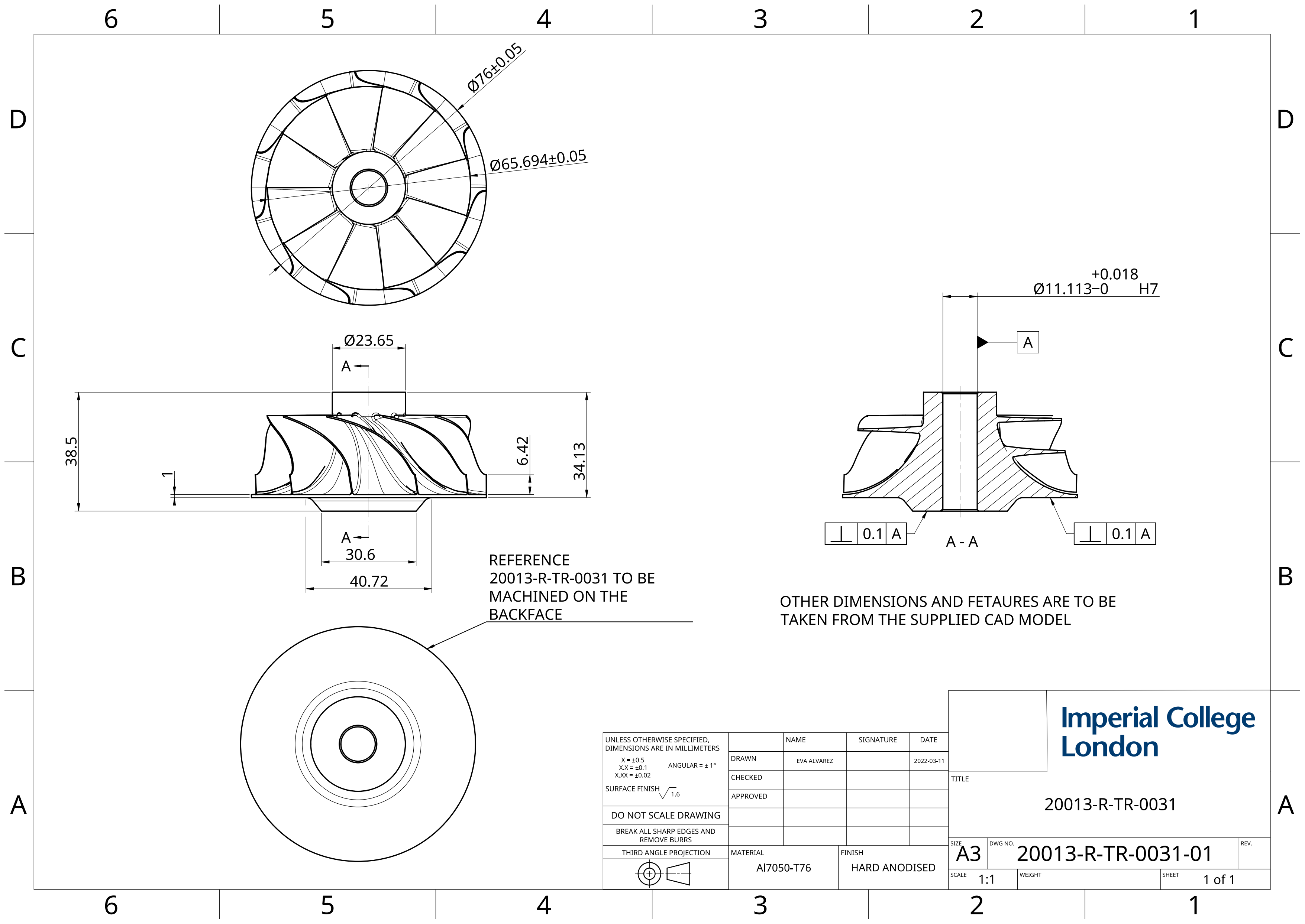

Figure A.1: CAD drawing of the radial fibre rotor

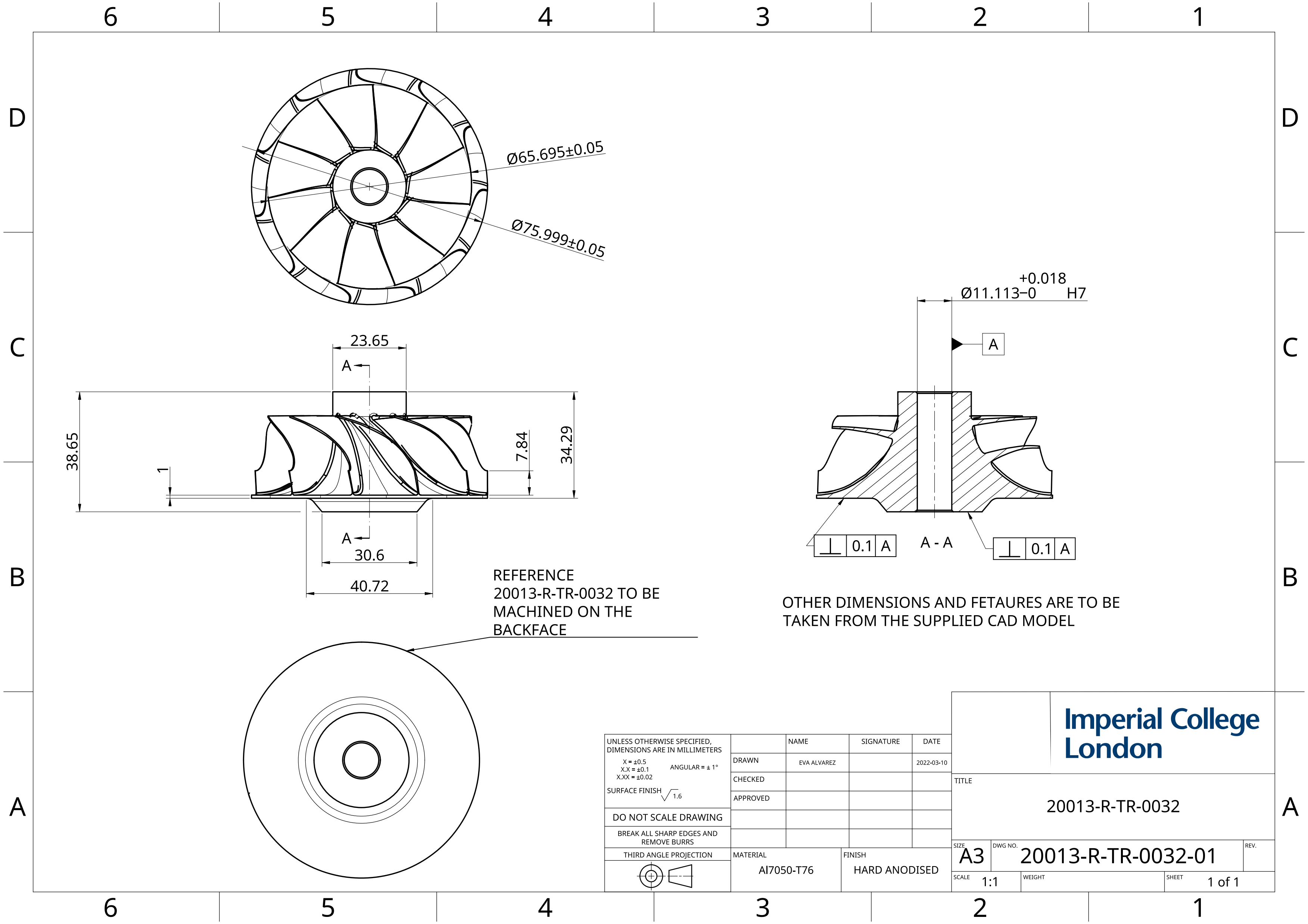

Figure A.2: CAD drawing of the non-radial fibre rotor

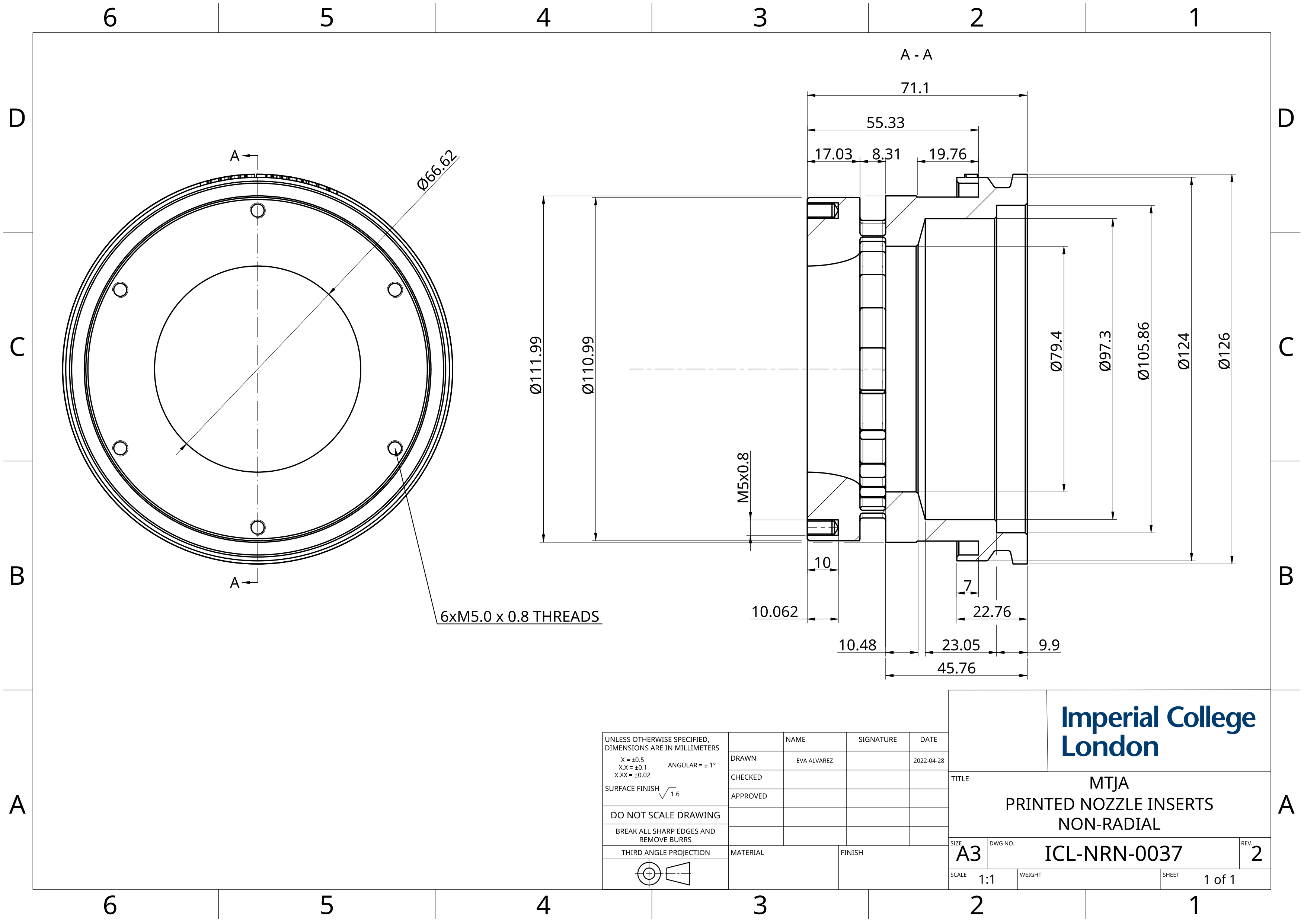

Figure A.3: CAD drawing of the nozzle for the radial fibre rotor

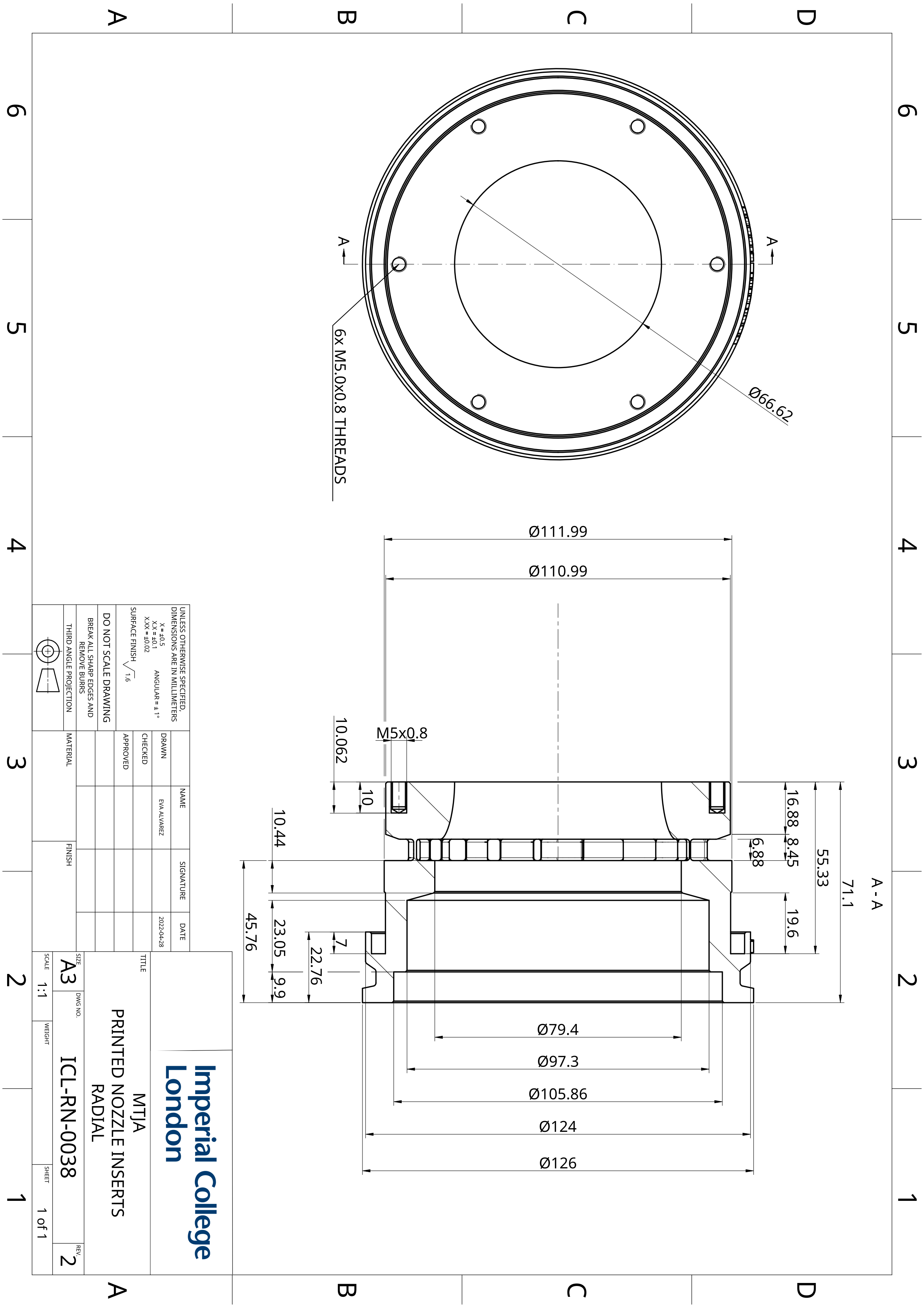

Figure A.4: CAD drawing of the nozzle for the non-radial fibre rotor

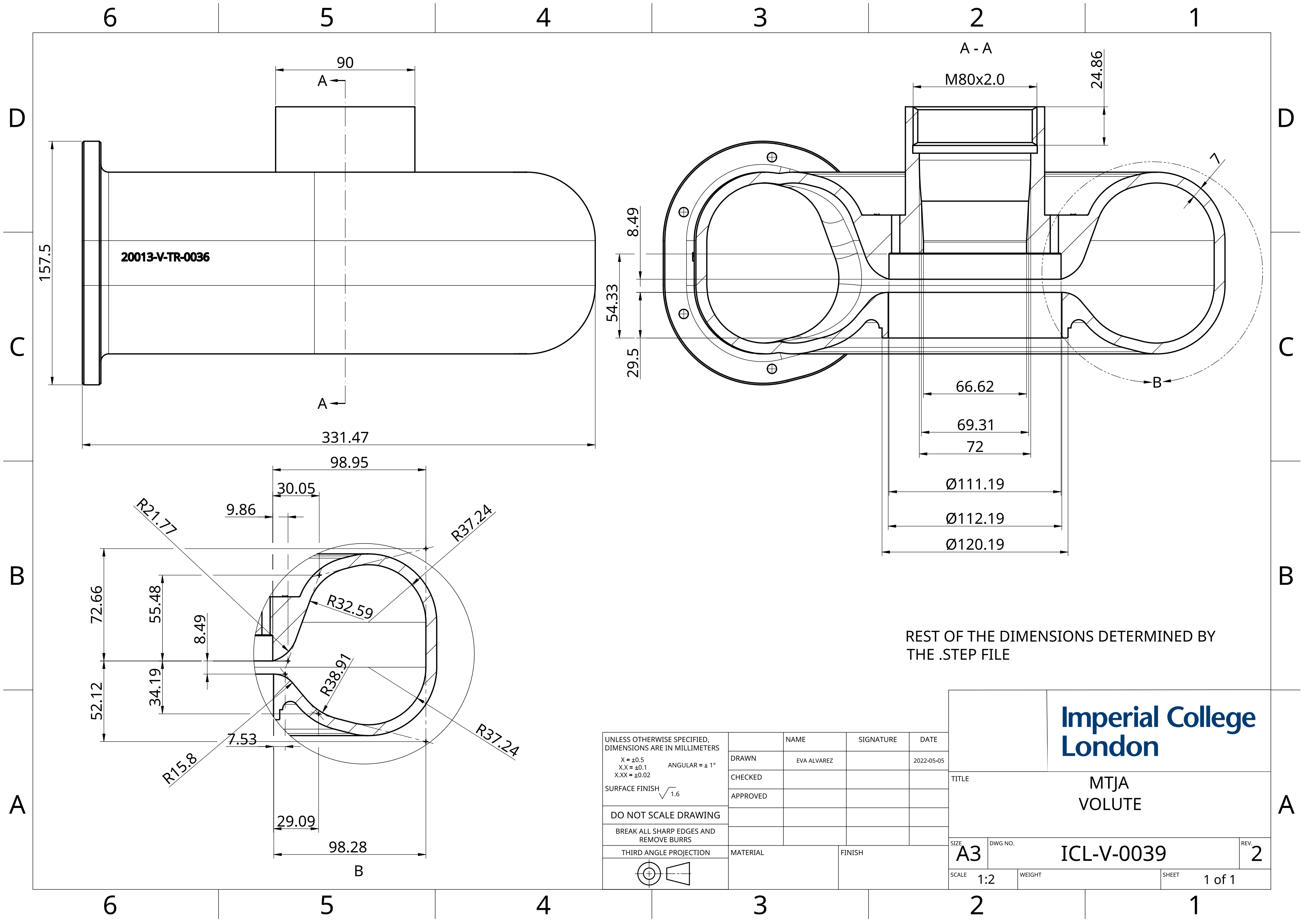

Figure A.5: CAD drawing of the volute

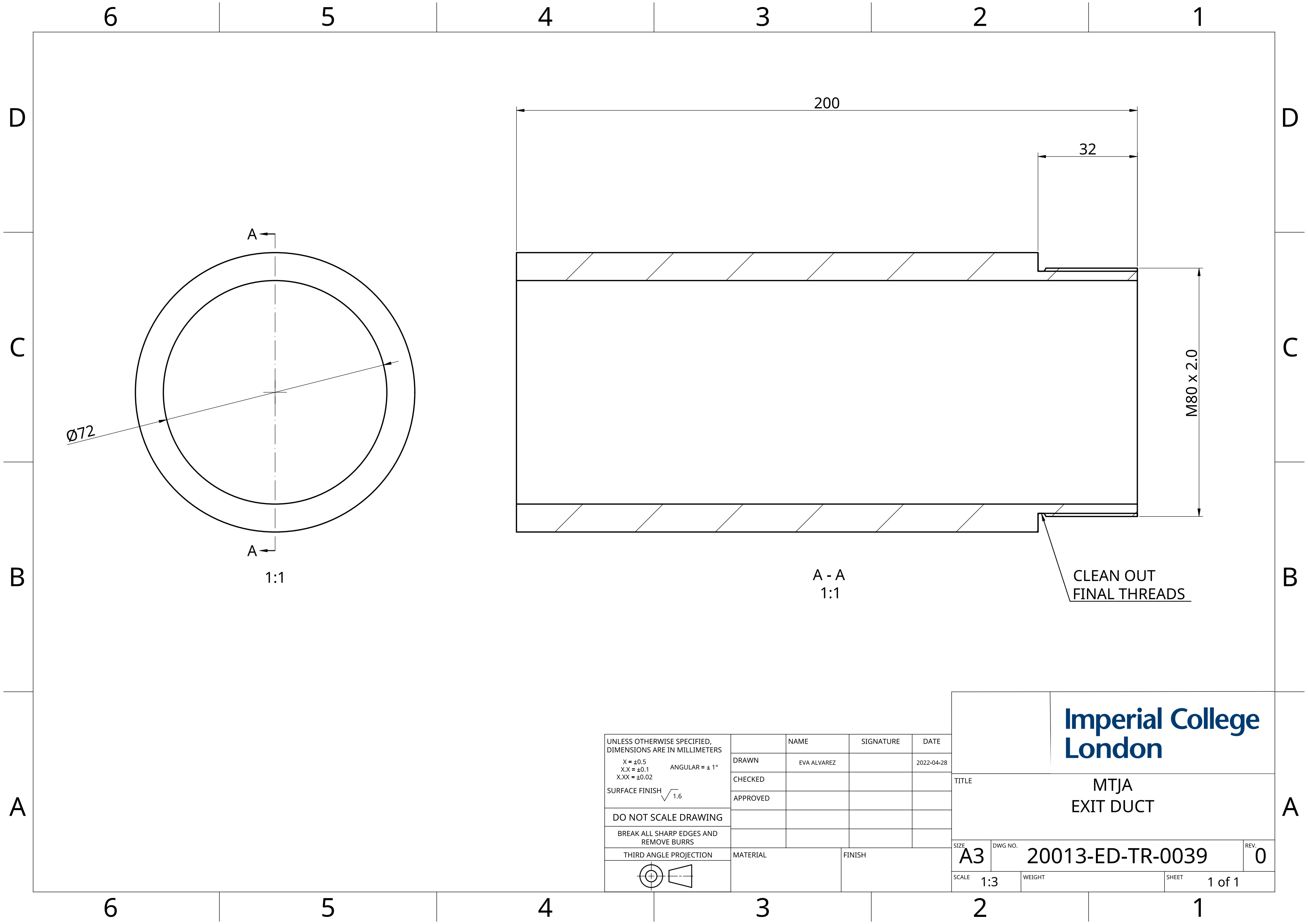

Figure A.6: CAD drawing of the exit duct

Appendix B

Experimental Results

All the experimental and CFD results compared between the radial fibre and non-radial fibre designs are summarised in Fig. B.1 and Fig.B.2 and Fig. B.3 for rotational speeds of $20,000rpm$, $28,000rpm$ and $38,000rpm$, respectively. All the experimental results at different rotational speeds are compared in Fig. B.4 for the radial fibre design and Fig. B.5 for the non-radial fibre design.

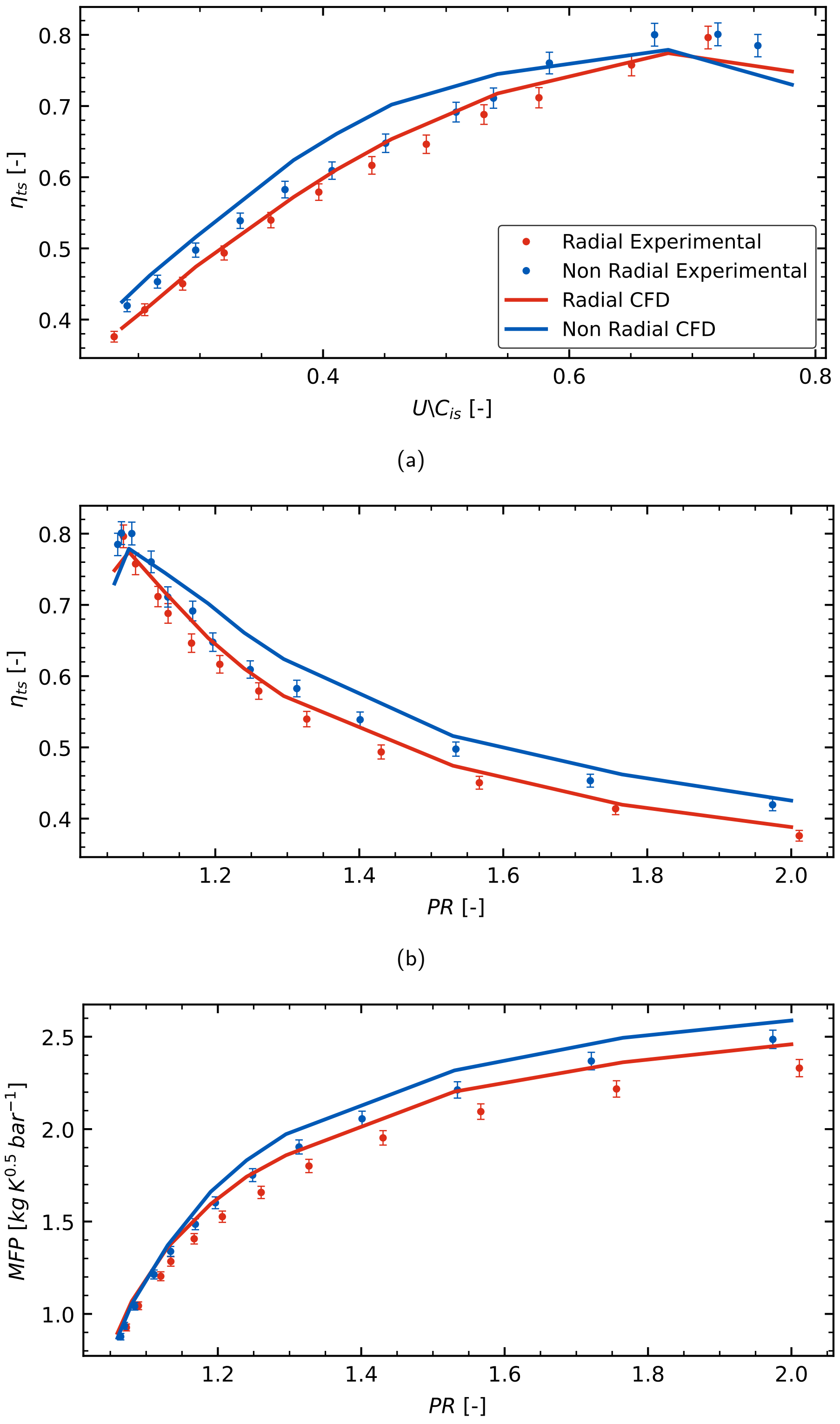

(a)

(b)

(c)

Figure B.1: Experimental (circle marker) and CFD (solid line) performance results for the radial fibre design (red) and non-radial fibre design (blue) for the design speedline, $20,000 rpm$: (a) η_{ts} as function of the velocity ratio, (b) η_{ts} as function of the PR and (c) MFP as function of the PR

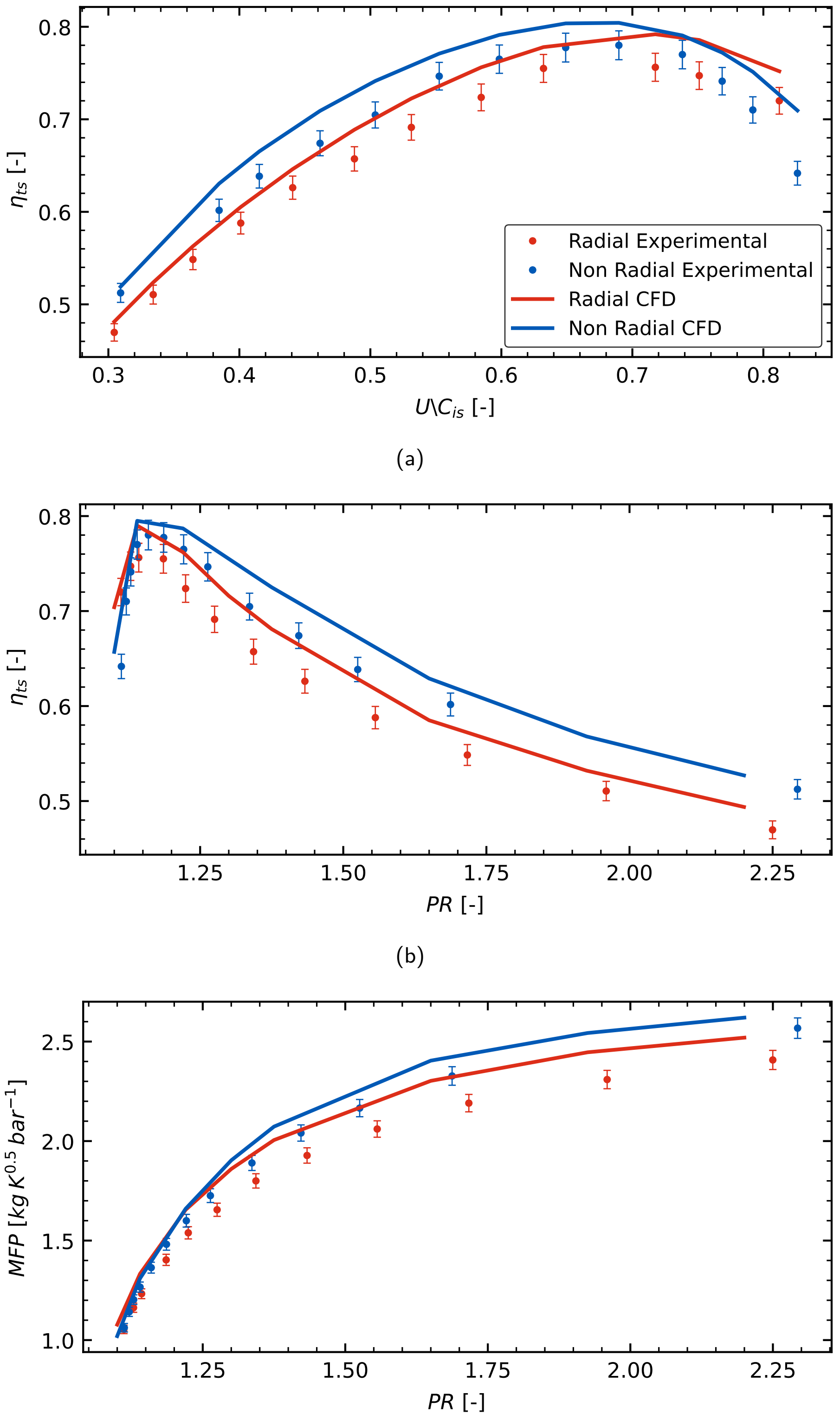

(a)

(b)

(c)

Figure B.2: Experimental (circle marker) and CFD (solid line) performance results for the radial fibre design (red) and non-radial fibre design (blue) for the design speedline, $28,000rpm$: (a) η_{ts} as function of the velocity ratio, (b) η_{ts} as function of the PR and (c) MFP as function of the PR

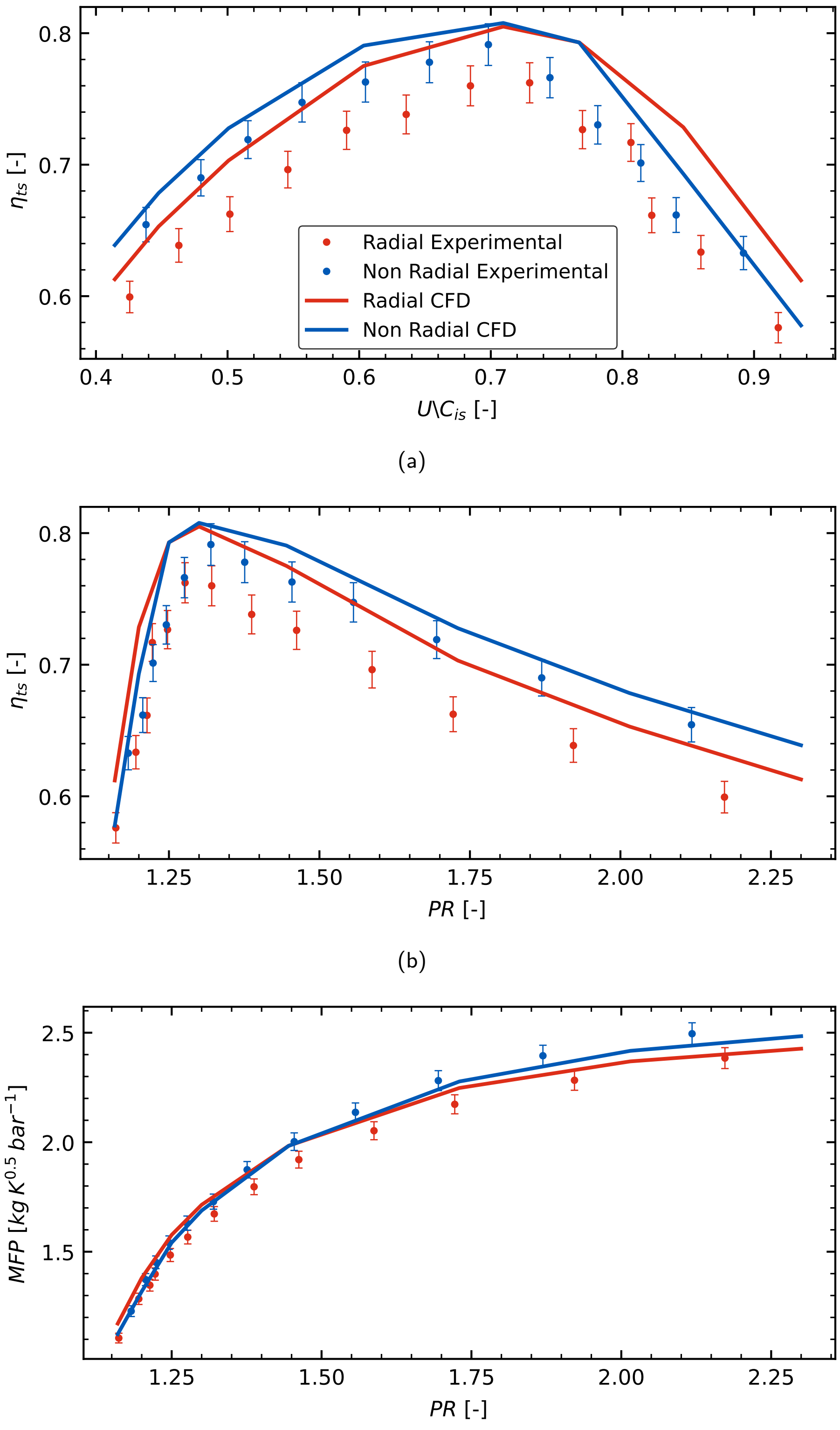

(a)

(b)

(c)

Figure B.3: Experimental (circle marker) and CFD (solid line) performance results for the radial fibre design (red) and non-radial fibre design (blue) for the design speedline, $38,000rpm$: (a) η_{ts} as function of the velocity ratio, (b) η_{ts} as function of the PR and (c) MFP as function of the PR

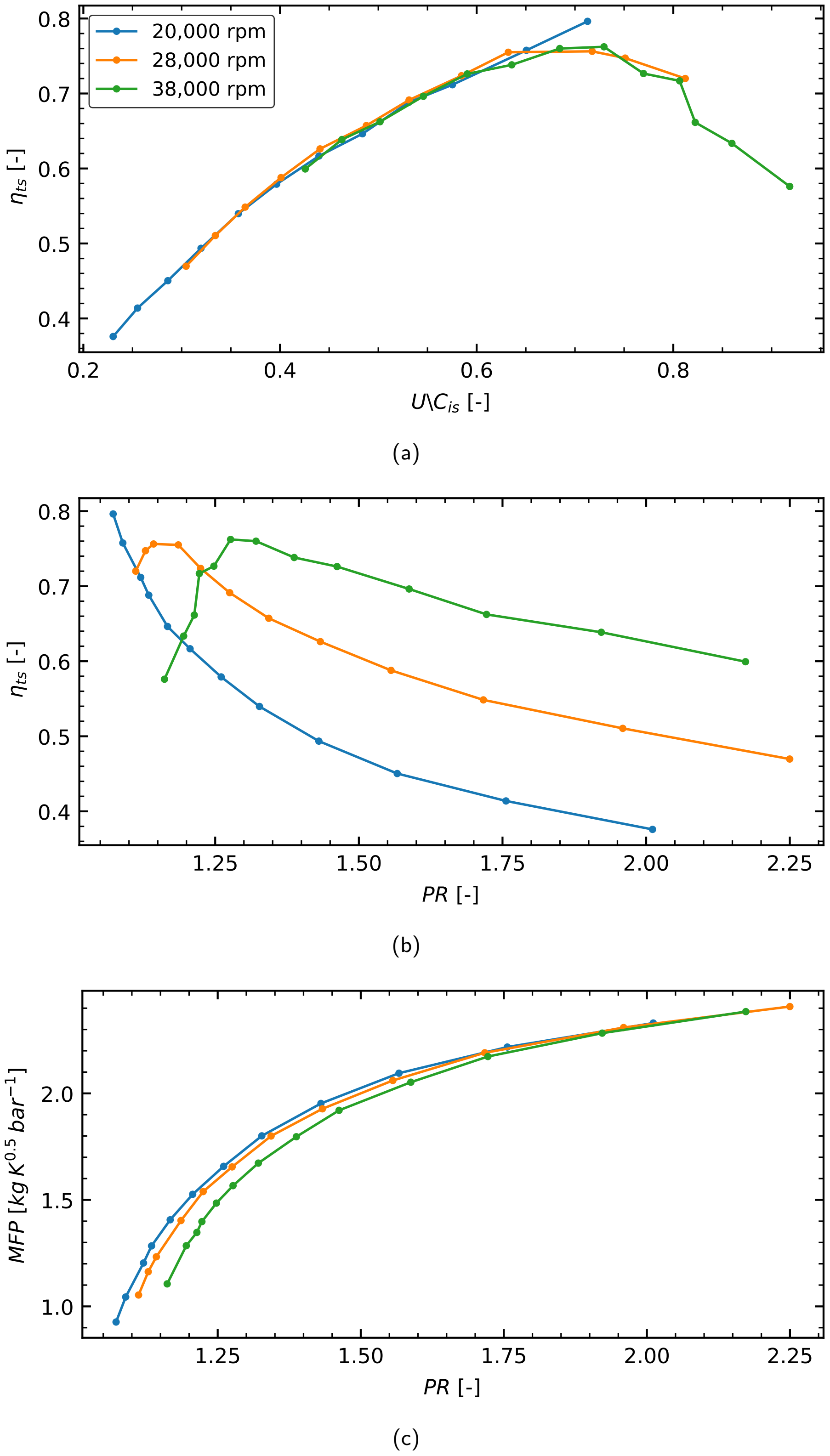

(a)

(b)

(c)

Figure B.4: Experimental performance results for the radial fibre design at different rotational speeds: (a) η_{ts} as function of the velocity ratio, (b) η_{ts} as function of the PR and (c) MFP as function of the PR

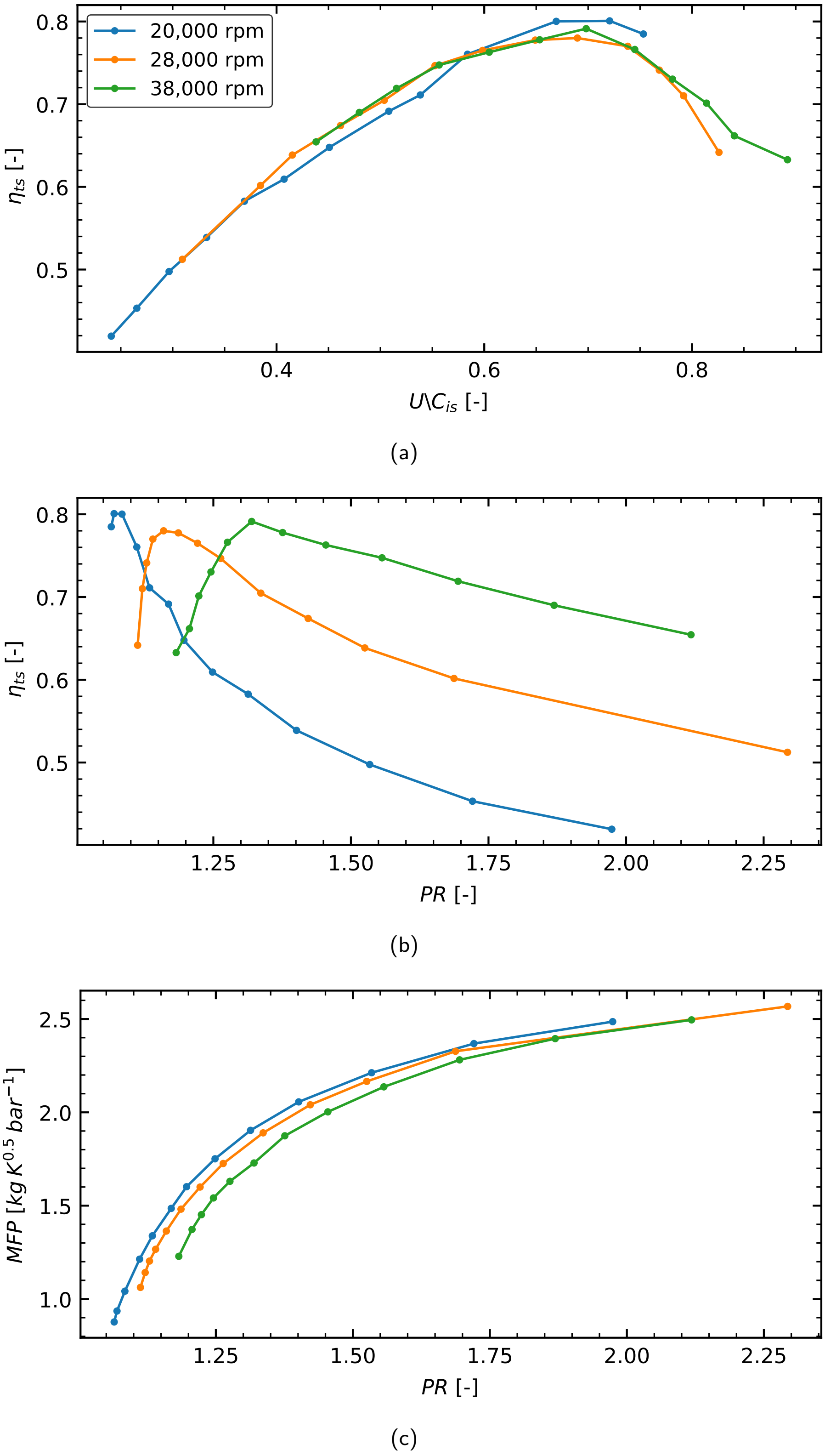

Figure B.5: Experimental performance results for the non-radial fibre design at different rotational speeds: (a) η_{ts} as function of the velocity ratio, (b) η_{ts} as function of the PR and (c) MFP as function of the PR